

Advances in Civil Engineering

Assessment and Prevention Methods of Collapse Disasters

Lead Guest Editor: Xiaohu Zhang

Guest Editors: Gan Feng, Jianping Sun, and Yuanchao Zhang





Assessment and Prevention Methods of Collapse Disasters

Advances in Civil Engineering

Assessment and Prevention Methods of Collapse Disasters

Lead Guest Editor: Xiaohu Zhang

Guest Editors: Gan Feng, Jianping Sun, and
Yuanchao Zhang



Copyright © 2021 Hindawi Limited. All rights reserved.

This is a special issue published in "Advances in Civil Engineering." All articles are open access articles distributed under the Creative Commons Attribution License, which permits unrestricted use, distribution, and reproduction in any medium, provided the original work is properly cited.






Chief Editor

Cumaraswamy Vipulanandan, USA










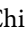



Associate Editors

Chiara Bedon , Italy
Constantin Chalioris , Greece
Ghassan Chehab , Lebanon
Ottavia Corbi, Italy
Mohamed ElGawady , USA
Husnain Haider , Saudi Arabia
Jian Ji , China
Jiang Jin , China
Shazim A. Memon , Kazakhstan
Hossein Moayedi , Vietnam
Sanjay Nimbalkar, Australia
Giuseppe Oliveto , Italy
Alessandro Palmeri , United Kingdom
Arnaud Perrot , France
Hugo Rodrigues , Portugal
Victor Yepes , Spain
Xianbo Zhao , Australia

Academic Editors

José A.F.O. Correia, Portugal
Glenda Abate, Italy
Khalid Abdel-Rahman , Germany
Ali Mardani Aghabaglou, Turkey
José Aguiar , Portugal
Afaq Ahmad , Pakistan
Muhammad Riaz Ahmad , Hong Kong
Hashim M.N. Al-Madani , Bahrain
Luigi Aldieri , Italy
Angelo Aloisio , Italy
Maria Cruz Alonso, Spain
Filipe Amarante dos Santos , Portugal
Serji N. Amirkhanean, USA
Eleftherios K. Anastasiou , Greece
Panagiotis Ch. Anastasopoulos , USA
Mohamed Moafak Arbili , Iraq
Farhad Aslani , Australia
Siva Avudaiappan , Chile
Ozgur BASKAN , Turkey
Adewumi Babafemi, Nigeria
Morteza Bagherpour, Turkey
Qingsheng Bai , Germany
Nicola Baldo , Italy
Daniele Baraldi , Italy

Eva Barreira , Portugal
Emilio Bastidas-Arteaga , France
Rita Bento, Portugal
Rafael Bergillos , Spain
Han-bing Bian , China
Xia Bian , China
Huseyin Bilgin , Albania
Giovanni Biondi , Italy
Hugo C. Biscaia , Portugal
Rahul Biswas , India
Edén Bojórquez , Mexico
Giosuè Boscato , Italy
Melina Bosco , Italy
Jorge Branco , Portugal
Bruno Briseghella , China
Brian M. Broderick, Ireland
Emanuele Brunesi , Italy
Quoc-Bao Bui , Vietnam
Tan-Trung Bui , France
Nicola Buratti, Italy
Gaochuang Cai, France
Gladis Camarini , Brazil
Alberto Campisano , Italy
Qi Cao, China
Qixin Cao, China
Iacopo Carnacina , Italy
Alessio Cascardi, Italy
Paolo Castaldo , Italy
Nicola Cavalagli , Italy
Liborio Cavaleri , Italy
Anush Chandrappa , United Kingdom
Wen-Shao Chang , United Kingdom
Muhammad Tariq Amin Chaudhary, Kuwait
Po-Han Chen , Taiwan
Qian Chen , China
Wei Tong Chen , Taiwan
Qixiu Cheng, Hong Kong
Zhanbo Cheng, United Kingdom
Nicholas Chileshe, Australia
Prinya Chindaprasirt , Thailand
Corrado Chisari , United Kingdom
Se Jin Choi , Republic of Korea
Heap-Yih Chong , Australia
S.H. Chu , USA
Ting-Xiang Chu , China

Zhaofei Chu , China
Wonseok Chung , Republic of Korea
Donato Ciampa , Italy
Gian Paolo Cimellaro, Italy
Francesco Colangelo, Italy
Romulus Costache , Romania
Liviu-Adrian Cotfas , Romania
Antonio Maria D'Altri, Italy
Bruno Dal Lago , Italy
Amos Darko , Hong Kong
Arka Jyoti Das , India
Dario De Domenico , Italy
Gianmarco De Felice , Italy
Stefano De Miranda , Italy
Maria T. De Risi , Italy
Tayfun Dede, Turkey
Sadik O. Degertekin , Turkey
Camelia Delcea , Romania
Cristoforo Demartino, China
Giuseppe Di Filippo , Italy
Luigi Di Sarno, Italy
Fabio Di Trapani , Italy
Aboelkasim Diab , Egypt
Thi My Dung Do, Vietnam
Giulio Dondi , Italy
Jiangfeng Dong , China
Chao Dou , China
Mario D'Aniello , Italy
Jingtao Du , China
Ahmed Elghazouli, United Kingdom
Francesco Fabbrocino , Italy
Flora Faleschini , Italy
Dingqiang Fan, Hong Kong
Xueping Fan, China
Qian Fang , China
Salar Farahmand-Tabar , Iran
Ilenia Farina, Italy
Roberto Fedele, Italy
Guang-Liang Feng , China
Luigi Fenu , Italy
Tiago Ferreira , Portugal
Marco Filippo Ferrotto, Italy
Antonio Formisano , Italy
Guoyang Fu, Australia
Stefano Galassi , Italy

Junfeng Gao , China
Meng Gao , China
Giovanni Garcea , Italy
Enrique García-Macías, Spain
Emilio García-Taengua , United Kingdom
DongDong Ge , USA
Khaled Ghaedi, Malaysia
Khaled Ghaedi , Malaysia
Gian Felice Giaccu, Italy
Agathoklis Giaralis , United Kingdom
Ravindran Gobinath, India
Rodrigo Gonçalves, Portugal
Peilin Gong , China
Belén González-Fonteboa , Spain
Salvatore Grasso , Italy
Fan Gu, USA
Erhan Güneyisi , Turkey
Esra Mete Güneyisi, Turkey
Pingye Guo , China
Ankit Gupta , India
Federico Gusella , Italy
Kemal Hacıefendioğlu, Turkey
Jianyong Han , China
Song Han , China
Asad Hanif , Macau
Hadi Hasanzadehshooiili , Canada
Mostafa Fahmi Hassanein, Egypt
Amir Ahmad Hedayat , Iran
Khandaker Hossain , Canada
Zahid Hossain , USA
Chao Hou, China
Biao Hu, China
Jiang Hu , China
Xiaodong Hu, China
Lei Huang , China
Cun Hui , China
Bon-Gang Hwang, Singapore
Jijo James , India
Abbas Fadhil Jasim , Iraq
Ahad Javanmardi , China
Krishnan Prabhakan Jaya, India
Dong-Sheng Jeng , Australia
Han-Yong Jeon, Republic of Korea
Pengjiao Jia, China
Shaohua Jiang , China

MOUSTAFA KASSEM , Malaysia
Mosbeh Kaloop , Egypt
Shankar Karuppanan , Ethiopia
John Kechagias , Greece
Mohammad Khajehzadeh , Iran
Afzal Husain Khan , Saudi Arabia
Mehran Khan , Hong Kong
Manoj Khandelwal, Australia
Jin Kook Kim , Republic of Korea
Woosuk Kim , Republic of Korea
Vaclav Koci , Czech Republic
Loke Kok Foong, Vietnam
Hailing Kong , China
Leonidas Alexandros Kouris , Greece
Kyriakos Kourousis , Ireland
Moacir Kripka , Brazil
Anupam Kumar, The Netherlands
Emma La Malfa Ribolla, Czech Republic
Ali Lakirouhani , Iran
Angus C. C. Lam, China
Thanh Quang Khai Lam , Vietnam
Luciano Lamberti, Italy
Andreas Lampropoulos , United Kingdom
Raffaele Landolfo, Italy
Massimo Latour , Italy
Bang Yeon Lee , Republic of Korea
Eul-Bum Lee , Republic of Korea
Zhen Lei , Canada
Leonardo Leonetti , Italy
Chun-Qing Li , Australia
Dongsheng Li , China
Gen Li, China
Jiale Li , China
Minghui Li, China
Qingchao Li , China
Shuang Yang Li , China
Sunwei Li , Hong Kong
Yajun Li , China
Shun Liang , China
Francesco Liguori , Italy
Jae-Han Lim , Republic of Korea
Jia-Rui Lin , China
Kun Lin , China
Shibin Lin, China

Tzu-Kang Lin , Taiwan
Yu-Cheng Lin , Taiwan
Hexu Liu, USA
Jian Lin Liu , China
Xiaoli Liu , China
Xuemei Liu , Australia
Zaobao Liu , China
Zhuang-Zhuang Liu, China
Diego Lopez-Garcia , Chile
Cristiano Loss , Canada
Lyan-Ywan Lu , Taiwan
Jin Luo , USA
Yanbin Luo , China
Jianjun Ma , China
Junwei Ma , China
Tian-Shou Ma, China
Zhongguo John Ma , USA
Maria Macchiaroli, Italy
Domenico Magisano, Italy
Reza Mahinroosta, Australia
Yann Malecot , France
Prabhat Kumar Mandal , India
John Mander, USA
Iman Mansouri, Iran
André Dias Martins, Portugal
Domagoj Matesan , Croatia
Jose Matos, Portugal
Vasant Matsagar , India
Claudio Mazzotti , Italy
Ahmed Mebarki , France
Gang Mei , China
Kasim Mermerdas, Turkey
Giovanni Minafò , Italy
Masoomah Mirrashid , Iran
Abbas Mohajerani , Australia
Fadzli Mohamed Nazri , Malaysia
Fabrizio Mollaioli , Italy
Rosario Montuori , Italy
H. Naderpour , Iran
Hassan Nasir , Pakistan
Hossein Nassiraei , Iran
Satheeskumar Navaratnam , Australia
Ignacio J. Navarro , Spain
Ashish Kumar Nayak , India
Behzad Nematollahi , Australia

Chayut Ngamkhanong , Thailand
Trung Ngo, Australia
Tengfei Nian, China
Mehdi Nikoo , Canada
Youjun Ning , China
Olugbenga Timo Oladinrin , United Kingdom
Oladimeji Benedict Olalusi, South Africa
Timothy O. Olawumi , Hong Kong
Alejandro Orfila , Spain
Maurizio Orlando , Italy
Siti Aminah Osman, Malaysia
Walid Oueslati , Tunisia
SUVASH PAUL , Bangladesh
John-Paris Pantouvakis , Greece
Fabrizio Paolacci , Italy
Giuseppina Pappalardo , Italy
Fulvio Parisi , Italy
Dimitrios G. Pavlou , Norway
Daniele Pellegrini , Italy
Gatheeshgar Perampalam , United Kingdom
Daniele Perrone , Italy
Giuseppe Piccardo , Italy
Vagelis Plevris , Qatar
Andrea Pranno , Italy
Adolfo Preciado , Mexico
Chongchong Qi , China
Yu Qian, USA
Ying Qin , China
Giuseppe Quaranta , Italy
Krishanu ROY , New Zealand
Vlastimir Radonjanin, Serbia
Carlo Rainieri , Italy
Rahul V. Ralegaonkar, India
Raizal Saifulnaz Muhammad Rashid, Malaysia
Alessandro Rasulo , Italy
Chonghong Ren , China
Qing-Xin Ren, China
Dimitris Rizos , USA
Geoffrey W. Rodgers , New Zealand
Pier Paolo Rossi, Italy
Nicola Ruggieri , Italy
JUNLONG SHANG, Singapore

Nikhil Saboo, India
Anna Saetta, Italy
Juan Sagaseta , United Kingdom
Timo Saksala, Finland
Mostafa Salari, Canada
Ginevra Salerno , Italy
Evangelos J. Sapountzakis , Greece
Vassilis Sarhosis , United Kingdom
Navaratnarajah Sathiparan , Sri Lanka
Fabrizio Scozzese , Italy
Halil Sezen , USA
Payam Shafigh , Malaysia
M. Shahria Alam, Canada
Yi Shan, China
Hussein Sharaf, Iraq
Mostafa Sharifzadeh, Australia
Sanjay Kumar Shukla, Australia
Amir Si Larbi , France
Okan Sirin , Qatar
Piotr Smarzewski , Poland
Francesca Sollecito , Italy
Rui Song , China
Tian-Yi Song, Australia
Flavio Stochino , Italy
Mayank Sukhija , USA
Piti Sukontasukkul , Thailand
Jianping Sun, Singapore
Xiao Sun , China
T. Tafsirojjaman , Australia
Fujiao Tang , China
Patrick W.C. Tang , Australia
Zhi Cheng Tang , China
Weerachart Tangchirapat , Thailand
Xiixin Tao, China
Piergiorgio Tataranni , Italy
Elisabete Teixeira , Portugal
Jorge Iván Tobón , Colombia
Jing-Zhong Tong, China
Francesco Trentadue , Italy
Antonello Troncone, Italy
Majbah Uddin , USA
Tariq Umar , United Kingdom
Muahmmad Usman, United Kingdom
Muhammad Usman , Pakistan
Mucteba Uysal , Turkey

Ilaria Venanzi , Italy
Castorina S. Vieira , Portugal
Valeria Vignali , Italy
Claudia Vitone , Italy
Liwei WEN , China
Chunfeng Wan , China
Hua-Ping Wan, China
Roman Wan-Wendner , Austria
Chaohui Wang , China
Hao Wang , USA
Shiming Wang , China
Wayne Yu Wang , United Kingdom
Wen-Da Wang, China
Xing Wang , China
Xiuling Wang , China
Zhenjun Wang , China
Xin-Jiang Wei , China
Tao Wen , China
Weiping Wen , China
Lei Weng , China
Chao Wu , United Kingdom
Jiangyu Wu, China
Wangjie Wu , China
Wenbing Wu , China
Zhixing Xiao, China
Gang Xu, China
Jian Xu , China
Panpan , China
Rongchao Xu , China
HE YONGLIANG, China
Michael Yam, Hong Kong
Hailu Yang , China
Xu-Xu Yang , China
Hui Yao , China
Xinyu Ye , China
Zhoujing Ye, China
Gürol Yildirim , Turkey
Dawei Yin , China
Doo-Yeol Yoo , Republic of Korea
Zhanping You , USA
Afshar A. Yousefi , Iran
Xinbao Yu , USA
Dongdong Yuan , China
Geun Y. Yun , Republic of Korea

Hyun-Do Yun , Republic of Korea
Cemal YİĞİT , Turkey
Paolo Zampieri, Italy
Giulio Zani , Italy
Mariano Angelo Zanini , Italy
Zhixiong Zeng , Hong Kong
Mustafa Zeybek, Turkey
Henglong Zhang , China
Jiupeng Zhang, China
Tingting Zhang , China
Zengping Zhang, China
Zetian Zhang , China
Zhigang Zhang , China
Zhipeng Zhao , Japan
Jun Zhao , China
Annan Zhou , Australia
Jia-wen Zhou , China
Hai-Tao Zhu , China
Peng Zhu , China
QuanJie Zhu , China
Wenjun Zhu , China
Marco Zucca, Italy
Haoran Zuo, Australia
Junqing Zuo , China
Robert Černý , Czech Republic
Süleyman İpek , Turkey

Contents

Parametric Sensitivity Study of Deep Excavation in Singapore Old Alluvium Formation

Lanting Wu, Jianping Sun , and Yuqiang Tong

Research Article (11 pages), Article ID 8644288, Volume 2021 (2021)

Classification and Disintegration Characteristics of the Carboniferous Rocks in Guangxi, China

Peng Mo, Junhui Luo , Decai Mi, Zhenchao Chang , Haifeng Huang, Tao Zhang, Guanhua Sun, Yan Li, Ling Zeng , and Shihai Wang 

Research Article (9 pages), Article ID 8929808, Volume 2021 (2021)

The Deformation Analysis of a Deep Frame Top-Down Excavation in Downtown Shanghai Based on the 3D FEM

Ting Bai  and Dong Xie



Research Article (9 pages), Article ID 2947544, Volume 2021 (2021)

Dynamic Response Study of Impulsive Force of Debris Flow Evaluation and Flexible Retaining Structure Based on SPH-DEM-FEM Coupling

Bailong Li , Changming Wang , Yanying Li , and Shuhua Zhang 


Research Article (12 pages), Article ID 9098250, Volume 2021 (2021)

Numerical Simulation Analysis of Slope Instability and Failure of Limestone Mine in Weibei

Kuiming Liu , Hui Li, Shihui Pang, Meng Mi , Jianping Chen, and Kui Sun


Research Article (14 pages), Article ID 5991348, Volume 2021 (2021)

Displacement Measurements and Numerical Analysis of Long-Term Rock Slope Deformation at Higashi-Shikagoe Limestone Quarry, Japan

Clement A. Amagu , Cheng Zhang, Jun-ichi Kodama, Kazuyuki Shioya, Tomoyuki Yamaguchi, Atsushi Sainoki, Daisuke Fukuda, Yoshiaki Fujii, and Mostafa Sharifzadeh


Research Article (15 pages), Article ID 1316402, Volume 2021 (2021)

Numerical Simulations on the Extinguishing Effect of Water Mist System with Different Parameters of Longitudinal Ventilation in Curve Tunnel Fire

Zhizhong Liu, Chen Chen, Mu Liu, Song Wang, and Yuzhu Liu 

Research Article (13 pages), Article ID 7373685, Volume 2021 (2021)

Quantitative Characterization of Heterogeneity in Different Reservoir Spaces of Low-Permeability Sandstone Reservoirs and Its Influence on Physical Properties

Fengjuan Dong , Na Liu, Zhen Sun, Xiaolong Wei, Haonan Wang, Junxiang Nan, and Dazhong Ren


Research Article (8 pages), Article ID 2399016, Volume 2021 (2021)

Experimental Study on the Influence of Freezing Pressure on the Uniaxial Mechanical Properties of Ice

Baosheng Wang , Weihao Yang, Peixin Sun, Xin Huang , Yaodan Zhang, and Fengjun Chen



Research Article (15 pages), Article ID 8651467, Volume 2021 (2021)

Research on Dynamic Stability Optimization of Rock Spreader considering Prevention of Geological Subsidence and Local Collapse in Reclamation Area

Baofu Kou , Pengliang Huo, and Xin Shi




Research Article (20 pages), Article ID 3409929, Volume 2021 (2021)

Microscale Mineral and Pore Structure Characterization of the Low-Permeability Sandstone in the Ordos Basin, China

Jie Gao , Zhen Sun, Jianping Liu, Chenyang Zhao, Dazhong Ren, Rongjun Zhang, Tingting Li, and Dengke Liu 

Research Article (9 pages), Article ID 6448271, Volume 2021 (2021)

Optimization of Stope Structure Parameters Based on the Mined Orebody at the Meishan Iron Mine

Mingzhi Sun , Fengyu Ren , and Hangxing Ding 


Research Article (14 pages), Article ID 8052827, Volume 2021 (2021)

Prediction and Evaluation of Rockburst Based on Depth Neural Network

Jin Zhang , Mengxue Wang, and Chuanhao Xi

Research Article (11 pages), Article ID 8248443, Volume 2021 (2021)

Study on the Mixed Materials Proportion of Stratum Based on the Modelling Experiment

Yijun Zhou and Tao Xu 

Research Article (13 pages), Article ID 9352208, Volume 2021 (2021)

Research Article

Parametric Sensitivity Study of Deep Excavation in Singapore Old Alluvium Formation

Lanting Wu,¹ Jianping Sun ,^{1,2} and Yuqiang Tong¹

¹China Communications Construction Company Limited (Singapore Branch), 1 Changi Business Park Central #02-110, Changi City, Singapore

²Nanyang Technological University, 50 Nanyang Ave, Singapore

Correspondence should be addressed to Jianping Sun; sunj0030@e.ntu.edu.sg

Received 17 August 2021; Revised 5 December 2021; Accepted 6 December 2021; Published 20 December 2021

Academic Editor: Qian Chen

Copyright © 2021 Lanting Wu et al. This is an open access article distributed under the Creative Commons Attribution License, which permits unrestricted use, distribution, and reproduction in any medium, provided the original work is properly cited.

Deep excavation supported by vertical retaining walls together with strutting system is commonly used in Singapore for the construction of underground infrastructure. In this paper, a series of numerical scenarios simulated by PLAXIS software are carried out to study the influence of different design parameters such as pre-auger loosening effect, the embedded depth of retaining wall into the stiff soil layer, and the elastic modulus of the ground improvement layer on excavation design especially on strut force, retaining wall deflection, and bending moment. The results show that there is high risk if only a single set of parameters are used as input to predict the performance of the retaining system. Sensitivity analysis shall be carried out to evaluate the effects of these parameter variations within a reasonable range on strut force, retaining wall deflection, and bending moment.

1. Introduction

Deep excavation supported by vertical retaining walls together with the strutting system is commonly used in Singapore for the construction of underground infrastructure. The widely used retaining wall types in Singapore are sheet pile, soldier pile with timber/sheet pile lagging, contiguous bored piles (CBP), secant bored piles (SBP), and diaphragm walls [1–4]. The excavation will induce lateral wall deflection [5] and vertical ground surface settlement which have negative impact on the nearby structures [6]. According to Singapore regulation [7], the allowable maximum wall deflection shall be less than 0.5%–1% of the excavation depth depending on the geotechnical condition and nearby structures.

There are four main types of geological materials in Singapore [8]: (a) Bukit Timah granite, (b) the sedimentary rocks [9–11], (c) old alluvium (OA), and (d) Kallang formation. The OA is about 2 to 7 million years old and extends from southern Johor to the east of Singapore [12]. The thickness of this formation is generally very high and has been proved to a depth up to 195 m. The OA varies in its

weathering degree from fully weathered at the top to unweathered at the bottom. The soil profile above the OA layer mainly consists deep deposit of soft marine clay overlain by a layer of reclamation fill.

At some areas, it was found that the reclaimed fill had been compacted to achieve a minimum relative density of 70% and the marine clay layer was in an over-consolidated stage. At such areas, the retaining wall installation (sheet pile or soldier pile) may become very difficult and pre-auger drilling is often used to loosen the soil for the installation. However, few scholars have systematically analysed the pre-auger loosen effect on the retaining wall performance [13].

According to the study by Shirlaw et al. [14], the base heave failure mode will occur when the clay with low shear strength is below the final excavation level directly and the retaining walls are not within the stiff soil layers. Therefore, the retaining walls are required to extend into OA formation at the current practice in Singapore. However, the effect of embedded length into OA on the performance of the retaining system is not understood very well by designers. At the same time, in order to effectively control wall movement and associated ground movement, the ground improvement

layer (GIW) is proposed at the base of the excavation in area where there is a significant depth of clay below the final excavation level [15–18]. For ground improvement in Singapore, the common practice in general is that the test results from all the samples during the construction stage will be higher than the design values. Most designers consider that the higher strength and stiffness of the ground improvement layer do not have any negative impact on the retaining wall system which needs further study in detail.

A parametric sensitivity study is carried out using finite-element modelling in the software PLAXIS 2D based on an actual project that we were involved in. The effects of pre-augering, embedment depth of retaining wall into OA formation, and strength of the ground improvement layer are studied in order to obtain an in-depth understanding of retaining wall design for deep excavation.

2. Case Study

2.1. Background. One actual project was studied which is located at the eastern part of Singapore. Typical soil profile consisted of 5 m to 15 m thick of sand fill, 5 m to 25 m thick of marine clay, and competent OA of varying weathering degree. Excavation was 35 m wide and 8.5 m to 16.7 m deep. With the consideration of existing site conditions, soldier pile wall and sheet pile lagging was proposed as temporary retaining wall with the laced strutting system. The retaining wall toe embedment criteria were that the soldier pile is to be embedded 3 m into OA formation. The construction method was bottom-up construction. According to the geology information, the excavation depth, and permanent structure, the whole site was classified into 13 typical excavation zones. A typical section with a depth of 10 m was studied in this paper. There were 3 layers of steel struts with 6 m spacing horizontally and 3 m spacing vertically. In order to effectively control wall movement and associated ground movement, a ground improvement slab of 3 m thick was proposed at the base of the excavation in area where there was a significant depth of marine clay below the final excavation level. The ground improvement slab was installed prior to excavation. Three rows of permanent bored piles with 1.5 m diameter piles at the centre row and 1.2 m diameter at the side rows were designed to support the permanent structure. The bored piles were at 6 m centre to centre along the longitudinal direction and were embedded into the OA layer. The bored piles and ground improvement layer worked together with retaining wall and steel struts as a robust earth retaining system. The summary of earth retaining wall system and their structural properties used in the analysis were shown in Table 1.

2.2. Finite-Element Modelling. The finite-element method offers the designer an analytical tool that can simulate the complex facets of the earth retaining structures except unquantifiable variables such as workmanship or geological uncertainties. It has the ability to predict both earth pressures and deformations with very minimal simplifying assumptions required. Both structure and soil are considered

interactively so that the effects of structural flexibility are taken into account. The commonly used commercial software in Singapore for finite-element modelling in geotechnical engineering is PLAXIS.

The excavation length of this project was 469 m which is 13.4 times the excavation width. Therefore, the 2D model was adopted based on the assumption of plane strain condition. To simulate discontinuous wall elements, such as soldier piles, the stiffness in the PLAXIS model was represented on a 'unit' length basis and the contribution of sheet pile lagging was not considered in the analysis. The boundary conditions were as follows.

The lower boundary has zero displacement at both the horizontal and vertical direction. The left and right vertical boundaries were only free at vertical direction, and the upper boundary was free from any direction.

Because the Mohr–Coulomb model (MC) may produce unrealistic soil behaviour [19], the hardening soil (HS) model became more popular in deep excavation analysis in Singapore which can generate more realistic soil response [20, 21]. The HS model was used in this study and the soil parameters in Table 2 were from the back analysis of similar geotechnical conditions in Singapore [15]. Fill layer was modelled as drained, and marine clay and old alluvium were modelled using the undrained B method.

Several ground improvement methods can be used to improve the properties of the soft ground such as wet speed mixing (WSM), deep cement mixing (DCM), and jet grouting pile (JGP). For this project, DCM was carried out as the main ground improvement method and the 1 m gap between DCM and the retaining wall was sealed by JGP. Quality of the DCM and JGP was confirmed by carrying out soil investigation boreholes and testing. There were 4 numbers of boreholes for each 1000 cubic meters of the treated soil. Unconfined compression tests on the coring samples were carried out to obtain the undrained strength C_u and elastic modulus E . The test results show that the ratio between elastic modulus E and undrained strength C_u mainly varies from 300 to 500 when C_u is less than 1200 kPa (Figure 1). In this project, the design values of E and C_u are 140 MPa and 300 kPa, respectively.

The construction sequence is modelled as follows: (1) initial condition, (2) activate the uniform load 20 kPa for 20 m length away from retaining wall at ground level of 2.5 mSHD to consider the surcharge load, (3) activate retaining wall and set ground improvement layer at the base of the excavation and activate bored piles, (4) excavate to 1 m below strut S1 which is at 2 mSHD and install strut S1 and apply preloading of 600 kN, (5) excavate to 1 m below strut S2 which is at -1 mSHD and install strut S2 and apply preloading of 1200 kN, (6) excavate to 1 m below strut S3 which is at -4 mSHD and install strut S3 and apply preloading of 1500 kN, and (7) excavate to final excavation level (FEL) at -7.5 mSHD. The construction of permanent structure, removal of struts, and backfill are not presented in this paper because the maximum wall deflection, wall bending moment, and strut force occur during the excavation stage for this project.

TABLE 1: Earth retaining wall system and their structural properties.

Type	Size	EA(kN)	EI (kNm ² /m)
Retaining wall	UB 762 × 267 × 147 kg/m @ 1.8 m c/c + hat-type sheet pile 10H	—	1.97e ⁵
Strut S1 at level 1	2 × UB 610 × 229 × 125 kg/m	6.64e ⁶	—
Strut S2 at level 2	2 × UB 610 × 229 × 155 kg/m	8.32e ⁶	—
Strut S3 at level 3	2 × UB 610 × 229 × 195 kg/m	7.98e ⁶	—
Bored pile at centre (30 m into OA)	1.5 m diameter	2.35e ⁷	3.31e ⁶
Bored pile at side (20 m into OA)	1.2 m diameter	1.75e ⁷	1.36e ⁶

TABLE 2: HS soil parameters based on the back analysis of similar geotechnical conditions [15].

Soil type	Model	γ (kN/m)	Poisson's ratio (ν_{ur})	$E_{50,ref}$ (kN/m ²)	$E_{ode,ref}$ (kN/m ²)	$E_{ur,ref}$ (kN/m ²)	c_{ref} (kN/m ²)/Cu (kN/m ²)	Φ (°)	Power m
Fill	Drained	20	0.15	1000	1300	3000	0.1	25	0.5
Marine clay	Undrained	16	0.2	3740	3740	11220	18.7	0	0
OA	Undrained	20	0.2	1.4e ⁵	1.4e ⁵	4.3e ⁵	250	0	0

Notes: $E_{50,ref}$ effective secant modulus (50% stress level) at confining pressure of 100 kPa; $E_{ode,ref}$ effective 1D compression modulus at a vertical stress of 100 kPa; $E_{ur,ref}$ effective unloading-reloading modulus at a confining pressure of 100 kPa; m , modulus exponent controlling the stress dependency of the modulus.

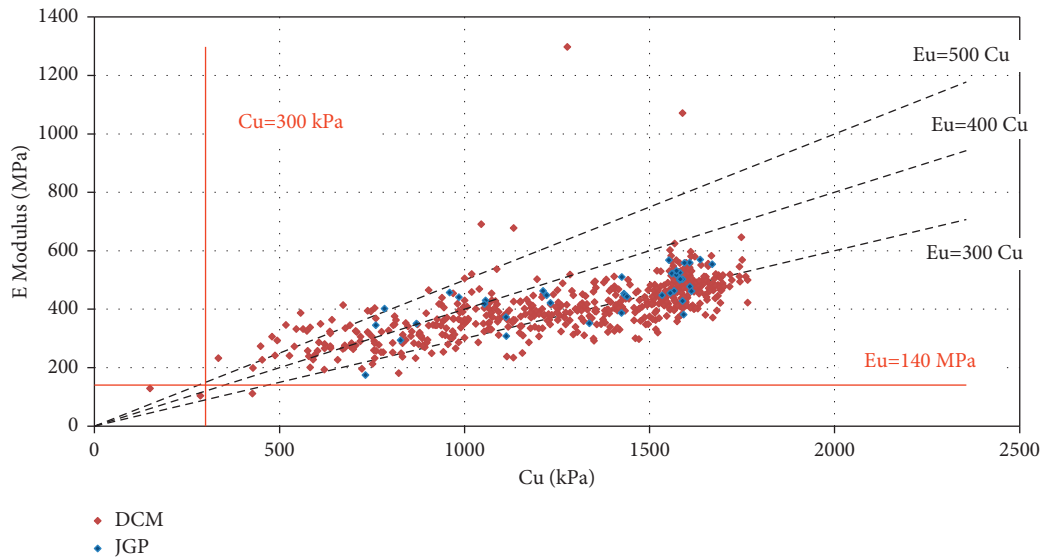


FIGURE 1: Relation between elastic stiffness and undrain strength of the ground improvement layer from coring samples.

The ground water level outside excavation is assumed at the ground level, and the ground water level within excavation will follow the level of each excavation stage, and the water pressure distribution is calculated in each step using the steady stage groundwater flow model.

The modelling area is 200 m in width and 80 m in depth, as shown in Figure 2, which is large enough to minimize the boundary effect on the simulation results.

To validate the numerical model, the wall deflection from numerical simulation was compared with the in-field monitoring results which were obtained from inclinometer readings (Figure 3). When the excavation level was 1 m below S2 strut, the maximum monitoring wall deflection was 14 mm and the maximum FE predicted wall deflection is 18 mm. These minor differences were accepted and the numerical model can be used for the parametric sensitivity study.

3. Parametric Sensitivity Study

3.1. Effect of Pre-Augering. At some areas, the reclaimed fill had been compacted and the marine clay layer was in an over-consolidated stage. And the retaining wall installation (sheet pile or soldier pile) became very difficult, and pre-auger drilling (Figure 4) was proposed to loosen the soil for the installation. The effect of pre-augering on the surrounding soil loosening shall be studied in detail below.

In PLAXIS 2D, active and passive earth pressures against the retaining walls are not input explicitly but are automatically generated in the program as a consequence of the changes of stress distribution in the finite-element mesh. Related to the wall lateral pressures, the wall adhesion is a factor of the soil strength and is defined in the model using Rinter. For clay, the suggested Rinter is 0.5 to account for

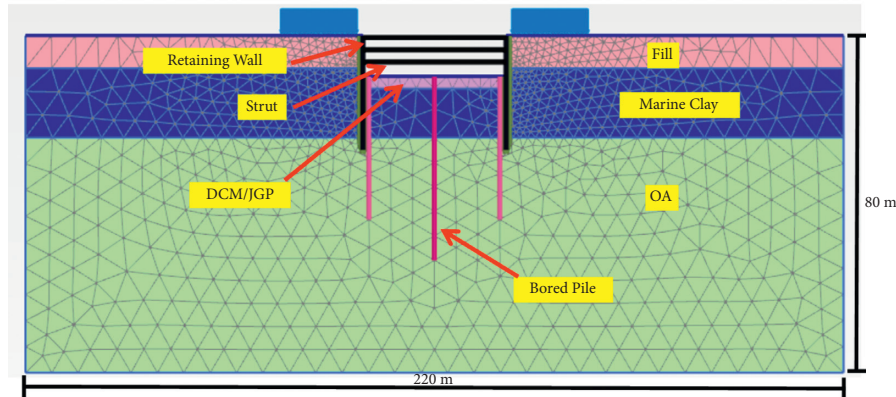


FIGURE 2: FEM mesh used in PLAXIS analysis.

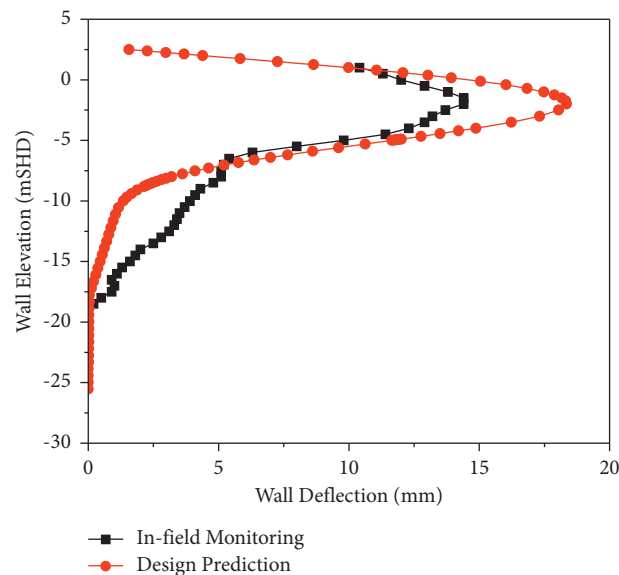


FIGURE 3: Observed and predicted wall deflection (excavation 1 m below strut S2).

high wall-soil slip compared to sands, where Rinter is generally taken as 0.67 [22]. In order to consider the loosening effect of pre-auger, a new reduction k with range between 0 and 1 is used and the overall wall adhesion is $k \times Rinter$. The lower bound value of $k=0$ means there is practically no friction between the retaining walls which is the extreme condition of pre-auger [13], and the upper bound value of $k=1$ means there is no loosening effect of pre-auger.

To evaluate the effects of pre-auguring on the retaining wall system, five cases with different k values were simulated. In cases 1–5, the k values were 1, 0.8, 0.6, 0.4, and 0.2, respectively. Figure 5 shows the relations of between different k values and wall deflection when the excavation reaches the final excavation level. Figure 5 illustrates that the soft marine clay below the final excavation level cannot provide sufficient horizontal restraint of the retaining wall, and the maximum wall deflection usually occurs below the final excavation level and the maximum wall deflection increases as k value decreases. The maximum wall deflection only increases from 50 mm to 55 mm when k value decreases

from 1 to 0.4. However, the maximum wall deflection increases abruptly from 55 mm to 68 mm when k value decreases from 0.4 to 0.2. Figure 6 presents the relations between different k values and the wall bending moment, and the similar trend demonstrates that the maximum bending moment increases from 388 kNm/m to 343 kNm/m and from 343 kNm/m to 488 kNm/m when k value decreases from 1 to 0.4 and from 0.4 to 0.2, respectively. Clearly, the pre-auger loosening effect only has considerable effect when the wall adhesion is very low. The pre-augering effect on the maximum strut force is also studied, as shown in Figure 7, and it indicates that there is insignificant impact on the strut force.

Therefore, the pre-augering loosening effect on the retaining wall is not significant if the wall adhesion does not reduce too much. In order to minimize the pre-augering effect, the pre-auger should be carried out on the excavation side of the retaining wall and before the ground improvement work so that the subsequent ground improvement work would almost cancel the effect of pre-augering. At the same time, the auger flights were rotated into the ground in



FIGURE 4: Pre-augering process to loosen soil for retaining wall installation.

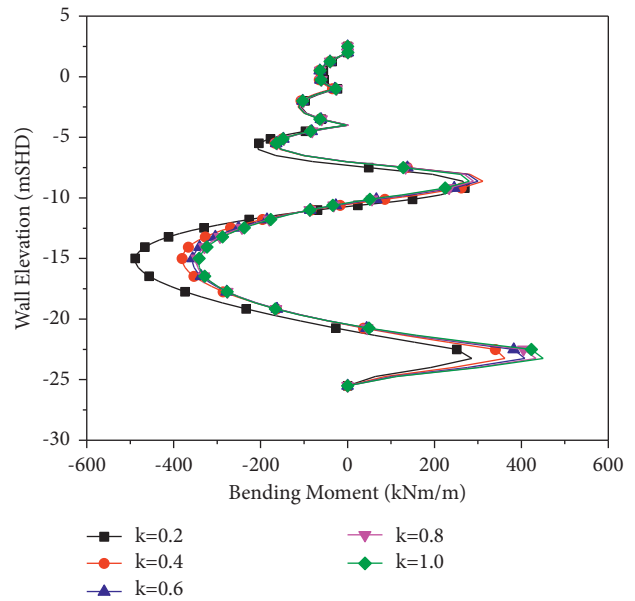


FIGURE 6: The relations between pre-augering loosening effect and wall bending moment at the excavation to the FEL stage.

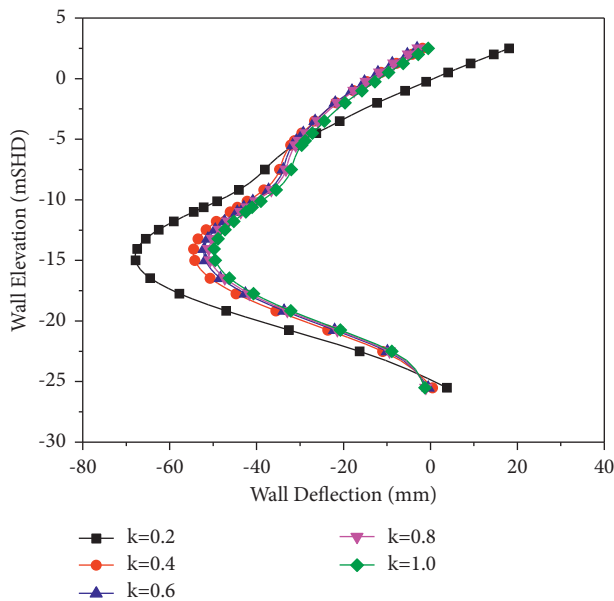


FIGURE 5: The relations between pre-augering loosening effect and wall deflections at the excavation to the FEL stage.

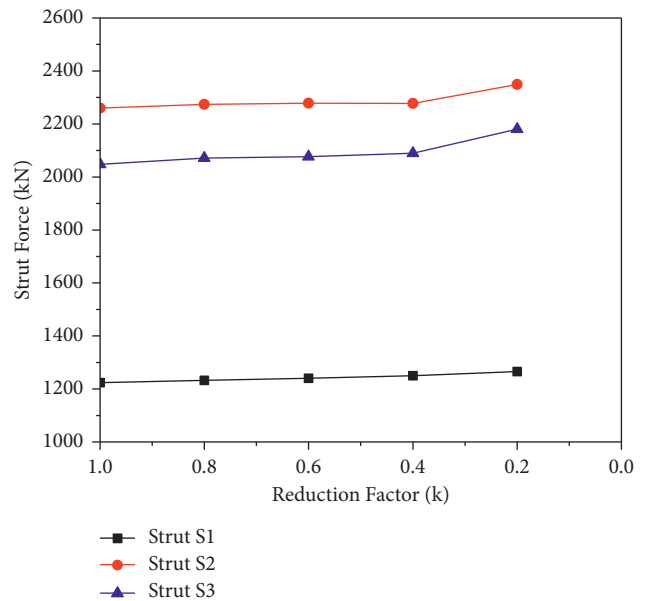


FIGURE 7: The relations between pre-augering loosening effect and the maximum strut forces.

one direction and removed from the ground by rotating in a counter direction leaving the sheared soil in place in the ground.

3.2. Effect of Retaining Wall Embedded Length. To evaluate the effects of the wall embedded depth in OA on retaining wall system, six cases with different wall embedded lengths into OA (-1, 0, 1, 2, 3, 4, and 5 m) were simulated. As shown in Figure 8, the wall deflection above the soffit of the ground

improvement layer was almost identical. However, the wall deflection at the retaining toe reduced from 38 mm to 0 mm when the embedded length increased from -1 m to 1 m. Figure 9 illustrates the effect of embedded length into OA on the wall bending moment envelop for the whole excavation process. The bending moments within the marine clay and the OA layer increased as the embedded length into OA increased and the bending moment above the soffit of the ground improvement layer was unaffected. Therefore, the increase of embedded length into OA only has impact on the

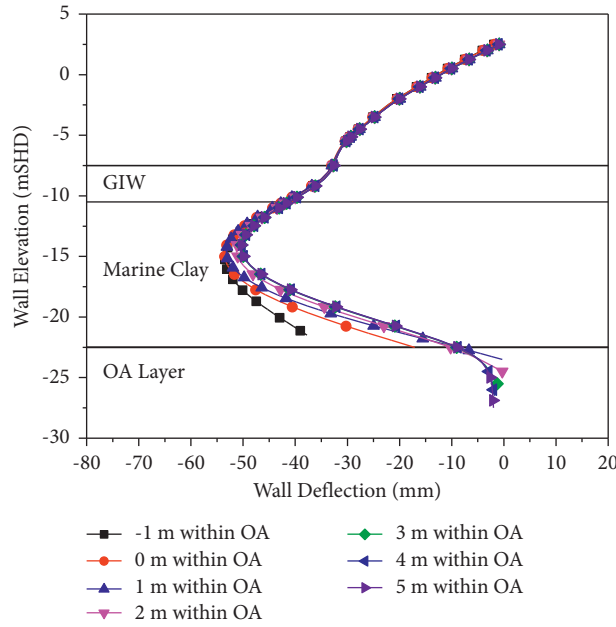


FIGURE 8: The effect of retaining wall embedded length into OA on wall deflection.

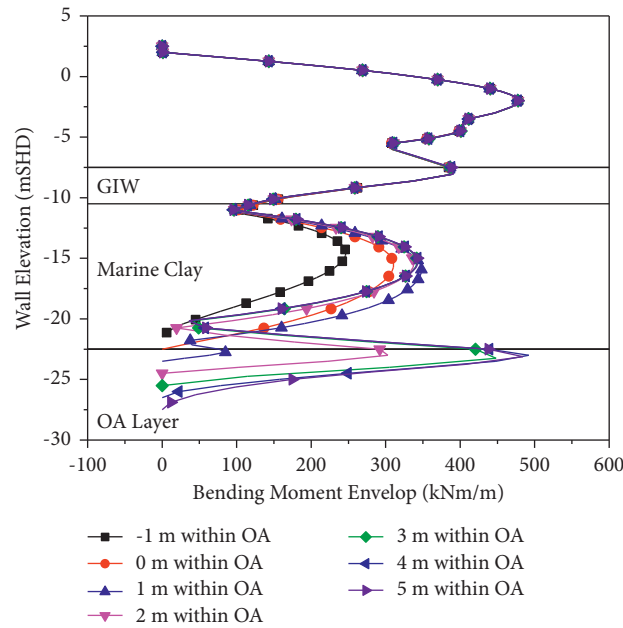


FIGURE 9: The effect of retaining wall embedded length into OA on wall bending moment.

retaining wall below the soffit of the ground improvement layers. Although the bending moment increases at some locations below the soffit of the ground improvement layer, it still is less than the maximum bending moment which is above the final elevation level except the case with the embedded length of 5 m. Therefore, the retaining wall section does not need to be increased for most cases.

On the contrary, when the embedded length was increased, the bending and tension forces of the bored pile were reduced. However, the effect became minor when the embedded length was larger than 3 m, as illustrated in Figures 10–12.

In brief, if a retaining system includes a ground improvement layer, the retaining wall can be embedded 2-3 m into the stiff soil layer, and extra depth will not reduce the wall deflection and bored pile forces.

3.3. Effect of Ground Improvement Layer. The ground improvement layer was modelled as the Mohr–Coulomb model (undrained B). The elastic modulus E_u varied from 120 to 600 MPa, as listed in Table 3. The wall deflection and the bending moment are shown in Figures 13–15 for different E_u values.

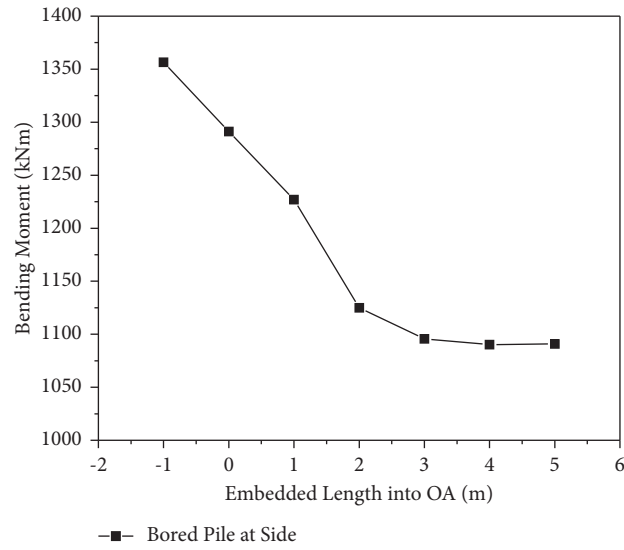


FIGURE 10: The effect of retaining wall embedded length into OA on bending moment of bore pile at side.

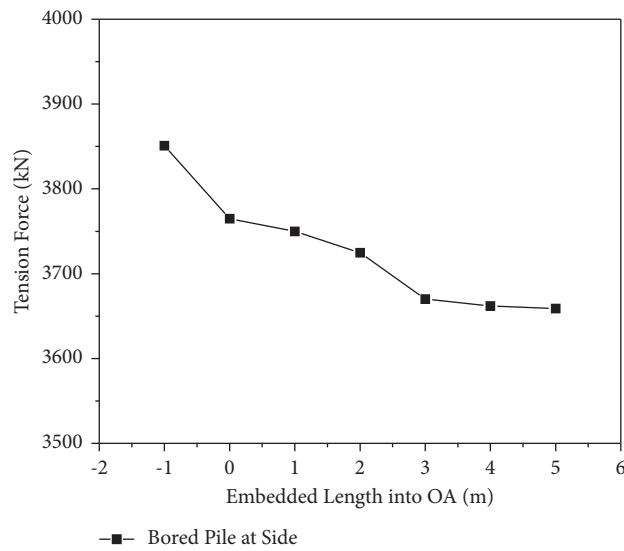


FIGURE 11: The effect of retaining wall embedded length into OA on tension force of bore pile at side.

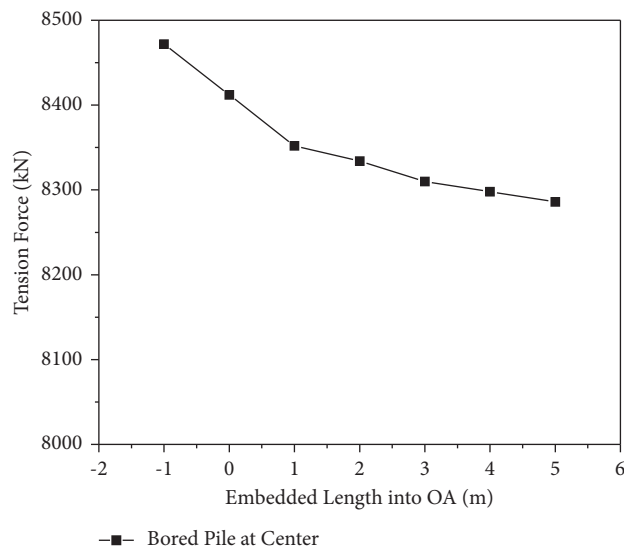


FIGURE 12: The effect of retaining wall embedded length into OA on tension force of bore pile at centre.

TABLE 3: Ground improvement layer parameters.

Case	Model	γ (kN/m ³)	Poisson's ratio (ν_{ur})	Eu (MPa)	Cu (kPa)
Case 1	Mohr-Coulomb	16	0.3	120	300
Case 2				240	600
Case 3				360	900
Case 4				480	1200
Case 5				600	1500

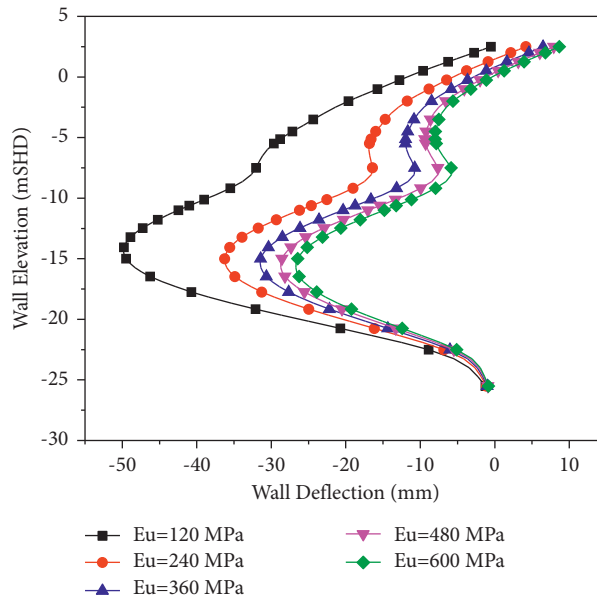


FIGURE 13: The effect of ground improvement Eu on wall deflection.

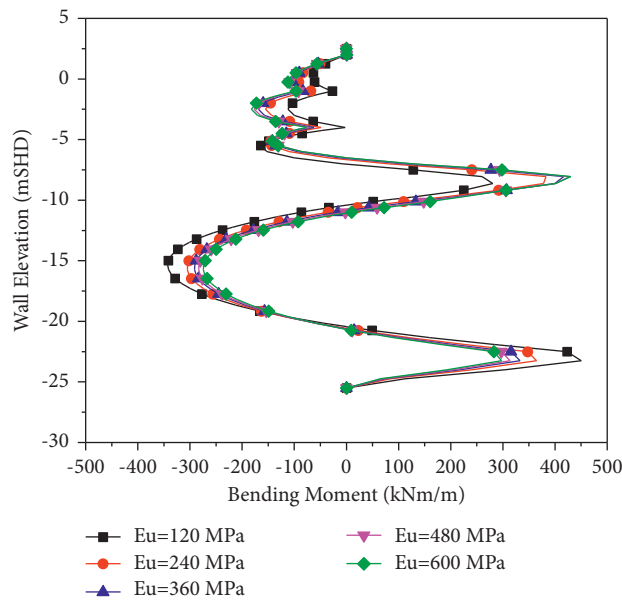


FIGURE 14: The effect of ground improvement Eu on wall bending moment.

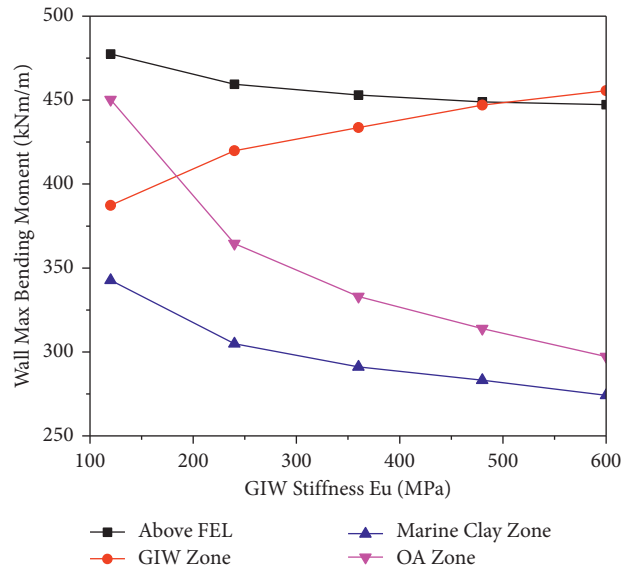


FIGURE 15: The effect of ground improvement Eu on maximum wall bending moment.

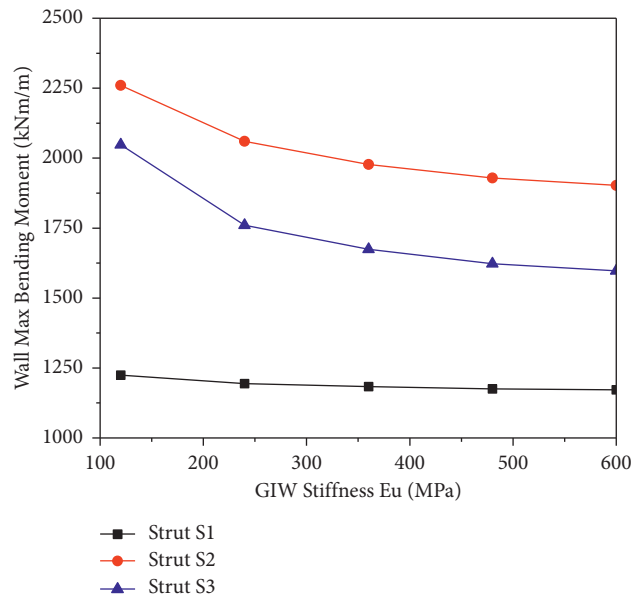


FIGURE 16: The effect of ground improvement Eu on strut force.

Clearly, the elastic modulus of the ground improvement layer had a significant impact on the support system. When the elastic modulus increased, the wall deflection decreased rapidly, as shown in Figure 13. The wall bending moment at the ground improvement layer increased as Eu increased and the wall bending moment at other area decreased, as illustrated in Figures 14 and 15. Therefore, it is recommended that the design of retaining wall with the ground improvement layer should consider both the lower and upper bound of Eu at the ground improvement layer because the wall may be under designed. The effect of Eu on

the strut forces was demonstrated in Figure 16, and it showed that the strut force near the ground improvement layer had more reduction compared with the struts at the shallower level.

The horizontal compressive stress of the ground improvement layer at the retaining wall interface area is shown in Figure 17. The maximum compressive stress located at the top part of the ground improvement layer which indicated that the possible failure model would start from that zone. Therefore, more attention should be paid to test results of the samples from the top of the coring.

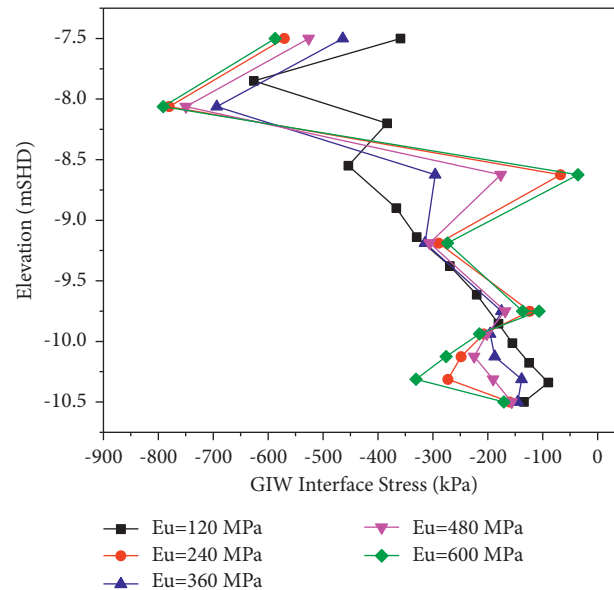


FIGURE 17: The effect of ground improvement E_u on GIW interface stress.

4. Conclusions

Based on a series of numerical simulations for an actual project in Singapore, the key findings are listed as below:

- (1) The pre-auger will loosen the surrounding soil of the retaining wall and the wall deflection, and bending moments increase as the wall adhesion reduces. However, the pre-augering loosening effect on the retaining wall is not significant if the wall adhesion does not reduce too much.
- (2) The retaining wall-embedded length into OA has contribution to reduce the wall toe movement and has positive impact to reduce the forces on the bored piles. Therefore, soldier pile walls are recommended to be 2-3 m within the OA layer.
- (3) The retaining wall bending moment at the ground improvement layer increases and the forces in struts located below the ground improvement layer decreases as elastic modulus of the ground improvement layer increases.
- (4) Based on the above parametric sensitivity analysis, there is high risk if only a single set of parameters are used as input to predict the performance of the retaining system. Sensitivity analysis shall be carried out to evaluate the effects of these parameter variations within a reasonable range on strut force, retaining wall deflection, and bending moment.

Data Availability

The data used to support the findings of the study are available from the corresponding author upon reasonable request.

Conflicts of Interest

The authors declare that they have no conflicts of interest.

References

- [1] C. Murugamoorthy, C. M. Kho, B. G. Vaidya, S. K. Tang, and T. Subramanian, "Behaviour of various support systems for deep excavations, changi airport underground MRT station," in *Proceedings of the RTS Conference*, Singapore, 2003.
- [2] H. O. Nick, B. S. Carlus, P. R. Prabhakara, and J. B. Vontivilu, *A Review of the Performance of Little India Station during Construction*, Underground Singapore, Singapore, 2014.
- [3] C. Zhu, M. C. He, X. H. Zhang, Z. G. Tao, Q. Yin, and L. F. Li, "Nonlinear mechanical model of constant resistance and large deformation bolt and influence parameters analysis of constant resistance behavior," *Rock and Soil Mechanics*, vol. 42, no. 7, pp. 1911–1924, 2021.
- [4] Y. H. S. Low, C. C. D Ng, Y. P. Y. Chin, and S. K. E. Ting, "A Singapore case history of temporary removable ground anchor design to TR26: 2010," *The IES Journal Part A: Civil & Structural Engineering*, vol. 5, no. 3, pp. 181–194, 2012.
- [5] A. T. C. Goh, F. Zhang, W. Zhang, Y. Zhang, and H. Liu, "A simple estimation model for 3D braced excavation wall deflection," *Computers and Geotechnics*, vol. 83, pp. 106–113, 2017.
- [6] P. Fok, B. H. Neo, K. H. Goh, and D. Wen, "Assessing the impact of excavation-induced movements on adjacent buildings," *The IES Journal Part A: Civil & Structural Engineering*, vol. 5, no. 3, pp. 195–203, 2012.
- [7] K. S. Yang, *Advisory Note 1/09 on Earth Retaining or Stabilizing Structures (ERSS)*, Building and Construction Authority, Singapore, 2009.
- [8] J. S. Sharma, J. Chu, and J. Zhao, "Geological and geotechnical features of Singapore: an overview," *Tunnelling and Underground Space Technology*, vol. 14, no. 4, pp. 419–431, 1999.

- [9] Q. Yin, J. Wu, C. Zhu, M. He, Q. Meng, and H. Jing, "Shear mechanical responses of sandstone exposed to high temperature under constant normal stiffness boundary conditions," *Geomechanics and Geophysics for Geo-Energy and Geo-Resources*, vol. 7, no. 2, p. 35, 2021.
- [10] X. Li, K. Peng, J. Peng, and H. Xu, "Effect of cyclic wetting-drying treatment on strength and failure behavior of two quartz-rich sandstones under direct shear," *Rock Mechanics and Rock Engineering*, vol. 54, no. 11, pp. 5953–5960, 2021.
- [11] X. S. Li, K. Peng, J. Peng, and D. Hou, "Experimental investigation of cyclic wetting-drying effect on mechanical behavior of a medium-grained sandstone," *Engineering Geology*, vol. 293, Article ID 106335, 2021.
- [12] K. S. Wong, W. Li, J. N. Shirlaw, J. C. W. Ong, D. Wen, and J. C. W. Hsu, "Old alluvium: engineering properties and braced excavation performance," in *Proceedings of the Underground Singapore*, Singapore, November 2001.
- [13] A. Piling, *Handbook*, ArcelorMittal Commercial RPS UK Ltd, Solihull, UK, 9th edition, 2016.
- [14] J. N. Shirlaw, T. S. Tan, and K. S. Wong, "Deep excavations in Singapore marine clay," in *Proceedings of the 5th International Conference of TC28 of the ISSMGE*, vol. 13-28, Amsterdam, Netherlands, March 2006.
- [15] G. J. Li, K. S. Wong, and P. B. Ng, "Back analysis of a braced excavation with DCM ground improvement," in *Proceedings of the Underground Singapore*, Singapore, January 2011.
- [16] G. A. Pittaro and G. Murphy, "Deep Excavation with Ground Improvement- a Study Using Statistics and Back Analysis from a Monitored Excavation," in *Proceedings of the Underground Singapore*, Singapore, September 2018.
- [17] W. Zhang, L. Hong, Y. Li, R. Zhang, A. T. C. Goh, and H. Liu, "Effects of jet grouting slabs on responses for deep braced excavations," *Underground Space*, vol. 6, 2020.
- [18] W. Zhang, Y. Li, A. T. C. Goh, and R. Zhang, "Numerical study of the performance of jet grout piles for braced excavations in soft clay," *Computers and Geotechnics*, vol. 124, Article ID 103631, 2020.
- [19] T. L. Guow, "Common mistakes on the application of Plaxis 2D in analyzing excavation problems," *International Journal of Applied Engineering Research*, vol. 9, no. 21, pp. 8291–8311, 2014.
- [20] T. Schanz, P. A. Vermeer, and P. G. Bonnier, "The hardening soil model: formulation and verification," *Beyond 2000 in computational geotechnics*, pp. 281–296, Routledge, Thames, UK, 1999.
- [21] P. L. Teo and K. S. Wong, "Application of the hardening soil model in deep excavation analysis," *The IES Journal Part A: Civil & Structural Engineering*, vol. 5, no. 3, pp. 152–165, 2012.
- [22] A. Gaba, S. Hardy, L. Doughty, W. Powrie, and D. Selematas, *Guidance on embedded retaining wall design*, Construction Industry Research and Information Association, London, UK, 2017.

Research Article

Classification and Disintegration Characteristics of the Carboniferous Rocks in Guangxi, China

Peng Mo,¹ Junhui Luo ,^{1,2} Decai Mi,² Zhenchao Chang ,¹ Haifeng Huang,¹ Tao Zhang,³ Guanhua Sun,⁴ Yan Li,⁴ Ling Zeng ,⁵ and Shihai Wang ¹

¹Guangxi Beitou Transportation Maintenance Technology Group Co., Ltd., Nanning, Guangxi 530029, China

²Guangxi Communication Design Group Co., Ltd., Nanning, Guangxi 530029, China

³Faculty of Engineering, China University of Geosciences, Wuhan 430074, China

⁴State Key Laboratory of Geomechanics and Geotechnical Engineering, Institute of Rock and Soil Mechanics, Chinese Academy of Sciences, Wuhan, Hubei 430071, China

⁵School of Civil Engineering, Changsha University of Science & Technology, Changsha 410114, China

Correspondence should be addressed to Shihai Wang; wangsh214@126.com

Received 22 August 2021; Revised 16 October 2021; Accepted 25 October 2021; Published 19 November 2021

Academic Editor: Xiaohu Zhang

Copyright © 2021 Peng Mo et al. This is an open access article distributed under the Creative Commons Attribution License, which permits unrestricted use, distribution, and reproduction in any medium, provided the original work is properly cited.

To investigate the disintegration characteristics of the carbonaceous rocks in Guangxi Province, the typical carbonaceous rocks in the section exposed by the Hechi-Baise Expressway were investigated in this study. First, based on their mineral compositions and contents, the carbonaceous rocks were divided into four types: carbonate chert, carbonaceous argillaceous limestone, carbonaceous illite clay mudstone, and carbonaceous illite clay shale. Then, through indoor wet-dry cyclic disintegration test, the disintegration characteristics of the four types of rocks were studied. The test results showed the following: (1) the disintegration residues of the carbonate chert and the carbonaceous argillaceous limestone decrease linearly as the number of wetting-drying cycles increases. (2) The disintegration index of the carbonaceous illite clay mudstone and the carbonaceous illite clay shale decreases exponentially as the number of wetting-drying cycles increases. (3) As the number of wetting-drying cycles increases, the disintegration index curves of the carbonaceous illite clay mudstone and the carbonaceous illite clay shale samples gradually become stable until the disintegration of the samples is completed. (4) The disintegration of carbonaceous rocks is mainly affected by the clay content, followed by the structural form, but it cannot be ignored.

1. Introduction

Carbonaceous rocks are normally defined as hand-soiling black or grayish black claystones containing large quantities of carbonized organic matter as a result of tectonic or sedimentary processes. Carbonaceous rocks are widely found throughout China, particularly in Guangxi, Guizhou, and Yunnan provinces [1]. Its unique geographical location and extensive tectonic and sedimentary history account for the complicated tectonic conditions in Guangxi Province, where carbonaceous rocks have been exposed by many road and bridge construction projects over the past years. Some of the examples include the construction sections along the Liuzhai-Renshui Secondary Highway, the Shuiren-Nanning

Expressway, the Yizhou-Liuzhai Expressway, the Liuzhai-Hechi Expressway, the Hechi-Baise Primary Expressway, the Jinchengjiang-Yizhou Primary Highway, and the Yizhou-Liuzhou Expressway. Despite their distinct regional physical properties and mineral contents, the carbonaceous rocks in Guangxi Province are quite similar in terms of their engineering characteristics. Typically, these engineering characteristics include a high initial strength, low weathering and slake durability, vulnerability to disturbance, complicated mineral compositions, and unsuitability for plant growth [2].

Sensitive to the natural environment, easy to shatter, disintegrate, and soften, carbonaceous rock generally refers to a particular clay rock whose engineering properties

change greater along with the natural environment [3, 4]. In Guangxi, the distribution of carbonaceous rock is not as widely as red clay. However, landslides, collapse, and other geological disasters often occur on the highway and railway slopes composed of carbonaceous rock, attracting the attention of various industries [5, 6]. It is well known that failure modes of carbonaceous rock slopes include two categories. The first kind mainly occurs in bedding sliding, the sliding deformation of the upper loose overburden along with the rock, and soil interface after the slope excavation. The second type is the collapse of surface rock mass caused by the changes of its properties after slope excavation, generally manifested as the spalling and disintegration of a surface rock mass [7, 8]. After the carbonaceous rock slope is excavated and exposed, the carbonaceous rock is prone to softening and collapse under the action of water immersion, resulting in slope collapse and affecting the stability of the slope (Figure 1). At present, the research on carbonaceous rocks mainly focuses on the material composition, structural characteristics, mineralized composition, physical and mechanical properties as well as deformation and failure mechanism, etc. Therefore, it is of greater significance to understand the softening and disintegration of carbonaceous rocks by carrying out relevant laboratory tests.

Rock slaking behavior has been widely studied all over the world. Gamble et al. [9, 10] deemed that one factor alone can hardly cause extensive slaking of carbonaceous mudstones. Instead, this is a process jointly controlled by temperature, humidity, and several other factors. Based on slaking tests on soft rock samples, Qu [11] concluded that the slaking rate of soft rocks is related not only to the mineral contents of the rocks but also to the degree of cementation of the rocks. Zhang et al. [12] deemed that the expansibility of these rocks is inversely correlated with the grain sizes of the fraction with the maximum content, effective grain size, and slake durability index of the collapsed scraps of the swelling rock. Liang et al. [13] investigated the changes in the morphology, static disintegration index, and disintegration ratio of four different kinds of soft rocks under slaking based on their mineral compositions and physical parameters. Guo et al. [14] carried out laboratory wetting and disintegration tests on typical red mudstone samples under different conditions. The results revealed that the moisture content during the wetting-drying cycles was the driving factor behind the disintegration of soft red mudstone. Surendra [15] examined the effects of the mineral composition on shale durability and suggested using inorganic salt modifiers to control the slaking of soft rocks. Nara et al. [16] studied the influences of temperature and humidity on subcritical crack growth in sandstone. Bailey [17] analyzed the particle degradation of soft rocks during compaction in subgrade construction. However, previous studies on rock slake durability have mainly focused on soft rocks, with less attention paid to the slaking behavior of carbonaceous rocks.

In view of this, investigating the slaking behavior of the carbonaceous rocks in Guangxi Province is of both engineering and theoretical significance.

2. Classification of the Carbonaceous Rocks in Guangxi Province

In engineering practice, hand-soiling rocks containing large quantities of dispersed carbonized organic matter are often collectively called carbonaceous rocks, which we do not think is appropriate because carbonaceous rocks containing different mineral components differ in terms of their physical-chemical properties, strengths, and slaking behaviors. Whole-rock mineral analysis and clay mineral quantification were conducted on carbonaceous rock samples from the Hechi-Baise Expressway (HBE) using powder X-ray diffraction (XRD, Figure 2).

To classify the carbonaceous rock samples from the HBE, first, the mineral compositions of these samples were investigated. The carbonaceous rock outcroppings at stakes K19–K22 were sampled and prepared (ground) for X-ray diffraction analysis (Figures 3 and 4). Table 1 lists the main mineral components and their percentage contents in the samples.

As shown in Table 1, the mineral contents of samples A1 and A2 are quartz, calcite, and a trace amount of dolostone, with quartz accounting for 69.63% and calcite accounting for 28.66%. Neither of these samples contains clay minerals. The main mineral contents of samples A3, B2, C2, and C3 are calcite, quartz, illite, and a lesser amount of pyrite, with calcite accounting for 43.30%–66.06% and quartz accounting for 5.90%–37.74%. In addition, the clay minerals, which are primarily illite, account for approximately 10%. Smectite was found in some of the samples, and the pyrite contents of all of these samples are less than 2.30%. The main mineral contents of samples C4, C5, D, E, F, and H are quartz, calcite, dolostone, illite, and pyrite, with quartz accounting for 45.69%–64.31%. Clay minerals, which are primarily illite, account for 20.65%–27.18%, and dolostone accounts for 7.12%–15.13%. Some of these samples contain calcite, which accounts for a maximum of 17.92%, and a minimal amount of pyrite, which accounts for a maximum of 2.64%.

Based on the mineral components and their percentage contents in the carbonaceous rock samples from the HBE, the main clay mineral in the carbonaceous rocks is illite, which generally accounts for less than 24.74%. Smectite is also present in a few of the rock samples. Except for sample B, all of the other samples have high quartz contents. Some of the samples contain small amounts of dolostone, pyrite, and other minerals.

Considering the external characteristics, mineral compositions, and contents of the rock samples, according to the Classification and Nomenclature Schemes of Sedimentary Rock (GB-T17412.2-1998), the rock samples from the HBE are named as follows:

- (i) Samples A1 and A2 are carbonate-bearing cherts
- (ii) Samples A3, B2, C2, and C3 are carbonaceous mud-bearing limestones
- (iii) Samples C4, C5, and D are carbonaceous illite claystones
- (iv) Samples E, F, and H are carbonaceous illite clay shales



FIGURE 1: Carbonaceous rock slope collapses.

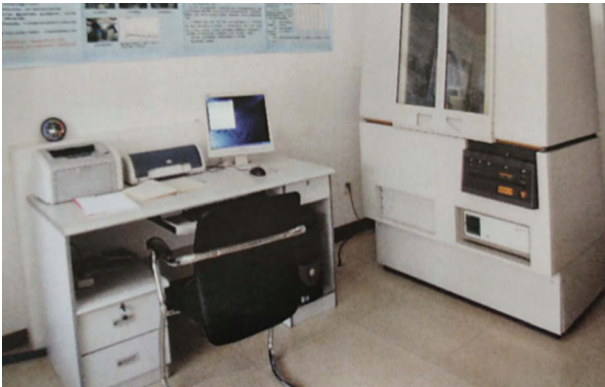


FIGURE 2: Advance X-ray diffraction machine.



FIGURE 3: Carbonaceous rock sample grinding process from Hebailu.

To facilitate discrimination during the subsequent experiments, the carbonaceous mud-bearing limestone samples were renumbered B1, B2, B3, and B4; the carbonaceous



FIGURE 4: Partial sample after grinding.

illite claystone samples were renumbered C1, C2, and C3; and the other samples were not renumbered.

3. Slake Durability Testing of the Carbonaceous Rocks in Guangxi Province

To establish the slake durability of the carbonaceous rock samples from the HBE, laboratory slaking tests were conducted on the samples under wetting-drying cycles according to the recommendations of the Standard for Tests Method of Engineering Rock Masses (GB/T 50266-2013) for the slake durability testing of rocks.

3.1. Test Equipment. Oven: an LY-660 precision industrial thermostatic air-dry oven was used (Figure 5). In our experiment, the drying temperature was maintained at approximately 105°C, as recommended by the standard. (2) Slake durability apparatus: the disintegrating tester at the Institute of Rock and Soil Mechanics, Chinese Academy of Sciences, was used (Figure 6). During operation, the speed of the apparatus was maintained at 20 r/min. The cylindrical screen drum is 100 mm (long) by 140 mm (diameter), with a mesh diameter of 2 mm. (3) Double-face rock grinder: an SCM-200 double-face rock grinder was used. The automatic grinding feed rate was 0.04–0.12 mm. In addition to these apparatus, electronic balances (with a precision of 0.01 g) and thermometers were also used as needed.

3.2. Sample Preparation. The rock samples were collected from the HBE and sealed with industrial parafilm (Figure 7). Then, the samples were placed in a plastic wrap to preserve their natural moisture content. The rock samples were reshaped into a rounded form. The mass of each of the specimens was maintained at 40–60 g using the rock grinder. Each specimen group contained at least 10 specimens (Figure 8). All four types of carbonaceous rocks were prepared into specimens and were tested separately.

TABLE 1: Main mineral compositions and percentage contents of the carboniferous rocks.

Sample number	Mineral content (%)							
	Quartz	Calcite	Dolomite	Illite	Montmorillonite	Kaolinite	Chlorite	Pyrite
A1	69.93	28.66	1.41	—	—	—	—	—
A2	75.41	23.05	1.55	—	—	—	—	—
A3 (B1)	37.74	45.91	2.82	11.24	—	—	—	2.3
B2	28.55	58.85	—	12.60	—	—	15.53	—
C2 (B3)	5.9	66.06	—	11.44	15.01	—	—	1.59
C3 (B4)	27.68	43.30	7.06	10.67	9.92	—	—	1.37
C4 (C1)	45.69	6.93	11.97	24.74	—	—	8.03	2.64
C5 (C2)	45.84	17.92	11.42	22.62	—	—	—	—
D (C3)	52.31	15.63	9.73	20.65	—	—	—	1.69
E	64.31	—	15.13	21.74	—	—	—	—
F	57.26	12.09	8.43	22.22	—	—	—	2.20
H	62.02	—	7.12	27.18	3.69	—	—	—



FIGURE 5: Oven.



FIGURE 7: Wax-sealed field rock samples.



FIGURE 6: Disintegrating tester.



FIGURE 8: Disintegrating test samples.

3.3. Test Procedure. First, the screen drum was dried and weighed. Next, the rock specimen was placed into the screen drum and dried at 105°C–110°C for 24 h. Then, the screen drum with the rock specimen was taken out of the oven and placed into the dryer to cool to room temperature before it was weighed again.

The screen drum with the rock specimen was placed in the water flume. Then, distilled water was poured into the flume to approximately 20 mm below the rotary shaft. The slake durability apparatus was started. The screen drum was run at a constant velocity of 20 r/min for 10 min, and then, the screen drum with the residual specimen was dried in the oven at 105°C–110°C for 24 h to a constant mass, cooled in the dryer to room temperature, and weighed. The second

step was repeated for the number of cycles required by the experiment, and the experimental data were recorded. The water temperature was maintained at $20^{\circ}\text{C} \pm 2^{\circ}\text{C}$ during the experiment. At the end of the experiment, the colors of the residual specimen and the water and the characteristics of any precipitate left in the water were described.

3.4. Results and Analysis. The rock slake durability index was calculated using the following equation:

$$I_{di} = \frac{m_r}{m_s} \times 100, \quad (1)$$

where I_{di} is the slake durability index of the rock after the i th wetting-drying cycle (%); m_s is the dried mass of the original sample (g); and m_r is the dried mass of the residual specimen (g).

The rock slake durability index is defined as the mass percentage after each standard wetting-drying cycle relative to the mass of the previous cycle:

$$I_{di} = \frac{m_i}{m_{i-1}} \times 100, \quad (2)$$

where I_{di} is the slake durability index of the rock after the i th wetting-drying cycle (%); m_i is the mass of the residue after the i th standard wetting-drying cycle (g); and m_{i-1} is the mass of the residue after the $(i-1)$ th standard wetting-drying cycle (g).

3.4.1. Slake Durability Indexes of the Carbonaceous Rocks.

Separate slaking tests were conducted on the different types of carbonaceous rock samples from the HBE. Each type was tested under six wetting-drying cycles, and their respective slake durability indexes were obtained. Tables 2 and 3 present the slake durability indexes of the rock samples. To facilitate observation, the data in these tables are also plotted in Figures 9 and 10.

From Figures 9 and 10, for the carbonate-bearing cherts (A1 and A2) and the carbonaceous mud-bearing limestones (B1, B2, B3, and B4), after six standard wetting-drying cycles, the slaking residues and slake durability indexes were linearly related to the number of cycles in all cases. The slake durability indexes remained higher than 90% after six wetting-drying cycles.

The slaking of both types of rocks (i.e., the mass reduction of the samples after the experiment) can be understood as a uniform mass reduction of the carbonate-bearing chert or carbonaceous mud-bearing limestone resulting from water erosion of the sample and the centrifugal pull from the rotation of the screen drum under laboratory wetting-drying cycles. The relationship between the residual mass of a specimen and the number of wetting-drying cycles is fitted by the following linear equations:

$$A1: y = -4.5729x + 391.33, \quad (3)$$

$$A2: y = -1.3786x + 472.95, \quad (4)$$

TABLE 2: Residual mass of each disintegration for the rock samples from Hebailu.

Sample number	Number of wetting-drying cycles						
	0	1	2	3	4	5	6
A1	392.24	385.94	381.97	377.84	372.41	368.52	364.36
A2	473.82	470.97	469.86	468.38	467.54	466.27	464.86
B1	297.50	296.58	291.71	288.60	287.00	283.30	281.43
B2	592.34	588.26	584.07	574.32	561.47	550.25	542.10
B3	488.22	483.40	480.00	476.19	474.52	472.37	469.95
B4	374.07	371.25	367.10	363.68	360.44	357.25	353.75
C1	416.16	386.6	343.32	282.8	262.68	247.25	234.01
C2	379.40	343.85	291.08	213.85	190.10	180.24	162.34
C3	446.94	382.44	290.29	225.71	192.67	171.08	154.75
E	478.89	464.31	430.25	380.10	354.17	332.55	318.97
F	479.88	461.20	441.62	420.28	399.19	368.65	342.87
H	356.90	354.59	346.62	324.62	308.75	294.60	282.03

TABLE 3: Disintegration resistance index of the Hebailu rock samples.

Sample number	Disintegration resistance index (%)						
	I_{d0}	I_{d1}	I_{d2}	I_{d3}	I_{d4}	I_{d5}	I_{d6}
A1	100	98.39	97.38	96.33	94.94	93.95	92.89
A2	100	99.40	99.16	98.85	98.67	98.41	98.11
B1	100	99.69	98.05	97.01	96.47	95.23	94.60
B2	100	99.31	98.60	96.96	94.79	92.89	91.52
B3	100	99.01	98.32	97.54	97.19	96.75	96.26
B4	100	99.25	98.14	97.22	96.36	95.50	94.57
C1	100	92.90	82.50	67.95	63.12	59.41	56.23
C2	100	90.63	76.72	56.37	50.12	47.51	42.79
C3	100	85.57	64.95	50.50	43.11	38.28	34.62
E	100	96.96	89.84	79.37	73.96	69.44	66.61
F	100	96.11	92.03	87.58	83.19	76.82	71.45
H	100	99.35	97.12	90.96	86.51	82.54	79.02

$$B1: y = -2.8386x + 297.96, \quad (5)$$

$$B2: y = -8.905x + 597.12, \quad (6)$$

$$B3: y = -2.9411x + 486.63, \quad (7)$$

$$B4: y = -3.415x + 374.18, \quad (8)$$

where y is the specimen's residual mass after slaking, and x is the number of wetting-drying cycles.

As can be seen from equations (3)–(8), the slaking residual mass of the carbonate-bearing cherts and carbonaceous mud-bearing limestones decreased linearly as the number of laboratory wetting-drying cycles increased. Except for specimen B2 (which had a slightly higher clay mineral content than the other specimens), which showed a mass reduction of 8–9 g after each wetting-drying cycle, all of the other specimens showed a mass reduction of less than 5 g. More importantly, the specimens showed virtually no cracks on the surface, and all of the specimens remained intact after six laboratory wetting-drying cycles. As such, we can assume that in the natural state, the carbonate-bearing

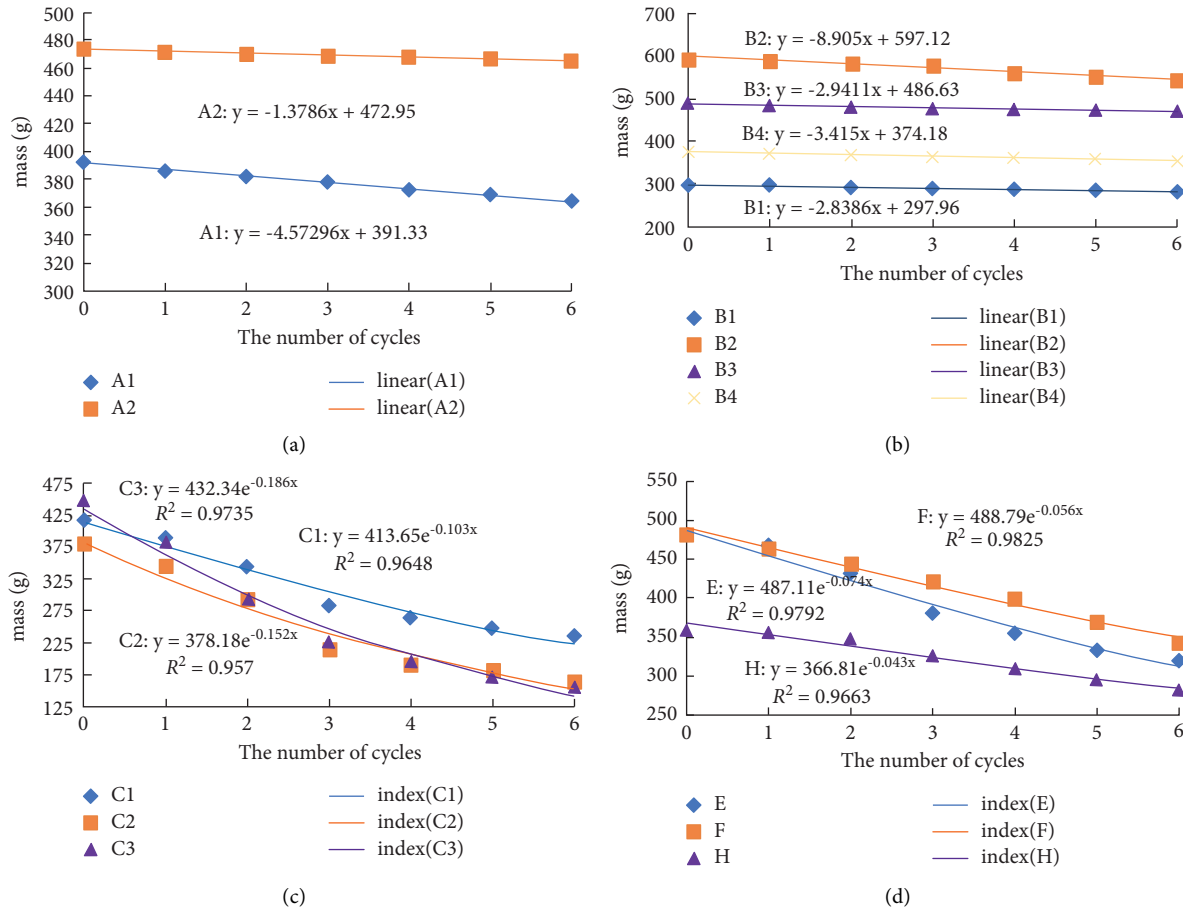


FIGURE 9: Variation curves of the residual disintegration masses of the four types of carboniferous rocks. (a) Carbonate cherts. (b) Carbonaceous argillaceous limestones. (c) Carbonaceous illite clay mudstones. (d) Carbonaceous illite clay shales.

chert and carbonaceous mud-bearing limestone from the HBE are very weakly slakable or not slakable at all.

In Figure 10, as the number of standard wetting-drying cycles increased, the slake durability index of the carbonaceous illite clay mudstones (C1, C2, and C3) and the carbonaceous illite clay shales (E, F, and H) from the HBE gradually decreased, with a 43%–66% reduction for the former and a 21%–33% reduction for the latter. The relationship between the number of standard wetting-drying cycles and the slake durability index of the specimen is fitted by the following equations:

$$C1: y = 99.399e^{-0.103x}, \quad (9)$$

$$C2: y = 99.68e^{-0.152x}, \quad (10)$$

$$C3: y = 96.736e^{-0.186x}, \quad (11)$$

$$E: y = 101.72e^{-0.074x}, \quad (12)$$

$$F: y = 101.72e^{-0.056x}, \quad (13)$$

$$H: y = 101.72e^{-0.043x}, \quad (14)$$

where y is the slake durability index; and x is the number of wetting-drying cycles.

In Figure 11, the specimen's slake durability under different numbers of cycles was close to the fitted curvilinear equation, suggesting that the slake durability of the specimen agrees well with equations (9)–(14), with modest data discretization and very little fluctuation about the curve. Based on the fitting formulas, the slake durability index of the carbonaceous illite clay mudstones and carbonaceous illite clay shales decreased exponentially as the number of wetting-drying cycles increased. Furthermore, as the number of wetting-drying cycles increased, the slake durability index curve gradually flattened until the specimens had completed slaking.

Figure 11 shows the relationship between the slake durability indexes and the number of wetting-drying cycles. As can be seen from this diagram, compared with the carbonaceous illite clay shales, the carbonate-bearing cherts and the mud-bearing limestones are very weakly slakable or not slakable at all. The carbonaceous illite clay shales appear

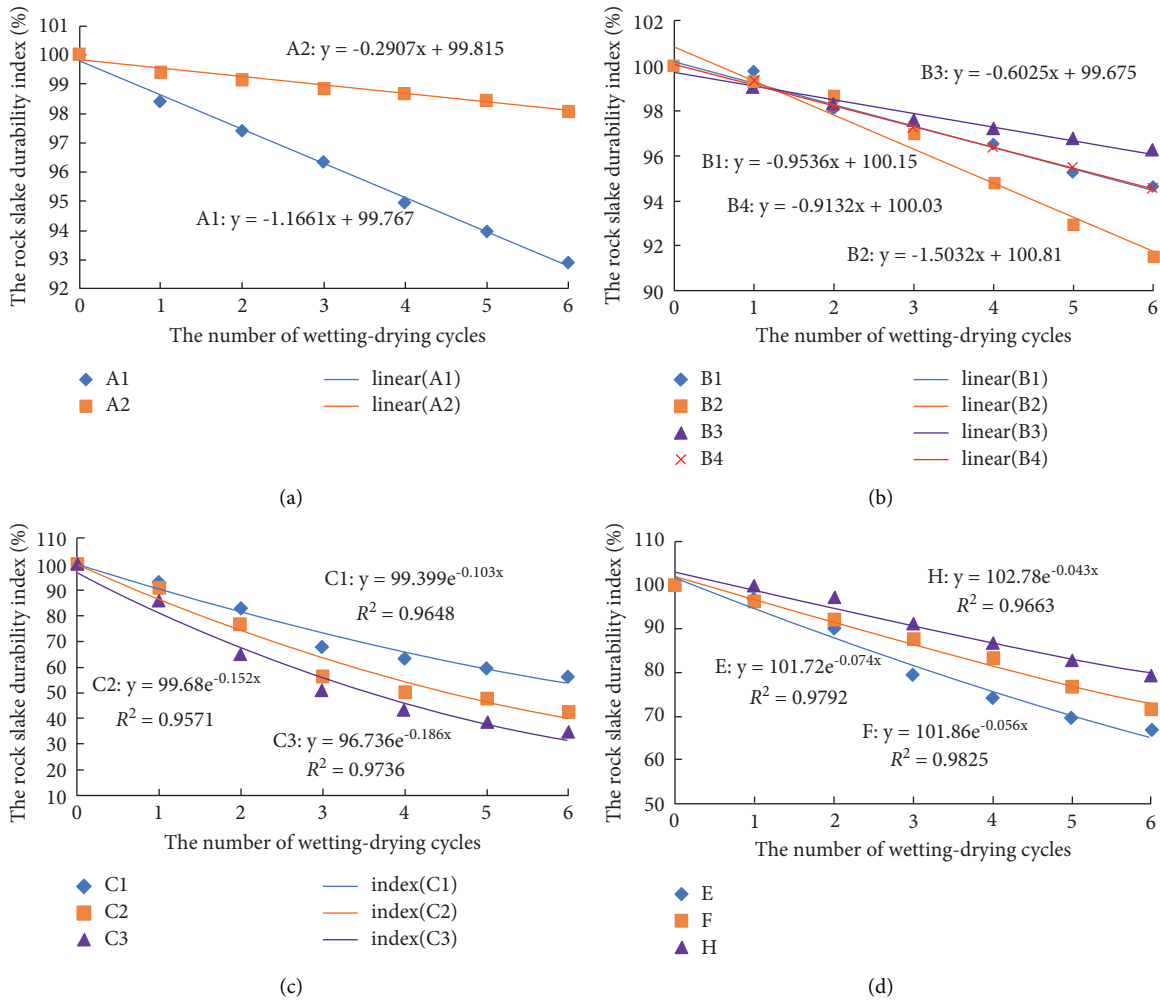


FIGURE 10: Relationship curves between the disintegration resistance index and the number of wetting-drying cycles for the carboniferous rocks. (a) Carbonate cherts. (b) Carbonaceous argillaceous limestones. (c) Carbonaceous illite clay mudstones. (d) Carbonaceous illite clay shales.

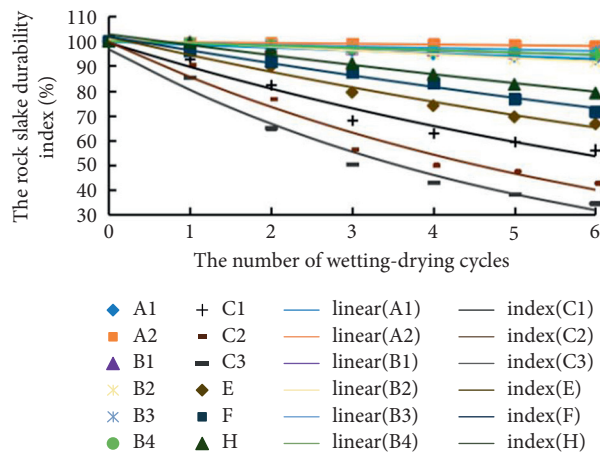


FIGURE 11: Relationship curves between the disintegration resistance index and the number of wetting-drying cycles for the different carboniferous rocks.

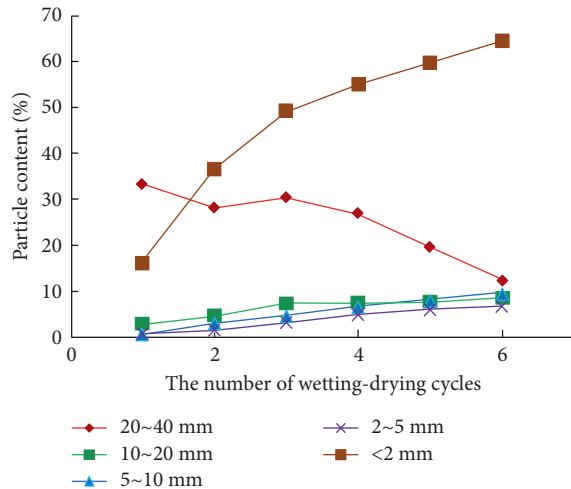


FIGURE 12: The change in the particle contents of the carbonaceous illite clay mudstones as the number of wetting-drying cycles increases.

to be quite slakable, and the carbonaceous illite mudstones are even more slakable.

3.4.2. Slaking Grain Size Analysis of the Carbonaceous Rocks. Figures 12 and 13 show the dependence of the grain size content of these rocks on the number of wetting-drying cycles. An analysis of these figures reveals the following.

As the number of wetting-drying cycles increased, the content of the 20–40 mm fraction in the slaking product of the carbonaceous illite clay mudstones gradually decreased, whereas the contents of all of the other grain sizes gradually increased. The content of the <2 mm fraction increased the fastest relative to all of the other grain sizes. The slaking product of the carbonaceous illite clay mudstones after the laboratory slaking test was mainly composed of grains <2 mm.

The carbonaceous illite clay shales were weakly slakable, with a low slaking speed and a lower slakability than the carbonaceous illite clay mudstones. Other than the content of the <2 mm fraction, which increased comparatively quickly, the contents of all of the other grain sizes changed slowly, with even smaller variations after the first two cycles. The carbonaceous illite clay shales were less slakable than the carbonaceous illite clay mudstones. The slaking of the carbonaceous illite clay shales typically occurred along the textures, resulting in many schistose structures in the slaking residues that could hardly pass through the small-size sieve holes. The larger sized grains were the main contributors.

Because the carbonaceous illite clay mudstones were more slakable than the carbonaceous illite clay shales, they slaked noticeably faster than the carbonaceous illite clay shales. The variations in the contents of the larger and smaller grain sizes were also greater. Thus, under the same conditions, the carbonaceous illite clay mudstones required fewer wetting-drying cycles to completely slake compared to the carbonaceous illite clay shales.

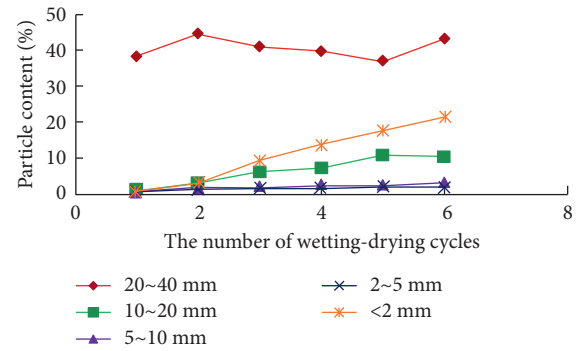


FIGURE 13: The change in the particle contents of the carbonaceous illite clay shales as the number of wetting-drying cycles increases.

4. Conclusions

The slaking phenomena and the behaviors of typical outcropping carbonaceous rock in the HBE in Guangxi under different numbers of wetting-drying cycles were investigated through laboratory slaking tests. The residual slaking grains of the rock samples were also analyzed for gradation. The following conclusions were drawn:

- (1) As the carbonate-bearing cherts contained no clay minerals and the mud-bearing limestones had a very low clay contents, both rock types appeared to be very weakly slakable or not slakable at all. The carbonaceous illite clay mudstones and carbonaceous illite clay shales, both of which contained more than 20% clay minerals, were highly slakable. Thus, the clay content constitutes the main driving factor behind the slaking behavior of carbonaceous rocks. Furthermore, despite their similar clay contents, the carbonaceous illite clay mudstones and carbonaceous illite clay shales also differed from each other in terms of their slaking behavior (the carbonaceous illite clay mudstone was more slakable) as a result of their different structural forms. These phenomena suggest that the slaking behavior of the carbonaceous rocks from the HBE was primarily determined by the clay content. The structural form also played a nonnegligible role.
- (2) As the number of wetting-drying cycles increased, the grain size contents of the slaking products of the carbonaceous illite clay mudstones and carbonaceous illite clay shales changed continuously, with similarities as well as differences between the two rocks. The carbonaceous illite clay mudstones slaked more quickly. The chunky specimen gradually slaked into smaller fragments and elliptical grains, with the 20–40 mm chunky fraction decreasing quickly, and the <2 mm granular fraction increasing quickly. Like the carbonaceous illite clay mudstones, as the number of wetting-drying cycles increased, the <2 mm fraction also prevailed in the slaking product of the carbonaceous illite clay shales. The unique stratification of this rock also resulted in the 20–40 mm schistose fraction predominating in the

residue, while all of the other grain size fractions increased slowly.

Data Availability

The data used to support the findings of the study are available from the corresponding author upon request.

Conflicts of Interest

The authors declare that there are no conflicts of interest regarding the publication of this paper.

Acknowledgments

This study was supported by the Science and Technology Project of Guangxi “Research on the Key Technologies of Highway Construction in Guangxi Carbonaceous Rock Area” (Grant no. GuikeAC16380119), the “Research and Application of Ecological Slope Protection Technology in Carbonaceous Rock Slopes” (Grant no. AD19110124), and the Key Science and Technology Project of Ministry of Transportation of The People’s Government of China “Reinforcement Theory and Technology of Multi-Point Restraint Anchor Cable and Monitoring Warning for Highway High Slope”(Grant no. 2020-MS3-082). The authors thank LetPub (<http://www.letpub.com>) for its linguistic assistance during the preparation of this manuscript.

References

- [1] J. H. Luo, D. C. Mi, and Q. Y. Ye, “Study on microscopic characteristics and physical and mechanical parameters of carbonaceous rocks,” *Materials Science Forum*, vol. 980, pp. 368–376, 2020.
- [2] J. Luo, D. Mi, and H. Huang, “Intelligent monitoring, stability evaluation, and landslide treatment of a carbonaceous mudstone and shale slope in Guangxi, China,” *International Journal of Safety and Security Engineering*, vol. 10, no. 3, pp. 373–379, 2020.
- [3] Q. Y. Ye, “Special engineering properties of carbonaceous rocks,” *Western China Communications Science & Technology*, no. 4, pp. 1–3, 2017.
- [4] F. Z. Zhang, X. P. Chen, H. F. Wu et al., “Experimental study on deformation properties and Duncan model parameters of soft clayey rocks,” *Rock and Soil Mechanics*, vol. 24, no. 4, pp. 610–613, 2003.
- [5] F. Q. Peng, X. Yuan, and H. Yuan, “Research on management and stability analysis of Lou-Xin high-speed complex geological slope,” *Journal of Railway Science and Engineering*, vol. 10, no. 4, pp. 106–111, 2013.
- [6] C. Y. Zhou, Y. M. Deng, X. S. Tan, Z. Q. Liu, W. Shang, and S. Zhan, “Experimental research on the softening of mechanical properties of saturated soft rocks and application,” *Chinese Journal of Rock Mechanics and Engineering*, vol. 24, no. 1, pp. 33–38, 2005.
- [7] S. Q. Deng, D. Xie, and Z. H. Tang, “Research on failure mode and treatment measures of carbonaceous rock slope,” *Western China Communications Science & Technology*, no. 6, pp. 10–12, 2014.
- [8] D. Stead, “The influence of shales on slope instability,” *Rock Mechanics and Rock Engineering*, vol. 49, no. 2, pp. 635–651, 2016.
- [9] J. C. Gamble, *Durability Plasticity Classification of Mudstones and Other Argillaceous Rock*, University of Illinois, IL, USA, 1971.
- [10] H. Yamaguchi, Y. Yoshida, I. Kuroshima, and M. Fukuda, “Slaking and shear properties of mudstone,” in *Proceedings of the ISRM International Symposium*, pp. 133–144, International Society for Rock Mechanics and Rock Engineering, Madrid, Spain, September 1988.
- [11] Y. X. Qu, “Engineering Geological Study on Argillaceous Cementation in Eastern China,” *Engineering Geomechanics Open Research experiment 1991 Annual Report*, Seismological press, Beijing, China, 1992.
- [12] W. Zhang, Y. J. Shang, Y. X. Qu, Y. C. Sun, D. M. Lin, and K. Y. Wang, “Grain size distribution of collapsed scraps of argillaceous rock and its relationship with expansibility: an experimental study,” *Rock and Soil Mechanics*, vol. 34, pp. 66–72, 2013.
- [13] B. Liang, Q. Cao, J. G. Wang, and L. Jiang, “Experimental study on slaking characteristics of feeble disintegration soft rock in drying-wetting cycle,” *China Safety Science Journal*, vol. 27, pp. 92–96, 2017.
- [14] Y. C. Guo, Q. Xie, and J. Q. Wen, “Laboratory test study on disintegration characteristics of red mudstone,” *Subgrade Engineering*, pp. 53–55, 2008.
- [15] M. Surendra, *Additives to Control Slaking in Compacted Shales*, pp. 161–165, Purdue university, West Lafayette, IN, USA, 1980.
- [16] Y. Nara, K. Morimoto, and T. Yoneda, “Effects of humidity and temperature on subcritical crack growth in sandstone,” *International Journal of Solids and Structures*, vol. 48, no. 7–8, pp. 1130–1140, 2011.
- [17] M. J. Bailey, *Shale Degradation and Other Parameters Related to the Construction of Compacted Embankments*, pp. 76–23, Purdue University, West Lafayette, IN, USA, 1976, MSCE Thesis.

Research Article

The Deformation Analysis of a Deep Frame Top-Down Excavation in Downtown Shanghai Based on the 3D FEM

Ting Bai  and Dong Xie

GuangXi Polytechnic of Construction, Nanning, Guangxi 530007, China

Correspondence should be addressed to Ting Bai; baitng1984@163.com

Received 8 August 2021; Accepted 4 October 2021; Published 5 November 2021

Academic Editor: Xiaohu Zhang

Copyright © 2021 Ting Bai and Dong Xie. This is an open access article distributed under the Creative Commons Attribution License, which permits unrestricted use, distribution, and reproduction in any medium, provided the original work is properly cited.

The deformation and environmental influence of the pit excavation in downtown is very important. A 3D FEM analysis is conducted to understand the deformation of a 13.9 to 15.2 m deep excavation with an in-plane dimension of about 189 m width and 251 m length constructed by the frame top-down method (FTDM) in the soft clay region in the Shanghai metropolitan area. The field monitoring results indicate that the magnitudes of wall deflections and ground settlements, along with the column's uplift difference, are relatively small, which are below the specified protection levels, and that the FTDM is feasible as one of the extralarge excavation construction methods. It is reasonable to predict wall deflection by 3D FEM simulation with qualitative comparison between the simulated column uplifts and the measured data, yet the prediction of the settlement distribution is of no satisfaction. This project studied in this paper not only serves as a special case study calibrated and verified by numerical tools but also provides insights into the design and construction of an extralarge deep excavation using the frame top-down method in soft soils and metropolitan environment.

1. Introduction

As the largest city and the commercial and financial center of China, Shanghai witnesses the construction of a growing number of high-rise buildings, subway transportation networks, and other underground structures, which provides broader platforms as well as higher challenges for excavation technology [1, 2]. The innovative researchers and engineers are exploring and applying new technologies in the practical construction of the excavation. Three construction methods can be employed in the construction of an excavation, namely, the bottom-up method (BUM), the top-down method (TDM), and the anchor method [3]. The poor soil conditions of Shanghai prevent the application of the anchor method, which makes the bottom-up method and the traditional top-down method (TTDM, one type of the TDM) the most commonly employed approaches. The BUM is not environment-friendly due to its utilization of a large amount of temporary supports which may cause serious waste of resources, and its temporary support system is generally not stiff enough to minimize the

deformation of the excavation. By using permanent flooring systems as support, it is stiff enough to minimize the deformation of the excavation, yet the TTDM requires hidden excavation [4–8]. Moreover, it will take a long period of time to construct the floor, such as form work, rebar, concreting, and curing, which leads to the extension of construction period as well as duration of unpropped wall exposure. Significant retaining wall deflections and ground movements may be induced due to the long construction period and unpropped wall exposure period caused by deep excavations in Shanghai in soft clay with high water content, low strength, and high rheology [9–12]. The frame top-down method (FTDM) is a special top-down method which applies beams as supports to make full use of advantages of both the BUM and the TDM. To be more specific, it not only is of higher support stiffness and environment-friendly but also avoids many other problems, such as long duration of unpropped wall exposure caused by hidden excavation.

Until now, there are two most promising ways for gaining an understanding of deep excavation performance, the finite

element method and experience shared through published case histories. Since the publication of [13], many researchers and engineers contributed a huge amount of field data to the knowledge of performance of excavations and adjacent facilities [14–22]. More importantly, the empirical and semiempirical methods are mainly derived from field observations of case histories. Numerical analysis is another effective way to study complex problems in deep excavation [20, 23–28]. Due to the various types of foundation pit supporting structures and building foundations, the finite element method is the main method to evaluate the impact of the settlement of adjacent deep foundation excavation [29]. It is easier and cheaper to study deep excavation behavior with finite element analysis than using the instrument and monitoring of deep excavations. The current finite element numerical methods of foundation pits are mostly based on plane strain analysis, but foundation pits have obvious spatial effects. Three-dimensional finite element numerical analysis can effectively simulate the excavation of deep foundation pits with complex surrounding environments [30], which has great advantages.

This paper presents a case study of a deep frame top-down excavation in soft clay within the metropolitan area of Shanghai, China. The 3D FEM is employed to simulate the excavation process. This project and the relevant field data do not only facilitate thorough understanding of the general behavior of deep excavations constructed by the FTDM in soft clay within congested urban environments but also provide a good case history to calibrate and verify numerical tools. The findings and experience yielded from this study will be beneficial to designers, practitioners, and contractors for better understanding of the excavation project within the congested urban environment and reducing the risk of design and construction of the excavations.

2. Project Information

2.1. Project Location. As the largest city with a population of about 20 million in China, Shanghai is located at the estuary of Yangtze River on China's east coast. The city sits on the flat alluvial plain known as Yangtze River Delta, which features high groundwater tables and thick soft clay in the upper layers. The investigated project, excavation pit of Tangdong Headquarters site, is carried out in Pudong New Area, and some tower and podium buildings will be constructed there. The tower buildings include one 42-storied building, two 29-storied buildings, and two 18-storied buildings in frame-tube structure. The 3-level basement is in frame structure. Excavation depth of the tower block is 13.9–15.2 m, while that of the podium block is 13.6 m. The excavation area is shaped like a rectangle sized approximately 251 m by 189 m in plane and covers 46240 m². Figure 1 presents the site plan of the project along with the instrumentation. On the north side of excavation, there is Jinkang Road which is 5.6 m away. On the south side are the Northern Jinjiang Hotel Phase 1 and Phase 2 buildings which are 22.6 m and 17.8 m away, respectively. On the western side, it is the Yanggao South Road with a 15 m-wide urban green belt in between. On the northern side, it is the Huamu Road with a 10 m-wide urban belt in between.

In order to avoid damage to adjacent structures and properties, Shanghai local code (SCMC, 2010) specifies three different protection grades (Table 1) for deep excavations; moreover, the criteria of deformation control of deep excavations are also established (refer to Table 2). According to this code, protection grade 2 is designated for construction of this deep excavation; i.e., the maximum excavation-induced wall deflection, δ_{hm} , should be no more than 41 mm and the maximum ground settlements, δ_{vm} , should be no more than 34 mm. In addition, the allowable nonuniform settlement of the interior steel columns is specified as less than or equal to 20 mm. These criteria are defined on the basis that the settlements should not cause apparent cracking to buildings nor severe damages to utilities.

2.2. Soil Properties. Prior to excavation, soil conditions at the site were explored by a series of field exploration programs (e.g., bore holes, standard penetration tests, and cone penetration tests). Soil profiles along with the basic soil properties are presented in Figure 2. The site was characterized by a thin layer of fill (layer I) in the upper 1.5 m below ground surface (BGS), followed by a layer of yellowish dark brown inorganic clay (layer II) at 3 m BGS. The next layer was very soft to soft silty clay (layer III) extending to 8 m BGS. Below layer III, there existed a layer of soft to firm silty clay (layer IV) extending to 17.5 m BGS. The next layer was grayish silty clay (layer V) extending to 24 m BGS, underlain by dark green stiff silty clay (layer VI) extending to 28 m BGS. Beneath layer VI, the field exploration encountered very dense silty fine sand interbedded with sandy silt (layer VII) till the termination at 75 m BGS. The observed depth of BGS of the long-term groundwater table ranged from 0.24 m to 1.30 m. The unit weight, friction angle, and compression modulus of the upper silty clay are smaller than those of the lower silty fine sand, while the water content and void ratio of the silty clay are lower than those of the lower dense silty fine sand interbedded with sandy silt. The cohesion of stiff silty clay is greater than that of dense silty fine sand interbedded with sandy silt. The compressive modulus of soil is negatively correlated with the void ratio. The larger the void ratio, the smaller the compressive modulus.

2.3. Construction Sequence and Procedure. Construction activities are summarized in Table 3. The site work began with construction of the retaining wall and the vertical support system as well as compaction grouting of the soils. The retaining wall is a contiguous pile wall which is usually adopted as a temporary wall in Shanghai. The contiguous piles were 28 m in length and 1050 mm in diameter, with a gap of 200 mm between two bored piles. Deep soil mixing columns, constructed at the back of contiguous pile walls, are used as waterproof curtains. The vertical support system is composed of steel lattice columns and bored piles which penetrate layer VII. The interior H-section steel columns (470 mm × 470 mm) were constructed in the deep-seated bored piles to sustain construction loads and serve as permanent structures for later use. Thereafter, excavation was initiated and strutting systems were propped as soils were

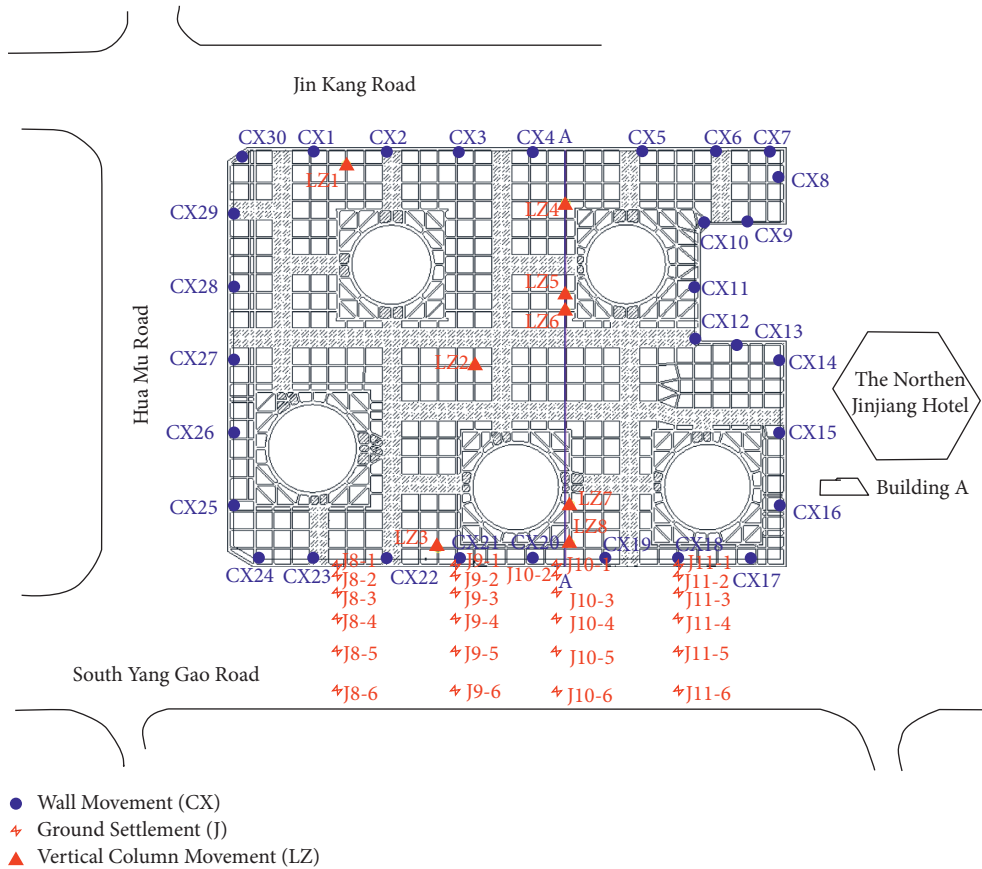


FIGURE 1: Plan of monitoring point arrangement.

TABLE 1: Protection grade of deep excavations.

Environmental conditions	Distance of the structure or properties from the excavation (s)	Protection grade
Heritage buildings, factory buildings with precision instruments and machines, important buildings with shallow foundations or short pile foundations, metro lines, flood control walls, very important services such as water mains and gas mains	$S \leq He$	I
	$He < S \leq 2 He$	II
	$2 He < S \leq 4 He$	III
Common buildings with shallow foundations or short pile foundations, important services such as water supply pipes, gas pipes, and sewage pipes	$S \leq He$	II
	$He < S \leq 2 He$	III

Note. He is the excavation depth.

TABLE 2: Control criteria for protection environment.

Protection grade	Maximum allowable displacement of the wall	Maximum allowable ground settlement
I	0.18% He	0.14% He
II	0.3% He	0.25% He
III	0.7% He	0.55% He

removed. The strutting systems were a combination of the beam and temporary reinforce concrete (RC) ring struts, which supported the contiguous pile wall. The underground structure was constructed in the base slabs, middle slabs, and roof slabs accompanied with removal of temporary RC ring struts. Young’s modulus, E , of the concrete used at this site was 3.5×10^7 kPa.

3. Field Monitoring

To verify design assumptions and monitor the performance of the deep excavation for securing the safety of this project, a long-term comprehensive instrumentation program was conducted in situ. The deflections of the diaphragm walls were monitored by 30 inclinometer tubes (designated as

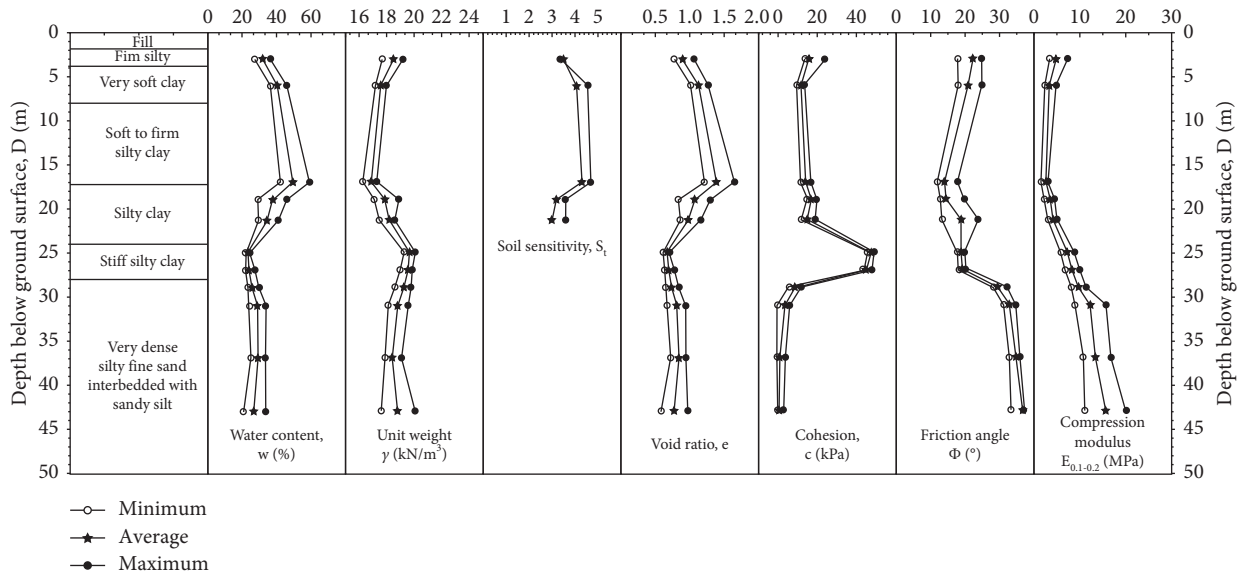


FIGURE 2: Soil profiles along with the material properties.

CX1 to CX30). In order to monitor the ground settlements behind the walls, 13 critical sections (designated as J1-1~JS1-6 to JS11-1~JS11-6) were selected for instrumentation. The vertical movements of the interior steel columns (designated as LZ1 to LZ28) were monitored using an electronic total station instrument. More detailed information of the field monitoring can be found in [31]. It is helpful for the constructors to take reasonable measures to control the displacement of the wall to locate the places where the maximum wall deflection occurs.

Ground settlement has always been one of the major tasks faced by engineers. Based on massive measured data, many researchers studied the magnitudes and distribution patterns of ground settlement and established many empirical prediction methods. Peck [13] noted that deep excavation dewatering caused consolidation of soil and led to settlement of the ground next to an excavation. It will cause settlements over a much larger area than the area affected by the excavation itself. As for this excavation, outer waterproof curtains of $\Phi 850@600$ triaxial cement/soil mixing piles which are 22.7 m long and pressure-reduction wells inside the pit which are 40 m deep are constructed, while shallowest surface of load-bearing water-containing strata at ⑦ layer is 27 m deep. The bottom of waterproof curtains fails to reach the load-bearing water-containing stratum which requires pressure reduction and dewatering, which leads to the failure of forming effective waterproof boundaries on load-bearing water-containing strata. This is why massive underground water pumped from the pit comes from horizontal runoffs below waterproof curtains, which will increase water level drop at load-bearing water-containing strata outside of the excavation pit and result in settlement of large areas outside of the excavation pit.

In these excavations by TDM, the magnitude of the interior column uplifts is an important criterion for quality assurance and quality control. As the deep-seated deflection of walls and base upheavals occur, soil outside of the pits

moves inward to the pits. During construction, the interior columns will lift up inevitably. Nonuniform column uplifts will produce sequential stress in the main structure or even induce failure of the main structure.

4. Numerical Model and Material Parameters

This excavation has a regular shape. This paper established a 1/4 area of the symmetrical model at the southeast of the existing excavation pit in the analysis process to save calculation resources and facilitate modeling (Figure 3). Figure 4 shows a 3D numerical basic model. The established model is strictly in accordance with the physical and mechanical parameters of this excavation without consideration of the coupling action of underground water in numerical analysis. The hardening soil (HS) model is used to simulate the behavior of soil [32], and the parameters for the HS model listed in Table 4 can be considered as the representative of Shanghai soil. In addition, the retaining piles are equivalent to the diaphragm wall in the analysis. The excavation wall, frame beams, and columns were assumed to behave as a linear-elastic material, for which both Young's modulus and Poisson's ratio were assumed constant.

The following calculation steps were performed:

- (i) Step 0: initial stress state
- (ii) Step 1: activate wall (wished-in-place), set displacements to zero
- (iii) Step 2: excavate to level -1.15 m
- (iv) Step 3: activate strut (roof beam) at level -0.58 m
- (v) Step 4: excavate to level -5.85 m
- (vi) Step 5: activate strut (middle beam 1) at level -5.05 m
- (vii) Step 6: excavate to level -10.05 m
- (viii) Step 7: activate strut (middle beam (2)) at level -9.05 m

TABLE 3: State of foundation pit construction.

Stage	Event	Date (yy/mm/dd)	Days spent
0	Construction of retaining wall, steel lattice column, and bored pile as the vertical support system and compaction grouting of the soils	20081217–20090914	272
1	Excavation to 1.15 m BGS; construction of the roof beam (0.8 m × 0.65 m) and level 1 temporary RC ring struts (1.6 m × 0.8 m)	20090915–20091110	57
2	Excavation to 5.85 m BGS; construction of middle beam 1 (1.0 m × 0.6 m) and level 2 temporary RC ring struts (1.8 m × 0.8 m)	20091111–20100206	88
3	Excavation to 10.05 m BGS; construction of middle beam 2 (1.2 m × 0.6 m) and level 3 temporary RC ring struts (2.0 m × 0.8 m)	20100301–20100705	127
4	Excavation to 13.6 m BGS (final level)	20100706–20100928	84
5	Construction of the base slab	20100928–20101126	58
6	Construction of the podium block	20100903–20110227	177
7	Construction of the tower block	20101205–20110531	178

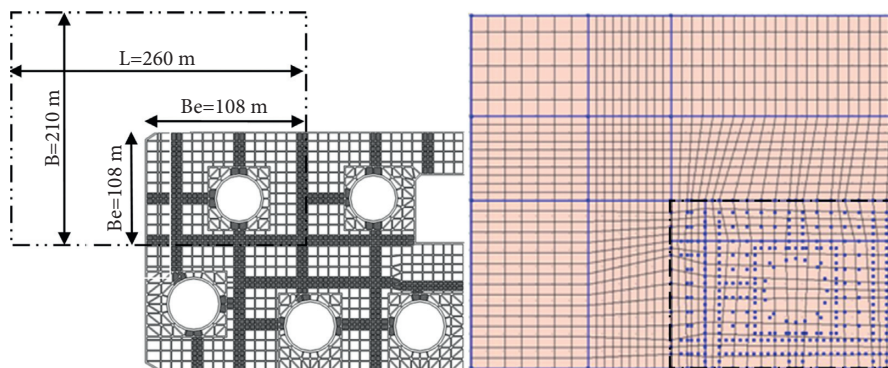


FIGURE 3: Plane size of the finite element model.

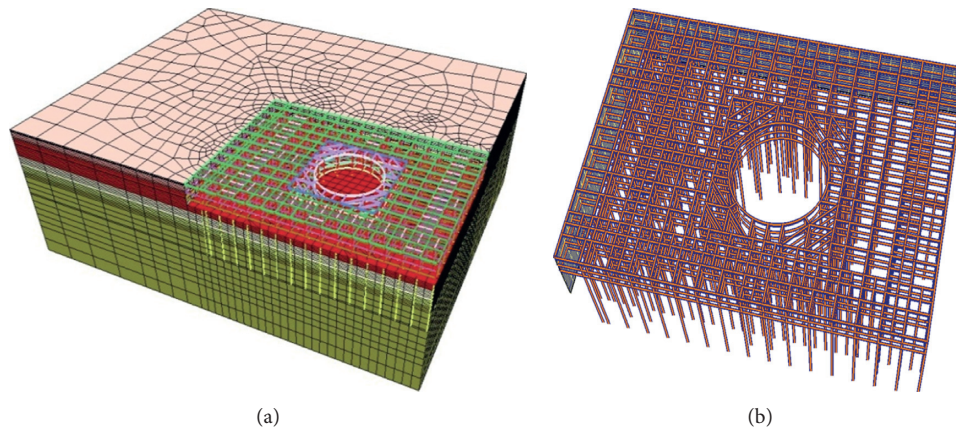


FIGURE 4: Numerical model. (a) Overall model. (b) Structural elements.

(ix) Step 8: excavate to level -13.6 m (final level)

(x) Step 9: construction of base slab

5. Results and Discussion

5.1. Deflections of Retaining Walls. Figure 5 shows the comparison of the wall displacements from field measurements and those from FEM. As shown in the figure, the observations and predictions match well at each stage and share basically consistent distribution profiles. The wall

deflection increases and the location of maximum wall deflection moves downwards as the excavation depth increases. The maximum wall deflection occurs near the excavation surface, where the data of wall deflection observed is smaller than the one predicted since the compaction grouting of the soils and area by area excavation were not considered in FEM. Wall deflection also occurs at the top of walls where the data of wall deflection observed is obviously larger than the one predicted because of the shrinkage and creepage of concrete structure beams.

TABLE 4: Parameters for the hardening soil model.

Layer	c' (kPa)	φ' ($^\circ$)	ψ ($^\circ$)	E_{oed}^{ref} (MPa)	E_{50}^{ref} (MPa)	E_{ur}^{ref} (MPa)	M	ν_{ur}	K_0^{nc}	R_f
II	7	30.2	0	4.86	7.29	29.16	0.8	0.2	0.47	0.9
III	2	32.7	0	3.41	5.115	20.46	0.85	0.2	0.48	0.6
IV	7	27.6	0	2.13	3.195	12.78	0.85	0.2	0.57	0.6
V	12	29.5	0	4.25	6.375	25.5	0.8	0.2	0.47	0.9
VI	30	29.0	0	7.31	10.965	43.86	0.8	0.2	0.46	0.9
VII	4	33	3	15.05	22.575	90.3	0.5	0.2	0.35	0.9

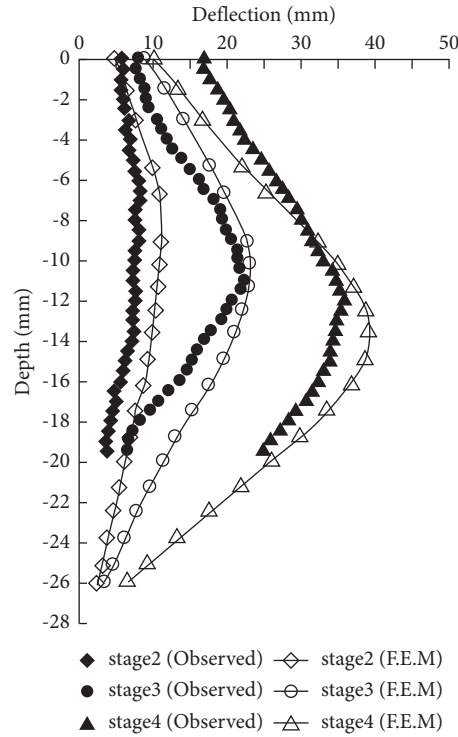


FIGURE 5: Comparison of the wall displacements from field measurements and from FEM at each stage.

5.2. Ground Settlements. The field observations of the ground settlement behind walls are located in the same section of the predictions in the FEM model, namely, sections J8-1~J8-6. According to the setting of the settlement observation point mentioned above, the area of the settlement observation section is approximately 900 m². The observations and predictions of settlement behind walls increase when the excavation depth increases and are roughly consistent with displacement of the walls (Figure 6). In numerical analysis, ground settlement curve is shaped like a groove, with an obvious primary influence zone (PIZ) and secondary influence zone (SIZ), while the location of maximum ground settlement moves backwards when excavation goes deeper. This significantly differs from the observations. Moreover, the maximum ground settlement in numerical simulation is 14.9 mm, about 0.11% He, and is close to the measured maximum ground settlement, both of which are less than $\delta_{vm} = 0.25\%$ He specified for the protection grade 2 (Table 2). Furthermore, statistic summary of 182 measured sections for subway excavation pits in Shanghai regions indicates that the maximum ground settlement is normally located at 0.5–0.7 He horizontally from the retaining wall [33]. From numerical

analysis of this project, it can be noticed that the maximum ground settlement is located at 0.75~1 He behind the wall, while ground settlement behind the wall after 1 He decreases quickly and ground settlement behind the wall after 3 He tends to be stable. This is consistent with Xu [34] in that extent of ground settlement of those excavations by TDM in Shanghai does not exceed 3 He yet differs greatly from the observations. The differences attribute to the fact that dewatering is not considered in numerical simulation.

5.3. Uplifts of Interior Steel Columns. Column uplift tendency approaches the observations, both of which increase as the excavation depth increases. At stage 4, column uplifts tend to be stable. Differing from continuous increment of column uplifts in field measurement, column uplifts increase in trapezoid-shaped increment form in FEM (Figure 7). The reason is that practical excavation is performed area by area while the excavation process is in a continuous increment stage. In numerical analysis, excavation is performed layer by layer in a simplified way. After the completion of excavation, the predictions of column

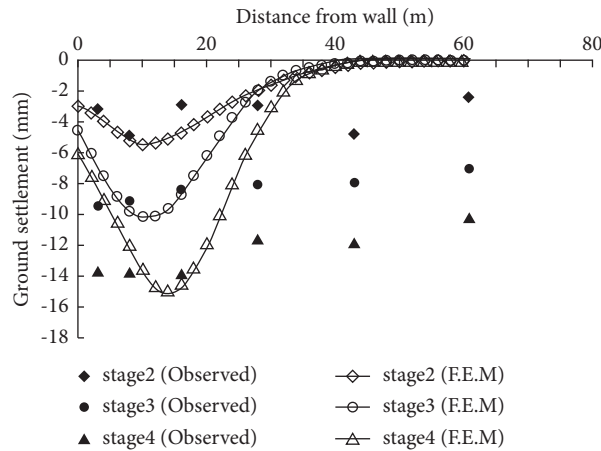


FIGURE 6: Comparison of the settlement profiles from field measurements and from FEM at each stage.

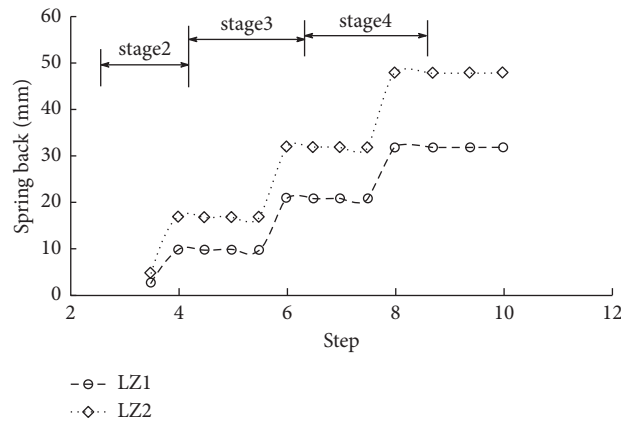


FIGURE 7: Vertical movements of interior steel columns observed from FEM at each stage.

maximum uplifts at two measure points are 46 mm and 31 mm, respectively, while the observations of two measure points are 35 mm and 20 mm, respectively. The predictions are slightly greater than the observations. The stress of the soil during the excavation of the foundation pit is released, and the soil in the pit rebounds. The load borne by the steel column includes the self-weight of the steel column and the friction resistance and the end resistance of the steel column. Because of the unloading due to the excavation, the steel column is uplifted by the soil around the column after each excavation stage. After the completion of excavation, the predictions of column maximum uplifts at two measure points are 46 mm and 31 mm, respectively, while the observations of those are 35 mm and 28 mm, respectively. The predictions are slightly greater than the observations. The reasons include the following: The practical working condition is excavating and concreting bottom slabs area by area, but it is simplified to large-area excavation layer by layer in numerical analysis. In practice, dewatering causes soil consolidation which results in soil stiffening; therefore, both the base upheavals and the column uplifts are restricted. It proves that technical measures mentioned above effectively limit the base upheavals and column uplifts.

Their uplifts differ when they are at different distances from wall at different stages. Column uplifts in the middle of the excavation pit are obviously greater, while the column uplifts close to the wall are usually smaller (Figure 8). At different stages, the steel columns at different positions in the foundation pit are subjected to different upward forces caused by the difference of soil surface height between the inside and outside of the foundation pit. With the increase in excavation depth, the upward force on the steel column in the foundation pit will be extremely large and the vertical displacement of the steel column will be extremely large, but because the steel column in different positions is subjected to different constraints, the rise of the steel column in different positions in the foundation pit will be different. For instance, the column uplift at LZ91 which is located in the middle of the excavation pit is 39 mm and the column uplift at LZ33 which is closer to the wall is 35 mm. In numerical simulation, column uplifts follow similar tendency with field measurements, yet the magnitude of them is greater with the maximum and minimum values being 46 mm and 40 mm, respectively, to be specific. In order to ensure the safety of structures, it is necessary to control the column uplifts difference. The Shanghai Construction and Management

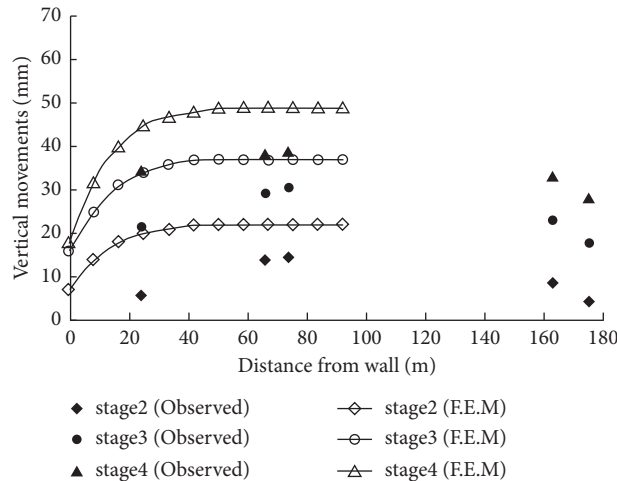


FIGURE 8: Comparison of the vertical movements of interior steel columns from field measurements and from FEM at section A-A.

Commission (2010) stipulates that column uplifts difference of two adjacent columns of the whole structure should be no more than 20 mm or $L/400$ (L refers to columns span). The observations and predictions of uplifts differences of adjacent columns are less than 5 mm, which is in accordance with the design requirements.

Like the displacement of the wall, column uplifts also increase as the excavation depth increases at different stages. Column uplifts demonstrate significant 3D characters by the fact that column uplifts are greater in the middle of the excavation pit and smaller when close to the wall. Although the predictions of column uplift are greater than the observations, 3D numerical analysis can simulate column uplifts qualitatively in frame top-down excavation.

6. Conclusions

Through a long-term comprehensive instrumentation program and 3D numerical analysis, the performance of a deep excavation constructed by the FTDM in soft clay within downtown Shanghai was extensively explored. Based on the measured and predicted results, the following major conclusions can be drawn:

- (1) As for those excavations using piles in row as the retaining wall, due to existence of ring beams and purlins, the displacement of the pile demonstrates space effects. However, the space effect of piles in row appears insignificantly compared with that of diaphragm walls. The time effects shall be taken into consideration in design and construction for the extralarge pit excavations in the sensitive soft soil, e.g., Shanghai soft soil. Compared with the observations, the predicted wall deflection from FEM without considering dewatering is relatively reasonable.
- (2) 3D numerical analysis can, to some extent, simulate retaining wall displacement, ground settlement, and column uplifts resulting from the frame top-down excavation and offers a beneficial supplement to the understanding of deformation of complex deep

excavation by FTDM. However, in the numerical analysis, issues such as selection of the soil constitutive model and simplification of numerical models (such as dewatering, frame beams' shrinkage, and seepage) should be taken into consideration. If this excavation is executed according to the finite element method, the displacement of the wall can be controlled properly and ground settlement will be underestimated, while column uplifts will be overestimated in practical construction. Hence, in project design, the designers or engineers should make a comprehensive judgment on the basis of numerical analysis and previous experiences.

Data Availability

All data can be made available from the authors upon request.

Conflicts of Interest

The authors declare that they have no conflicts of interest.

Acknowledgments

The authors thank the support from Professor Jingpei Li at Tongji University. This work was supported by the Key Research and Development Program of Jiangxi Province, China (Grant no. AB18281010).

References

- [1] Y. Tan and D. Wang, "Characteristics of a large-scale deep foundation pit excavated by the central-island technique in Shanghai soft clay. I: bottom-up construction of the central cylindrical shaft," *Journal of Geotechnical and Geoenvironmental Engineering*, vol. 139, no. 11, pp. 1875–1893, 2013.
- [2] P. He, Z. Xu, W. Wang, and Z. Li, "Observed performance of an ultra large deep excavation in Shanghai soft clay," in *Proceedings of the Geoshanghai 2018 International Conference*, pp. 161–170, Shanghai, China, May 2018.

- [3] N. S. Agrawal, V. Harne, J. Chouhan, and L. Gangwani, "Construction of plunge column by using top down construction method," *Helix*, vol. 10, no. 1, pp. 170–173, 2020.
- [4] J. L. C. Mission and H.-J. Kim, "Design charts for elastic pile shortening in the equivalent top-down load-settlement curve from a bidirectional load test," *Computers and Geotechnics*, vol. 38, no. 2, pp. 167–177, 2011.
- [5] H. Zheng, J. A. Dijkman, and R. P. Behringer, "Shear jamming in granular experiments without basal friction," *EPL (Europhysics Letters)*, vol. 107, no. 3, 2014.
- [6] H. Zheng, D. Wang, X. Tong, L. Li, and R. P. Behringer, "Granular scale responses in the shear band region," *Granular Matter*, vol. 21, no. 4, 2019.
- [7] M. M. Wang, D. Wang, J. E. S. Socolar, H. Zheng, and R. P. Behringer, "Jamming by shear in a dilating granular system," *Granular Matter*, vol. 21, no. 4, 2019.
- [8] G. W. Clough and T. D. O'Rourke, "Closure to "construction induced movements of insitu walls" by G. W. Clough and thomas D. O'ourke (june 18-21, 1990, no. 25)," *Journal of Geotechnical Engineering*, vol. 118, no. 4, pp. 665–666, 1992.
- [9] Y. Mei, D. B. Zhou, X. Y. Wang et al., "Deformation law of the diaphragm wall during deep foundation pit construction on lake and sea soft soil in the Yangtze river Delta," *Advances in Civil Engineering*, vol. 2021, Article ID 6682921, 11 pages, 2021.
- [10] M.-G. Li, O. Demeijer, and J.-J. Chen, "Effectiveness of servo struts in controlling excavation-induced wall deflection and ground settlement," *Acta Geotechnica*, vol. 15, no. 9, pp. 2575–2590, 2020.
- [11] Y. Q. Zhao, J. Bares, H. Zheng, J. Socolar, and B. P. Behringer, "Shear-jammed, fragile, and steady states in homogeneously strained granular materials," *Physical Review Letters*, vol. 123, no. 15, 2019.
- [12] M. Long, "Database for retaining wall and ground movements due to deep excavations," *Journal of Geotechnical and Geoenvironmental Engineering*, vol. 127, no. 3, pp. 203–224, 2001.
- [13] R. B. Peck, "Deep excavation and tunneling in soft ground," in *Proceedings of the 7th International Conference on Soil Mechanics and Foundation Engineering*, pp. 225–281, Mexico, 1969.
- [14] A. I. Mana and G. W. Clough, "Prediction of movements for braced cuts in clay," *Journal of the Geotechnical Engineering Division*, vol. 107, no. 6, pp. 759–777, 1981.
- [15] C.-Y. Ou, P.-G. Hsieh, and D.-C. Chiou, "Characteristics of ground surface settlement during excavation," *Canadian Geotechnical Journal*, vol. 30, no. 5, pp. 758–767, 1993.
- [16] P.-G. Hsieh and C.-Y. Ou, "Shape of ground surface settlement profiles caused by excavation," *Canadian Geotechnical Journal*, vol. 35, no. 6, pp. 1004–1017, 1998.
- [17] J. Roboski and R. J. Finno, "Distributions of ground movements parallel to deep excavations in clay," *Canadian Geotechnical Journal*, vol. 43, no. 1, pp. 43–58, 2006.
- [18] G. T. Kung, C. H. Juang, E. C. Hsiao, and Y. M. Hashash, "Simplified model for wall deflection and ground-surface settlement caused by braced excavation in clays," *Journal of Geotechnical and Geoenvironmental Engineering*, vol. 133, no. 6, pp. 731–747, 2007.
- [19] Y. M. A. Hashash, A. Osouli, and C. Marulanda, "Central artery/tunnel project excavation induced ground deformations," *Journal of Geotechnical and Geoenvironmental Engineering*, vol. 134, no. 9, pp. 1399–1406, 2008.
- [20] F. Scharinger, H. F. Schweiger, and G. N. Pande, "On a multilaminar model for soil incorporating small strain stiffness," *International Journal for Numerical and Analytical Methods in Geomechanics*, vol. 33, no. 2, pp. 215–243, 2009.
- [21] Y. Tan and B. Wei, "Observed behaviors of a long and deep excavation constructed by cut-and-cover technique in Shanghai soft clay," *Journal of Geotechnical and Geoenvironmental Engineering*, vol. 138, no. 1, pp. 69–88, 2012.
- [22] Y. Tan and B. Wei, "Performance of an overexcavated metro station and facilities nearby," *Journal of Performance of Constructed Facilities*, vol. 26, no. 3, pp. 241–254, 2012.
- [23] A. J. Whittle, Y. M. A. Hashash, and R. V. Whitman, "Analysis of deep excavation in boston," *Journal of Geotechnical Engineering*, vol. 119, no. 1, pp. 69–90, 1993.
- [24] C.-Y. Ou, D.-C. Chiou, and T.-S. Wu, "Three-dimensional finite element analysis of deep excavations," *Journal of Geotechnical Engineering*, vol. 122, no. 5, pp. 337–345, 1996.
- [25] Y. M. A. Hashash and A. J. Whittle, "Ground movement prediction for deep excavations in soft clay," *Journal of Geotechnical Engineering*, vol. 122, no. 6, pp. 474–486, 1996.
- [26] Y. M. A. Hashash and A. J. Whittle, "Mechanisms of load transfer and arching for braced excavations in clay," *Journal of Geotechnical and Geoenvironmental Engineering*, vol. 128, no. 3, pp. 187–197, 2002.
- [27] L. Zdravkovic, D. M. Potts, and H. D. St John, "Modelling of a 3D excavation in finite element analysis," *Géotechnique*, vol. 55, no. 7, pp. 497–513, 2005.
- [28] A. Osouli, Y. M. A. Hashash, and H. Song, "Interplay between field measurements and soil behavior for capturing supported excavation response," *Journal of Geotechnical and Geoenvironmental Engineering*, vol. 136, no. 1, pp. 69–84, 2010.
- [29] J. Chen, H. Mo, and S. Liu, "Evaluation on effect of building settlement due to adjacent deep excavation," in *Proceedings of the 2nd International Conference on Civil Engineering, Architecture and Building Materials (CEABM 2012)*, Yantai, China, May, 2012.
- [30] C.-Y. Ou, B.-Y. Shiau, and I.-W. Wang, "Three-dimensional deformation behavior of the Taipei National Enterprise Center (TNEC) excavation case history," *Canadian Geotechnical Journal*, vol. 37, no. 2, pp. 438–448, 2000.
- [31] M. G. Li, J. H. Wang, J. J. Chen, A. M. Asce, and Z. Zhang, "Responses of a newly built metro line connected to deep excavations in soft clay," *Journal of Performance of Constructed Facilities*, vol. 31, no. 6, 2017.
- [32] T. Schanz, P. A. Vermeer, and P. G. Bonnier, "The hardening soil model: formulation and verification," in *Computational Geotechnics*, pp. 281–296, Taylor and Francis, Boca Raton, NJ, USA, 1999.
- [33] L. Tao, "Study on foundation pit safety assessment and deformation forecast on basis of numerical excavation," Ph.D. thesis, Tongji University, Shanghai, China, 2007.
- [34] Z. H. Xu, "Deformation behavior of deep excavations supported by permanent structures in Shanghai soft deposit," Ph.D. thesis, Shanghai Jiaotong University, Shanghai, China, 2007.

Research Article

Dynamic Response Study of Impulsive Force of Debris Flow Evaluation and Flexible Retaining Structure Based on SPH-DEM-FEM Coupling

Bailong Li ¹, Changming Wang ¹, Yanying Li ¹, and Shuhua Zhang ²

¹College of Construction Engineering, Jilin University, Changchun 130021, China

²College of Information Communication, Changchun University of Technology, Changchun 130021, China

Correspondence should be addressed to Changming Wang; wangcm@jlu.edu.cn and Shuhua Zhang; zhangshuhua@ccut.edu.cn

Received 17 June 2021; Accepted 11 October 2021; Published 23 October 2021

Academic Editor: Xiaohu Zhang

Copyright © 2021 Bailong Li et al. This is an open access article distributed under the Creative Commons Attribution License, which permits unrestricted use, distribution, and reproduction in any medium, provided the original work is properly cited.

Flexible retaining structure is demonstrated to be an effective measure for debris flow prevention in mountainous areas, which can effectively separate water and stone, reduce particle mass, and dissipate kinetic energy. In order to explore the impulsive force and dynamic response of flexible retaining structure impacted by solid-liquid two-phase debris flow, a complex dynamic interaction model of particle-fluid-structure has been established by employing the SPH-DEM-FEM coupling numerical analysis method. In the present study, the process, impulse force, and dynamic response of a flexible retaining structure subjected to debris flow under different slopes were investigated, respectively. The numerical results are compared with those of the calculation formula of the peak impulsive force of the semiempirical debris flow. Meanwhile, the effectiveness of the coupling numerical simulation is verified. The simulation results show that the coupled SPH-DEM-FEM numerical analysis method can visualise the impact of the solid-liquid two-phase debris flow on the flexible retaining structure, reproducing the impact, retaining, water-stone separation, climbing, silting, and deposition process of debris flow. The dynamic time-history curve of the coupling numerical analysis method for the flexible retaining structure is consistent with the results of the existing literature. The debris flow evaluation results of flexible retaining structure impacted by solid-liquid two-phase debris flow are in an order of magnitude with the empirical formula results. Moreover, the results are reliable. The obtained results have a certain reference value for the study on the impulsive force and dynamic response of the flexible retaining structure impacted by solid-liquid two-phase debris flow and the engineering design of the flexible retaining structure.

1. Introduction

Debris flow is a solid-liquid two-phase mixed fluid containing a large number of rubbles and sediments, showing the movement characteristics of viscous laminar flow or dilute turbulent flow. It is the result of the combined action of topography, meteorology, hydrology, soil, and vegetation in the basin [1]. Debris flows are characterized by rapid flow velocity, large flow velocity, sudden eruption, and amazing destructive power. It is a special fluid-solid coupling material formed by rainfall confluence. Limited by a certain slope groove, it pours down to the accumulation area at a significantly fast speed, which can cause great damage to a variety of buildings along the way [2].

Debris flow disasters are extensively distributed around the world, while China is a mountainous country and the mountainous area accounts for approximately 69% of the total land area. The Tianshan Mountains, Kunlun Mountains, Himalayas, Qinling Mountains, Hengduan Mountains, and Changbai Mountains in China are all high-risk areas of debris flow. The total area of debris flow distribution is 4.3 million km², of which 1.3 million km² is an intense active area [3]. In China, there have been many major debris flow disasters, among which, the most notable one is the August 8 Zhouqu debris flow disaster in Gansu Province, with the severe consequences of 1,481 deaths, 1,824 injuries, 284 missing persons, and nearly 20,000 people affected [3]. The data show that debris flow

composed of particles and fluids has great kinetic energy and impulsive force and can cause devastating damage to the structure [4].

Debris flow study is relatively complex, and previous studies are generally simplified into pure particle matter and fluid. For example, Ashwood and Hungr [5] used quartz sand and rubble for performing the physical simulation test to study the impact of debris flow. Ng [6] et al. studied the impact performance of dry sand and viscous fluid by the conducting centrifugal test. However, some scholars have studied the mixture of solid-liquid debris flow. Haas [7] et al. studied the solid-liquid mixture composed of rubble, sand, clay, and water. The results proved that the performance of solid-liquid mixture was significantly different from that of single-phase flow. The interaction between solid particles and fluid of debris flow would significantly change the movement characteristics and impulsive force of debris flow. It is challenging to describe and quantify the formation, movement, impact, and deposition process of solid-liquid two-phase debris flow due to solid-liquid interaction, which has always been the difficulty of study.

In addition to the formation, movement, impact, and deposition process of debris flow, the prevention and control measures of debris flow have also dominated a vital role in the protection of life and property [8–10]. As for the design of debris flow retaining structure, the impact of debris flow should be considered; otherwise, structural damage will be caused and the safety of life and property downstream will be seriously threatened [11–13]. The retaining structure can generally be divided into rigid retaining structure and flexible retaining structure [14], and the peak impulsive force of debris flow plays a key role in the design of retaining dam. At present, it is generally based on the fluid statics model, fluid dynamics model, or hybrid model [15]. In particular, the fluid dynamics model has been widely applied in engineering design due to the reliability of data. However, because of the different conditions, the value of empirical coefficient varies greatly among different scholars, seriously affecting the accurate prediction of the peak impulsive force of debris flow [16].

In recent years, the flexible retaining dam becomes increasingly popular because of its simple installation, high construction efficiency, good economy, and small impact on the environment [17]. Compared with the rigid retaining structure, the flexible retaining structure can generate large deformation under the impact, resulting in a better energy dissipation mechanism, thereby lowering the peak impulsive force [18]. However, the dynamic coupling among the particle-fluid flexible retaining structure is significantly complex, which depends on the hydrodynamic mechanism, the particle movement characteristics, and the deformation and mechanical characteristics of the flexible retaining structure, as well as the energy conversion and dissipation between them. It remains a highly challenging topic. At present, there is no reasonable theoretical basis for the design of flexible retaining structure. Therefore, a limited test and numerical simulation are carried out and the engineering is only designed and constructed by experience. Although the failure analysis of flexible retaining dam under debris flow impact is rarely discussed, this is the key issue of engineering design [19].

One of the main aspects of the study of the coupling effects of debris flow and flexible support structure is the numerical simulation method, which is mainly divided into continuous environment calculation method, discrete environment method, and mixed environment method [17, 20, 21]. The continuous environment calculation method relies on the continuous distribution of mass and deformation of the object under study. The equations describing the dynamic characteristics are established. These equations are discretized on the computational domain based on grids or particles and solved by combining the initial and boundary conditions [18, 22]. The main continuous medium calculation methods are the finite element method and the smooth particle kinematics method, or in other words, both debris flow and flexible retaining structures are simulated by the finite element method or the SPH method. This method is more mature and has been verified in theory and experiment. The discrete medium method in the analysis of debris flow and flexible retaining structure is mainly the discrete element method [19, 23]. Leonardi et al. [24] employed the DEM method to study the coupling effect of debris flow and flexible retaining structure and compared with the experimental results. The results showed that the DEM method could better reflect the interaction between debris flow and flexible retaining structure and was close to the experimental results, thus verifying the effectiveness of numerical analysis method.

In order to make full use of the advantages of different methods, the coupling numerical analysis method of debris flow and retaining structure has become a research hotspot in recent years. Leonardi et al. [25–27] used the LBM-DEM method to address the effect of the debris flow on the structure and adopted the coupling numerical analysis method to conduct a series of analysis and numerical verification, proving the robustness of the method in various cases. The debris flow impact of different flexible retaining structures was carried out, and the failure mode of the flexible retaining structure was explored. Li and Zhao [28, 29] adopted the coupled CFD-FEM method to simulate the debris flow, as well as the impact on rigid and flexible retaining dams. The model revealed that the actual simulation of the debris flow needs to consider the solid-liquid interaction. In addition, the effect of erosion on the impulsive force of debris flow was taken into account. The results showed that the debris flow impulsive force was significantly influenced by the slope and the solid-liquid ratio. The impact law and failure mode of flexible retaining dam are studied by employing the coupling numerical analysis method. Liu et al. [30, 31], respectively, used SPH-FEM and DEM-FEM to investigate the impact characteristics of debris flow, large stone, and retaining dam as well as the coupling effect of debris flow and flexible retaining structure. The results showed that the coupling numerical method could well reproduce the impact-climbing-silting process of debris flow and the impact issue of flexible retaining structure. Li et al. [32] used the SPH-DEM method to study the dynamic performance and impact force of debris flow on a rigid retaining structure. Although the coupling numerical analysis method provides the basis and

reference for the theory and method of this paper, there is no research and discussion on the mechanical properties and impulsive force of flexible retaining structure. The flow process of debris flow is shown in Figure 1 [3].

In summary, there is no reasonable theoretical basis for the design of flexible retaining structure. Instead, the design and construction of the project only depend on experience, and no corresponding specification for the prevention and control of debris flow by flexible retaining dams has been formulated in various countries. There are very few research studies on dynamic response analysis of flexible retaining structure impacted by debris flow. Currently, the research only concentrates on the retaining structure affected by large rock, debris flow fluid, or debris flow fluid along with large rock. Only few numerical analysis methods are used to analyze the coupling effect of debris flow and flexible retaining structure. The SPH-DEM-FEM numerical analysis method is applied to investigate the dynamic response of a retaining structure impacted by debris flow here, providing a certain reference for debris flow prevention engineering practice.

2. Numerical Calculation Theory

LS-DYNA code is adopted for SPH-DEM-FEM numerical simulation, in which SPH is used to simulate liquid debris flow, DEM is used to simulate solid particles, and FEM is used to simulate flexible retaining structure and debris flow channel. The SPH-DEM-FEM coupling analysis method is adopted to establish a complex dynamic interaction model of particle-fluid-structure, which can truly simulate the dynamic interaction between actual debris flow and flexible retaining structure. The realization principle and control equations of numerical simulation are introduced in this chapter.

2.1. DEM Control Equation. Debris flow particles in the solid phase are modelled by DEM. An elastic model is adopted for the contact between solid-phase debris flow particles [33–36].

The expression of force on particles is shown as follows:

$$\left. \begin{aligned} f_n &= -(k_n \lambda + c_n \nu_{ij} \cdot n_n) n_n \\ f_t &= -(k_t \delta + c_t s_{ij} \cdot n_t) n_t \end{aligned} \right\} \quad (1)$$

Among which, λ and δ represent the overlapping distances of normal direction and tangential direction, respectively, and k_n and k_t denote normal stiffness and tangential stiffness, respectively.

The resulting external force and the resulting external moment on the particles are expressed as follows:

$$\left. \begin{aligned} F_i &= \sum_{j=1}^k (f_{nij} + f_{tij}) \\ T_i &= \sum_{j=1}^k r_i (f_{sij} \cdot n_t) \end{aligned} \right\} \quad (2)$$

Among which, f_s represents the friction between particles.



FIGURE 1: Dynamic process of debris flow [3].

An elastic material model is adopted for the interaction force between particles, and the constitutive model of the material is shown as follows:

$$\sigma_e = E_e \varepsilon_e. \quad (3)$$

Among which, E_e represents the particle elastic model and ε_e is the particle elastic strain.

2.2. SPH Control Equation. In this paper, SPH is used to simulate the flow of debris in the liquid phase. The basic concept of this method is to regard the fluid (or solid) as continuous one and describe it by interacting particle groups. Each particle point carries various physical parameters, including mass and velocity [37–40].

The approximate function of particles is shown in the following formula:

$$\Pi^h f(x) = \int W(x-y) dy, \quad (4)$$

where W is the kernel function.

Kernel function W can be obtained by function θ , and their relation is shown in the following formula:

$$W(x, h) = \frac{1}{h(x)^d} \theta(x), \quad (5)$$

where d is the spatial dimension and h is the smooth length that varies with time and space.

In this paper, the smooth kernel function is shown as follows:

$$\theta(u) = C \times \begin{cases} 1 - \frac{3}{2}u^2 + \frac{3}{4}u^3; & |u| \leq 1, \\ \frac{1}{4}(2-u)^3; & 1 \leq |u| \leq 2, \\ 0; & 2 < |u|, \end{cases} \quad (6)$$

where C is a generalized constant depending on the spatial dimension.

The SPH method bases on the integral formula of moving particles $((x_i(t)))$, $i \in \{1, 2, \dots, N\}$, among which $x_i(t)$ is the spatial position vector of particle i , which moves along the velocity field v .

At this time, the approximation function of particle can be expressed by the following formula:

$$\Pi^h f(x_i) = \sum_{j=1}^N w_j f(x_j) W(x_i - x_j, h), \quad (7)$$

where $w_j = (m_j/\rho_j)$, and the gravity of the particle w_j changes in proportion to the divergence of the fluid.

2.3. SPH-DEM-FEM Coupling Control Equation. The DEM-FEM coupling equation is used to describe the complex dynamic interaction between solid-phase particles and a flexible containment structure, which can be found in the following equation [18, 41–43]:

$$\left. \begin{aligned} m_i \ddot{u}_i &= m_i g + \sum_{k=1}^m (f_{n,ik} + f_{t,ik}) + \sum_{j=1}^l (f_{n,ij} + f_{t,ij}) \\ I_i \ddot{\theta}_i &= \sum_{k=1}^m T_{ik} + \sum_{j=1}^l T_{ij} \\ M \ddot{X} + C \dot{X} + K X &= f_a + f_b \end{aligned} \right\}, \quad (8)$$

where $f_{n,ij}$ and $f_{t,ij}$ represent the normal and the tangential contact force.

The DEM-FEM coupling equation is shown as follows:

$$M \ddot{U} + CU + K d = F + F_C. \quad (9)$$

The SPH-DEM coupling control equation is used to describe the complex dynamic interaction between the particles in the solid phase of the debris flow and the fluid in the liquid phase of the debris flow [18], as presented in the following equation:

$$\left. \begin{aligned} m_i^s \frac{du_i^s}{dt} &= F_i^c + F_i^{bs} + m_i^f f_i^{fs} \\ I_i \frac{d\omega_i^s}{dt} &= M_i^c + M_i^{fs} + M_i^{bs} \\ \frac{du_i^f}{dt} &= - \sum_{j=1}^N m_j \left(\frac{p_i}{\rho_i} + \frac{p_j}{\rho_j} + \Pi_{ij} + R_{ij} f_{ij}^A \right) \nabla_i W_{ij} + f_i^{sf} + f_i^{bf} \end{aligned} \right\}, \quad (10)$$

where F_i^{bs} and F_i^{bs} are the force on each other and M_i^{fs} , M_i^{bs} , and M_i^c denote the torque.

3. Calculation Model

This paper selects Nanjiaogou as the prototype. The rugged topography in the ditch is sharp, the gullies can be found anywhere, and the slope of the main ditch formation area is $19^\circ \sim 47^\circ$, which belong to a vast debris flow ditch. The detailed geological information of Nanjiaogou can be found in [32].

In order to study the impulsive force and dynamic response of flexible retaining structure impacted by debris flow, a complex dynamic interaction model of particle-fluid-

structure is established in the present study. Considering that the debris flow impulse force and the dynamic response of the flexible retaining structure are mainly studied in this paper and the actual gully is basically in trapezoidal distribution, to facilitate the study, the debris flow gully is simplified into trapezoidal one, and retaining and governance measures are performed on the main gully formation area with the steep slope. Considering that the slope of the main ditch formation area is $19^\circ \sim 47^\circ$, the average slope of the main gully formation area is confirmed at 30° . In this paper, the impulsive force and dynamic response of flexible retaining structure are analyzed, when the slope of gully is 15° , 20° , 30° , 40° , and 50° .

3.1. Geometric Model. The geometric model of the debris flow is shown in Figure 2, and the geometric model of the flexible retaining structure is presented in Figure 3. The specific parameters of the geometric model are displayed in Table 1. The parameters such as debris flow channel and DEM particle density, elastic modulus, and Poisson's ratio are shown in the literature [32], and the specific mechanical parameters of the flexible retaining net and support cable are shown in the literature [24, 28, 29].

The research object of this paper is mainly the impact force and dynamic response of the flexible retaining structure. Then, according to the field survey, the channel is roughly trapezoidal distribution and the bottom and the side of the gully are then simplified into the trapezoidal section according to the on-site situation. Furthermore, in view of the fact that the slope of the main ditch formation area is $19^\circ \sim 47^\circ$, the average value 30° is selected; debris flow is composed of solid particles and fluids, which impacts the flexible retaining structure under the action of gravity, reproducing scenery of the impact, blocking by the flexible retaining structure, climbing along the flexible retaining structure, and water-rock separating in the process of impacting by debris flow. And this paper studies the impulsive force and dynamic response of flexible retaining structure impacted by solid-liquid two-phase debris flow.

The flexible retaining structure consists of flexible retaining nets and support cables. The four support cables are numbered as NO.1, NO.2, NO.3, and NO.4 from the bottom to top. The distance between the support cables is 0.5 m. The geometric model of the flexible retaining structure is shown in Figure 3. With a diameter of 20 mm, the flexible retaining net is formed by steel wires winding. The hexagonal side length of the retaining net is 0.1 m, which can smoothly discharge debris flow and effectively prevent debris flow particles from flowing out. The support cable is formed by a steel wire winding with a diameter of 20 mm, having an equivalent diameter of 0.1 m. The flexible retaining net and the supports cable are fixedly connected to bear the force in a better way. The specific mechanical parameters of the flexible retaining net and support cable are shown in the literature [24, 28, 29].

3.2. Constitutive Model of Materials. Because the channel rock mass in this paper relatively remains stable, the debris flow channel is simulated by rigid shell material. In this

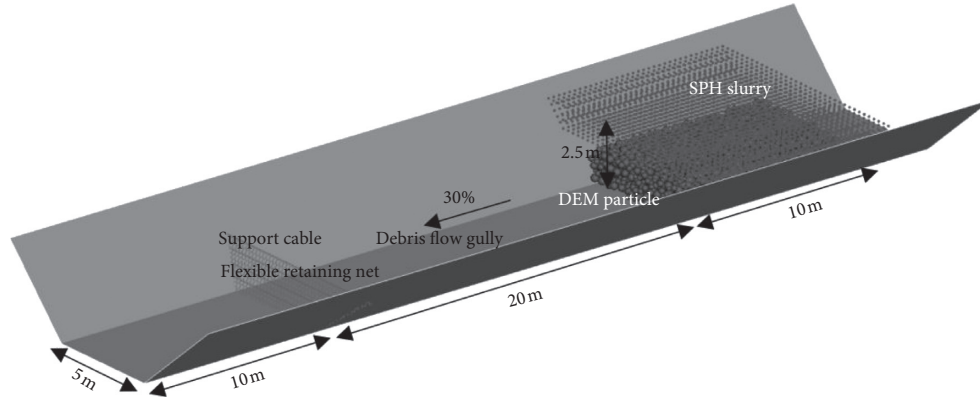


FIGURE 2: Geometric model of debris flow.

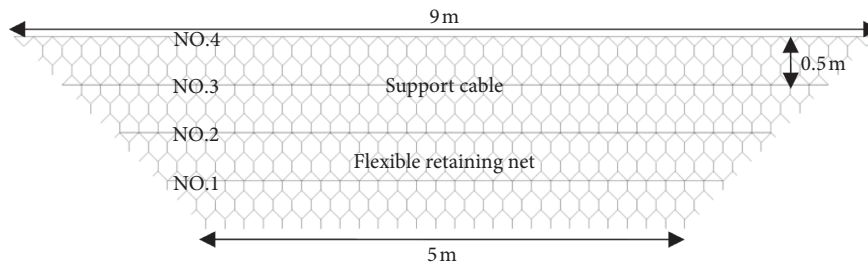


FIGURE 3: Geometric model of flexible retaining structure.

TABLE 1: Basic setting parameters of simulation.

	Density (kg/m^3)	Elastic modulus (GPa)	Poisson's ratio	Yield strength (MPa)	Ultimate strain	Constitutive model
Channel	3000	30.0	0.24	—	—	RIGID
DEM particles	2650	30.0	0.30	—	—	ELASTIC
Flexible retaining net	7850	177	0.30	1770	0.05	PLASTIC_KINEMATIC
Support cable	7850	177	0.30	1770	0.05	PLASTIC_KINEMATIC

paper, the RIGID material model is adopted, with 6056 shell elements in total. The parameters of debris flow channel adopt the numerical simulation parameters in the literature [19].

According to the field sampling test, the measured average density of solid particles in debris flow source is $2650 \text{ kg}/\text{m}^3$. Based on the field survey and laboratory test, we measured that the particle size range of provenance is 0.2~0.4 m. The size range of DEM particles set by us is consistent with the field test results. The solid-liquid ratio of debris flow exerts a great influence on the characteristics of debris flow. In this paper, the ratio of solid to liquid is 1:1. This paper uses discrete element particle simulation. The LS-DYNA ELASTIC model is adopted for the material constitutive, the LS-DYNA DE_BY_PART contact model is adopted for the interaction between the particles, and the LS-DYNA DE_SURFACE_COUPLING model is used for the contact between the particles and the channel. In addition, the LS-DYNA DE_TO_BEAM_COUPLING model is used for the contact between particles and flexible retaining

structure, with a total of 2236 particles in the above-mentioned models.

The object of this paper is the low-speed moving dilute debris flow, without considering the effect of viscous force for the time being. The density of water is $1000 \text{ kg}/\text{m}^3$, and the friction force between fluids is 0.12. The value of friction coefficient will be described in detail in Section 3.3. The SPH model is used for analysis, and the constitutive model employs the NULL material model, with the viscosity coefficient of 0.001. The constitutive model of water is involved in this paper, while the constitutive model uses the EOS_MURNAGHAN model, and the constant of state equation GAMMA is 7.0, with K_0 of 150,000. To sum up, there are totally 4351 particles in the model. The SPH_DE_COUPLING contact model is adopted for the interaction between SPH particles and DEM particles, and the AUTOMATIC_NODES_TO_SURFACE model is adopted for the contact between SPH particles and channels. The parameters of fluids adopt the numerical simulation parameters in the literature [19].

The support cable of flexible retaining structure is modelled by cable element, with the density of 7850 kg/m^3 and yield strength of 1770 MPa . Because the flexible retaining structure bears the dynamic impact, the material constitutive model adopts the PLASTIC_KINEMATIC model, with the ultimate strain of 0.05. The flexible retaining net is simulated by BEAM element, with the density of 7850 kg/m^3 and yield strength of 1380 MPa . Because the flexible retaining structure bears the dynamic impact, the constitutive model of the material adopts the PLASTIC_KINEMATIC model. The specific mechanical parameters of flexible retaining nets and support cables can be found in the literature [24, 28, 29].

3.3. Boundary Conditions. The channel and the flexible retaining structure are firmly connected with the ground. The bottom and both sides of the debris channel are completely fixed and capped. The flexible retaining net and the supporting cable are connected with the ground through the anchor cable. Therefore, the flexible retaining net and support cables are fully fixed in this paper.

The coefficient of friction between debris flow solids is typically 0.1–0.5 [16–18] by analyzing and comparing the experimental and simulation results in a large amount of relevant literature. According to similar studies, the trial-and-error method is generally used to explore and compare the numerical simulation results with actual cases. When the peak velocity data of debris flow numerical simulation are close to the experimental or actual data, the parameters are regarded to be more accurate. After adopting the trial-and-error method and reviewing similar literature, it can be found that the simulated results are close to the actual results, when the coefficient of friction between the debris flow solids and the channel and the retaining wall is 0.3 and the coefficient of friction between the debris flow fluid and the channel and the flexible retaining structure is 0.12.

We use the dynamic explicit method of LS-DYNA code for performing the analysis. The analysis step time is 10 s. The debris flow begins to slide with an initial velocity of 0 m/s^2 . The gravitational acceleration of both the debris flow fluid and the debris flow solid particles is 9.8 m/s^2 . Totally, the calculation gets 1974743 incremental steps. The CPU time is 22 h 3 min 43 s.

4. Establishment of Calculation Model

4.1. Impacting Process. The impact, retaining, water-rock separation, and deposition process of flexible retaining structure impacted by debris flow are shown in Figure 4. When $t = 0.9 \text{ s}$, the debris flow starts to move, and at this time, “dragon head, dragon body, and dragon tail” have basically taken shape. Debris flow fluid and solid particles yield complex dynamic coupling interaction. When $t = 2.3 \text{ s}$, the solid-liquid two-phase debris flow reaches the bottom of the flexible retaining structure. At this moment, the maximum velocity of debris flow reaches 10.52 m/s , and the particle-fluid-structure joint is forced to produce complex dynamic interaction and impact the flexible retaining

structure. Meanwhile, the “dragon head” of debris flow impacts the flexible retaining structure, climbing high and separating water-rock, and the solid particles remain at the bottom of the retaining structure under the action of retaining structure. At the same time, most of the fluid is discharged from the retaining structure. When $t = 3.5 \text{ s}$, the “dragon body” impacts the flexible retaining structure. Most of the debris flow solid particles are retained at the bottom, and the fluid is discharged. The debris flow will continue to impact the flexible retaining structure. At this time, because of the climbing effect, the bottom of the flexible retaining structure produces a dead load due to particle deposition, while the top part is still impacted by the dynamic impact of the debris flow. The SPH method can greatly deal with the splash and diffusion of fluid particles and participate in complex dynamic interaction with flexible retaining structure and debris flow particles. The numerical simulation well reflects the complex dynamic interaction of particle-fluid-structure. When $t = 5.2 \text{ s}$, the debris flow silts back and the particles finally deposit at the bottom of the retaining dam to produce a dead load. The fluid is slowly discharged.

4.2. Climbing and Silting Process. The climbing and silting process of the flexible retaining structure impacted by debris flow is illustrated in Figure 5. When $t = 2.5 \text{ s}$, debris flow particles reach the bottom of the flexible retaining structure and start to impact the debris flow retaining dam and climb high. At this time, the water-rock separation has already taken shape and the fluid is discharged through the retaining structure. The flexible retaining structure is deformed. Besides, the most deformed parts are the middle and bottom of the flexible retaining structure. When $t = 3.0 \text{ s}$, debris flow particles continue to climb high and some even silt back in certain part. At this time, it can be observed that particle-fluid-structure shapes complex dynamic interaction, and the current climbing height is 1.3 m. When $t = 3.5 \text{ s}$, the “dragon body” impacts the retaining dam, and the debris flow particles climb to the highest level, with obvious back silting and particle splashing. The climbing height is as high as 2.1 m. When $t = 5.2 \text{ s}$, the debris flow silts back, finally producing a dead load at the bottom of the retaining dam. At this moment, the height of silting is the height of the retaining structure.

4.3. Analysis of Displacement Change of Flexible Retaining Structure over Time. The displacement change over time in the middle position of four support cables (NO.1, NO.2, NO.3, and NO.4) of flexible retaining structure under different slopes is monitored in Figure 6. The results reveal that when the slope is 50 degrees and $t = 3 \text{ s}$, the displacement of the middle position of NO.4 support cable of flexible retaining structure reaches the maximum, and the maximum value is 0.265 m. Then, it decreases rapidly to 0.160 m after reaching the peak value. When the slope is 15 degrees, 20 degrees, 30 degrees, and 40 degrees, the peak displacement value of the middle position of the support cable of the flexible retaining structure is 0.0283 m, 0.071 m, 0.164 m, and 0.221 m, respectively. Subsequently, all decrease to dead

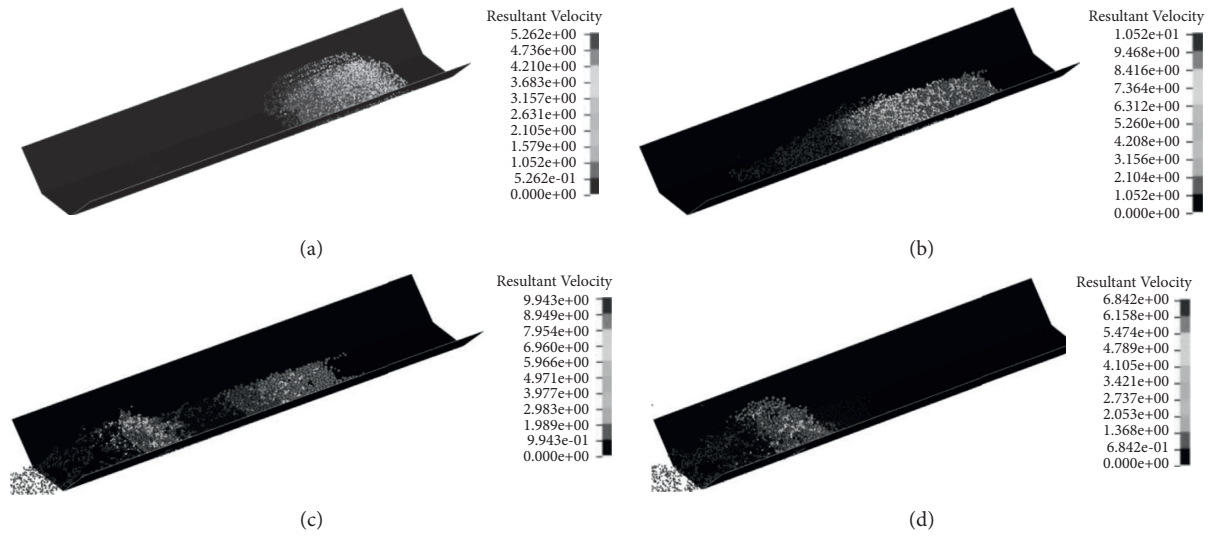


FIGURE 4: Process of flexible retaining structure impacted by debris flow. (a) $t=0.9$ s. (b) $t=2.3$ s. (c) $t=3.5$ s. (d) $t=5.2$ s.

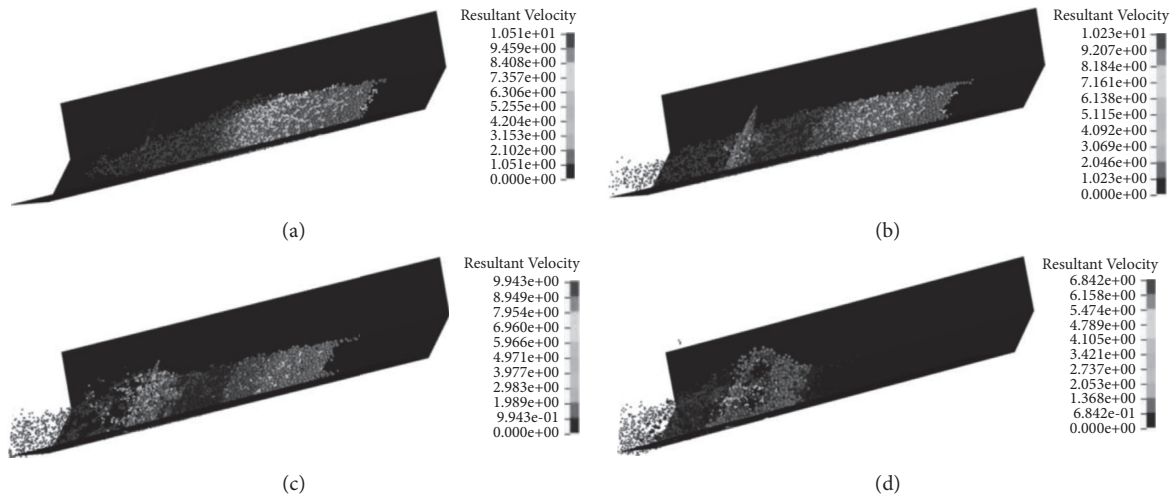


FIGURE 5: Climbing and silting process of debris flow. (a) $t=2.5$ s. (b) $t=3.0$ s. (c) $t=3.5$ s. (d) $t=5.2$ s.

displacement, which are 0.0146 m, 0.055 m, 0.122 m, and 0.170 m, respectively. When the slope is 15°, 20°, 30°, 40°, and 50°, the difference between the maximum peak displacement and static displacement of the flexible barrier structure is 0.0137 m, 0.016 m, 0.042 m, 0.051 m, and 0.105 m, respectively. Moreover, the simulation results are identical to the numerical simulation and test results performed by Leonardi et al. [24–27], showing that the above method is suitable for simulating the flexible retaining structure impacted by debris flow.

4.4. Analysis of Impulsive Force Change over Time. The impulsive force change of flexible retaining structures with different slopes (15°, 20°, 30°, 40°, and 50°) over time is displayed in Figure 7. It can be observed from the figure that when the slope is 50 degrees and $t=2.9$ s, the impulsive force of the debris flow on the retaining dam reaches its peak value,

which is 6089 kN, and then decreases rapidly to 3832 kN. When the slope is 15°, 20°, 30°, and 40°, the peak values of impulsive force of the retaining dam are 987 kN, 1983 kN, 3690 kN, and 4625 kN, respectively, and subsequently all decrease to dead loads. With the increase of the slope, the start time of the debris flow impact force is 3.4 s, 3.2 s, 3 s, 2.5 s, and 2 s, respectively. In addition, the peak time of the debris flow impact force is 4.9 s, 4.7 s, 3.9 s, 3.2 s, and 2.9 s, respectively.

We compare the numerical calculation results according to the semiempirical formula of impulsive force peak value of the debris flow based on hydrodynamic theory proposed by Kwan [44]:

$$F_{\max} = \kappa \rho v^2 h_0 w \sin \beta, \quad (11)$$

where $\kappa = aFr^b$ is the dynamic pressure coefficient, ρ represents the density, v is the impulsive velocity, w is the width, and h_0 is the height of debris flow.

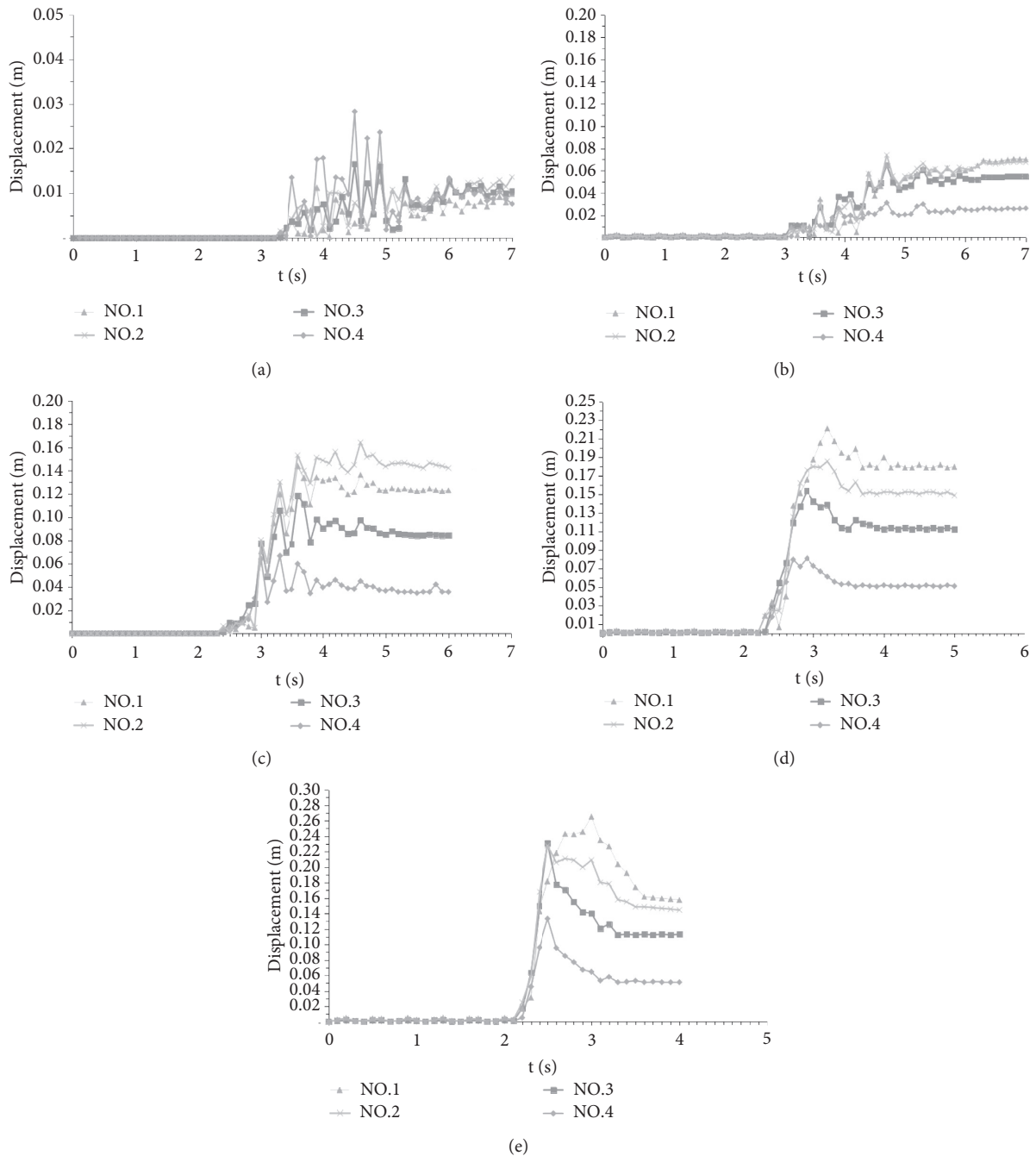


FIGURE 6: Analysis of the displacement change on the monitoring point of the flexible barrier structure over time. (a) 15 degrees. (b) 20 degrees. (c) 30 degrees. (d) 40 degrees. (e) 50 degrees.

The calculation results are obtained from the numerical calculation method in this paper, and the existing empirical formulas are shown in Table 2. The calculation error ranges from 12.1% to 27.4%. Comparing the numerical calculation method adopted in the present study with the empirical values, the impulsive force results of the two methods are relatively close. However, the empirical methods do not consider the water-rock separation and the complex dynamic interaction of particle-fluid-structure. Therefore, the numerical analysis method is more reasonable than the empirical methods.

4.5. Maximum Deformation of Flexible Retaining Structure.

The maximum deformation of flexible retaining structure with different slopes (15° , 20° , 30° , 40° , and 50°) can be found in Figure 8. The maximum deformation of flexible retaining structure is positively associated with the channel slope, and the maximum deformation position is located in the middle of flexible retaining structure, which is consistent with the observed results in practice. When the slope is 15° , 20° , 30° , 40° , and 50° , the maximum peak displacement values in the middle of the flexible retaining structure are 0.0283 m,

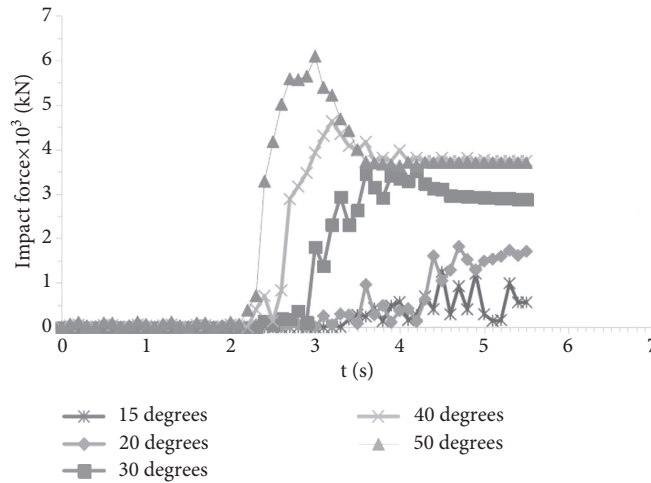


FIGURE 7: Analysis of impulsive force change of flexible retaining structure over time.

TABLE 2: Comparison of maximum impact force.

	15°	20°	30°	40°	50°
Kwan empirical value (kN)	1359	2532	4516	5409	6927
Method adopted in this paper (kN)	987	1983	3690	4625	6089
Error (%)	27.4	21.7	18.3	14.5	12.1

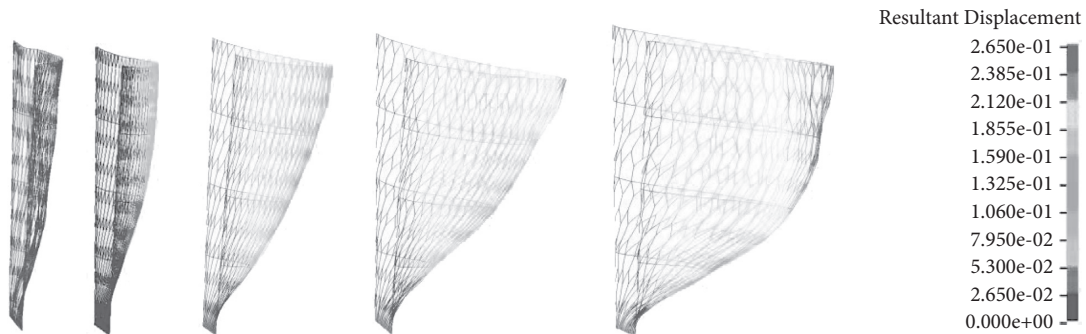


FIGURE 8: Maximum deformation of flexible retaining structure.

0.071 m, 0.164 m, 0.221 m, and 0.265 m, respectively. Clearly, it can be seen that the support cable can restrain the flexible retaining net from deformation. Because the flexible retaining net and the supporting cables are fixed to each other, the deformation of the two is consistent with each other. In addition, the deformation of the flexible retaining net between the supporting cables is bigger than the deformation of the supporting cable, showing a convex shape.

5. Discussion

According to the results, the SPH-DEM-FEM coupling numerical analysis method vividly simulates the complex dynamic interaction of particle-fluid-structure, reproducing the impact, retaining, water-stone separation, climbing, silting, and deposition process of debris flow. The SPH method can greatly handle the splashing and diffusion of fluid particles and participate in complex dynamic interaction with flexible retaining structure and debris flow

particles. The water-stone separation phenomenon can well reproduce the real debris flow blocking process, which is difficult to be reflected by other numerical analysis methods, which can also build up a good foundation for better evaluating the accuracy of debris flow impact assessment of flexible retaining structure. The displacement change of flexible retaining structure over time is analyzed here. Moreover, the simulation results and laws are consistent with the existing research results.

The analysis of impulsive force change over time is carried out. Although the analysis results are similar to the existing empirical formula, the empirical formula does not consider the water-rock separation and the complex dynamic interaction between particle-fluid-structure, and the error between the numerical simulation results and the empirical formula ranges from 12.1% to 27.4%. Therefore, the numerical analysis method is more reasonable than the empirical method. The peak impulsive force of debris flow is positively correlated with the slope of the channel, and the

larger the slope is, the greater the peak impulsive force of debris flow is. Then, the impulsive force of debris flow is decreased to a dead load, with enormous decrease in amplitude. When the slope is small, the peak impulsive forces of debris flow are close to a dead load. The impulsive force of debris flow will decrease slowly in the later stage, which is caused by the fluid removal from the flexible retaining structure due to the water-rock separation. It cannot be presented by employing the empirical formula method and traditional numerical analysis method. The results of the coupled numerical analysis method are more convincing than the empirical formula method.

The maximum deformation of flexible retaining structure is analyzed, and the deformation is positively associated with the slope of the channel. This is because when the slope of the channel is sharp, the gravitational potential energy of debris flow is relatively large, and once the debris flow takes shape, the kinetic energy and impulsive force produced by debris flow will be far greater than when the slope is small. Li et al. [32] explore the impulsive force and dynamic performance of rigid retaining structure impacted by debris flow by adopting the SPH-DEM-FEM method. By comparing impulsive force and dynamic performance of flexible retaining structure impacted by solid-liquid two-phase debris flow discussed in this paper, the dynamic performance and impact characteristics of flexible retaining structure and rigid retaining structure are quite different. Because of the water-rock separation and the remarkable ability to absorb energy, the impulsive force of the flexible retaining structure is much smaller than that of the rigid retaining structure. This also indicates that the traditional impulsive force formula of debris flow is not applicable to the flexible retaining structure, which is also the research significance of the present study. The results show that the mechanical performance of flexible retaining structure is more reasonable than that of rigid retaining structure.

Since the rigidity of the flexible retaining structure is much smaller than that of the rigid retaining structure, the dynamic characteristics between them are significantly different. The displacement change over time between the flexible retaining structure and rigid retaining structure is different by two orders of magnitude. The recovery ability after deformation of the flexible retaining structure is far less than that of the rigid retaining structure, requiring us to accordingly monitor the deformation of the flexible retaining structure in order to prevent dam collapse from bringing devastation to the downstream. The maximum deformation position is located in the middle of the flexible retaining structure, which gradually decreases to both sides. The support cable plays an obvious role in restraining the flexible retaining net and acts as a major carrier in bearing and transmitting force. The results of numerical simulation are compared with the deformation of real flexible retaining structure, showing good consistence.

In this article, the terrain conditions are simplified, considering neither the impact of the unevenness of the movement path on the motion characteristics of the debris flow and the dynamic characteristics of the flexible retaining structure nor the impact of the loose accumulation layer on

the movement path on the impulsive force of the debris flow and the dynamic characteristics of the flexible retaining structure. All the abovementioned problems are the research difficulties and can be further studied in future research.

6. Conclusion

- (1) Based on the coupling numerical method, this article considers the complex dynamic interaction of particle-fluid-structure, reproducing the whole process of flexible retaining structure impacted by debris flow, such as impact, retaining, water-rock separation, climbing, siltation, and deposition.
- (2) We compare the dynamic response analysis of flexible retaining structure impacted by debris flow under different slopes, monitoring the displacement change of the middle position of four support cables (NO.1, NO.2, NO.3, and NO.4) of flexible retaining structure over time. It can be found that the simulation results and laws are consistent with the existing research results.
- (3) We compare the change law of the impulsive force of debris flow under different slopes. However, the empirical formula does not consider the water-rock separation and the complex dynamic interaction of particle-fluid-structure, and thus, the error of empirical formula results and the numerical simulation results ranges from 12.1% to 27.4%. As a result, the numerical analysis method is more reasonable than the empirical method.
- (4) We analyze the maximum deformation of the flexible retaining structure, concluding that the deformation is positively associated with the slope of the channel. The maximum deformation is located in the middle of the flexible retaining structure, and the support cable can obviously restrain the flexible retaining net.

Data Availability

The data for this study are available on request to the corresponding author.

Conflicts of Interest

The authors declare that there are no conflicts of interest regarding the publication of this paper.

Acknowledgments

This research was funded by the Natural Science Foundation of China (grant no. 41972267).

References



- [1] J. L. Miao, W. Z. Zhang, and J. Y. Zhou, "Numerical simulation of the accumulation state of viscous debris flow by smooth particle hydrodynamics method," *Journal of Natural Disasters*, vol. 22, no. 6, pp. 125–130, 2013.

- [2] M. Jakob, O. Hungr, and D. M. Jakob, "Debris-flow hazards and related phenomena," *Environmental and Engineering Geoscience*, vol. 8, no. 1, pp. 165–171, 2007.
- [3] C. A. Dowling and P. M. Santi, "Debris flows and their toll on human life: a global analysis of debris-flow fatalities from 1950 to 2011," *Natural Hazards*, vol. 71, no. 1, pp. 203–227, 2014.
- [4] C. Tang, N. Rengers, T. W. J. van Asch, Y. H. Yang, and G. F. Wang, "Triggering conditions and depositional characteristics of a disastrous debris flow event in Zhouqu city, Gansu province, northwestern China," *Natural Hazards and Earth System Sciences*, vol. 11, no. 11, pp. 2903–2912, 2011.
- [5] W. Ashwood and O. Hungr, "Estimating total resisting force in flexible barrier impacted by a granular avalanche using physical and numerical modeling," *Canadian Geotechnical Journal*, vol. 53, no. 10, pp. 1700–1717, 2016.
- [6] C. W. W. Ng, D. Song, C. E. Choi, L. H. D. Liu, and J. S. H. Kwan, "Impact mechanisms of granular and viscous flows on rigid and flexible barriers," *Canadian Geotechnical Journal*, vol. 54, no. 2, pp. 188–206, 2016.
- [7] T. Haas, L. Braat, J. R. Leuven, I. R. Lokhorst, and M. G. Kleinhans, "Effects of debris flow composition on runout, depositional mechanisms, and deposit morphology in laboratory experiments," *Journal of Geophysical Research: Earth Surface*, vol. 120, no. 9, pp. 19493–1972, 2015.
- [8] X. B. Zhou, *Debris Flow's Harm to Bridge Engineering and its Prevention*, Tongji University, Shanghai, China, 2006.
- [9] Z. Tao, M. Li, C. Zhu, M. He, X. Zheng, and S. Yu, "Analysis of the critical safety thickness for pretreatment of mined-out areas underlying the final slopes of open-pit mines and the effects of treatment," *Shock and Vibration*, vol. 2018, no. 2, pp. 1–8, 2018.
- [10] X. J. Yang, J. M. Wang, C. Zhu, M. C. He, and Y. Gao, "Effect of wetting and drying cycles on microstructure of rock based on SEM," *Environmental Earth Sciences*, vol. 78, no. 6, pp. 1866–6280, 2019.
- [11] Z. Liang, C. Wang, D. Ma, and K. U. J. Khan, "Exploring the potential relationship between the occurrence of debris flow and landslides," *Natural Hazards and Earth System Sciences*, vol. 21, no. 4, pp. 1247–1262, 2021.
- [12] L. Ban, C. Zhu, C. Qi, and Z. Tao, "New roughness parameters for 3D roughness of rock joints," *Bulletin of Engineering Geology and the Environment*, vol. 78, no. 6, pp. 4505–4517, 2019.
- [13] C. Zhu, K. Zhang, H. Cai et al., "Combined application of optical fibers and CRLD bolts to monitor deformation of a pit-in-pit foundation," *Advances in Civil Engineering*, vol. 2019, no. 1, 16 pages, Article ID 2572034, 2019.
- [14] A. Leonardi, F. K. Wittel, M. Mendoza, and J. Herrmann, "Multiphase debris flow simulations with the discrete element method coupled with a lattice-Boltzmann fluid," in *Proceedings of the III International Conference on Particle-based Methods Fundamentals and Applications*, pp. 276–287, Stuttgart (Germany), 2013.
- [15] A. Armanini, "On the dynamic of debris flows," *Recent Development on Debris Flows*, pp. 208–226, Springer, Heidelberg, Germany, 1997.
- [16] C. Lichtenan, *Die berechnung von sperren in beton und eisenbeton, kolloquium on torrent dams odc 384.3*, pp. 91–127, Mitteilungen der Forstlichen Bundes-Versuchsanstalt, Wien, 1973.
- [17] A. Albaba, S. Lambert, F. Kneib, B. Chareyre, and F. Nicot, "DEM modeling of a flexible barrier impacted by a dry granular flow," *Rock Mechanics and Rock Engineering*, vol. 50, no. 11, pp. 3029–3048, 2017.
- [18] W. Anthony, G. Laurence, and V. Guillaume, "Grains3D, a flexible DEM approach for particles of arbitrary convex shape part I: numerical model and validations," *Powder Technology*, vol. 224, pp. 374–389, 2012.
- [19] C. Scheidl, M. Chiari, R. Kaitna et al., "Analysing debris-flow impact models, based on a small scale modelling approach," *Surveys in Geophysics*, vol. 34, no. 1, pp. 121–140, 2013.
- [20] Z. Tao, H. Zhang, C. Zhu, Z. Hao, X. Zhang, and X. Hu, "Design and operation of App-based intelligent landslide monitoring system: the case of Three Gorges Reservoir Region," *Geomatics, Natural Hazards and Risk*, vol. 10, no. 1, pp. 1209–1226, 2019.
- [21] Z. G. Tao, C. Zhu, M. C. He, and K. M. Liu, "Research on the safe mining depth of anti-dip bedding slope in Changshanhao Mine," *Geomechanics and Geophysics for Geo-Energy and Geo-Resources*, vol. 36, no. 6, pp. 1–20, 2020.
- [22] Z. Liang, C.-M. Wang, Z.-M. Zhang, and K.-U.-J. Khan, "A comparison of statistical and machine learning methods for debris flow susceptibility mapping," *Stochastic Environmental Research and Risk Assessment*, vol. 34, no. 11, pp. 1887–1907, 2020.
- [23] Z. Tao, Q. Geng, C. Zhu et al., "The mechanical mechanisms of large-scale toppling failure for counter-inclined rock slopes," *Journal of Geophysics and Engineering*, vol. 16, no. 3, pp. 541–558, 2019.
- [24] A. Leonardi, F. K. Wittel, M. Mendoza, R. Vetter, and H. J. Herrmann, "Particle-fluid-structure interaction for debris flow impact on flexible barriers," *Computer-Aided Civil and Infrastructure Engineering*, vol. 31, no. 5, pp. 323–333, 2016.
- [25] A. Leonardi, F. K. Wittel, M. Mendoza, and J. Hans, "Multiphase debris flow simulations with the discrete element method coupled with a lattice-Boltzmann fluid," in *Proceedings of the III International Conference on Particle-based Methods Fundamentals and Applications*, pp. 276–287, Stuttgart (Germany), 2013.
- [26] A. Leonardi, F. K. Wittel, M. Mendoza, and H. J. Herrmann, "Lattice-Boltzmann method for geophysical plastic flows," *Recent Advances In Modeling Landslides And Debris Flows*, pp. 131–140, Springer, Cham, Switzerland, 2015.
- [27] A. Leonardi, F. K. Wittel, M. Mendoza, and H. J. Herrmann, "Coupled DEM-LBM method for the free-surface simulation of heterogeneous suspensions," *Computational Particle Mechanics*, vol. 1, no. 1, pp. 3–13, 2014.
- [28] X. Li and J. Zhao, "A unified CFD-DEM approach for modeling of debris flow impacts on flexible barriers," *International Journal for Numerical and Analytical Methods in Geomechanics*, vol. 42, no. 14, pp. 1643–1670, 2018.
- [29] X. Li and J. Zhao, "Dam-break of mixtures consisting of non-Newtonian liquids and granular particles," *Powder Technology*, vol. 338, pp. 493–505, 2018.
- [30] C. Liu, Z. Yu, and S. Zhao, "Quantifying the impact of a debris avalanche against a flexible barrier by coupled DEM-FEM analyses," *Landslides*, vol. 17, no. 1, pp. 33–47, 2020.
- [31] C. Liu, Z. X. Yu, and L. R. Luo, "Dynamic behavior of a concrete dam impacted by debris flows with rock," *Journal of Vibration and Shock*, vol. 38, no. 14, pp. 161–168, 2019.
- [32] B. Li, C. Wang, Y. Li et al., "Dynamic response analysis of retaining dam under the impact of solid-liquid two-phase debris flow based on the coupled SPH-DEM-FEM method," *Geofluids*, vol. 2020, Article ID 6635378, 12 pages, 2020.
- [33] H.-k. Chen, H.-m. Tang, and Y.-i. Chen, "Research on method to calculate velocities of solid phase and liquid phase in debris

- flow,” *Applied Mathematics and Mechanics*, vol. 27, no. 3, pp. 399–408, 2006.
- [34] Q.-X. Meng, W.-Y. Xu, H.-L. Wang, X.-Y. Zhuang, W.-C. Xie, and T. Rabczuk, “DigiSim - an open source software package for heterogeneous material modeling based on digital image processing,” *Advances in Engineering Software*, vol. 148, Article ID 102836, 2020.
- [35] C. Zhu, M.-c. He, M. Karakus, X.-h. Zhang, and Z. Guo, “The collision experiment between rolling stones of different shapes and protective cushion in open-pit mines,” *Journal of Mountain Science*, vol. 18, no. 5, pp. 1391–1403, 2021.
- [36] Q. Yin, J. Y. Wu, C. Zhu et al., “Shear mechanical responses of sandstone exposed to high temperature under constant normal stiffness boundary conditions,” *Geomechanics and Geophysics for Geo-Energy and Geo-Resources*, vol. 7, no. 2, 2021.
- [37] W. Wang, G. Chen, Z. Han, S. Zhou, H. Zhang, and P. Jing, “3D numerical simulation of debris-flow motion using SPH method incorporating non-Newtonian fluid behavior,” *Natural Hazards*, vol. 81, no. 3, pp. 1981–1998, 2016.
- [38] Q. Wang, Z. Jiang, B. Jiang, H. Gao, Y. Huang, and P. Zhang, “Research on an automatic roadway formation method in deep mining areas by roof cutting with high-strength bolt-grouting,” *International Journal of Rock Mechanics and Mining Sciences*, vol. 128, Article ID 104264, 2020.
- [39] Y. Wang, W. K. Feng, R. L. Hu, and C. H. Li, “Fracture evolution and energy characteristics during marble failure under triaxial fatigue cyclic and confining pressure unloading (FC-CPU) conditions,” *Rock Mechanics and Rock Engineering*, vol. 54, no. 2, pp. 799–818, 2021.
- [40] Q. Wang, Y. Wang, M. He et al., “Experimental research and application of automatically formed roadway without advance tunneling,” *Tunnelling and Underground Space Technology*, vol. 114, no. 3, Article ID 103999, 2021.
- [41] F. Wu, R. Gao, J. Liu, and C. Li, “New fractional variable-order creep model with short memory,” *Applied Mathematics and Computation*, vol. 380, Article ID 125278, 2020.
- [42] F. Wu, H. Zhang, Q. Zou, C. Li, J. Chen, and R. Gao, “Viscoelastic-plastic damage creep model for salt rock based on fractional derivative theory,” *Mechanics of Materials*, vol. 150, Article ID 103600, 2020.
- [43] A. Li, F. Dai, Y. Liu, H. Du, and R. Jiang, “Dynamic stability evaluation of underground cavern sidewalls against flexural toppling considering excavation-induced damage,” *Tunnelling and Underground Space Technology*, vol. 112, Article ID 103903, 2021.
- [44] J. S. H. Kwan, “Supplementary technical guidance on design of rigid debris-resisting barriers,” *Geotechnical Engineering Office*, Civil Engineering Dept, Chennai, India, 2012.

Research Article

Numerical Simulation Analysis of Slope Instability and Failure of Limestone Mine in Weibei

Kuiming Liu ^{2,3}, Hui Li,^{2,3} Shihui Pang,^{2,3} Meng Mi ^{2,3}, Jianping Chen,¹ and Kui Sun¹

¹Key Laboratory of Mine Geological Hazards Mechanism and Control, Xian 710054, China

²State Key Laboratory for Geomechanics and Deep Underground Engineering, China University of Mining and Technology (Beijing), Beijing 100083, China

³School of Mechanics and Civil Engineering, China University of Mining and Technology (Beijing), Beijing 100083, China

Correspondence should be addressed to Meng Mi; 294704212@qq.com

Received 4 May 2021; Accepted 16 September 2021; Published 21 October 2021

Academic Editor: Gan Feng

Copyright © 2021 Kuiming Liu et al. This is an open access article distributed under the Creative Commons Attribution License, which permits unrestricted use, distribution, and reproduction in any medium, provided the original work is properly cited.

Weibei area is the largest limestone resource area in Shaanxi Province, which is an important boundary to distinguish the climate difference between the south and the north of China, and also a significant ecological safety protection barrier in the northwest of China. The complex geological environment and harsh environment make the mining area have serious geological disaster hidden danger. Based on the site engineering geological data of typical limestone quarry slope in Weibei, this paper constructs a three-dimensional geological model, uses FLAC3D software to simulate excavation, and analyzes the stress and strain law of the quarry slope. SlopeLE software was used to analyze the safety factor of slope stability and the potential slip surface before and after taking reinforcement measures. The results show the following: (1) Limestone is the main rock component of the mine, followed by mudstone. The joint and fissure are developed, the rock mass is broken, and the hidden danger of engineering geological disaster is high. (2) There is a sliding trend in both sides during excavation, and the maximum vertical displacement is 2.1 cm. (3) If the slope is reinforced according to the design scheme, the slope stability safety factor will be increased from 1.062 to 1.203 in a stable state, which greatly improves the stability of the slope and provides a guarantee for human and financial resources.

1. Introduction

Weibei area in Shaanxi Province is the dividing line of climate between the north and south of China and an important ecological security barrier. It has many functions, such as regulating climate, conserving soil and water, and maintaining biodiversity. The Party Central Committee and the State Council attach great importance to the mine geological environment protection and management planning in Weibei area. With the continuous extension of open-pit mining, the stability of open-pit slope is more and more concerned by mining enterprises, and the potential safety problems caused by slope instability are more and more prominent [1]. Moreover, the geological environment of Weibei limestone mining area is complex, which is affected by the external environment. There are serious geological disasters in the mining area. Especially in recent years, the

mining area has developed rapidly, but there is a lack of long-term monitoring and control of the geological environment in the mining area, so the geological environment in the mining area has deteriorated sharply, and geological disasters occur frequently, which seriously threatens the safety of people in the mining area and the development of mining resources [2–4].

The numerical calculation method [5–20] is widely used in geotechnical engineering. It can present the realistic slope and its geological environment, strata, and lithology and whether there is joint surface in the computer software and analyze the failure mechanism according to the results of simulation calculation. At present, a series of numerical methods have been developed for different types of sliding bodies, such as finite difference method (FDM) and finite volume method (FVM). In terms of model establishment and control theory, such as discrete element (DEM),

discontinuous deformation (DDA), Dan, smoothed particle flow (SPH), particle flow program (PFC), and tsunami ball, some numerical simulation software came into being, such as FLAC, UDEC, PFC, 3DEC, and geo slope. Among them, FLAC3D numerical simulation software [21–28] is good at analyzing large deformation problems in geotechnical engineering, and it adopts display calculation method, which can ensure that better calculation results can be obtained even without convergence of calculation.

Zhu et al. [29] put forward a constitutive model that can reflect the working principle of yielding anchor cable and successfully realized the numerical simulation method of yielding anchor cable slope reinforcement by combining FLAC3D software and FORTRAN programming language. Gao et al. [30] used the discrete element method to study the deformation and failure characteristics of a total of 270 slope models under different working conditions. Wang et al. [31] proposed that the most effective methods for studying the influence of rainfall factors on slope stability are indoor and outdoor experiments and numerical simulation methods. Tan et al. [32] used the discrete element method to carry out the full-time dynamic analysis of the slope rock mass and discussed the dynamic response law and stability of the slope rock mass under the action of earthquake. Yang et al. [33] used numerical simulation to determine the critical length of instability failure during excavation of a multilayer soft interbedded rock slope. Liu et al. [34] used discrete element UDEC software to simulate the antidipping soft and hard rock mass interbedded slope and systematically studied the deformation and failure mechanism of its seismic response. Chen et al. [35] used FLAC3D to establish a numerical model of a large-scale open-air slope, and through three-dimensional numerical simulation revealed the mechanical environment of a large-scale open-air slope, and discussed the movement and deformation, stress distribution, and failure mechanism of surrounding rock. Gu et al. [36] proposed that three-dimensional numerical simulation is more targeted for the deformation analysis of irregular section slope, and the influence of section morphology change on slope deformation can be considered. The calculated results are highly consistent with the actual deformation state.

FLAC3D can very accurately simulate the flow and plastic failure of materials and can be used for foundation design and slope stability. It has great advantages in solving geotechnical engineering problems and has been recognized by many scholars [37, 38]. Therefore, this paper will use FLAC3D numerical simulation method to carry out numerical simulation analysis on the slope of limestone quarry in Weibei area to reproduce and analyze the specific process of slope deformation and failure.

2. Regional Geological Features

2.1. Physical Geographic Features. Xianyang City is located in the south of Taiao of Shaanxi-Gansu-Ningxia. From the fold fault band of Shaanxi-Gansu-Ningxia sag to the north and south of the two III structural units, the structure changes from strong to weak, from complex to simple, and Jinghe-Lishan fault basically crosses Xianyang City. Baoji City is located at the western end of the Weihe Fault Depression. The

east-west and northwest-trending fault structures are extremely developed. The Guguan-Yangpingzhen fault runs through Baoji and develops northward, and the Longxian-Mazhao fault is located between Xianyang and Baoji, developing in the northeast direction. The distribution of structural faults in Weibei area is shown in Figure 1. Groundwater in this mine area mainly includes quaternary unconsolidated pore, fissure water, bedrock fissure water, and carbonate pore water, and its recharge is mainly by atmospheric rainfall.

2.2. Mine Geological Environmental Problems. In the dual role of nature, man-made behaviors often make mine geological disasters occur frequently, which will make the mine geological ecological environment deteriorate and cause economic losses. At the same time, it will greatly threaten the survival and development of human beings and also endanger the mineral resources on which human beings depend for survival and development. At present, there are many kinds of mines in China, with a wide distribution area, which has a great impact on the national development and people's life. In recent years, the mine hazards in Weibei area have also shown an upward trend. The goaf collapse, landslide, collapse, soil erosion, debris flow, and other geological disasters occur frequently, which has become the most important types of hazards. There are 9 mine geological disasters, including 3 small- and medium-sized landslides, 6 collapses, and hidden dangers. Small- and medium-sized geological disasters are the main types of geological disasters in Weibei area, accounting for 72% of the total, while large- and medium-sized geological disasters account for 28%. The open-pit limestone mining process not only caused great damage to the landscape, but also formed a large area of high steep rock faces, pits, vegetation stripping, and exposed rocks, full of greens, and was extremely inconsistent with the surrounding emerald-covered landforms. Moreover, according to statistics, mine waste in the Weibei area currently has a total of 350×10^4 t, all of which are waste rock slag, with an annual output of 30×10^4 t and an annual utilization of 10×10^4 t (Figure 2).

3. FLAC3D Numerical Simulation Analysis of Limestone Mine Slope Instability Caused by Excavation

3.1. Introduction to FLAC3D. With the continuous progress of science and technology, the numerical simulation method has been applied to geotechnical engineering by more and more experts and scholars. It can simulate and analyze the failure mechanism of real slope and its geological environment, stratum, lithology, and joint surface in computer software. FLAC3D is a fast three-dimensional Lagrangian analysis program, which uses explicit Lagrangian algorithm and hybrid discrete partition technology to simulate the three-dimensional mechanical properties of geotechnical materials. The program can simulate the failure and plastic flow of the geological body under the strength and yield limit, especially suitable for analyzing the gradual failure and

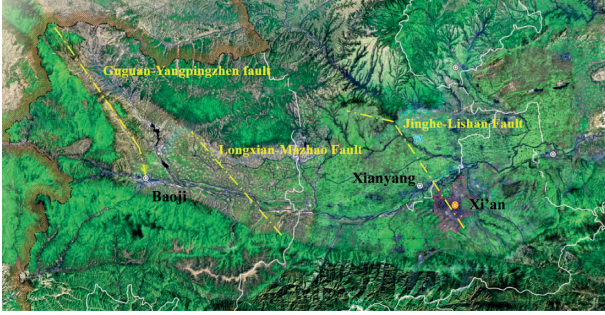


FIGURE 1: Geological structure characteristics in Weibei area.

instability process of slope and simulating the large deformation of slope. In summary, the main calculation process of FLAC3D includes repetitive processes such as modeling, calculation solution, result review, and recommissioning (Figure 3), which can monitor the change process of a point's displacement, velocity, acceleration, stress, and other parameters.

The choice of constitutive model is an important step that affects the accuracy of numerical simulation. The FLAC3D software contains 12 constitutive models, including the Mohr-Coulomb plastic model, which are suitable for the mechanical properties of different engineering materials. The Mohr-Coulomb model is one of the most widely used models in slope stability analysis. It has the advantages of less requirements for relevant material parameters and easy access. Therefore, the Mohr-Coulomb constitutive model is used to simulate the mechanical properties and progressive failure process of the rock-soil mass of the bottom slope.

The stress on each surface of the model and the displacement constraints in each direction are important factors that affect the final calculation results of the numerical model. According to the different purposes of different models, displacement constraints in different directions are added. For the numerical simulation model, the specific boundary displacement constraint expression is as follows:

- (1) Apply horizontal displacement constraints on the left, right, front, and back of the model, and set the initial displacement to zero.
- (2) Set the horizontal and vertical initial displacements of the top and bottom boundaries of the model to be zero.

The stress condition of the model is determined by the stress condition, and the horizontal displacement constraint condition is taken in the X direction:

$$\begin{aligned} u_{x=0} &= 0, \\ u_{x=401} &= 0. \end{aligned} \quad (1)$$

Take the horizontal displacement constraint condition in the Y direction:

$$\begin{aligned} u_{y=0} &= 0, \\ u_{y=390} &= 0. \end{aligned} \quad (2)$$

Set the vertical displacement constraint conditions on the top and bottom boundaries:

$$u_{z=0} = 0. \quad (3)$$

When considering the geological structural stress, the load applied to the model is the structural stress. According to the field measured data, the stress servo control program is used to generate the initial ground stress. There are 6 boundaries in this model, where all nodes on the Z -axis speed plane are fixed at the bottom boundary, the X -axis speed of the model is fixed at the left and right twice, and the Y -axis speed model is fixed at the front and rear sides (Figure 4).

According to the lithology and engineering geological characteristics of the simulation area, fully considering the size effect, the final size of the model is $401 \text{ m} \times 390 \text{ m} \times 318 \text{ m}$, and the grid densification is carried out in the key research area. Finally, a total of 225 733 grids are established, and the overall model of four times of distributed excavation is established. The third and fourth excavation are two steps of the open pit, respectively. The model information and excavation sequence are shown in Figure 5.

3.2. Numerical Simulation Analysis of Slope Stability under Excavation Conditions. Under the influence of its own load, the stratum in natural state will be affected by the relevant stress. Therefore, before excavation, the linear elastic model should be used to carry out the self-balance under the condition of gravity field, and then the calculation should be carried out in the elastic-plastic stage of Moore Coulomb model, with the maximum unbalanced force less than the convergence criterion $1e^{-5} \text{ N}$ as the end mark.

Figure 6 shows the stress-strain nephogram in Z direction after the initial in situ stress of limestone mine, in which the cold color indicates larger strain and the warm color indicates smaller strain. Figure (6a) is the stress nephogram of Z -direction generated by initial in situ stress. It is obvious that the stress field in the mine presents a relatively uniform distribution, which is consistent with the actual situation. It can be seen from Figure 6(b) that, after the initial in situ stress, its Z -axis displacement gradually increases from the bottom to the top, and the displacement field is evenly distributed. The maximum settlement is 4.48 cm, which mainly occurs at the top of the terrain on the right upper part of the mine. It shows that the consolidation settlement of the model is sufficient under natural condition.

3.2.1. First Excavation. After the in situ stress is balanced, the displacement field and velocity field generated are reset to zero, and the Mohr-Coulomb model is used to simulate the stress and strain state of the studied mine in the excavation area. The following is the stress and strain cloud diagram after the first excavation of the mine after the ground stress is generated, as shown in Figures 7 and 8.

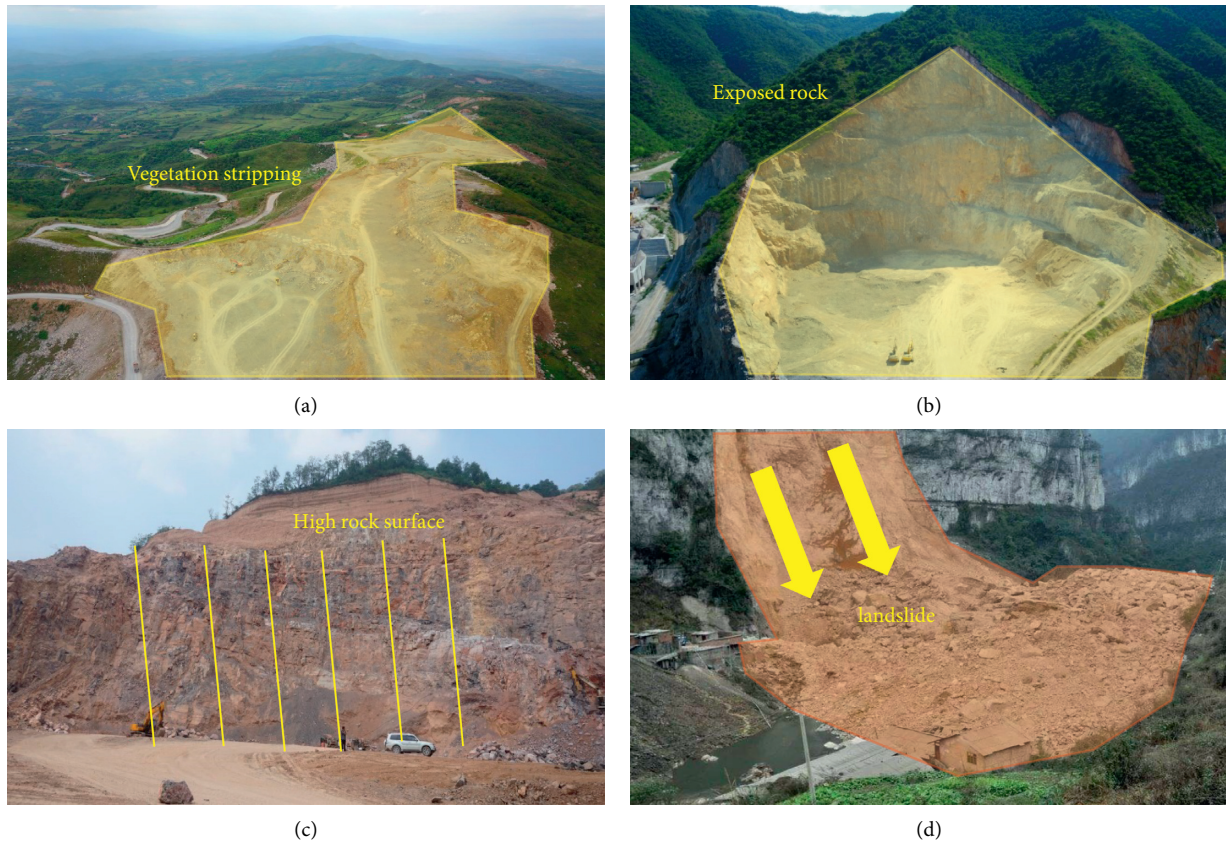


FIGURE 2: Main geological disasters in Weibei area. (a) Vegetation stripping. (b) Exposed rock. (c) High rock surface. (d) Landslide.

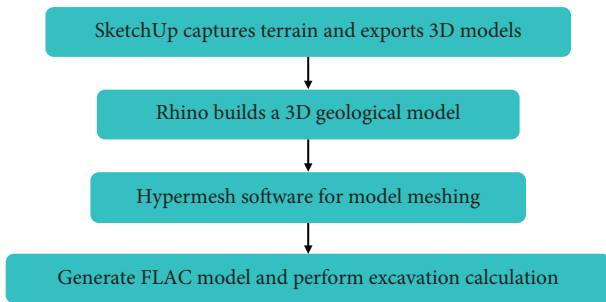


FIGURE 3: The modeling process.

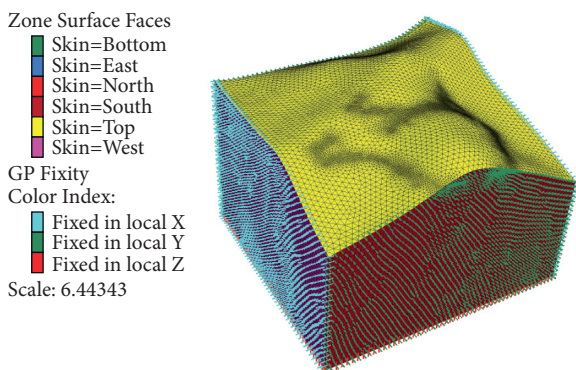


FIGURE 4: Boundary constraint condition.

After the excavation is completed, the stress around the excavation area is released and the stress value is reduced due to the unloading effect (Figure 7). The stress concentration phenomenon at the foot of the excavation slope can be clearly seen from the stress nephogram in X and Y directions. The stress in the surface of the mine excavation area is mainly between -1.18 MPa and 0.51 MPa, and the stress in Z direction is mainly between -1.35 MPa and -0.71 MPa. The initial stress state is basically maintained in the position away from the mine excavation area.

As shown in Figure 8, after the excavation of the first layer, obvious rebound occurs in the excavation area, in which the displacement rebound amount in Z direction at the foot of the slope in the excavation area is the largest, with the maximum displacement of 0.11 cm. The slope top in the excavation area presents the trend of sliding in X direction, with the maximum displacement of 0.19 cm. In the displacement vector diagram (the displacement vector cloud diagram can represent the displacement size and the direction of the overall displacement), the arrow direction represents the displacement direction of the solution unit.

3.2.2. Second Excavation. After the balance of the first excavation, the second excavation is simulated, and the stress-strain nephogram is shown in Figures 9 and 10.

After the second excavation, the stress distribution is similar to that of the first excavation, and there is obvious stress concentration at the foot of the slope (Figure 9). The

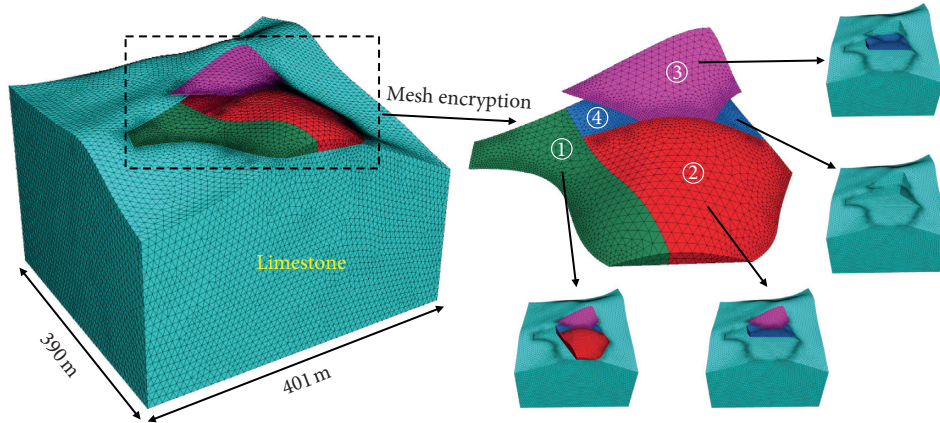


FIGURE 5: Model size and excavation sequence.

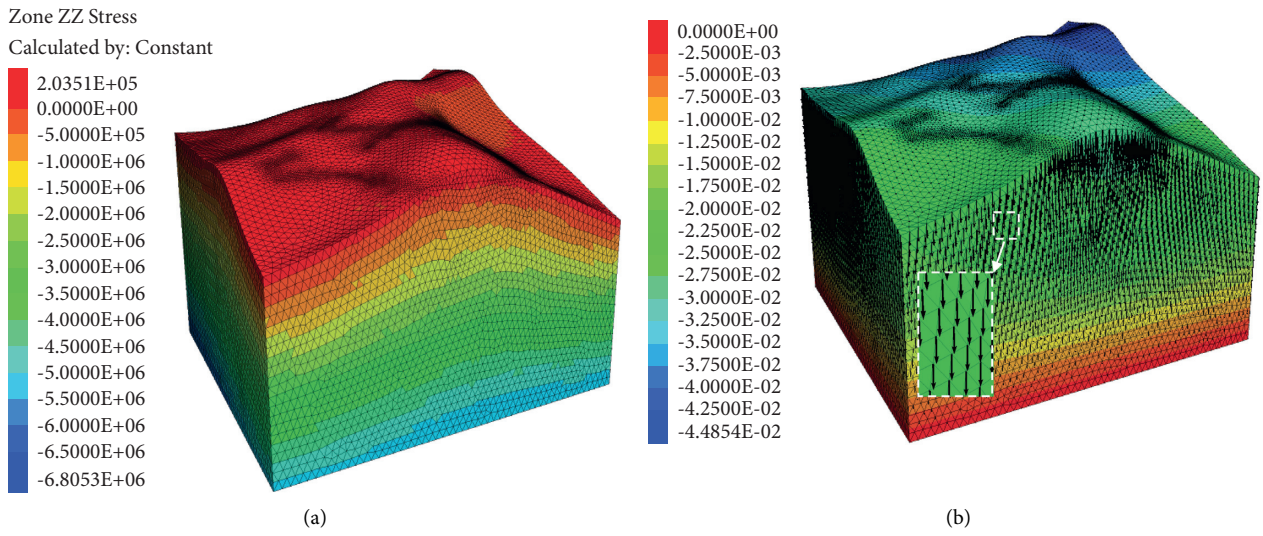


FIGURE 6: Stress-strain nephogram after initial in situ stress. (a) Z-direction stress nephogram and (b) Z-direction strain nephogram.

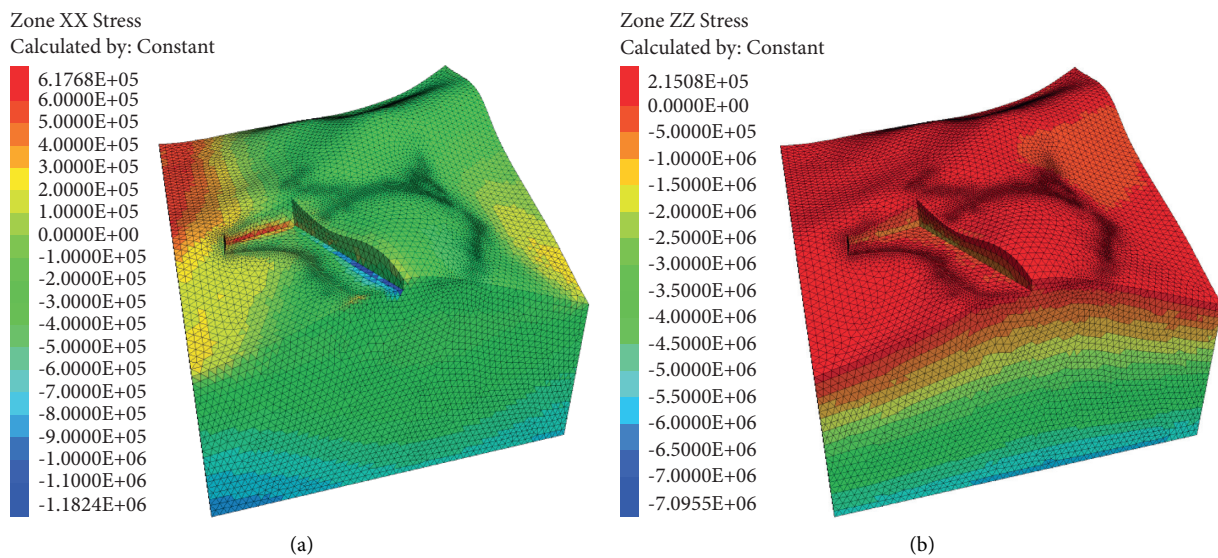


FIGURE 7: Stress nephogram after first excavation. (a) X-direction stress nephogram and (b) Z-direction stress nephogram.

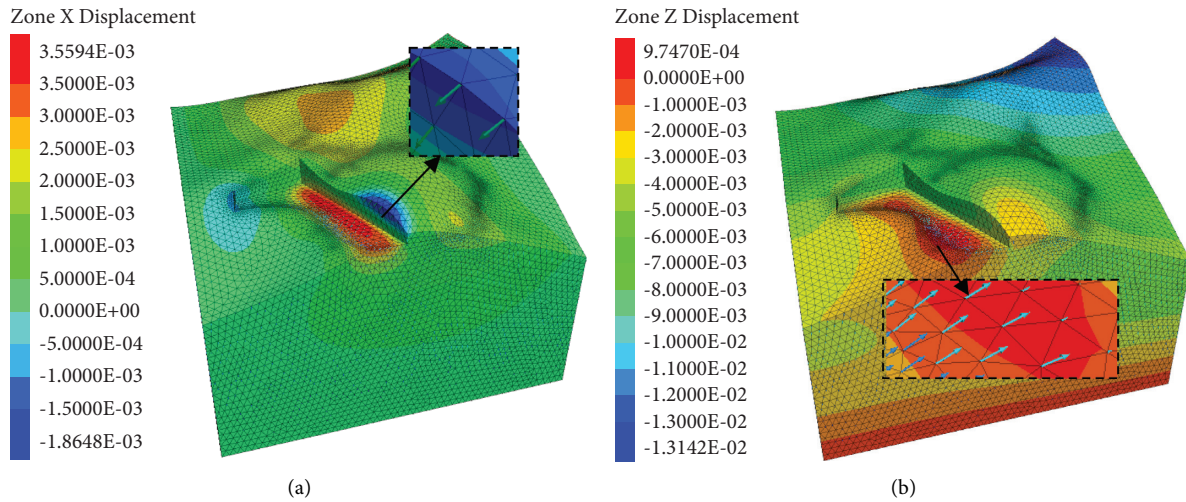


FIGURE 8: Strain nephogram after first excavation. (a) X-direction strain nephogram and (b) Z-direction strain nephogram.

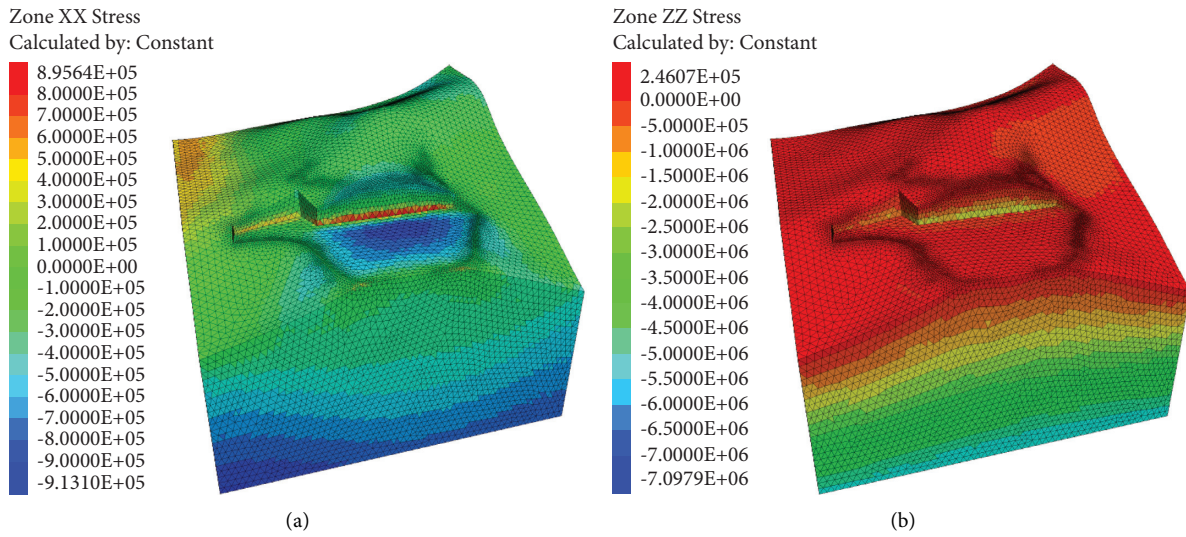


FIGURE 9: Stress nephogram after second excavation. (a) X-direction stress nephogram and (b) Z-direction stress nephogram.

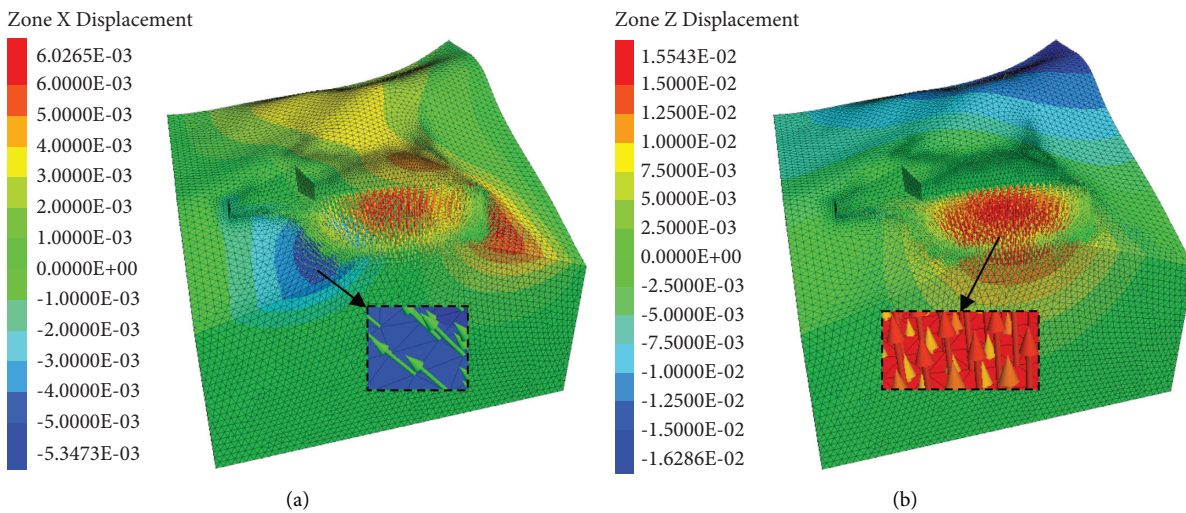


FIGURE 10: Strain nephogram after second excavation. (a) X-direction strain nephogram and (b) Z-direction strain nephogram.

stress distribution in Z direction is relatively uniform, and the stress value increases gradually from surface to core. The stress in X direction is mainly between -0.23 MPa and 0.67 MPa, and the stress in Z direction is mainly between -2.23 MPa and 0.11 MPa.

There is a small amount of X -direction displacement on the slope outside the excavation area in Figure 10, which shows the trend of sliding to both sides. The maximum displacement on the left side of the excavation area is 0.53 cm, and the maximum displacement on the right side is 0.59 cm. In the excavation area, there is a positive displacement in Z direction, because the slope rebounds due to the unloading effect in the excavation area. In the center of the excavation area, the displacement rebound in Z direction is the largest, and the maximum displacement in Z direction is 1.56 cm.

3.2.3. Third Excavation. After the second excavation balance, the third excavation simulation of the mine is carried out, that is, the excavation of the first step. The stress-strain nephogram is shown in Figures 11 and 12.

After the third excavation, the stress distribution is different from that of the first two (Figure 11). There are obvious stress concentrations at the toe of the excavation and the residual toe of the second excavation; the maximum stress concentration at the toe of the upper slope is 0.42 MPa, and the maximum stress concentration at the bottom is 0.59 MPa, which shows that the stress concentration in the lower layer is more serious than that in the upper layer. The stress distribution in Z direction is relatively uniform, and the stress value increases gradually from the surface to inner core. The stress in X direction is mainly between -0.52 MPa and -0.18 MPa, and the stress in Z direction is mainly between -0.19 MPa and -0.01 MPa.

Besides the first step excavation area and the second excavation area, the slope still shows X -direction sliding (Figure 12). The maximum displacement on the left side of the upper excavation area is 0.23 cm, and the maximum displacement on the right side is 0.54 cm; the maximum displacement on the left side of the lower second excavation area is 0.58 cm, and the maximum displacement on the right side is 0.62 cm. Within the excavation area, the maximum displacement caused by the bottom heave is 0.6 cm in the upper layer and 1.6 cm in the lower layer. The overall analysis shows that the excavation of the first step has less impact on the upper mine than on the lower mine. The reason may be that the excavation has less soil and the impact is not enough to offset the effect of large-scale excavation.

3.2.4. Fourth Excavation. After the third excavation balance, the first step of the quarry has been formed. Continue to carry out the fourth excavation simulation of the mine, that is, the excavation of the second step. The stress-strain nephogram is shown in Figures 13 and 14.

After the excavation of the second step, the stress distribution is similar to that of the first step (Figure 13). There is an obvious stress concentration at the foot of the second

step and the first step; the maximum stress concentration in the upper layer is 0.29 MPa, and the maximum stress concentration in the lower layer is 0.79 MPa. It can be seen that the stress concentration in the lower layer is still more serious than that in the upper layer. The stress distribution in Z direction is relatively uniform, and the stress value increases gradually from surface to core. The stress in X direction is mainly between -0.78 MPa and -0.15 MPa, and the stress in Z direction is mainly between -0.21 MPa and -0.02 MPa.

After the excavation of the second step in Figure 14, the slope outside the excavation area still shows X -direction sliding; the maximum displacement on the left side of the excavation area is 0.72 cm, and the maximum displacement on the right side is 0.75 cm. Within the excavation area, the maximum displacement of the floor heave caused by the excavation of the second step is 2.1 cm, the maximum value appears in the center of the excavation area, and the floor heave does not appear in the excavation area of the first step.

3.3. Stress-Strain Monitoring and Slope Reinforcement Location Selection. In order to compare the stress concentration and displacement difference between the first step and the second step more intuitively, and to strengthen the slope effectively, the monitoring points are set up for the numerical model. A total of 13 strain monitoring points are arranged, including 6 first steps and 7 second steps, which are evenly distributed in the area with obvious stress concentration at the foot of the slope, 1.5 m high from the step, and the distance between the two monitoring points is 30 m (the influence range of reinforcement is 30 m). A total of 41 displacement monitoring points are arranged, including 14 first steps and 27 second steps. The height from the step is 5 m, and the distance between the two monitoring points is 30 m, as shown in Figure 15.

As shown in Figures 16(a) and 16(b) stress-strain monitoring curves, the stress and strain of monitoring points are in an increasing state after the completion of the first three excavations. After the fourth excavation, because part of the soil of the first step was excavated, the stress concentration became smaller, while the maximum stress concentration appeared at the foot of the second step, and the floor heave also increased. It can be concluded that the best reinforcement monitoring point is near the corner of the second step, followed by the foot of the first step.

4. Slope Stability Analysis Based on SlopeLE

4.1. Introduction of SlopeLE. It can simply calculate the stability of the slope and the remaining sliding force, or automatically search for the minimum stability coefficient or the maximum remaining sliding force of the slope, which is the most important function of the slope calculation software SlopeLE. This software is widely used because of its simple interface, simple modeling process, easy operation, and other characteristics. The intermediate data in the calculation process can also be listed item by item in the form of a list, and the table can correspond to the diagram,

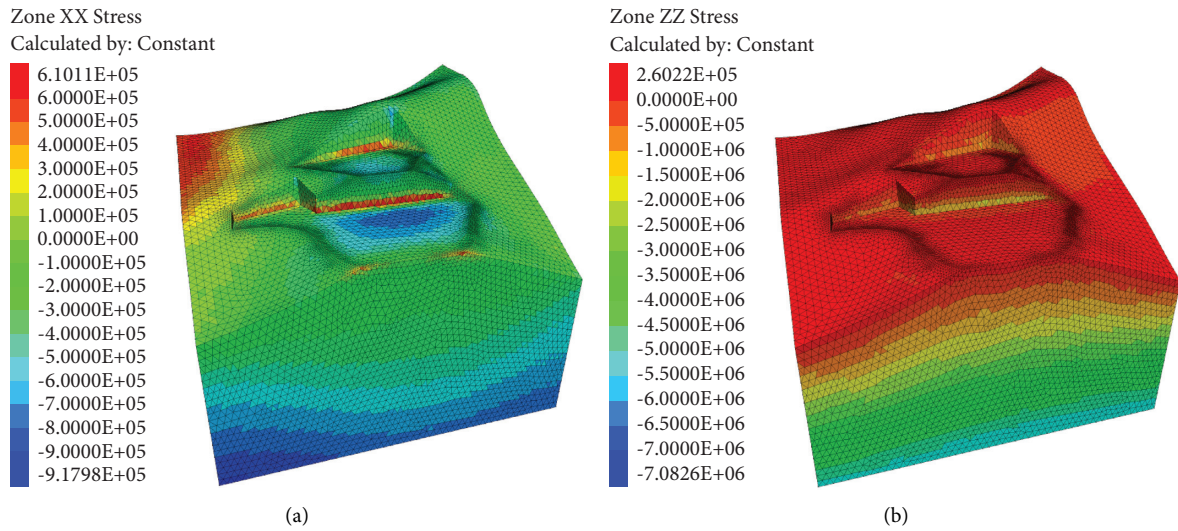


FIGURE 11: Stress nephogram after third excavation. (a) X-direction stress nephogram and (b) Z-direction stress nephogram.

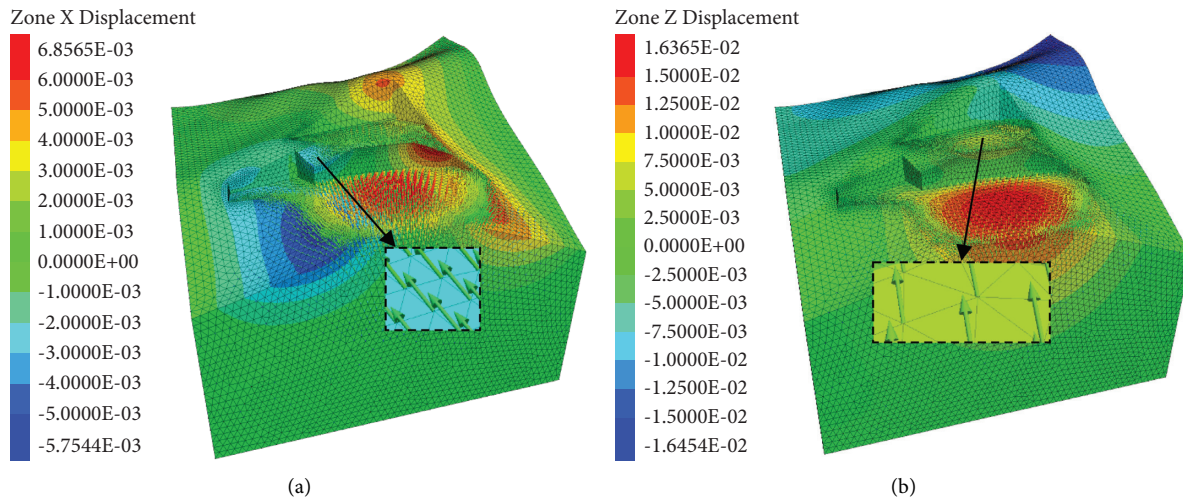


FIGURE 12: Strain nephogram after third excavation. (a) X-direction strain nephogram and (b) Z-direction strain nephogram.

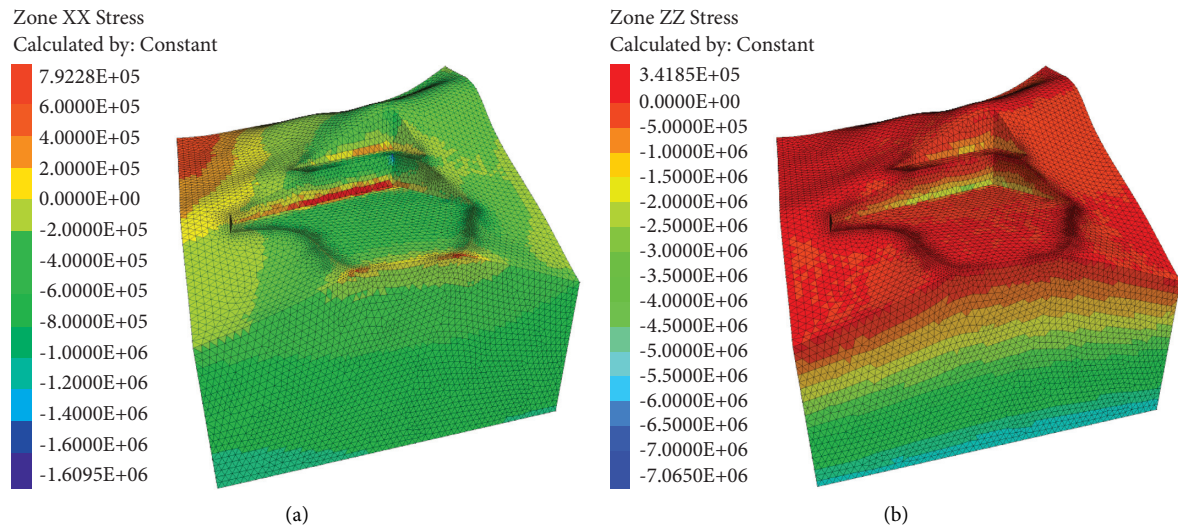


FIGURE 13: Stress nephogram after fourth excavation. (a) X-direction stress nephogram and (b) Z-direction stress nephogram.

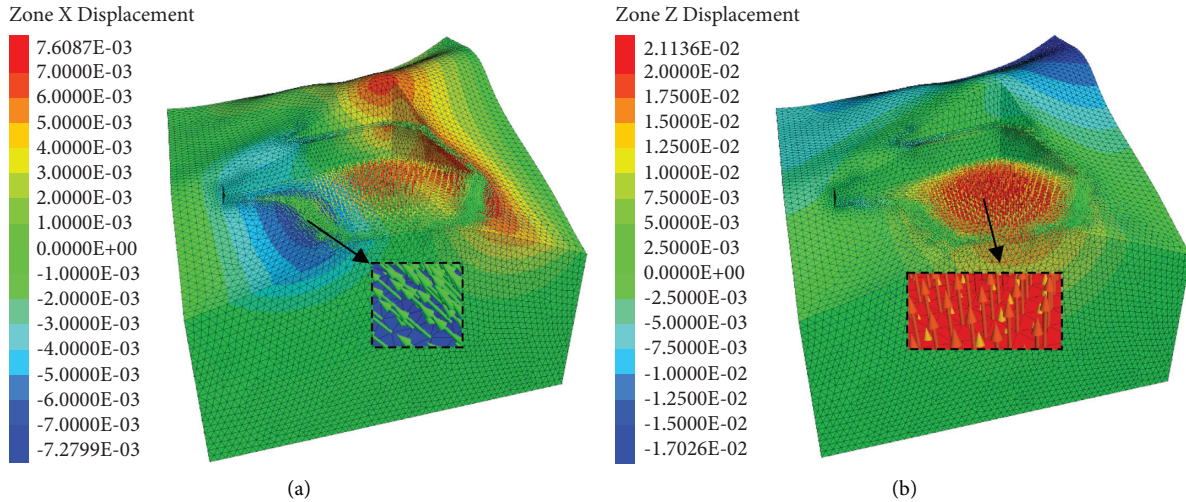


FIGURE 14: Strain nephogram after forth excavation. (a) X-direction strain nephogram and (b) Z-direction strain nephogram.

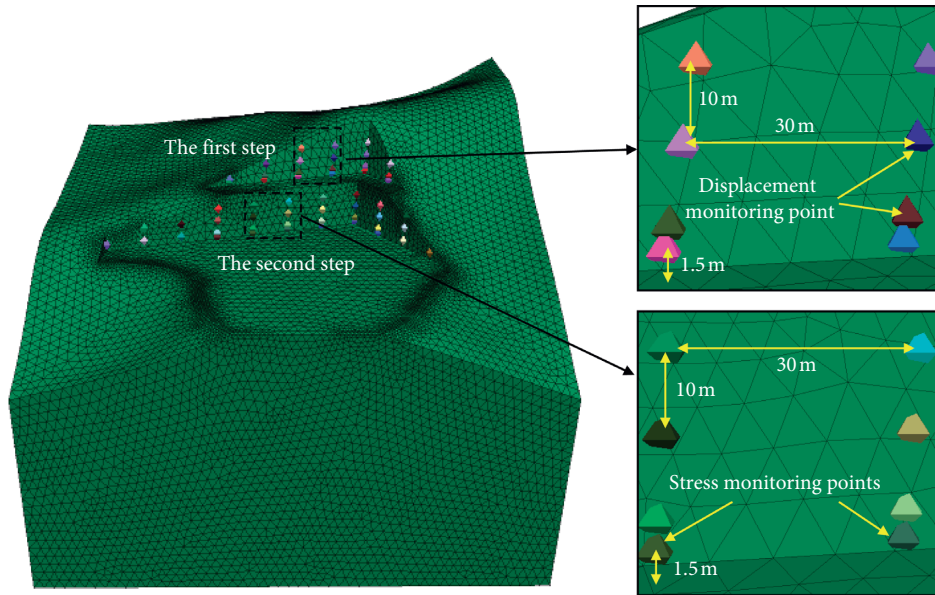


FIGURE 15: Arrangement of stress and strain monitoring points.

which provides convenience for the check work. Another advantage of SlopeLE software is that it makes full use of AutoCAD’s powerful editing functions and realizes easy and quick export and import of AutoCAD graphics data (Figure 17).

The main calculation methods of SlopeLE software are divided into Swedish section method, simplified Bishop method, transfer coefficient method, engineering group method, Spencer method, and Morgenstern-Price method. The following are three common calculation methods.

4.1.1. Swedish Division. The principle of Swedish division method is very simple, and the amount of calculation is very small, so it has been widely used. It is assumed that the circular arc is a sliding surface, and the sliding body is

divided into several rigid vertical soil strips. It is considered that the force between the strips is very small, which will not affect the slope sliding and can be ignored, and the safety factor can be calculated only through the balance of the whole moment of sliding soil. Therefore, the stability safety factor F_s under the Swedish slice method (without considering pore water pressure) can be written as

$$F_s = \frac{\sum (c_i l_i + W_i \cos \alpha_i \tan \varphi_i)}{\sum W_i \sin \alpha_i} \quad (4)$$

Here, c_i and φ_i are, respectively, the shear strength indexes of the bottom of the i th soil strip. W_i , l_i , and α_i are the total weight (natural bulk density for water and saturated bulk density for water), the bottom length, and the bottom dip angle of the soil strip I, respectively.

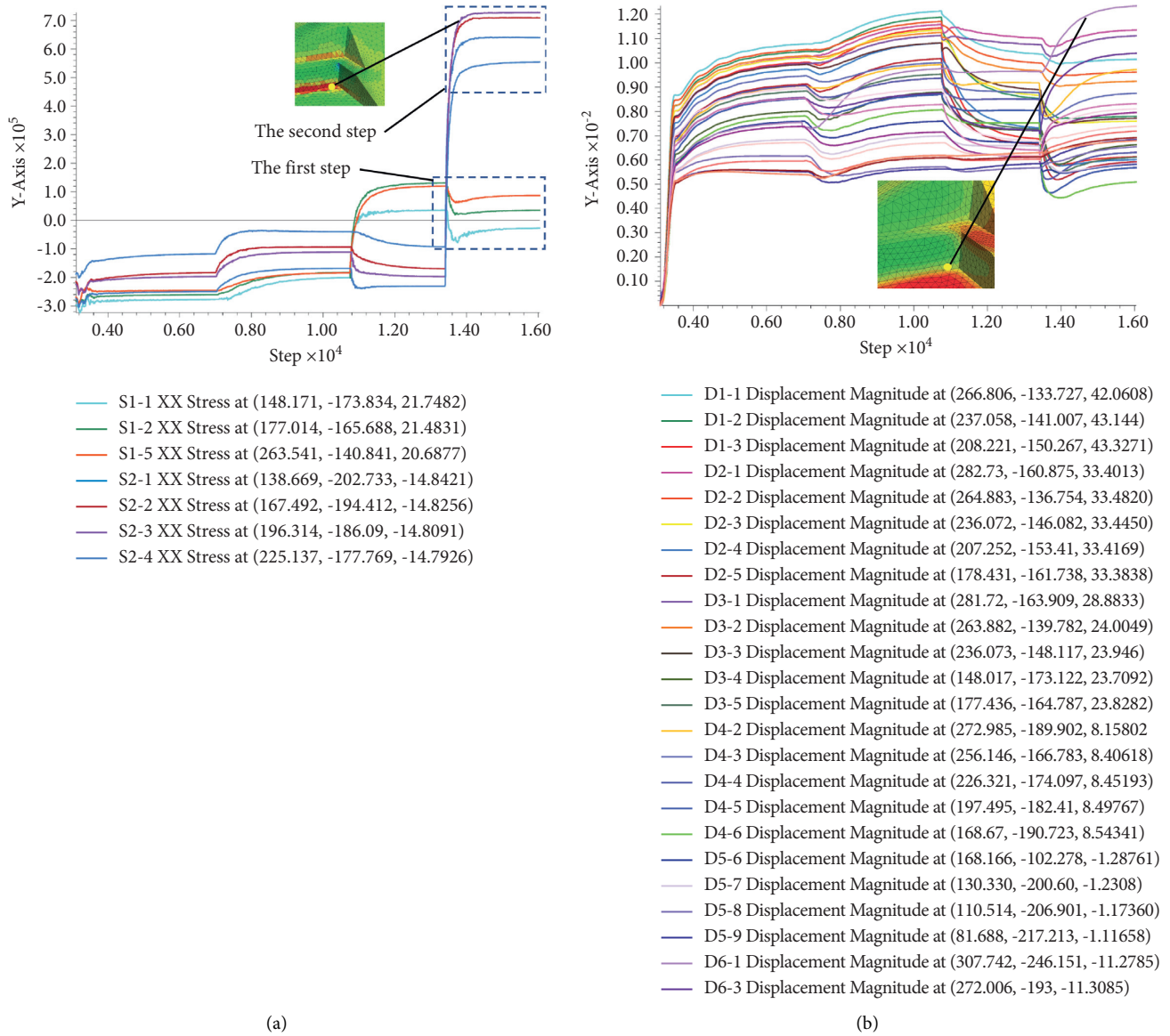


FIGURE 16: Stress strain monitoring curve. (a) Stress monitoring curve and (b) strain monitoring curve.

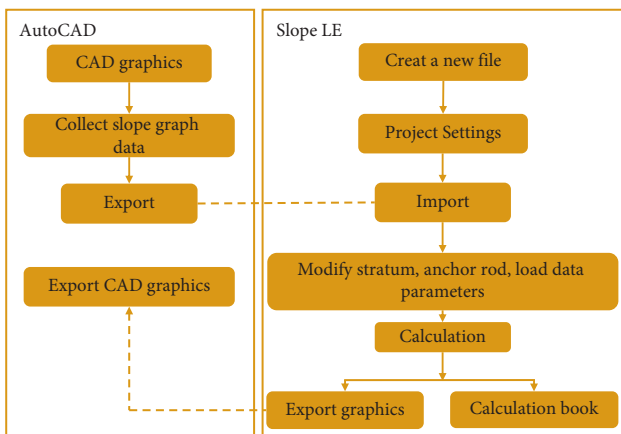


FIGURE 17: CAD and SlopeLE using flow chart.

4.1.2. *Simplify Bishop's Method.* The Bishop method is simple and has high accuracy. It is regarded as the best method to calculate the safety factor of circular sliding surface and is the most popular method in engineering. The difference between the method and the simple method is that the horizontal force between the soil strips is taken into consideration.

$$F_s = \frac{M_r}{M_s} = \frac{\sum(N_i \tan \varphi_i + c_i l_i)}{\sum W_i \sin \alpha_i} \tag{5}$$

where M_r and M_s are antiskid moment and sliding moment, respectively, and N_i , W_i , φ_i , and α_i are, respectively, the bottom normal force, gravity, friction angle, and bottom dip

TABLE 1: Slope stability state grading table.

Stability factor f_s	$F_s < 1.00$	$1.0 \leq F_s < 1.05$	$1.05 \leq F_s < 1.15$	$F_s \geq 1.15$
Slope steady state	Unstable	Understable	Basically stable	Stable

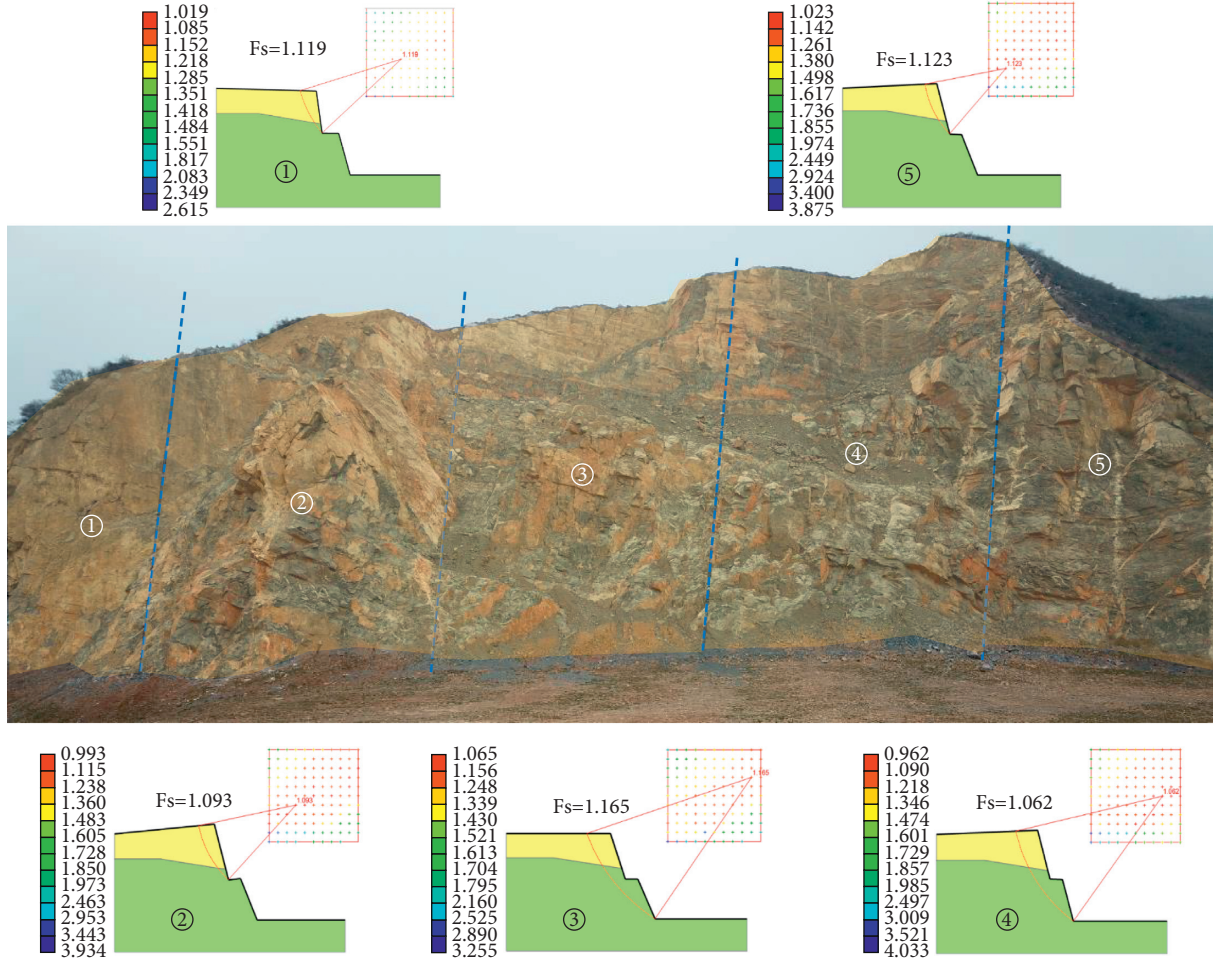


FIGURE 18: Safety factor of mine slope stability.

angle of the i th soil strip. c_i and l_i are the cohesive force and bottom length of the i -th soil strip, respectively.

4.1.3. *Transfer Coefficient Method.* Since computers were not widely used in the past, the explicit solution of the transfer coefficient (KT load increase) appeared, and the transfer coefficient was simplified. Assume that the safety

factor in the transfer coefficient is 1, which simplifies the calculation and is more convenient to solve. It has been widely used in China, and a lot of experience has been obtained in how to value the safety factor. Because the explicit method adopts the method of increasing the sliding force, the calculation error is large. The specific calculation formula is as follows:

$$\begin{aligned}
 &\text{residual sliding force: } E_i = E_{i-1} \times \psi_{i-1} + F_s \times T_i - R_i \text{ (when } T_i < 0, F_s = 1; \text{ when } E_i < 0, E_i = 0), \\
 &\text{transfer coefficient: } \psi_{i-1} = \cos(\alpha_{i-1} - \alpha_i) - \sin(\alpha_{i-1} - \alpha_i) \times \tan \varphi_i.
 \end{aligned} \tag{6}$$

The implicit solution of the transfer coefficient method (R/K strength reduction) is also called the strength reduction safety factor method. In the stability analysis using the

implicit solution method, the slip surface strength parameter is firstly reduced by F_s times until the residual slip force of the last band is 0. At this point, the safety factor of the

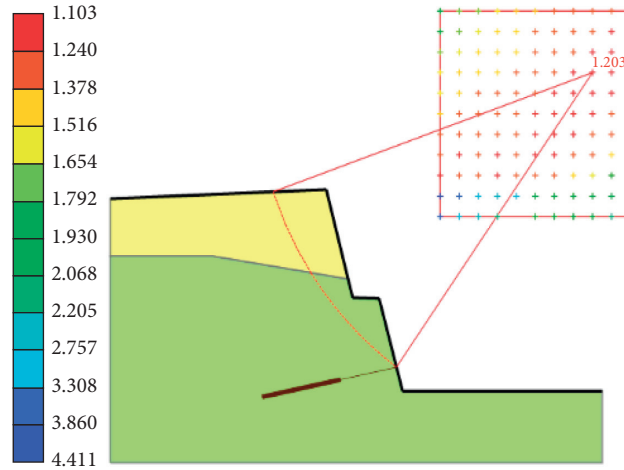


FIGURE 19: Safety factor after reinforcement.

strength reduction is the stability factor of the landslide. The specific calculation formula is as follows:

$$\text{residual sliding force: } E_i = E_{i-1} \times \psi_{i-1} + T_i - \frac{R_i}{F_s} \quad (\text{when } E_i < 0, E_i = 0),$$

$$\text{transfer coefficient: } \psi_{i-1} = \cos(\alpha_{i-1} - \alpha_i) - \sin(\alpha_{i-1} - \alpha_i) \times \frac{\tan \varphi_i}{F_s}.$$

4.2. Calculation of the Safety Factor of Mine Slope Stability. In the analysis of slope stability by many experts and scholars, the safety factor is generally used as the main standard to measure the stability of the slope, and according to this standard to carry out the corresponding slope treatment. Therefore, the value of the safety factor of the slope can have the most direct impact on the safety and engineering benefits of the slope. Generally speaking, the ratio of antisliding force and sliding force along the assumed sliding surface is called the safety factor of slope stability. According to article 9.4.6 of code for investigation of landslide prevention and control engineering, the stable state of slope should be determined according to its safety factor of stability according to Table 1.

In order to investigate the slope stability and safety state of Weibei limestone mine research area, the study is divided into five parts along its strike, geological characteristics, and joint distribution (Figure 18). The most dangerous position of each part is taken to calculate the slope safety factor, the numerical value is compared and analyzed, and corresponding treatment measures are taken. It can be seen from Figure 18 that the safety factor of slope stability at Part 4 is the smallest, $F_S = 1.062$, which is between under stable and basically stable state. The F_S of the other four parts are 1.119, 1.123, 1.093, and 1.165, respectively, which are basically stable, and the results are the same as those of FLAC3D numerical simulation part above. Therefore, the dangerous slope of Part 4 is reinforced.

Figure 19 shows the solution of safety factor of the fourth dangerous slope after reinforcement. The NPR constant resistance and large deformation anchor cable is used to reinforce the slope. The incident angle is 25° , the length is 30 m, and the preloading force is 30 T. Finally, $F_S = 1.203$, and the slope is in a stable state.

5. Conclusions

Due to the extremely harsh engineering geological conditions of the limestone mine in Weibei, the slope caused by blasting quarrying in the early stage is seriously deformed and the gravel piles up in large quantities, especially the slope near the south and north stope. Both research approaches of engineering geology in mining areas and the comprehensive treatment measures of limestone slope are of certain significance to the development of mining technology and enrichment of scientific theories. They are summarized as follows:

- (1) A three-dimensional mechanical calculation model for the main stope of Weibei Limestone Mine was established, in which a total of 13 strain monitoring points and 41 displacement monitoring points were set up. According to comprehensive judgment criteria such as displacement cloud diagram, stress cloud diagram, and the convergence of numerical calculations, and referring to the stress-strain monitoring curve, the analysis and calculation

results show that the excavation of the main stope according to the original design will produce greater stress concentration at the slope toe of the excavation area. The final excavation may cause overall instability and damage.

- (2) Use SlopeLE software to analyze the stability and safety status of the slope in the study area of Weibei Limestone Mine. The mine is divided into 5 parts along its strike, geological characteristics and joint distribution, and the most dangerous position of each part is taken to solve the slope safety factor. The minimum safety factor for slope stability is $F_s=1.062$, and the rock mass is between the understable state and the basic stable state, so reinforcement measures are taken for it, and $F_s=1.203$ after reinforcement.

Data Availability

The data that support the findings of this study are available from the corresponding author upon reasonable request.

Conflicts of Interest

The authors declare that there are no conflicts of interest regarding the publication of this paper.

Acknowledgments

This study was supported by the Key Laboratory of Mine Geological Hazards Mechanism and Control (no. KF2019-02), Funding for the Special Survey Project of the Geological Environment of Typical Limestone Mines in Weibei (no. 20180205), and the Key Research and Development Project of Zhejiang Province (no. 2019C03104).


References

- [1] Q. Gao, G. L. Xue, Z. Q. Yang, and D. Chen, "Study of the equivalent identification of rock mass mechanical parameters and numerical simulation of the slope stability," *Journal of China University of Mining & Technology*, vol. 44, no. 3, pp. 423–429, 2015.
- [2] Q. Wang, M. C. He, S. C. Li et al., "Comparative study of model tests on automatically formed roadway and gob-side entry driving in deep coal mines," *International Journal of Mining Science and Technology*, vol. 31, 2021.
- [3] Q. Wang, Y. Wang, M. C. He et al., "Experimental research and application of automatically formed roadway without advance tunneling," *Tunnelling and Underground Space Technology*, vol. 114, 2021.
- [4] A. Li, F. Dai, Y. Liu, and D. Hongbo, "Dynamic stability evaluation of underground cavern sidewalls against flexural toppling considering excavation-induced damage," *Tunnelling and Underground Space Technology*, vol. 112, Article ID 103903, 2021.
- [5] C. Qiao, G. Q. Ou, H. L. Pan, J. Wang, and Y. Yu, "Review on numerical modeling methods of debris flow," *Journal of Earth Sciences and Environment*, vol. 38, no. 1, pp. 134–142, 2016.
- [6] H. S. Shi, D. D. Sun, and K. Wu, "Development on micro-structure and numerical simulation of interfacial transition zone," *Journal of the Chinese Ceramic Society*, vol. 44, no. 5, pp. 678–685, 2016.
- [7] D. Huang, F. X. Liu, C. Yang, and R. Q. Huang, "A numerical simulation method for time-dependent growth of cracks in rocks and its validation," *Chinese Journal of Rock Mechanics and Engineering*, vol. 36, no. 7, pp. 1623–1633, 2017.
- [8] D. F. Chen, X. T. Feng, D. P. Xu, Q. Jiang, G.-F. Liu, and C.-L. Jian, "An equivalent numerical method for evaluating the reinforcing effectiveness of grouted bolts," *Rock and Soil Mechanics*, vol. 36, no. 4, pp. 1195–1204, 2015.
- [9] M. Geni and R. Imin, "Modern numerical simulation methods and its practical applications in engineering," *Engineering Mechanics*, vol. 31, no. 4, pp. 11–18, 2014.
- [10] A. H. Liu, Q. Yang, and J. P. Wu, "A practical ansys 3-D numerical simulation method for in-situ stress field," *Journal of Geomechanics*, vol. 19, no. 02, pp. 133–142, 2013.
- [11] B. Q. Zhang, H. Zhou, H. M. Chen, and S. B. Sheng, "Time-space domain high-order finite-difference methods for seismic wave numerical simulation based on new stencils," *Chinese Journal of Geophysics*, vol. 59, no. 5, pp. 1804–1814, 2016.
- [12] X. G. Liu, W. C. Zhu, J. Wei, and K. Guan, "Time-space domain high-order finite-difference methods for seismic wave numerical simulation based on new stencils," *China Mining Magazine*, vol. 25, no. 1, pp. 155–160, 2016.
- [13] L. D. Mi, H. Q. Jiang, and J. J. Li, "Investigation of shale gas numerical simulation method based on discrete fracture network model," *Natural Gas Geoscience*, vol. 25, no. 11, pp. 1795–1803, 2014.
- [14] X. R. Liu, B. Xu, Y. Q. Liu, J. Wang, and G. Lin, "Cumulative damage and stability analysis of bedding rock slope under frequent microseisms," *Chinese Journal of Geotechnical Engineering*, vol. 42, no. 4, pp. 632–641, 2020.
- [15] L. L. Xu, Q. L. Zhang, and R. Feng, "Numerical simulation of backfill strength based on optimization of stope structural parameters," *Gold Science and Technology*, vol. 29, no. 3, pp. 421–432, 2021.
- [16] Z. A. Jiang, Y. P. Wang, and L. G. Men, "Ventilation control of tunnel drilling dust based on numerical simulation," *Journal of Central South University*, vol. 28, 2021.
- [17] Z. G. Tao, C. Zhu, M. C. He, and M. Karakus, "A physical modeling-based study on the control mechanisms of Negative Poisson's ratio anchor cable on the stratified toppling deformation of anti-inclined slopes," *International Journal of Rock Mechanics and Mining Sciences*, vol. 138, Article ID 104632, 2021.
- [18] C. Zhu, M. He, M. Karakus, X. Zhang, and Z. Tao, "Numerical simulations of the failure process of anaclinal slope physical model and control mechanism of negative Poisson's ratio cable," *Bulletin of Engineering Geology and the Environment*, vol. 80, no. 4, pp. 3365–3380, 2021.
- [19] Y. Wang, W. K. Feng, R. L. Hu, and C. H. Li, "Fracture evolution and energy characteristics during marble failure under triaxial fatigue cyclic and confining pressure unloading (FC-CPU) conditions," *Rock Mechanics and Rock Engineering*, vol. 54, no. 2, pp. 799–818, 2021.
- [20] B. Li, R. Bao, Y. Wang, R. Liu, and C. Zhao, "Permeability evolution of two-dimensional fracture networks during shear under constant normal stiffness boundary conditions," *Rock Mechanics and Rock Engineering*, vol. 54, no. 3, pp. 1–20, 2021.
- [21] C. B. Wang, W. Q. Ding, and Y. F. Qiao, "Development and application of hardening soil constitutive model in FLAC3D," *Chinese Journal of Rock Mechanics and Engineering*, vol. 33, no. 1, pp. 199–208, 2014.

- [22] S. Y. Yang, J. C. Wang, and X. P. Bie, "Comparative analysis for solving slope safety factor by ANSYS and FLAC3D," *Journal of Water Resources and Architectural Engineering*, vol. 8, no. 1, pp. 104–106+119, 2010.
- [23] L. Feng, P. Z. Chen, and W. J. Chu, "Development of FLAC3D software computing platform based on cloud computing technology," *Geotechnical Engineering Technique*, vol. 33, no. 6, pp. 311–313+352, 2019.
- [24] L. Wang, B. Hu, Y. Li, Y. Yao, and X. L. Chen, "A method of 3D geologic numerical modeling based on 3D mine-ANSYS-flac3d," *Low Temperature Architecture Technology*, vol. 39, no. 8, pp. 83–85+102, 2017.
- [25] Y. P. Li, X. L. Ding, and Z. Y. Wang, "Secondary development and application of visco-elastic constitutive model in FLAC3D software," *Journal of Yangtze River Scientific Research Institute*, vol. 2, pp. 10–13, 2014.
- [26] Q. Zhang and Z. Liu, "Optimization of foundation pit excavation program based on FLAC3D," *Subgrade Engineering*, vol. 05, pp. 69–72, 2011.
- [27] X. J. Yang, J. M. Wang, C. Zhu, M. He, and Y. Gao, "Effect of wetting and drying cycles on microstructure of rock based on SEM," *Environmental Earth Sciences*, vol. 78, no. 6, p. 183, 2018.
- [28] L. Ban, C. Zhu, C. Qi, and Z. Tao, "New roughness parameters for 3D roughness of rock joints," *Bulletin of Engineering Geology and the Environment*, vol. 78, no. 6, pp. 4505–4517, 2019.
- [29] A. L. Zhu, Y. Zhang, M. L. Miao, and J. Q. Xu, "Reinforcement mechanism of slopes with yielding anchor cables based on numerical simulation of FLAC3D," *Chinese Journal of Geotechnical Engineering*, vol. 39, no. 4, pp. 713–719, 2017.
- [30] Y. T. Gao, S. Xiao, S. C. Wu, and Q. M. Tian, "Numerical simulation of the deformation and failure characteristics of consequent rock slopes and their stability," *Chinese Journal of Engineering*, vol. 37, no. 11, pp. 1403–1409, 2015.
- [31] H. B. Wang, J. M. Li, Y. X. Jin, B. Zhou, and Y. Zhou, "The numerical methods for two key problems in rainfall-induced slope failure," *Rock and Soil Mechanics*, vol. 40, no. 2, pp. 777–784, 2019.
- [32] R. J. Tan, M. S. Li, P. X. Xu, R. Hu, and Y. Su, "Numerical simulation of dynamic stability of slope rock mass under seismic loading," *Chinese Journal of Rock Mechanics and Engineering*, vol. 28, no. s2, pp. 3986–3992, 2009.
- [33] C. Yang, Q. F. Qiao, and S. Lei, "Numerical simulation analysis of critical length of instable failure for bedding rock slope," *Northwestern Geology*, vol. 52, no. 4, pp. 250–262, 2019.
- [34] Y. P. Liu, H. Deng, R. Q. Huang, J. L. Song, and J. K. Yuan, "Numerical simulation of seismic response of anti-dumping rock slope interbedded by hard and soft layers," *Hydrogeology & Engineering Geology*, vol. 39, no. 3, pp. 30–37, 2012.
- [35] Z. C. Chen, B. Yu, J. J. Hu, P. Wu, and L. Zheng, "Stability analysis of oversize open-pit slope based on numerical simulation using FLAC3D," *Mining and Metallurgy*, vol. 22, no. 3, pp. 1–6, 2013.
- [36] W. Z. Gu, G. W. Li, G. J. He, J. B. Zhang, and R. Wang, "Anchorage scheme against imminent failure of slope based on 3-D numerical modeling back analysis," *China Civil Engineering Journal*, vol. 48, no. S2, pp. 202–207, 2015.
- [37] W. D. Han, M. Y. Gu, X. Y. Yang, and X. Wang, "Slope stability based on FLAC3D numerical simulation," *Journal of Liaoning Technical University*, vol. 32, no. 9, pp. 1204–1208, 2013.
- [38] Y. F. Duan, "Study on numerical simulation of mining induced secondary geological hazard assessment," *Energy and Energy Conservation*, vol. 8, pp. 37–42+44, 2021.

Research Article

Displacement Measurements and Numerical Analysis of Long-Term Rock Slope Deformation at Higashi-Shikagoe Limestone Quarry, Japan

Clement A. Amagu ¹, Cheng Zhang,¹ Jun-ichi Kodama,¹ Kazuyuki Shioya,² Tomoyuki Yamaguchi,² Atsushi Sainoki,³ Daisuke Fukuda,¹ Yoshiaki Fujii,¹ and Mostafa Sharifzadeh⁴

¹Rock Mechanics Laboratory, Graduate School of Engineering, Hokkaido University, N13 W8, Kita-Ku, Sapporo 060-8628, Japan

²Nittetsu Mining Co. Ltd., Yusen Building, 3-2, Marunouchi 2-Chome, Chiyoda-Ku, Tokyo 100-8377, Japan

³International Research Organization for Advanced Science and Technology, Kumamoto University, Kumamoto 860-8555, Japan

⁴Western Australia School of Mine (WASM), Curtin University, Kalgoorlie, Australia

Correspondence should be addressed to Clement A. Amagu; amaguclementgk@gmail.com

Received 2 September 2021; Accepted 28 September 2021; Published 11 October 2021

Academic Editor: Xiaohu Zhang

Copyright © 2021 Clement A. Amagu et al. This is an open access article distributed under the Creative Commons Attribution License, which permits unrestricted use, distribution, and reproduction in any medium, provided the original work is properly cited.

The Higashi-Shikagoe limestone quarry is an open-pit mine situated in Hokkaido Prefecture, Japan, that has experienced four slope failure incidents since 1996. The rock slope behaviour has been monitored since the first failure event by measuring the rock slope surface displacement using an automated polar system. Recent measurements have revealed a gradual decrease of the distance between the beam generator and mirrors over time; however, the displacements and decrease rate differs between the centre and left- and right-hand sides of the quarry. This implies that the deformation characteristics of the rock slope and factors influencing the slope deformation differ at the centre and left- and right-hand sides of the quarry. In this study, the two-dimensional finite element method was used to identify the causes of slope deformation by investigating the effects of limestone excavation at the foot of the rock slope, the deterioration of a ~70 m-thick clay layer at the rock slope foot wall, and shear failure owing to rainfall infiltration. The numerical results show that slope deformation on the left-hand side and centre of the quarry are induced by clay deterioration, whereas the right-hand side of the quarry is deformed owing to floor excavation and/or shear sliding. The rock slope is presently stable because the magnitude of the rate of displacement decrease is small and no acceleration is observed.

1. Introduction

Rock slope stability poses a major challenge to rock engineering projects worldwide, including open-pit mines. Rock slopes instability can seriously affect mining operations and lead to high economic losses [1, 2]. The degree of the rock slope stability must therefore be ensured, not only for economics purposes but also to minimise risks related to operation safety [3]. There are a variety of practical methods to assess slope stability, including laboratory tests on rock core samples, rock mass classification [4–6], field measurements [1], and limit equilibrium analysis [7–10].

Recently, Tao et al. [11] proposed a physical model experiment to study the control mechanisms of toppling deformation of anti-inclined slopes during slope excavation using model-scale NPR anchor cable. From the above studies, it can be said that continuous rock slope deformation measurement is vital in mining operation stage to assess slope stability [12], predict future failure, and design potential countermeasures.

An automated polar system (APS) has been used to monitor slope movement at the Higashi-Shikagoe limestone quarry, Japan, since July 2002 following the first of four slope failure incidents by measuring rock slope surface

displacement. Cutting measures were adopted on the upper part of the rock slope after the second slope failure event occurred in July 2004 to increase slope stability by reducing the slope angle. However, the rock slope has been observed to continuously deform. An accident involving the sudden collapse of 300,000–400,000 m³ of rock slope was reported in the Kagemori limestone quarry, Japan, following the continuous development of cracks on the slope surface [8]. An understanding of the continuous rock slope deformation mechanism at the Higashi-Shikagoe limestone quarry is therefore a crucial issue to assess the rock slope stability.

Rainfall-induced landslides and slope failure pose serious threats worldwide. In Japan, for example, nearly 2700 landslides and slope failure disasters have been induced owing to rainfall effects [13]. Okata et al. [14], Sugiyama et al. [15], and Shuin et al. [16] performed statistical analyses on the connection between landslides and slope failure with rainfall intensity, duration, and antecedent rainfall. Cai and Ugai [17] pointed out that rainfall infiltration increases the groundwater level and pore-water pressure, consequently reducing the shear strength of rocks and possibly leading to landslides or slope failure. In cold regions, lowered rock strength can likely be attributed to the effects of snowmelt water infiltration [18, 19], which causes a large amount of surface water flowing through tension cracks to recharge potential surface weaknesses, thus triggering landslides and slope failure.

Several cases of slope failure induced by ground motion have been also reported [20–22]. Orense [23] reported cases of slope failure induced by large-magnitude ground shaking and soil liquefaction of weathered tuffaceous sandstones, mostly at the boundaries between fill and cut slope sections during the 2011 Tohoku earthquake in Japan. To account for the difficulties in obtaining realistic slope stability evaluations during an earthquake, Lu et al. [22] proposed a numerical model involving dynamic slope stress and deformation to consider the effect of groundwater level, material stiffness, deformation, and geosynthetics. Lu et al. [21] defined slope failure during an earthquake to occur when a cumulative plastic displacement induced by a dynamic response exceeds a critical displacement value estimated by a static parameter.

The above studies indicate that the rock slope deformation at the Higashi-Shikagoe limestone quarry may be induced by rainfall and/or earthquake activity. However, the effect of earthquakes is not considered particularly serious because rock slope surface displacement changes were not observed before or after the large 2018 Hokkaido Eastern Iburi earthquake. In contrast, rainfall and snowmelt are considered to be more strongly affect rock slope stability at the Higashi-Shikagoe limestone quarry because the maximum rainfall per day is at least 150 mm and the cumulative snowfall is >1000 mm.

Another factor that likely affects slope deformation at the Higashi-Shikagoe limestone quarry is an approximately 70 m-thick clay layer distributed at the foot wall of the rock slope. Previous studies on engineering structures have indicated that clay plays a vital role in the stability of slopes in tunnels and mines [24–27]. In particular, Erguler and

Shakoor [28] showed that the exposure of clay-bearing rocks to natural climatic conditions (e.g., freeze-thaw cycles) effectively causes rock slaking and disintegration. Erguler and Ulusay [29] consequently established that clay-bearing rocks can reduce rock slope strength and cause deformation owing to its weak strength and high sensitivity to water content variations. This is particularly relevant for the water sensitivity of clay minerals that tend to swell (e.g., montmorillonite). Van Eeckhout [30] listed five processes of strength loss in shale: fracture energy reduction; capillary tension decrease; pore pressure increase; frictional reduction; and chemical and corrosive deterioration. The results of these studies indicate that the rock slope at the Higashi-Shikagoe limestone quarry likely deforms owing to deterioration of the clay seam at the foot wall of the rock slope.

It should be noted that natural slope displacement is often induced by inelastic deformation (e.g., sliding), but the displacement of a cut rock slope in an open-pit mine may also result from elastic deformation owing to excavation [1, 31]. Kaneko et al. [31] demonstrated that rock slope deformation behaviour in open-pit mines depends on the magnitude and direction of rock stress, mostly the ratio of horizontal stress (σ_H) to vertical stress (σ_V) because excavation typically relieves stress from a rock mass. They concluded that a rock slope contracts when σ_H/σ_V is small and extends when σ_H/σ_V is large. Kodama et al. [1] conducted case studies to investigate long-term rock slope deformation observed at the Ikura limestone quarry under excavation processes. They concluded that the rock slope deformation can be interpreted as elastic deformation owing to excavation. These studies indicate that excavation is expected to be a significant cause of the slope deformation at the Higashi-Shikagoe limestone quarry. However, these studies estimated the rock slope deformation by assuming rock mass was homogeneous and elastic material.

From the above discussion, it can be said that a number of studies have been undertaken to understand characteristics of slope deformation and several principal factors triggering slope instability in an open-pit mine. However, the study on the impact of clay layer on mining-induced deformation is limited. Thus, understanding the elastoplastic behaviour of clay rock is deemed necessary in assessing slope stability at Higashi-Shikagoe limestone quarry. This is mainly because mechanical properties of clay rocks are certainly different from those of limestone. Furthermore, clay rocks are likely to show elastoplastic behaviours due to release of confining stress by excavation.

The present study aims at clarifying the causes of long-term slope deformation at Higashi-Shikagoe limestone quarry using numerical simulation and to assess the rock slope stability considering the impact of the clay layer. At first, the characteristics of the rock slope deformation were clarified by analysing surface displacement measured using an automated polar system (APS). The relationship between the slope deformation characteristics and elevation of the quarry was established. Secondly, deformation resulting from the deterioration of a ~70 m-thick clay layer at the rock slope foot wall was predicted. Thirdly, the impact of excavation at the foot of the rock slope on the slope deformation

was estimated by considering elastoplastic behaviours of the clay layer. Fourthly, the influence of rainfall was examined assuming that groundwater reduces the shear strength of rock mass. Finally, the stability of the rock slope at the quarry was assessed by ascertaining the possible factors affecting the rock slope deformation based on comparisons between the measured and simulated results.

2. Description of the Higashi-Shikagoe Limestone Quarry

The Higashi-Shikagoe limestone quarry is a small-scale mine situated in Minami Furano, Central Hokkaido Prefecture, Japan. The site is approximately 400 m from artificial Lake Kanayama. The quarry has been in operation for more than 100 years and operated by Nittetsu Mining Co., Ltd. with an annual production of 200,000 tons. The rock mass at the quarry is predominantly composed of high-grade limestone and schalstein (Figure 1) of the pre-Cretaceous Hidaka Group. Although there are other types of rock such as low-grade limestone and slate, this altered with the main rock types. The limestone deposit lies irregularly and is lenticular with a N30°E strike, 680 m length, and 100–200 m thickness. The quarried limestone is mainly used in sugar production because of its grade. The major geological structure in the quarry is characterized as a right lateral faults, which strike and dip at N70°E-80°S and N70°E-75°N, respectively. The topographical layout of the rock slope as of July 2019 in Figure 2 is viewed from the direction indicated by the yellow arrow in Figure 1. The quarry has been developed by the bench cut method with a bench height of 10 m and overall slope angle of 42°. The working face is presently located at the 340 m level and the old working face at the northern side below the 340 m level has been used for backfilling. A massive rock slope of 130 m in height has been formed with the increasing excavation level, as sketched in Figure 2. A clay seam of approximately 70 m in thickness (elevation 440–370 m) occurs at the foot wall of the rock slope, as illustrated in Figure 2.

Figure 3 illustrates the series of events that occurred at the quarry from 1996 to 2020, including four slope failure incidents. The first massive slope failure occurred at the 480 m level in December 1996. The slope failure then extended to the 515 m level in July 2004 (Figure 4(a)). Failure later occurred in April 2009 at the north end of the face of the 2004 failure (Figure 4(b)) and then reoccurred in May 2017. However, mechanism of the slope failures was not discussed in this study as the evidence is not yet clear. More significantly, rock slope displacement was begun to be measured using an APS in July 2002 to monitor the rock stability behaviour by installing two mirrors at the 480 (ET480-1) and 500 m levels (ET500-1). To ensure rock slope stability, slope angle reduction and cutting measures were taken at the upper part of the slope from April 2007 until July 2009, as shown in Figure 5. In February 2012, 16 surface displacement monitoring points (mirrors) were set along the rock slope to monitor the deformation of the entire quarry, as shown in Figure 6. Countermeasures such as planting and support systems installation (shotcrete and rock bolts shown in Figure 2) have been undertaken since 2018.

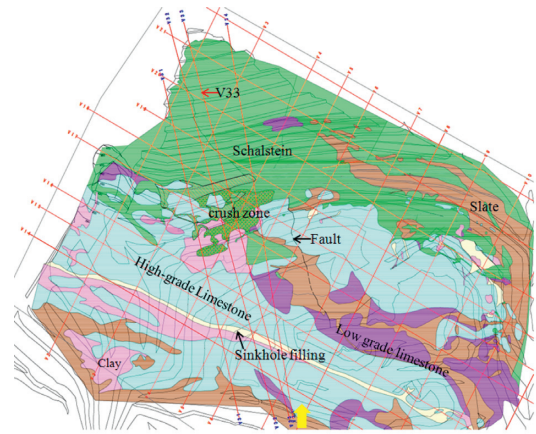


FIGURE 1: Geological map of the quarry. Yellow arrow shows the directional view of the rock slope's layout in Figure 2.

3. Data and Methods

3.1. An Automated Polar System (APS) Setup for Displacement Measurement at the Quarry. The APS consists of a laser beam generator located 470 m from the top of the slope at an altitude of 380 m on the western side of the quarry (Figure 6). Data were collected from three nearby stations of the nationwide GPS array of Japan to determine the stability of the base point. In this study, the change in distance from 11 monitoring points (i.e., APS mirror points) installed on the left- and right-hand sides and the centre of the quarry was used to investigate the overall rock slope deformation behaviour.

3.2. Laboratory Test of Effect of Water Content on Young's Modulus of Clay Specimen. As discussed in Section 2, the clay layer at the foot wall may influence the strength reduction and deformability of the rock slope. Erguler and Ulusay [29] proposed that a slight increase of water content may strongly reduce the strength and deformability of clay-bearing rocks. In this section, the effect of increasing water content on clay deformability was investigated experimentally in terms of the effect on Young's modulus. Also, Young's modulus of the clay as input parameters for numerical simulation was also selected.

Cylindrical clay specimens were difficult to prepare by drilling owing to the inherently weak nature of clay-bearing rocks. Cubic specimens with approximate dimensions of 50 × 50 × 50 mm were thus cut from a clay block. The specimens were dried at 80°C in an oven for more than 24 h until reaching a constant mass and then cooled to room temperature for a minimum of one week prior to testing. Uniaxial compressive stress tests were then applied on the specimens at a constant loading rate of 0.4 N/s using a load frame manufactured by Instron company.

The experiments were carried out on the specimens under three water content conditions. In the first stage, the specimen was subjected to three loading cycles. The water content of the specimens cooled at room temperature was approximated to 1%. The specimens were then covered with a wet towel for 24 h to increase their water content. Three loading cycles were then applied to the specimens under

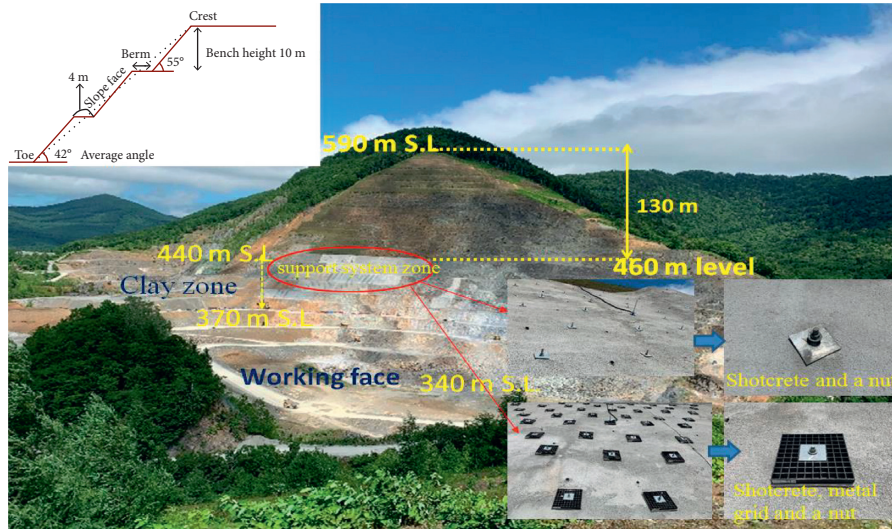


FIGURE 2: The layout of rock slope at the quarry (photo taken in the direction of yellow arrow shown in Figure 1). The support system zone is the area where rock bolts and shotcrete is installed to control the deformation.

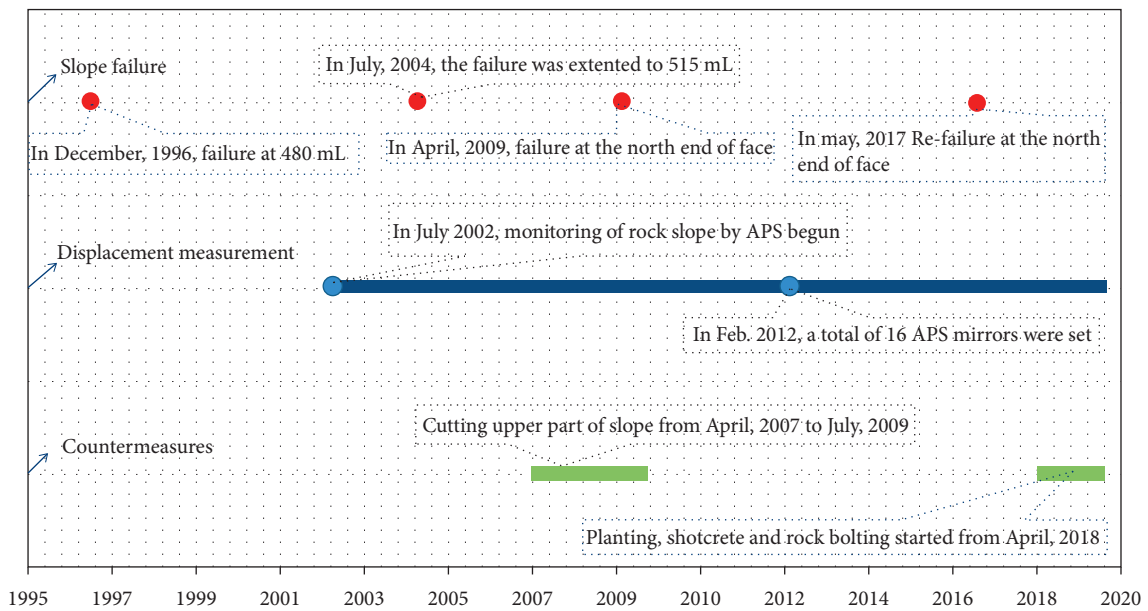


FIGURE 3: An illustration of events that have occurred at the quarry.



FIGURE 4: Slope failure that occurred at the quarry in (a) July 2004 and (b) April 2009.



FIGURE 5: Layout of the rock slope (a) before and (b) after cutting upper part of the slope in July, 2004 and November, 2009.

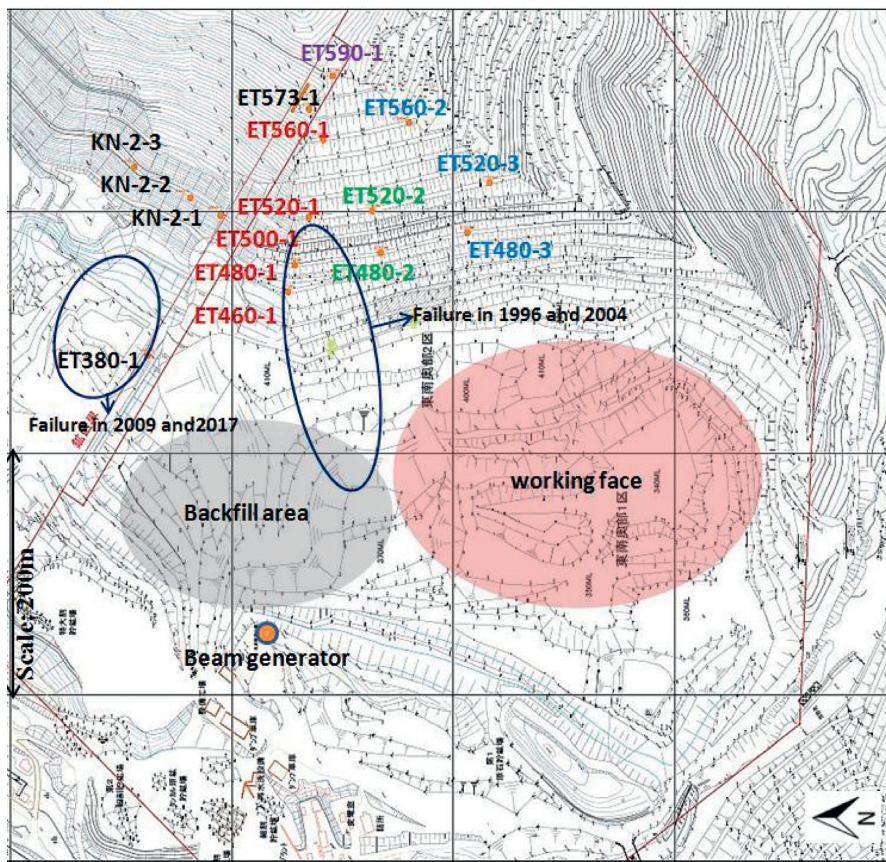


FIGURE 6: Map showing the APS at the quarry. The ET represents the mirror point locations of the automated polar system (APS) set on the rock slope. Each mirror point is represented with a number that indicates its level of elevation.

water contents of approximately 11%. The specimens were then covered with a wet towel for another 24 h, and three loading cycles were applied again under water contents of approximately 19%. The peak loading stress was set to 0.145 MPa. The stress-strain curves were linear in the stress range of 0.08–0.145 MPa. As mentioned, cyclic loading was applied to the specimens in each stage to eliminate the effects of stress release and consolidation on the specimen deformability. For example, the specimens might have loosened upon release of the overburden.

The relationship between Young’s modulus and water content of the clay specimens is shown in Figure 7. Young’s modulus is found to rapidly decrease with increasing water content from 21, 55, and 50 MPa in the first, second, and third load cycles, respectively, for water contents of approximately 1% to 3, 17, and 21 MPa for water contents of approximately 19%. These results demonstrate that Young’s modulus of clay in the quarry considerably decreases with increasing water content under both loose and consolidated conditions.

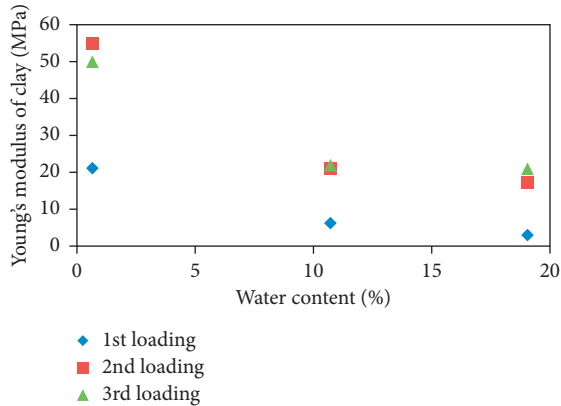


FIGURE 7: Young's modulus of the clay specimens at different water contents.

3.3. Numerical Model Description of the Rock Slope Deformation Characteristics. The potential causes of rock slope deformation at the Higashi-Shikago limestone quarry are investigated by numerical analysis. The two-dimensional finite element method (2D FEM) was used to simulate deformation induced by clay deterioration, excavation, and shear failure. A numerical analysis model of layered rock slope established using a commercial finite element program (MIDAS GTS/NX 2014 (V2.1)) [32] was used in this study. The geological profile of the rock slope along the cross-sectional area of the quarry designated as V33 (Figure 1) was used to build the numerical model shown in Figure 8(a). The finite element meshes shown in Figure 8(b) were generated using six-node triangular elements based on the elevation readings from the cross-sectional area of the quarry. The entire analytical model has dimensions of 830 m from north to south and 1489 m from east to west.

In this model, the ground types are classified into two groups, hard rock mass (limestone, schalstein, and slate) and clay, based on their notably different Young's modulus [33]. Young's modulus of the rock specimens can be relatively evaluated by various laboratory tests [33]. However, an estimation of rock mass mechanical properties from test results of rock specimens can be difficult, except for in situ tests because the rock specimens are strongly affected by inhomogeneity [3]. The quality of the hard rock and clay seam are therefore assumed to average and poor, respectively. Young's modulus of the hard rock was set to 1 GPa, whereas that of the clay was assumed to be 1/20 and 1/50 of that of the hard rock, with the aim of examining the key role played by the presence of clay in causing rock slope instability. The unit weight and Poisson's ratio of the hard rock were assumed to be 26.2 kN/m³ and 0.2, respectively, which fall within the reasonable range of values for a good quality rock mass [34, 35]. These properties are presented in Table 1. The unit weight and Poisson's ratio of the clay were set to 18.0 kN/m³ and 0.3, respectively, which fall within the properties of soft clay estimated by Chai and Miura [36]. It should be noted, however, that elastoplastic analyses to investigate behaviour of rock mass intersected with a weak clay zone are critical in assessing the slope stability [37]. In this regard, assuming the elastoplastic behaviour of the clay rock for the numerical simulation is vital to assess the slope

stability in the study quarry. In this study, for simplicity, clay rock was assumed to be perfect elastoplastic material, whereas the hard rock mass was assumed to be isotropic elastic material. All analyses were carried out under plane strain conditions. Normal displacements to the surface at the right and left sides and bottom face of the model (Figure 8(b)) were fixed to zero. For comparison with the measurement results, the change in distance was analysed between several points on the slope surface at different elevations and beam generator points. The displacement vector on the slope surface and beam generator point was also analysed to understand the causes of the distance change. In this study, a qualitative comparison between the analytical and measurement results is given because Young's modulus of the hard rock was set to a unit value. The changes in distance were normalised to the maximum value, and a relative magnitude was assigned to the displacement vectors as discussed detail in the later section.

4. Results and Analysis

4.1. Analysis of Measured Results. In this study, the change in distances from 11 APS monitoring points installed at the left and right-hand sides and centre of the quarry was analysed to investigate the overall characteristics of the rock slope deformation. Figure 9 shows that the change in distance between the beam generator and each mirror gradually decreased between January 2014 and April 2019. The total distance change ranges between approximately 20 and 100 mm. The trends are generally similar for all mirror positions, but the decreasing rates differ. This implies that the rock slope deformation depends on the position of the quarry.

The relationship between the change in distance and elevation was analysed to better understand the rock slope deformation characteristics of the entire quarry by classifying the mirrors into three groups: north (i.e., left-hand side of the quarry: ET460-1, ET480-1, ET500-1, ET520-1, and ET560-1); central (central side of the quarry: ET480-2 and ET520-2); and south (right-hand side of the quarry: ET480-3, ET520-3, and ET560-2). ET590-1 is installed at the top of the slope and is common in all of the three groups. The mirrors are, respectively, indicated as red, green, blue, and purple in Figure 6. The correlation of each group (Figure 10) clearly shows that the greatest reductions of distance occurred in the middle (elevation: 520 m) of the rock slope (Figures 10(a) and 10(b)). In contrast, the decrease in distance reaches a maximum at the slope foot as shown in Figure 10(c). These results indicate that the factors that influence the slope deformation on the left-hand side and central part of the quarry are likely similar, but differ from those that influence the slope deformation on the right-hand side of the slope.

4.2. Analysis of Numerical Results. In this section, the numerical calculations were qualitatively analysed to identify the causes of the slope deformation at the Higashi-Shikago limestone quarry using the two-dimensional finite element method (2D FEM). The deformation characteristics based on the numerical simulations were then compared with the

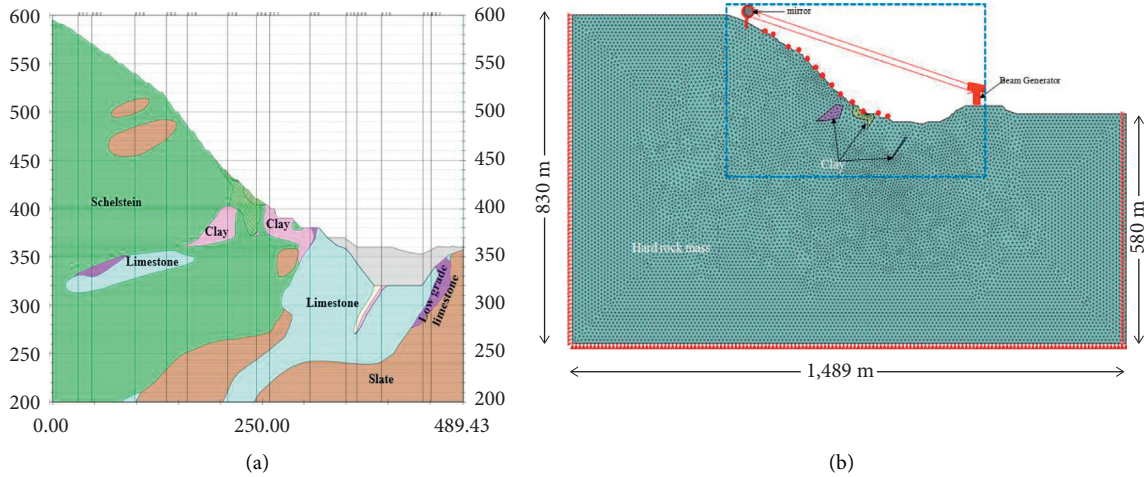


FIGURE 8: (a) Geological cross section along the line V33 in Figure 1 and (b) entire analytical model of the quarry. Simulated results of induced displacement in the blue rectangle are shown.

TABLE 1: Mechanical properties of the rock materials.

Properties	Hard rock mass	Clay
Unit weight, γ (kN/m ³) ^a	26.2 ^a	18.0 ^c
Young's modulus, E (GPa) ^b	1	0.05 and 0.02
Poisson's ratio, ν	0.2 ^a	0.3 ^c
Cohesion, c (MPa)	30 ^d	0.02 ^e
Friction angle, ϕ (°)	40 and 50 ^d	35 ^e

^aThe unit weight adopted from Bell. ^bAssumed. ^cAdopted from Chai and Miura. ^dCalculated from laboratory test results by Bandazi. ^eAdopted from Chai et al..

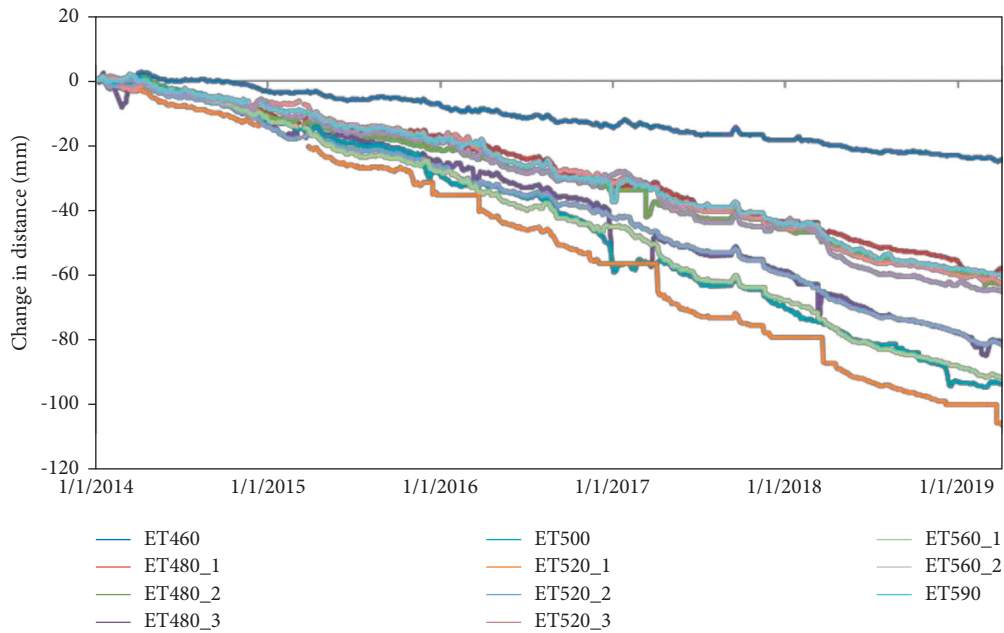


FIGURE 9: Change in distance with time for periods of five years, from 2014~2019.

measured displacement results to ascertain the possible factors affecting the rock slope deformation as observed at the quarry as discussed detail in the later section.

4.2.1. *Displacement Induced by Clay Deterioration.* To clarify the effect of the reduced Young's modulus of the clay on the rock slope deformation, two basic cases (Case _a and

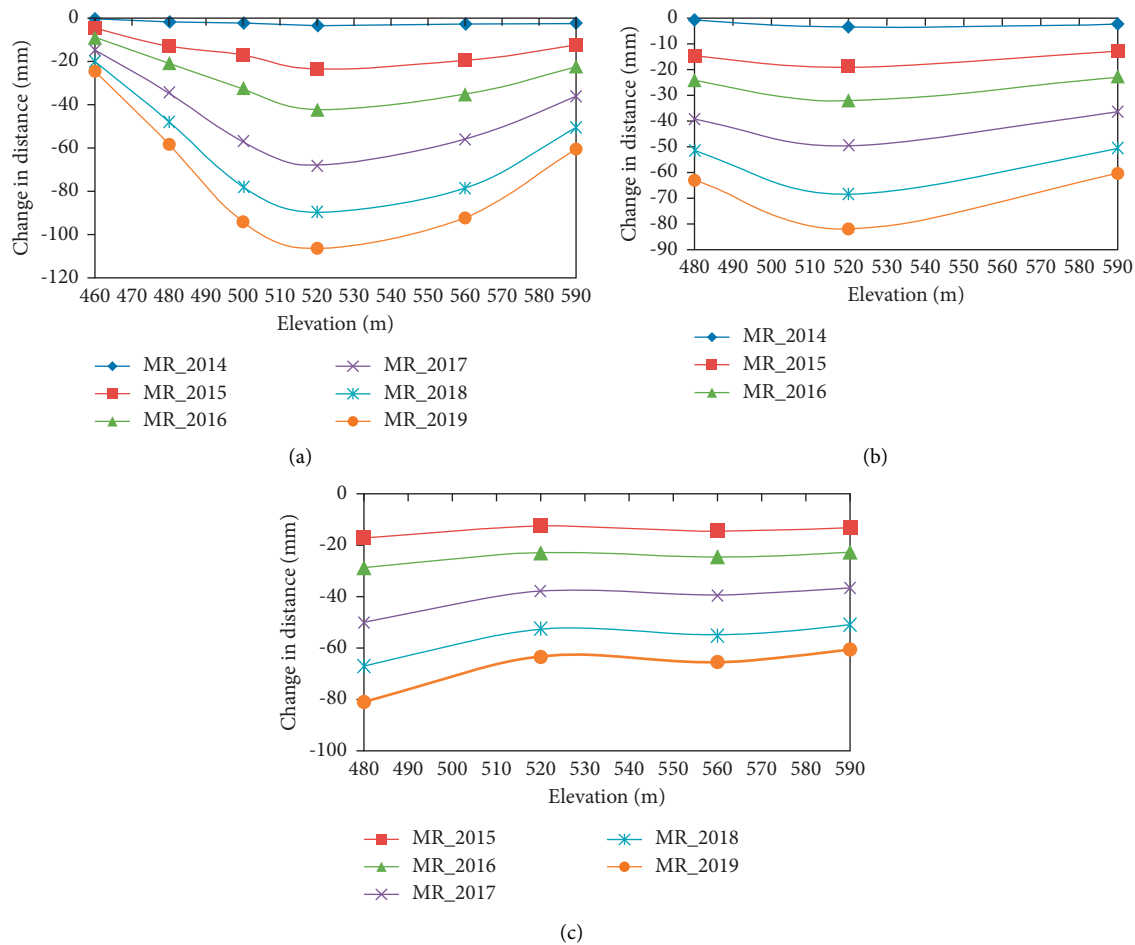


FIGURE 10: Relationship between change in distance from 2014 to 2019 and elevations at (a) the left-hand side, (b) centre, and (c) right-hand side of the quarry.

Case_b; Table 2) were modelled following the simulation conditions described in Section 3.3. Based on the experimental results described in Section 3.2, Young's modulus of clay was set to 50 and 20 MPa in the initial stages and then assumed to deteriorate to 20 and 3 MPa, respectively, owing to increased water contact, whereas Young's modulus of the hard rock was set to 1 GPa (Table 2). The mechanical properties presented in Tables 1 and 2 were used. The relative displacements induced by the reduced Young's modulus of the clay were then calculated for each model by subtracting the displacement in the initial model from that in the deteriorated model. Figure 11 shows the displacement vectors at the surface of the rock slope in Case_a (50 MPa \rightarrow 20 MPa) and Case_b (20 MPa \rightarrow 3 MPa). Figure 12 depicts the change in distance at an elevation of 460–590 m calculated from the displacement vectors. The change in distances were normalised by the maximum value in case_a and plotted relatively to the quarry elevations as shown in Figure 12. As seen in Figure 11, the displacement vectors show an overall trend of downslope displacement of the rock mass from the top to the toe of the rock slope surface in both cases. The maximum displacement was observed mostly within the clay zone near the foot of the

slope. In Figure 12, it can be seen that the distance decreased at all elevations between 460 and 590 m in both cases. The change in distance is considered to decrease because of a large displacement within the clay zone due to deterioration, which induces downslope displacement above the clay zone. It should be noted that the maximum decreasing rate of the distance was observed in the middle (\sim 520 m) of the rock slope in both cases although the maximum value in case_a is greater than that in case_b.

4.2.2. Excavation-Induced Displacement. Displacement owing to excavation is a considerable factor for assessing the deformation mechanism. The deformation of rock slope often occurs because the rock mass within an excavation zone is subjected to considerable redistributions of the initial stress state [38]. Zhu et al. [39] conducted case studies to investigate the deformation characteristics and failure mechanism of the anti-dip rock slope induced by mining excavation at the Changshanhao open-pit mine in Neimenggu province, China. They concluded that the rock mass in the deformed area bended and moved downwards as a result of the stress redistribution in the slope caused by the

TABLE 2: Young’s modulus of hard rock mass and clay rock.

Cases	Clay (GPa)		Hard rock mass (GPa)
	Initial	After deterioration	
Case_a	0.05	0.02	1
Case_b	0.02	0.003	1

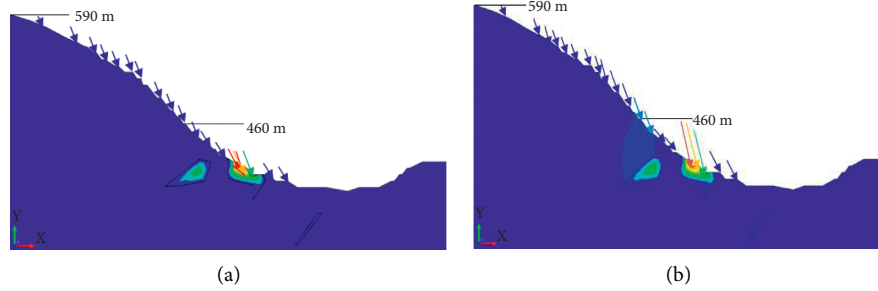


FIGURE 11: Total displacement vector at the surface of rock slope induced by reduction in Young’s modulus of clay, case_a (a) and case_b (b) in the blue dotted rectangle in Figure 8(b). The arrows indicate the direction of the displacement, whereas the length of the arrow is proportional to the magnitude of the displacement.

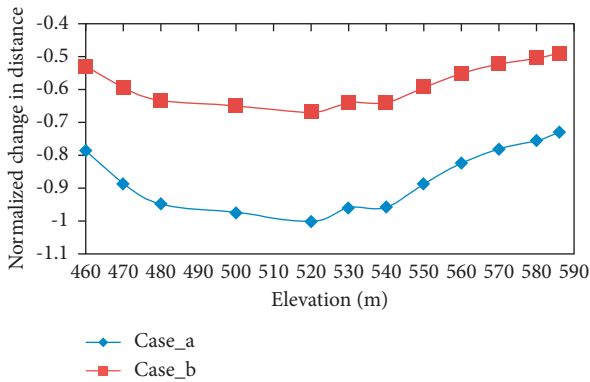


FIGURE 12: Normalized change in distance calculated from simulated results.

continuous excavation of the slope at the mine. As mentioned in Section 2, the limestone had been excavated by the bench cut method on the floor of the quarry. Excavation is thus expected to have deformed the rock slope because both gravity and horizontal stress applied to the floor were released during excavation. To address these effects, the slope deformation resulting from excavation was simulated by elastoplastic analysis.

In this section, numerical models for two stress conditions are established, and five cases are modelled in each set for the progressive excavation levels from 2015 to 2019. Excavation at the 400 m level was completed at the end of 2015 and resumed at the 360 m level in 2019. The basic configuration of the analytical models is the same as that discussed in Section 3.3 using the mechanical properties presented in Table 1. However, the geometry of the blue dotted rectangle in Figure 8(b) changed as the excavation progressed. Figure 13 shows the analytical models of the quarry in 2015–2019. Some of the boundary conditions are

different in the first model, which shows the analysis of displacement induced by horizontal stress release. A unit horizontal rock stress (σ_{xx}) of 1 MPa was applied to the right-hand side of the model. In the second model, the simulation conditions including the boundary conditions for the analysis of displacement induced by gravity release are the same as with the conditions described in Section 3.3. In both models, the displacement increment due to excavation from 2014 was simulated using the excavation analysis function equipped in MIDAS GTS/NX 2014 (V2.1) [32].

Examples of the displacement vector at the surface of the rock slope and beam generator point induced by excavation are shown in Figure 14. The changes in distance calculated from the distribution of the surface displacement vectors along the slope and beam generator point are plotted relative to the quarry elevation between 460 and 590 m, as shown in Figure 15. The changes in distance were normalised by the maximum value in 2019. In Figure 14(a), the displacement vectors show the forward displacement of the rock mass from the top to the toe of the slope. It is clearly seen in Figure 15(a) that the distance decreased with similar tendencies along both the slope and at the beam generator point owing to the horizontal stress release as the rock floor was excavated likely because of the forward displacement of the rock mass. As expected, the displacement magnitude increased upon approaching the slope foot with the greatest displacement concentrated near the clay zone. The highest decreasing distance rate is also notably observed near the foot of the rock slope. The displacement vectors along the rock slope shown in Figure 14(b) indicate upward and leftward movement of the rock mass, whereas the vectors at the beam generator point show upward and rightward displacement owing to the gravity release when the rock floor of the pit was excavated. Figure 15(b) shows that the distance at elevation 590–460 m increased with progressive

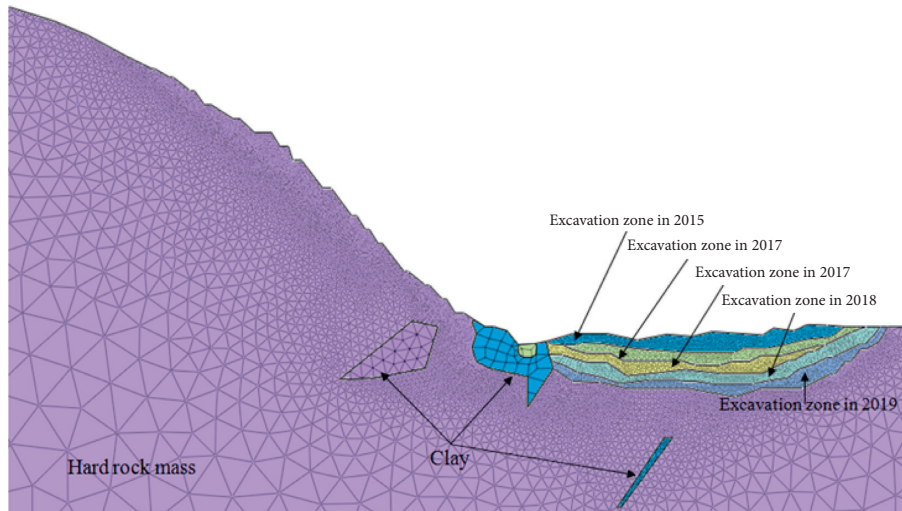


FIGURE 13: FEM meshes in terms of excavation yearly, in blue dotted rectangle in Figure 8(b).

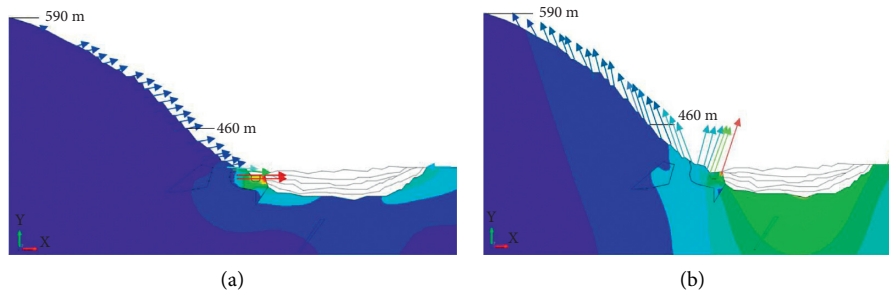


FIGURE 14: Examples of total displacement vector at the surface of rock slope induced by excavation due to (a) release of horizontal stress and (b) gravity in 2019 at the blue dotted rectangle in Figure 8(b). The arrows indicate the directions of the displacement, whereas the length of the arrow is proportional to the magnitude of the displacement.

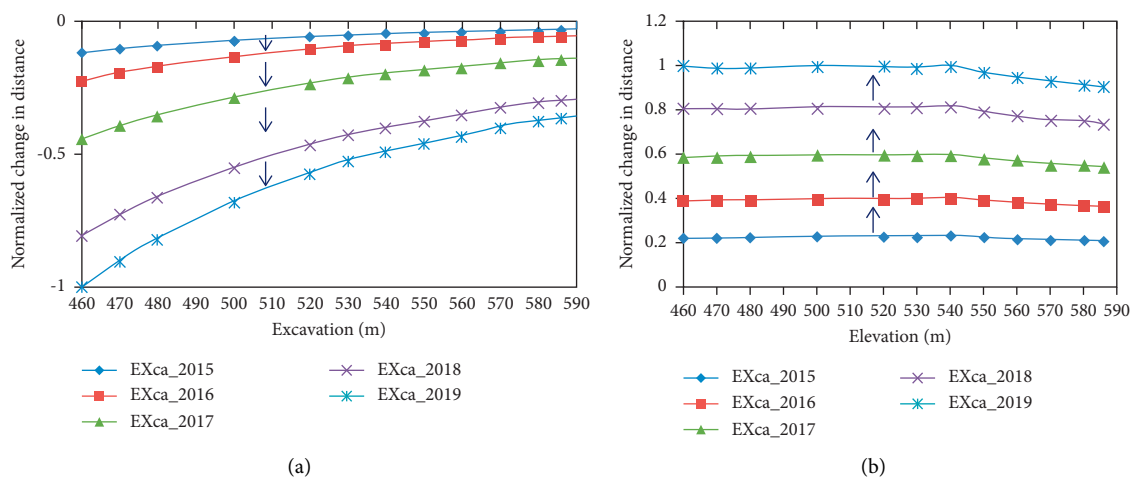


FIGURE 15: Normalized change in distance of the simulated results of displacement induced by (a) release of horizontal stress and (b) gravity.

yearly excavation owing to the leftward and rightward displacement of the rock mass along the slope and at the beam generator point. The maximum distance increase is observed near the foot of the rock slope, where the largest displacement magnitude is concentrated.

4.2.3. Displacement Caused by Reduced Shear Strength. The shear strength reduction method (SSRM), where both the hard rock mass and clay are assumed to behave as perfect elastoplastic materials, was adopted to understand rock slope displacement caused by reduced shear strength after rainfall infiltration. The SSRM is one of the most popular techniques for performing FEM slope analysis [40, 41] mainly because it simulates progressive shear failure of the slope under complex geometric conditions [42, 43]. The SSRM also determines a stress reduction factor or factor of safety value that brings a slope to the verge of its failure limit [44, 45] according to

$$C_F = \frac{C}{F}, \quad (1)$$

$$F = \tan^{-1}\left(\frac{\tan \phi}{F}\right).$$

where C and ϕ are the actual cohesion and friction angle, respectively, C_F and ϕ_F are the reduced strength characteristics (cohesion and friction angle), and F is a reduction factor that controls the reduction rate of C and ϕ . As noted by Dawson et al. [40] and Griffiths and Lane [41], C and ϕ gradually decrease until the final slope failure is detected.

The basic model configuration, including the shape, size, and boundary conditions, was the same as in Section 3.3. This analytical simulation is aimed at clarifying the effect of shear failure due to reduction in shear strength of rock mass on the slope deformation. As discussed by Griffiths and Lane [41] that deformation and progressive failure can be simulated by varying the friction angle and/or cohesion of the material gradually. Thus, in addition to the elastic modulus and unit weight, the cohesion and friction angle were also included in the simulation. The C and ϕ values of the hard rock mass were estimated from standard triaxial compression tests [46]. In these laboratory tests, the friction angles of limestone and schalstein were approximated as 40° and 50° , respectively. The friction angle of hard rock was set to 40° and 50° for two analytical cases. In this model, shear strength parameters of the clay were adopted from Chai et al. [47], as presented in Table 1. Using input parameter presented in Table 1, the simulation was performed. In this simulation, the reduction factor increment ΔF and maximum iteration number were set to 0.01 and 50 cycles, respectively. The displacement increment induced by plastic deformation owing to sequential failure of elements was analysed.

The surface displacement vector of the rock slope at $\phi = 40^\circ$ is shown in Figure 16 with the shear strain distribution. The change in distance calculated from the surface displacement vectors is plotted against the quarry elevation

for comparison, as shown in Figure 17. The change in distance is normalised by the maximum value at $\phi = 50^\circ$. Figure 16 shows that the downslope movement of the rock mass occurred at the top of the rock slope. The slope clearly slid relatively downward from the top to the intense shear strain zone in the middle of the slope, resulting in massive forward displacement of the middle of the rock slope surface. The change in distance decreased as a result of the downslope movement along the slope and at the beam generator point. The maximum decreasing rate of the distance is shown at 460 m for both friction angles (Figure 17).

5. Discussion

As described in Section 4.1, the distance between the beam generator and each mirror gradually decreases with time (Figure 9). The reduced distance is greatest at the middle of the rock slope (elevation 520 m) in the left-hand side and centre of the quarry, but at the foot of the slope in the right-hand side of the quarry (Figure 10). The following deformation characteristics were estimated based on the numerical simulations, as discussed in Section 4.2. The lowered Young's modulus of the clay seam reduced the distance, and the maximum decrease is seen at the middle of the slope (Figure 12). The change in distance owing to excavation of the pit floor depends on the rock stress conditions (Figure 15). The distance increases under gravity force conditions and decreases under horizontal stress conditions. The magnitude of the distance reduction under horizontal stress conditions is greatest at the foot of the slope. As the shear sliding progressed in the rock slope owing to reduced rock mass strength, the distance decreased with the greatest magnitude at the foot of the slope (Figure 17). According to the above results, the possible causes of the continuous deformation of the rock slope at the Higashi-Shikagoe limestone quarry are deduced as follows. (a) The rock slope displacement at the left-hand side and centre of the quarry is caused by deterioration of the existing clay layer. (b) The rock slope displacement at the right-hand side is caused by floor excavation and/or shear sliding of the slope.

As seen in Figure 1, clay is mainly distributed on the left-hand side and centre of the quarry, which consequently exhibits significant strength reductions and deformability as a result of the clay's contact with water [29]. For simplicity, clay deterioration owing to water was modelled by reducing its Young's modulus. However, clay also shows other deterioration types, including plastic deformation, cracking, and breaking [48]. It is therefore noted that water induces slope displacement resulting from clay deterioration. For confirmation, rainfall time series were analysed and compared with the measured result, as shown in Figure 18. The comparison confirms that the distance tends to decrease with increasing rainfall accumulation rate. This relationship indirectly verifies that the clay deterioration is induced by water. It should be noted that clay deterioration can also be caused by other factors. Nicholson and Hencher [49] explained that clay deterioration includes the

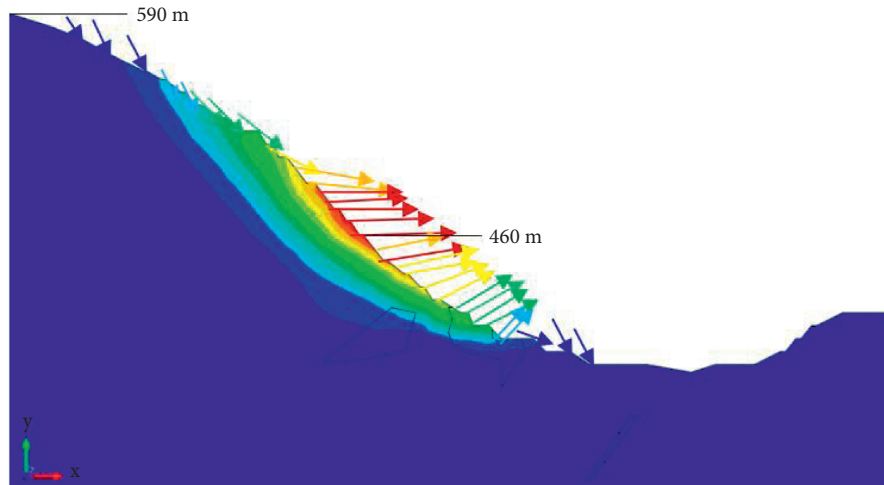


FIGURE 16: Displacement vector along the rock slope at $\phi = 40^\circ$ in the blue dotted rectangle in Figure 8(b). The arrow indicates the direction of the displacement, whereas the length of the arrow is proportional to the magnitude of the displacement.

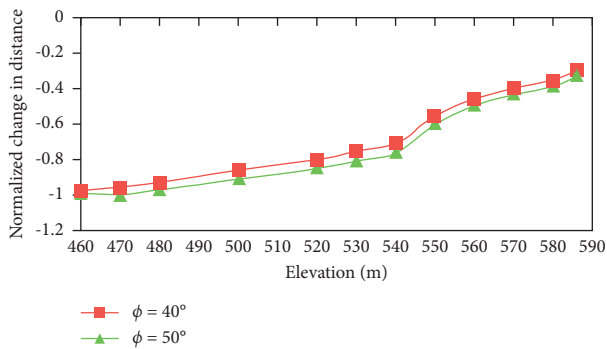


FIGURE 17: Normalized change in distance calculated from SSR simulation results.

progressive physical and chemical alteration of rock, which is facilitated by stress release, freeze-thaw, and wet-dry cycles [19, 28] when exposed to natural climate conditions. In particular, slaking, which is caused by repeated exposure to dry and wet conditions, is also an important mechanism of clay deterioration [28, 50]. The clay in the quarry is therefore also possibly susceptible to deterioration via slaking.

Excavation is expected to be one of the dominant causes of the slope displacement on the right-hand side of the quarry because the limestone on the pit floor of this area has been excavated since 2014 (Figure 6). Reduced distances will therefore occur if the regional horizontal stress at the Higashi-Shikago limestone quarry is sufficiently high. In this case, the effect of horizontal stress is expected to be greater than that of the gravity release. For example, Obara et al. [51] suggested that rock slope exhibits elastic extension by excavation, resulting in forward displacement of the rock slope at a horizontal stress to vertical stress ratio of 1.0. However, this ratio tends to increase with inverse depth and is therefore likely to be greater than 1.0 in open pit mines [52].

Figure 19 shows the change in distance at the 480–500 m level from the beginning of measurement (July 2002) until the second slope failure (July 2004). For comparison, the changes in distance at the same points between April 2014 and March 2019 are also shown. The decrease ratio of the distances from 2014 to 2019 is significantly smaller than that from 2002 to 2004. The total change of distance during the slope failure in July 2004 is closer to 1500 mm, whereas that from 2014 to 2019 is less than 50 mm. As seen in Figure 19, an apparent accelerating decrease is observed in the curves from 2002 to 2004. In contrast, the distance from 2014 to 2019 decreases at a nearly linear rate with no apparent acceleration (Figure 19), this was probably due to the effect of the undertaken countermeasures such cutting upper part of the slope, planting, and support systems installation (shotcrete and rock bolt). These results indicate that the risk of rock slope shear failure is presently low even though the distance decrease on the south side of the quarry is caused by shear movement of the slope. It can therefore be concluded that the slope is not unstable, even though continuous deformation is observed.

Pit floor excavation is one of the dominant causes of slope deformation. Three-dimensional (3D) analysis is therefore necessary because excavation-induced deformation is expected to depend on 3D geometry. As discussed earlier, other factors such mining-induced plastic behaviour of the clay rock at foot wall of the rock slope encompassing the orientation of the clay rock, geological conditions including discontinuities (e.g., fault shown in Figure 1), and rainfall and snowmelt-water infiltration are likely to have significant effects on the deformational behaviour of the rock slope. Based on the characterized deformation, future study will analyse the deformation with a 3D numerical model based on the aforementioned factors. The effect of countermeasures (e.g., rock bolts and shotcrete) should also be investigated because they are expected to effectively prevent further clay deterioration.

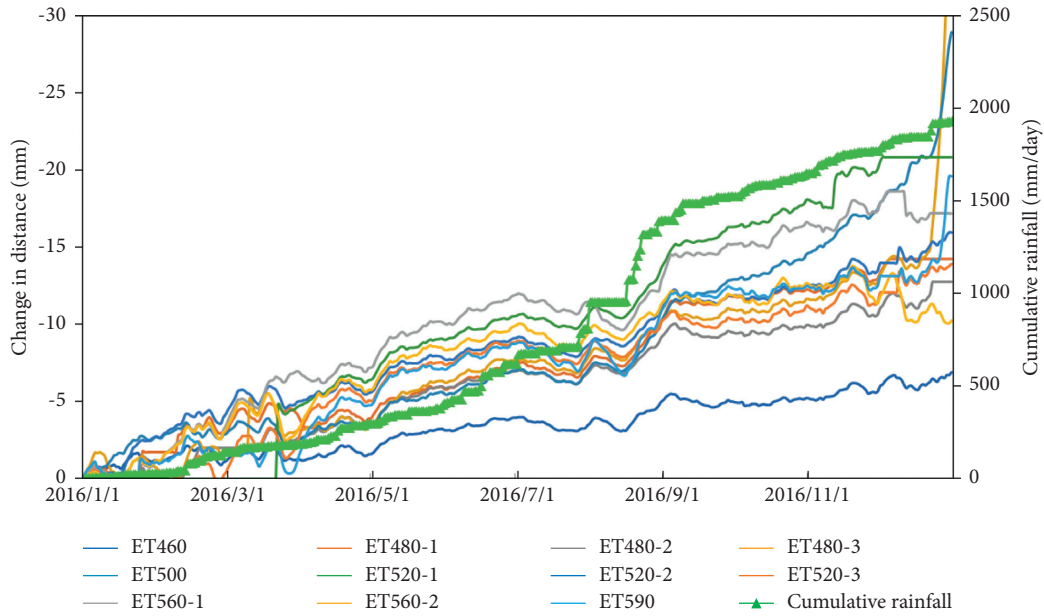


FIGURE 18: The comparison between cumulative rainfall and measured change in distance.

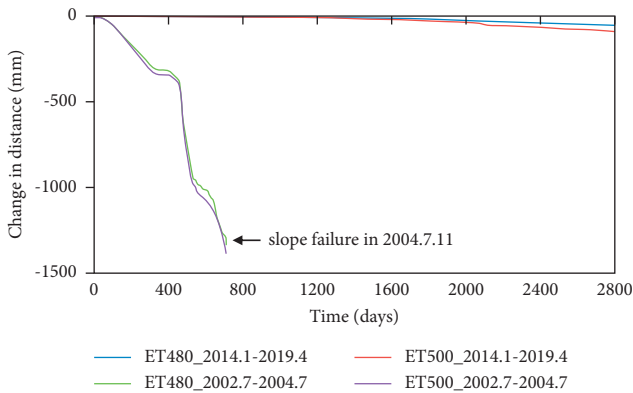


FIGURE 19: The change in distance from 2002.4 to 2004.7 and 2014.1 to 2019.4.

6. Conclusions

This paper investigates the characteristics and causes of long-term rock slope deformation at the Higashi-Shikagoe limestone quarry in Japan. The analysed rock slope displacement characteristics in the quarry were measured by an APS. The likely causes of the continuous rock slope deformation were then investigated numerically using 2D FEM techniques and discussed based on the characteristics of the measured displacements. The conclusions of this study are summarised as follows:

- (1) The measured results reveal that the distance between the beam generator and mirrors is gradually decreasing with time throughout the slope, but the magnitude of decrease depends on the slope position in the quarry. The rate of decreasing distance is greatest at the middle of the slope on the left-hand

side and centre of the quarry, but at the foot of the slope on the right-hand side of the quarry.

- (2) The simulated results of the change in distance between the beam generator point and slope surface reveal that the distance decreases owing to a reduction of Young's modulus of clay. The distance reduction owing to pit floor excavation increases under gravity force conditions, but decreases under horizontal stress conditions. The distance decreases owing to shear movement in the rock slope caused by strength reduction of the rock mass. The magnitude of the decrease in distance owing to the lowered Young's modulus of clay is the greatest in the middle of the rock slope, whereas the highest magnitude of decreased distance owing to excavation and shear strength reduction occurs at the slope foot.
- (3) The possible causes of the continuous deformation of the rock slope at the Higashi-Shikagoe limestone quarry are as follows. (a) Clay deterioration owing to increased water content is one of the dominant causes of slope displacement on the left-hand side and centre of the quarry. (b) The excavation of the pit floor can cause slope displacement on the right-hand side of the quarry if the horizontal stress is sufficiently large. The shear sliding of rock mass owing to reduced shear strength is also a considerable cause of the slope deformation. However, the risk of shear failure of the slope is presently quite low because the magnitude of the decreasing distance is small and no acceleration is observed.

Data Availability

The data used in supporting the results of our study are included within the article.

Conflicts of Interest

The authors declare no conflicts of interest.

Acknowledgments

This research was fully supported by the Ministry of Education, Culture, Sports, Science and Technology, Japan, through the Japanese Government (MEXT) Scholarship Program. The authors also wish to thank the Nittetsu Mining Co. Ltd. for the opportunity to carry out the research and their staff for their immeasurable contribution to displacement measurements over the years.

References

- [1] J. Kodama, E. Nishiyama, and K. Kaneko, "Measurement and interpretation of long-term deformation of a rock slope at the Ikura limestone quarry, Japan," *International Journal of Rock Mechanics and Mining Sciences*, vol. 46, no. 1, pp. 148–158, 2009.
- [2] A. R. Bye and F. G. Bell, "Stability assessment and slope design at Sandsloot open pit, South Africa," *International Journal of Rock Mechanics and Mining Sciences*, vol. 38, no. 3, pp. 449–466, 2001.
- [3] D. C. Willie and C. W. Mah, *Rock Slope Engineering*, pp. 320–327, Spon Press, 4th edition, 2004.
- [4] B. Hassan and M. Hani, "Application of rock mass classification systems to rock slope stability assessment: a case study," *International Journal of Rock Mechanics and Geotechnical Engineering*, vol. 9, pp. 993–1009, 2017.
- [5] L. Pantelidis, "Rock slope stability assessment through rock mass classification systems," *International Journal of Rock Mechanics and Mining Sciences*, vol. 46, no. 2, pp. 315–325, 2009.
- [6] Y.-C. Liu and C.-S. Chen, "A new approach for application of rock mass classification on rock slope stability assessment," *Engineering Geology*, vol. 89, no. 1-2, pp. 129–143, 2007.
- [7] A. W. Bishop, "The use of the slip circle in the stability analysis of slopes," *Géotechnique*, vol. 5, no. 1, pp. 7–17, 1955.
- [8] U. Yamaguchi and T. Shimotani, "10. A case study of slope failure in a limestone quarry," *International Journal of Rock Mechanics and Mining Science & Geomechanics Abstracts*, vol. 23, no. 1, pp. 95–104, 1986.
- [9] M. Ataei and S. Bodaghabadi, "Comprehensive analysis of slope stability and determination of stable slopes in the Chador-Malu iron ore mine using numerical and limit equilibrium methods," *Journal of China University of Mining and Technology*, vol. 18, no. 4, pp. 488–493, 2008.
- [10] D. Stead, E. Eberhardt, and J. S. Coggan, "Developments in the characterization of complex rock slope deformation and failure using numerical modelling techniques," *Engineering Geology*, vol. 83, no. 1-3, pp. 217–235, 2006.
- [11] Z. G. Tao, C. Zhu, M. C. He, and M. Karakus, "A physical modeling-based study on the control mechanisms of Negative Poisson's ratio anchor cable on the stratified toppling deformation of anti-inclined slopes," *International Journal of Rock Mechanics and Mining Sciences*, vol. 138, Article ID 104632, 2021.
- [12] N. D. Rose and O. Hungr, "Forecasting potential rock slope failure in open pit mines using the inverse-velocity method," *International Journal of Rock Mechanics and Mining Sciences*, vol. 44, no. 2, pp. 308–320, 2007.
- [13] H. Fujiita, "State of the art of the landslide control in Japan and the issues in the future," *Journal of Japanese Geotechnical Social*, vol. 45, no. 6, pp. 1–4, 1997, in Japanese.
- [14] K. Okata, T. Sugiyama, H. Muraishi et al., "Statistical risk estimating method for rainfall on surface collapse of a cut slope," *Soils and Foundations*, vol. 34, no. 93, pp. 49–58, 1994.
- [15] T. Sugiyama, K. Okada, H. Muraishi, T. Noguchi, and M. Samizo, "Statistical rainfall risk estimating method for a deep collapse of a cut slope," *Soils and Foundations*, vol. 35, no. 4, pp. 37–48, 1995.
- [16] Y. Shuin, N. Hotta, M. Suzuki, and K.-i. Ogawa, "Estimating the effects of heavy rainfall conditions on shallow landslides using a distributed landslide conceptual model," *Physics and Chemistry of the Earth, Parts A/B/C*, vol. 49, pp. 44–51, 2012.
- [17] F. Cai and K. Ugai, "Numerical analysis of rainfall effects on slope stability," *International Journal of Geomechanics*, vol. 4, no. 2, pp. 69–78, 2004.
- [18] T. Ishikawa, T. Tokoro, and M. Seiichi, "Geohazard at volcanic soil slope in cold regions and its influencing factors," *Japanese Geotechnical Society Special Publication*, vol. 1, no. 1, pp. 1–20, 2015.
- [19] N. Matsuoka, "Frost weathering and rockwall erosion in the southeastern Swiss Alps: long-term (1994–2006) observations," *Geomorphology*, vol. 99, no. 1-4, pp. 353–368, 2008.
- [20] S. Ohtsuka and M. Matsuo, "Rigid plastic dynamic deformation analysis of structures," in *Proceedings of the 1st International Conference on Earthquake, Geotechnical Engineering*, pp. 1147–1152, Tokyo, Japan, November 1995.
- [21] L. Lu, Z. J. Wang, X. Y. Huang, Z. Bin, and K. Arai, "Dynamic and static combination analysis method of slope stability analysis during earthquake," *Mathematical Problems in Engineering*, vol. 2014, Article ID 573962, 13 pages, 2014.
- [22] L. Lu, Z. J. Wang, M. L. Song, and K. Arai, "Stability analysis of slopes with ground water during earthquakes," *Engineering Geology*, vol. 193, pp. 288–296, 2015.
- [23] R. P. Orense, "Soil liquefaction and slope failures during the 2011 Tohoku. Japan Earthquake," in *Proceedings of the 2012 NZSEE Annual Technical Conference and AGM*, pp. 1–8, Wellington, New Zealand, April 2012.
- [24] T. Ivasuc and E. Olinic, "The effect of clay desensitization with granular materials on slope stability analysis," *Agriculture and Agricultural Science Procedia*, vol. 6, pp. 459–466, 2015.
- [25] D. S. Park and B. L. Kutter, "Static and seismic stability of sensitive clay slopes," *Soil Dynamics and Earthquake Engineering*, vol. 79, pp. 118–129, 2015.
- [26] X. Bian, Z.-S. Hong, and J.-W. Ding, "Evaluating the effect of soil structure on the ground response during shield tunnelling in Shanghai soft clay," *Tunnelling and Underground Space Technology*, vol. 58, pp. 120–132, 2016.
- [27] K. V. Jessu, T. R. Kosteci, A. J. S. Spearing, and J. Zhang, "Influence of varying bedding thickness of underclay on floor stability," *International Journal of Mining Science and Technology*, vol. 27, no. 3, pp. 517–523, 2017.
- [28] Z. A. Erguler and A. Shakoor, "Quantification of fragment size distribution of clay-bearing rocks after slake durability testing," *Environmental and Engineering Geoscience*, vol. 15, no. 2, pp. 81–89, 2009.
- [29] Z. A. Erguler and R. Ulusay, "Water-induced variations in mechanical properties of clay-bearing rocks," *International Journal of Rock Mechanics and Mining Sciences*, vol. 46, no. 2, pp. 355–370, 2009.

- [30] E. M. V. Eeckhout, "The mechanisms of strength reduction due to moisture in coal mine shales," *International Journal of Rock Mechanics and Mining Sciences*, vol. 13, pp. 61–67, 1976.
- [31] K. Kaneko, M. Kato, Y. Noguchi, and N. Nakamura, "Influence of initial stress on rock slope stability," in *Proceedings of the international symposium on rock stress, Balkema Rotterdam*, pp. 429–434, Kumamoto, Japan, October 1997.
- [32] N. X. Gts, "MIDAS information Technology Co., Ltd," 2014, <http://www.midasGTSNX.com>.
- [33] S. Sakurai, "In-situ test of rock masses and interpretation of the results," *Journal of the Society of Materials Science, Japan*, vol. 31, no. 347, pp. 759–769, 1982, in Japanese.
- [34] E. Hoek and E. T. Brown, "Practical estimates of rock mass strength," *International Journal of Rock Mechanics and Mining Sciences*, vol. 34, no. 8, pp. 1165–1186, 1997.
- [35] F. G. Bell, *Engineering Properties of Soils and Rocks*, Blackwell Scientific, Oxford, United Kingdom, 4th edition, 2000.
- [36] J.-C. Chai and N. Miura, "Investigation of factors affecting vertical drain behavior," *Journal of Geotechnical and Geoenvironmental Engineering*, vol. 125, no. 3, pp. 216–226, 1999.
- [37] D. Mao and B. Nilson, "Numerical analysis of effects of weakness zones on tunnel stability 2D versus 3D. Advances in underground space development," *Research publishing service*, pp. 388–398, 2013.
- [38] M. C. He, J. L. Feng, and X. M. Sun, "Stability evaluation and optimal excavated design of rock slope at Antaibao open pit coal mine, China," *International Journal of Rock Mechanics and Mining Sciences*, vol. 45, no. 3, pp. 289–302, 2008.
- [39] C. Zhu, M. He, M. Karakus, X. Cui, and Z. Tao, "Investigating toppling failure mechanism of anti-dip layered slope due to excavation by physical modelling," *Rock Mechanics and Rock Engineering*, vol. 53, no. 11, pp. 5029–5050, 2020.
- [40] E. M. Dawson, W. H. Roth, and A. Drescher, "Slope stability analysis by strength reduction," *Géotechnique*, vol. 49, no. 6, pp. 835–840, 1999.
- [41] D. V. Griffiths and P. A. Lane, "Slope stability analysis by finite elements," *Géotechnique*, vol. 49, no. 3, pp. 387–403, 1999.
- [42] T. Matsui and K. C. San, "Finite element slope stability analysis by shear strength reduction technique," *Soils and Foundations*, vol. 32, no. 1, pp. 59–70, 1992.
- [43] J. Shen, S. D. Priest, and M. Karakus, "Determination of mohr-coulomb shear strength parameters from generalized hoek-Brown criterion for slope stability analysis," *Rock Mechanics and Rock Engineering*, vol. 45, no. 1, pp. 123–129, 2012.
- [44] O. C. Zienkiewicz, C. Humpheson, and R. W. Lewis, "Associated and non-associated visco-plasticity and plasticity in soil mechanics," *Géotechnique*, vol. 25, no. 4, pp. 671–689, 1975.
- [45] N. Farshidfar and A. Nayeri, "Slope stability analysis by shear strength reduction method," *Journal of Civil Engineering and Urbanism*, vol. 5, no. 1, pp. 35–37, 2015.
- [46] C. N. Bandazi, *Measurement and Analysis of Rock Slope Displacement at Higashi Shikagoe limestone Quarry, Japan*, Master thesis, Master thesis in Hokkaido University, Sapporo, Japan, 2017.
- [47] J. Chai, Y. Igaya, T. Hino, and J. Carter, "Finite element simulation of an embankment on soft clay - case study," *Computers and Geotechnics*, vol. 48, pp. 117–126, 2013.
- [48] W. Zhang, Q. Sun, and Y. Zhang, "Correlation analyses of effects of temperature on physical and mechanical properties of clay," *Environmental Earth Sciences*, vol. 77, no. 17, p. 614, 2018.
- [49] D. T. Nicholson and S. R. Hencher, "Assessing the potential for deterioration of engineered rock slopes," in *Eng Geol the Env*, P. G. Marinos, G. C. Koukis, G. C. Tsiambaos, and G. C. Stournaras, Eds., pp. 911–917, Balkema, Rotterdam, Netherlands, 1997.
- [50] T. P. Gautam and A. Shakoor, "Slaking behavior of clay-bearing rocks during a one-year exposure to natural climatic conditions," *Engineering Geology*, vol. 166, pp. 17–25, 2013.
- [51] Y. Obara, N. Nakamura, S. S. Kang, and K. Kaneko, "Measurement of local stress and estimation of regional stress associated with stability assessment of an open-pit rock slope," *International Journal of Rock Mechanics and Mining Sciences*, vol. 37, no. 8, pp. 1211–1221, 2000.
- [52] E. T. Brown and E. Hoek, "Trends in relationships between measured in-situ stresses and depth," *International Journal of Rock Mechanics and Mining Science & Geomechanics Abstracts*, vol. 15, no. 4, pp. 211–215, 1978.

Research Article

Numerical Simulations on the Extinguishing Effect of Water Mist System with Different Parameters of Longitudinal Ventilation in Curve Tunnel Fire

Zhizhong Liu,^{1,2} Chen Chen,^{1,2} Mu Liu,^{1,2} Song Wang,³ and Yuzhu Liu³ 

¹Hebei Provincial Expressway Yanqing-Chongli Construction Office, Zhangjiakou 075000, China

²Hebei Provincial Expressway Yanqing-Chongli Management Center, Zhangjiakou 075000, China

³Key Laboratory of Transportation Tunnel Engineering, Ministry of Education, Southwest Jiaotong University, Chengdu 610031, China

Correspondence should be addressed to Yuzhu Liu; liuyuzhu@my.swjtu.edu.cn

Received 2 August 2021; Accepted 5 September 2021; Published 24 September 2021

Academic Editor: Gan Feng

Copyright © 2021 Zhizhong Liu et al. This is an open access article distributed under the Creative Commons Attribution License, which permits unrestricted use, distribution, and reproduction in any medium, provided the original work is properly cited.

Once a fire occurs in a long curve tunnel, the mixing of hot smoke flow and cold air leads to turbulence due to the curvature's impact. This phenomenon results in a greater thermal pressure difference at the fire source and a substantially greater temperature field than in the straight tunnel. The longitudinal air flowing along the wall loses a lot of velocity in the curve tunnel due to the massive wall friction. Under the same fire extinguishing conditions, the curve tunnel and straight tunnel have different requirements for longitudinal ventilation. Factors such as tunnel curvature, longitudinal ventilation operation time, and ventilation velocity were all evaluated in order to investigate the influence of longitudinal ventilation parameters on the fire extinguishing effect of water mist in the curve tunnel. The fire extinguishing effect of water mist coupling with longitudinal ventilation in the curve tunnel is studied by numerical simulation, and the recommended values of ventilation operation time and ventilation velocity in the curve tunnel with the participation of the water mist system are given. The results show that (1) the fire extinguishing effect of water mist decreases with the increase of curvature under longitudinal ventilation and (2) fire prevention effect is best when water mist and longitudinal ventilation are used in the curved tunnel, and the ventilation velocity should be greater than 2 m/s.

1. Introduction

The mountain tunnels tend to be characterized by crossing deep valleys and high mountains. In order to avoid traversing unfavorable geology and overcome terrains with large elevation differences, more curve tunnels have emerged. The curvature varies from 1/254 to 1/3000. Tunnel fire is the most dangerous disaster during operation period since a large amount of hot and toxic smoke are generated by fire, which seriously affect the safety of passengers and the stability of the lining structure. In addition, the smoke diffusion in the curve tunnel is quite different from that of the straight tunnel due to the interaction of curvature and centrifugal force.

In the curved tunnel, a great number of studies have been performed for the limit and control of smoke. Zhong et al.

[1] conducted a full-scale experimental study on the development of flue gas in inclined large curved tunnels of underground natural ventilated spaces under three different fire powers. The experiments measured the vertical smoke temperature rise, the flow characteristics of the fire plume near the fire source, and the variation of maximum smoke temperature during the growth, stabilization, and attenuation phases of the fire. Lou et al. [2] studied the effects of curvature on smoke diffusion by using the software of FDS in a curved tunnel fire, for understanding the correlations between the range of influence and the degree of the tunnel curvature. Li and Xie [3] established a full-scale curve tunnel model based on computational fluid dynamics theory and fire turbulence numerical simulation theory by using the numerical simulation method. The fire and ventilation

conditions of the full-scale curve tunnel were studied by CFD simulation software. Caliendo et al. [4] proposed a CFD model simulating the impact of curved bi-directional highway tunnel fire, focusing on the impact of tunnel fire location, tunnel geometry, longitudinal ventilation of jet fans, and existence of the traffic flow on tunnel fire. Although there are a lot of research studies on the curved tunnel, the research on fire extinguishing by water mist in the curved tunnel is still blank. Zhang et al. [5] used FDS 5.5.3 to numerically study the length of the smoke back layer and the critical ventilation velocity of a series of curved subway tunnels with turning radius of 300 to 1000 m at the exothermic rate of 5 and 10 MW. Wang [6] studied the numerical simulation results of critical ventilation speed and smoke movement of fire at different lateral positions of the curved tunnel and also gave the back layer length of three lateral fire positions. Liu [7] described full-scale tests of the water mist fire suppression system under forced desmoking conditions. The smoke exhaust had a strong effect on the water mist to result in a fire that could not be extinguished when the ventilation rate increased to $120.0 \text{ m}^3/\text{min}$. This study employed a computer modeling to verify the water mist system in a compartment space and determine how the water mist system could be optimized.

However, only grasping the law of smoke diffusion in curved tunnels is not enough to guide engineering practice. With the deepening of tunnel smoke control, water mist fire extinguishing systems have gradually become one of the auxiliary measures for tunnel fire control. Therefore, a large number of studies have been carried out based on the water mist system. Blanchard et al. [8] focused on the fire in mid-scale tunnels and conducted experiments and numerical simulations. In their research, water spray was sprayed directly on the fire source to control the fire, opening the longitudinal ventilation system and exploring the law of temperature changes inside the tunnel. The results show that the water mist plays an important role in the absorption of heat, and most of the heat is absorbed by the water droplets. Tang et al. [9] conducted an experimental study on the longitudinal critical velocity. The experimental results show that the critical velocity of the tunnel decreases after the activation of the water-based fire extinguishing system. Li et al. [10] described and analyzed experiments using water mist segments (curtains) to prevent smoke and heat transmission in mesoscale tunnels. The experimental results show that the activation of the water mist section can generally reduce the temperature under the inner ceiling of the reserve. The blocking effect of the water mist section is better when the nozzle is more active and the water pressure is higher. Garo et al. [11] studied the influence of a mist addition as an opposed flow to a small-scale liquid (heptane) pool fire structure, confirming that radiation attenuation cannot be identified as a predominant mechanism of extinguishment. Liang et al. [12] conducted a numerical study on the interaction between lateral ventilation and water mist curtains in large tunnels. The results show that the combination of water curtain and transverse ventilation system can effectively limit fire and smoke, and the environment in the restricted area is suitable for evacuation. Cui and Liu [13] proposed that, without weakening the fire extinguishing effect of water mist, proper mechanical

ventilation systems can effectively reduce flue gas concentration, thermal radiation intensity, and total heat flux intensity. It can also increase the concentration of O_2 and reduce CO volume fraction. To some extent, the combined action of mechanical ventilation systems and water mist will help ensure personnel safety in the fire ground. Chen et al. [14] found that when the interval between the mist nozzle and fire source enlarges, the relationship curve between fire suppression time and ventilation velocity shows a 'V' figure.

However, the research object of the above research is mainly straight tunnels. There are less research studies on the coupling of curved tunnels. Excessive air reduces fire extinguishing efficiency, but appropriate ventilation can slightly enhance fire combustion and further strengthen the effect of cooling by water mist. The incomplete combustion of combustibles produces CO and fumes, which form a thick and dense smoke layer. The hot smoke layer is hardly penetrated by finer droplets, but smoke concentration can be decreased by the dilution of air and the complete combustion of fuel. This effect helps water droplets reach the fire. Meanwhile, convective heat transfer and radiation attenuation caused by fresh air play their active roles in decreasing the radiant heat feedback of smoke on combustibles. When the water mist system and ventilation system are used at the same time in the tunnel, a complex situation of water mist, fire, and ventilation coupling is formed, which mainly affects the fire extinguishing. There are many cases in which two kinds of systems are used at the same time and the ventilation system is longitudinal ventilation. The specific engineering results are shown in Table 1 [15, 16], including the Jinjiazhuang Tunnel. Longitudinal ventilation will often have adverse effects on water mist fire extinguishing, which is mainly reflected in two aspects: (1) the longitudinal ventilation system will change the original motion trajectory of the water droplets while removing high temperature and toxic smoke, causing the water droplets to deviate from the fire source, which may cause the water mist with a small particle size to fail to reach the root of the flame, as shown in Figure 1. The fire extinguishing effect is reduced because the mechanical exhaust increases the buoyancy of the fire plume and affects the momentum of the water mist reaching the root of the flame. (2) Longitudinal ventilation in the highway tunnel will bring a lot of fresh air, which will bring sufficient oxygen to the fire source in the tunnel and even play a combustion-supporting effect. This is not good for tunnel fire extinguishing. These adverse effects not only appear in the straight tunnel but also apply to the curve tunnel.

Current research mostly focuses on exploring the influence of longitudinal ventilation in linear highway tunnels on water mist fire extinguishing [17–19]. Therefore, according to the actual size of the Jinjiazhuang Tunnel and the method of FDS numerical simulation, this paper studies the interaction between the longitudinal ventilation and the water mist system, the reasonable opening time, and the design wind speed of the longitudinal ventilation under different curvatures. And, the corresponding suggested values are given. The results can provide references for tunnel designers in the design of tunnel fire control and smoke exhaust.

2. Numerical Simulation

2.1. Introduction of FDS. Fire dynamics simulation software (FDS) is a commonly used fire simulation tool, which can comprehensively consider the various processes of fire smoke flow. FDS can also realize the coupled simulation of two-phase flow, smoke, and particles. The Large Eddy Simulation turbulence model was used in this FDS numerical calculation. The main governing equations of FDS [20] are as follows:

Conservation of mass:

$$\frac{\partial \rho}{\partial t} + \nabla \cdot (\rho u) = 0. \quad (1)$$

Conservation of momentum:

$$\rho \left(\frac{\partial u}{\partial t} + (u \cdot \nabla) u \right) + \nabla p = \rho g + f + \nabla \cdot \tau. \quad (2)$$

Conservation of energy:

$$\frac{\partial}{\partial t} (\rho h) + \nabla \cdot \rho h u - \frac{Dp}{Dt} = \dot{q}''' - \nabla \cdot q_r + \nabla \cdot k \nabla T + \nabla \cdot \sum_I h_I (\rho D)_I \nabla Y_I. \quad (3)$$

Conservation of species:

$$\frac{\partial}{\partial t} (\rho Y_I) + \nabla \cdot \rho Y_I u = \nabla \cdot (\rho D)_I \nabla Y_I + \dot{m}'''. \quad (4)$$

The spray characteristics are defined by a set of parameters, including fluid thermal characteristics, droplet size distribution, and spray characteristics. In the FDS spray model, Lagrange particles are used to represent water droplets. The droplet size distribution is represented by lognormal distribution and Poisson distribution:

$$F(d) = \begin{cases} \frac{1}{\sqrt{2\pi}} \int_0^d \frac{1}{\sigma d'} e^{-[\ln(d'/d_m)]^2 / 2\sigma^2} dd' & (d \leq d_m) \\ 1 - e^{-0.693(d/d_m)'} & (d_m < d) \end{cases} \quad (5)$$

The mass and energy transfer formula of the vapor phase or droplet is as follows:

$$m_l C_l \frac{dT_l}{dt} = Ah(T_g - T_l) + Ah_s(T_s - T_l) + q_r + \frac{dm_l}{dt} h_v. \quad (6)$$

2.2. Numerical Model. Based on the real size of Jinjiazhuang Tunnel, a numerical model is established, and the curvatures are 1/860, 1/500, and straight. The size of the numerical model is 300 m × 13 m × 8.7 m (length × width × height). The height of the water mist nozzle is 5 m, and the distance

between adjacent nozzles is 3 m. The total length of the water mist fire extinguishing area is 50 m. The velocity of the nozzle is 10 m/s, and the flow rate is 15 L/min. The nozzle working pressure is 12 MPa, and the diameter of the water mist droplet is 300 μm. The fire source is an oil basin filled with heptane, the fire source area is 0.36 m², the fire size is 30 MW, and the fire source is located 50 m away from the entrance of the tunnel.

The simulated ambient temperature is 20°C, and the boundary conditions of inlet and outlet are set as “open.” The inlet boundary condition is changed to “supply” to represent longitudinal ventilation in the tunnel.

The water mist system is activated 90 s after ignition, and the visibility and temperature concentration measurement points are arranged at the height of the human eye (2.0 m from the ground) and the height of the vault. The visibility and temperature are recorded every 1 second. Figure 2 shows the locations of the measuring points discussed in the numerical simulation. In addition, in order to monitor the flow and temperature field, horizontal slices at different heights (medium height $z = 2.0$ m and slightly lower than the ceiling $z = 4.9$ meters) and longitudinal slices at different distances from the fire source (10 m, 20 m, 30 m, 50 m, and 100 m from the fire source) are defined.

Considering the radius of curvature, the speed of longitudinal ventilation, the opening time of longitudinal ventilation, and other factors, 21 working conditions are designed, as shown in Table 2. Calculation condition 1–20 is used to study the effect of water mist fire extinguishing under multifactor coupling. To verify the accuracy of FDS, calculation condition 21 is designed according to the experiment of small-sized tunnel longitudinal smoke exhaust and high-pressure water mist [21].

2.3. Sensitivity Study on the Grid Size. During the FDS fire simulation, the size of the grid determines the accuracy of the simulation results. As the number of grids increases, the calculation results are more accurate, but the calculation time increases. Therefore, the grid size is usually determined by the characteristic fire diameter D^* of the fire source. It is suggested that when the grid size is taken as 1/10 of the characteristic fire diameter, the simulation results are accurate. The D^* calculation formula [22] is as follows:

$$D^* = \left(\frac{Q}{\rho_{\infty} c_{\infty} T_{\infty} \sqrt{g}} \right)^{2/5}. \quad (7)$$

The heat release rate is the key factor directly affecting the fire characteristics. For a 30 MW fire, the value of D^* is about 3.66 m. This means that a mesh size of 0.36 m or less should provide reliable results. To obtain the proper grid sizes, grid sensitivity analyses are carried out as in the previous studies [17]. The grid sizes of 0.2 m, 0.25 m, and 0.5 m are selected in the current work.

Figure 3 shows the temperature distribution of the tunnel longitudinal section near the fire source with different grid sizes. The 0.5 m grid size has a faster temperature rise because the location of the fire source is larger than other

TABLE 1: Typical engineering application of the water mist fire extinguishing system in the tunnel space.

Application place	Country	Fire extinguishing system	Ventilation system
Hugh L. Carey Tunnel	USA	Water mist	Longitudinal
Gran Sasso National Laboratory Underground Tunnel	Germany	Water mist	Longitudinal
Virgolo Tunnel	Italy	Water mist	Longitudinal
Eurotunnel	France and UK	Water mist	Longitudinal
New Tyne Crossing	UK	Water mist	Longitudinal
Saadiyat Island Service Tunnel	Abu Dhabi	Water mist	Longitudinal

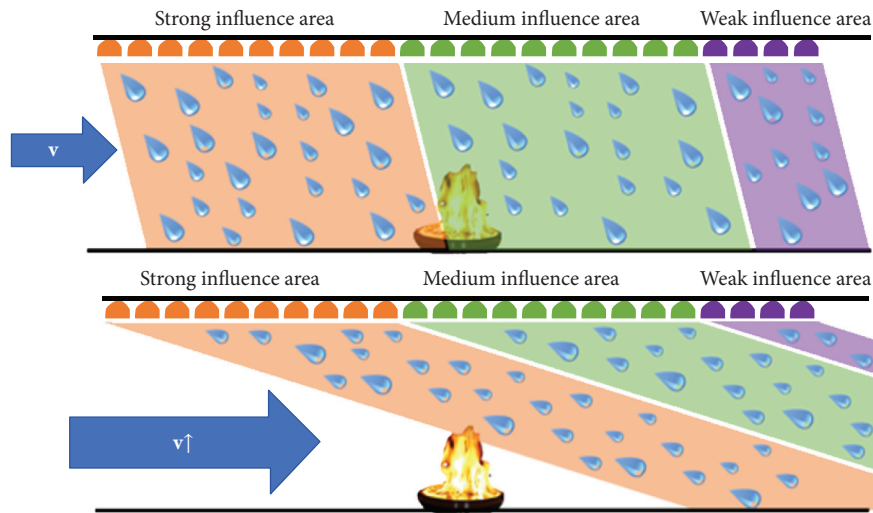


FIGURE 1: Water mist droplets have long downstream distance at higher longitudinal ventilation.

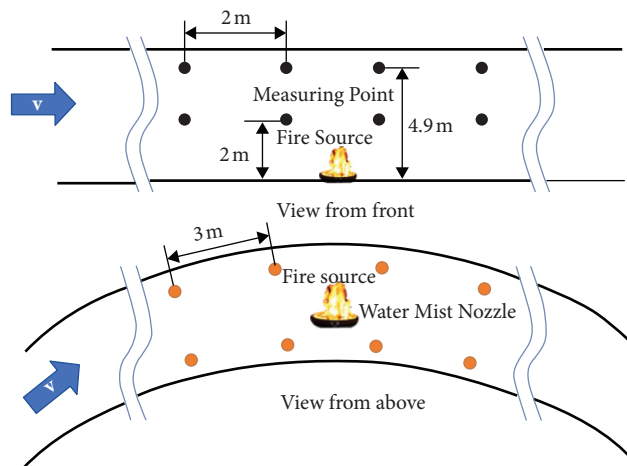


FIGURE 2: Schematic diagram of the arrangement of fire source, water mist nozzle, and measuring points.

grids. Thicker mesh has thicker layer of smoke, and results of grid sizes of 0.2 m and 0.25 m are nearly the same. Therefore, the grid size used in FDS calculation in this study is 0.25 m.

3. Result and Discussion

3.1. Validation Work. To verify the correctness of the FDS calculation, a small-scale tunnel longitudinal smoke exhaust and high-pressure water mist coupling experimental model of Zhang et al. [21] is selected for numerical simulation. The

model size (length × width × height) is 6 m × 1.5 m × 2 m, and a small diesel pool fire (250 mm × 200 mm) is used as the research object. The oil pool is located directly under the water mist nozzle. One of the calculation is selected for verification. Under this calculation condition, the working pressure of the water mist nozzle is 15 MPa. The actual flow rate is 19 L/min, and the droplet diameter is $\leq 200 \mu\text{m}$. The fan is opened to ensure that the longitudinal ventilation wind speed reaches 1 m/s. Both longitudinal ventilation and water mist turn on 90 s after the oil pool is ignited.

TABLE 2: Simulation scenario.

Calculation condition	Radius of curvature	Fire scale	Opening time of water mist (s)	Longitudinal ventilation speed (m/s)	Opening time of longitudinal ventilation (s)
1					-
2	0	30 MW	90	2	60
3					90
4					120
5					-
6	500	30 MW	90	2	60
7					90
8					120
9					-
10	860	30 MW	90	2	60
11					90
12					120
13					-
14	500	30 MW	90	1	90
15				2.5	
16				3	
17				4	
18	860	30 MW	90	1	90
19				2.5	
20				3	
21				4	
21	0	35 kW	90	1	90

Measuring points at a height of 500 mm directly above the fire source and a height of 1500 mm from the ground are set to measure the fire field temperature.

The comparison between FDS calculation results and model test results is shown in Figure 4. The trends of FDS simulation results and the experimental results are in general agreement. The temperature of the measuring point increases continuously before the water mist is turned on. It rises for a short time after the activation of water mist and then decreases. The error is controlled within 15% to meet the error requirements [23]. Therefore, the results obtained by FDS are credible.

3.2. The Effect of Longitudinal Ventilation on Water Mist System under Different Curvatures. The water mist has a more stable form without mechanical ventilation, which plays a better role in blocking the smoke and reducing the temperature significantly. However, the movement of the droplets will be greatly disturbed with the opening of longitudinal ventilation. The droplets fall on the road at a long downstream distance, reducing the effect of smoke insulation and cooling. Generally speaking, the airflow is more likely to be disturbed at a small particle size under the action of forced ventilation. The disturbance causes the droplets' velocity to be unstable, reducing the momentum of droplets, which has an adverse effect on extinguishing fire.

Figure 5 shows the vault temperature change curve of a tunnel with a curvature of 1/500 and 1/860 under different longitudinal ventilation speeds. With the increase of ventilation speed under different curvatures, the variation trend of temperature is consistent. Under the same curvature, the higher the longitudinal ventilation speed, the lower the temperature in the tunnel. The highest temperature is 261°C

at the vault height, and the lowest temperature is 20°C. When the longitudinal ventilation speed is 2 m/s, the high temperature danger zone (the area where the temperature is higher than 60°C at human eye height) near the fire source is the shortest. The upstream of the tunnel is kept at a normal temperature of 20°C, as the longitudinal ventilation speed increases to 3-4 m/s. Within 100 m downstream the fire source, the temperature fluctuates due to the flue gas's disturbance by the convection of cold and hot air. With the increase of the longitudinal ventilation speed, the fluctuation becomes more intense.

The temperature change curve of the tunnel with a curvature of 1/500 at different longitudinal wind speeds at the height of the human eye is shown in Figure 5(b). The temperature in the upstream of the fire source is basically kept within the safety limit and reaches 100°C near the fire source. With the increase of ventilation speed, the disturbance of the smoke flow becomes more severe, and the temperature at the height of the human eye within 50 m downstream of the fire source fluctuates continuously. When the longitudinal ventilation speed is 2 m/s, the high temperature danger zone is the shortest. The temperature fluctuation tends to be stable after 50 m downstream of the fire source, and the temperature only fluctuates between 35–45° after 100 m.

3.3. Operation Time of Ventilation System under Different Curvatures

3.3.1. Temperature Variation under Different Curvatures. The smoke generated in highway tunnel fire has a very high temperature. For the lining, the high temperature will cause the concrete lining structure to burst, which will affect the

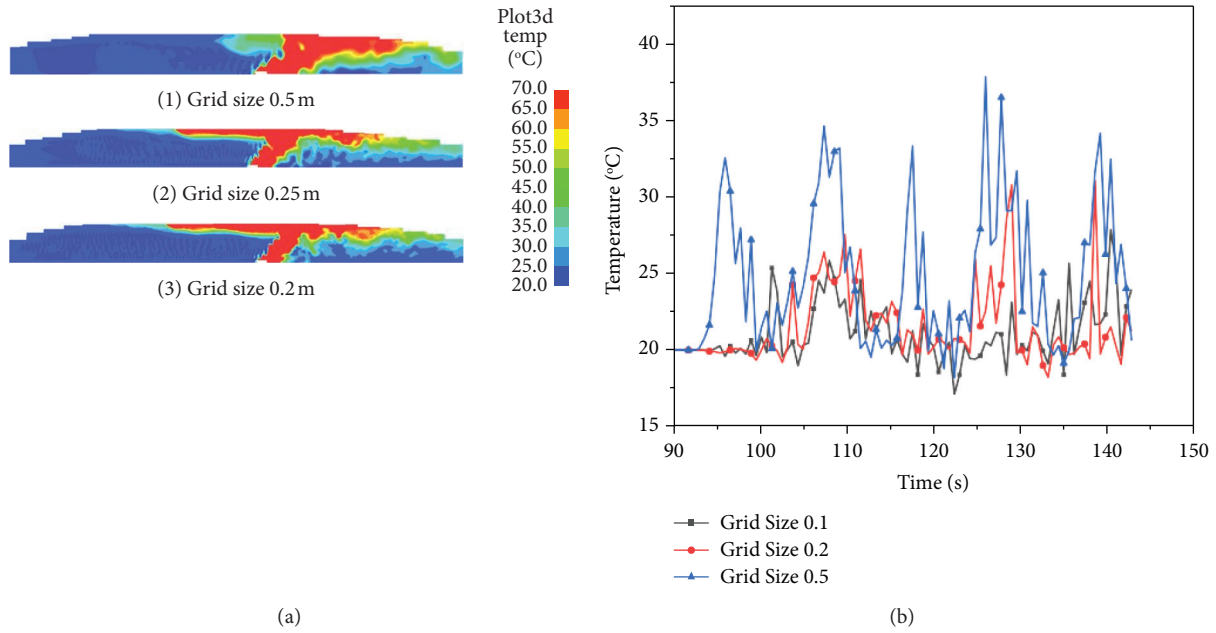


FIGURE 3: Grid sensitivity: comparison of temperature contour plots in the vertical midplane for 3 mesh cell sizes for simulation 11. (a) Temperature contour plots in the vertical midplane. (b) Temperature change curve at human eye height under different grid sizes.

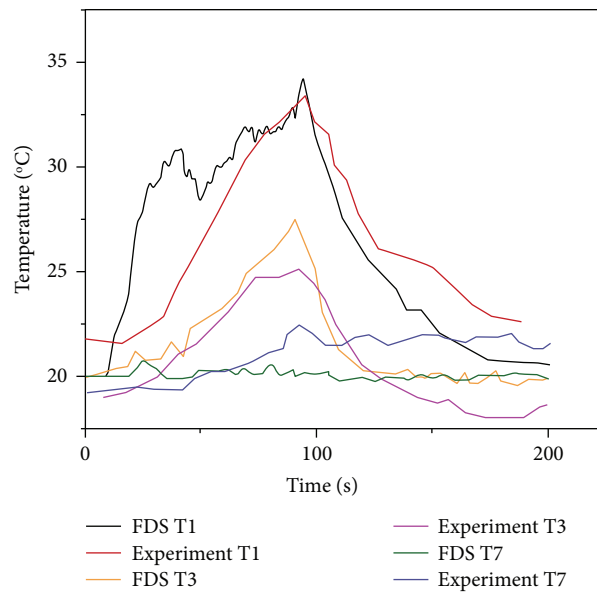


FIGURE 4: The temperature observed by Zhang et al. vs. the results reproduced by FDS.

safety of the lining structure. For people, the heat radiation in the fire causes burns. Therefore, it is necessary to launch the study of the temperature change at the height of the eye and the height of the vault under the coupling of tunnel fire, water mist, and longitudinal ventilation.

(1) *Temperature Variation at Vault Height.* The temperature distribution is studied to explore the influence of the coupling of longitudinal ventilation and fine water mist in tunnels with different curvatures. Figure 6 shows the temperature changes of tunnel vaults of various curvatures when longitudinal ventilation is turned on at 60 s,

90 s, and 120 s and without longitudinal ventilation. The flue gas temperature fluctuates greatly near the fire source. As the curvature increases, the resistance and the temperature at the same height increases. After the longitudinal ventilation is turned on in various simulation conditions, the temperature drops significantly, as shown in Figure 6. With the axial flow fan operation time in advance, the cooling time is shortened. Longitudinal ventilation is started in 60 s, 90 s, and 120 s, and the time required for the temperature of the vault above the fire source to stabilize at about 60 °C is 150 s, 130 s, and 140 s, respectively.

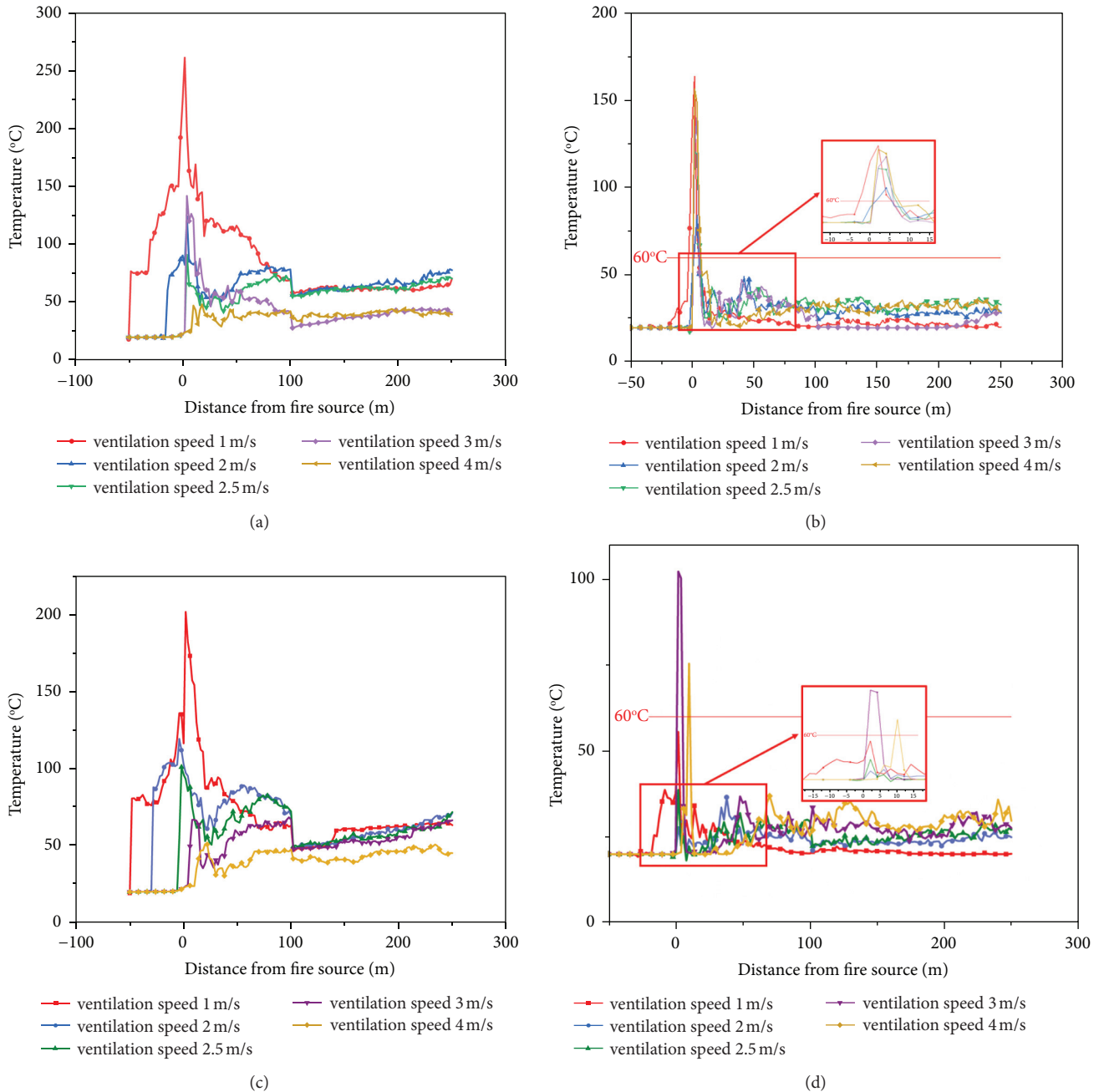


FIGURE 5: Variation of temperature at different heights in curvature 1/500 and 1/860 tunnels under different longitudinal ventilation speeds. (a) Variation of vault temperature in curvature 1/500 tunnel under different longitudinal ventilation speeds and variation of vault temperature in curvature 1/860 tunnel under different longitudinal ventilation speeds. (b) Variation of eye height temperature in curvature 1/500 tunnel under different longitudinal ventilation speeds and variation of eye height temperature in curvature 1/860 tunnel under different longitudinal ventilation speeds.

The cooling effect under the condition of 120 s longitudinal ventilation is better than that the condition without longitudinal ventilation, which shows that turning on the longitudinal ventilation has a significant effect on reducing the temperature in the tunnel. As shown in Figure 6, when the longitudinal ventilation and water mist are turned on at the same time, the temperature in the tunnel is relatively low, basically maintaining below 35°C. Comparing the calculation simulations of different operation times, it is not that

the temperature in the tunnel drops faster when the ventilation is opened earlier. The longitudinal temperature distribution in the tunnel is related to the degree of influence of longitudinal ventilation on the water mist. When the longitudinal ventilation is turned on too early, the temperature drop is not obvious due to the downstream distance of water mist droplets. The hot smoke cannot be eliminated in time with the delayed opening of longitudinal ventilation. Since the initial water mist has a higher flow rate and a lower

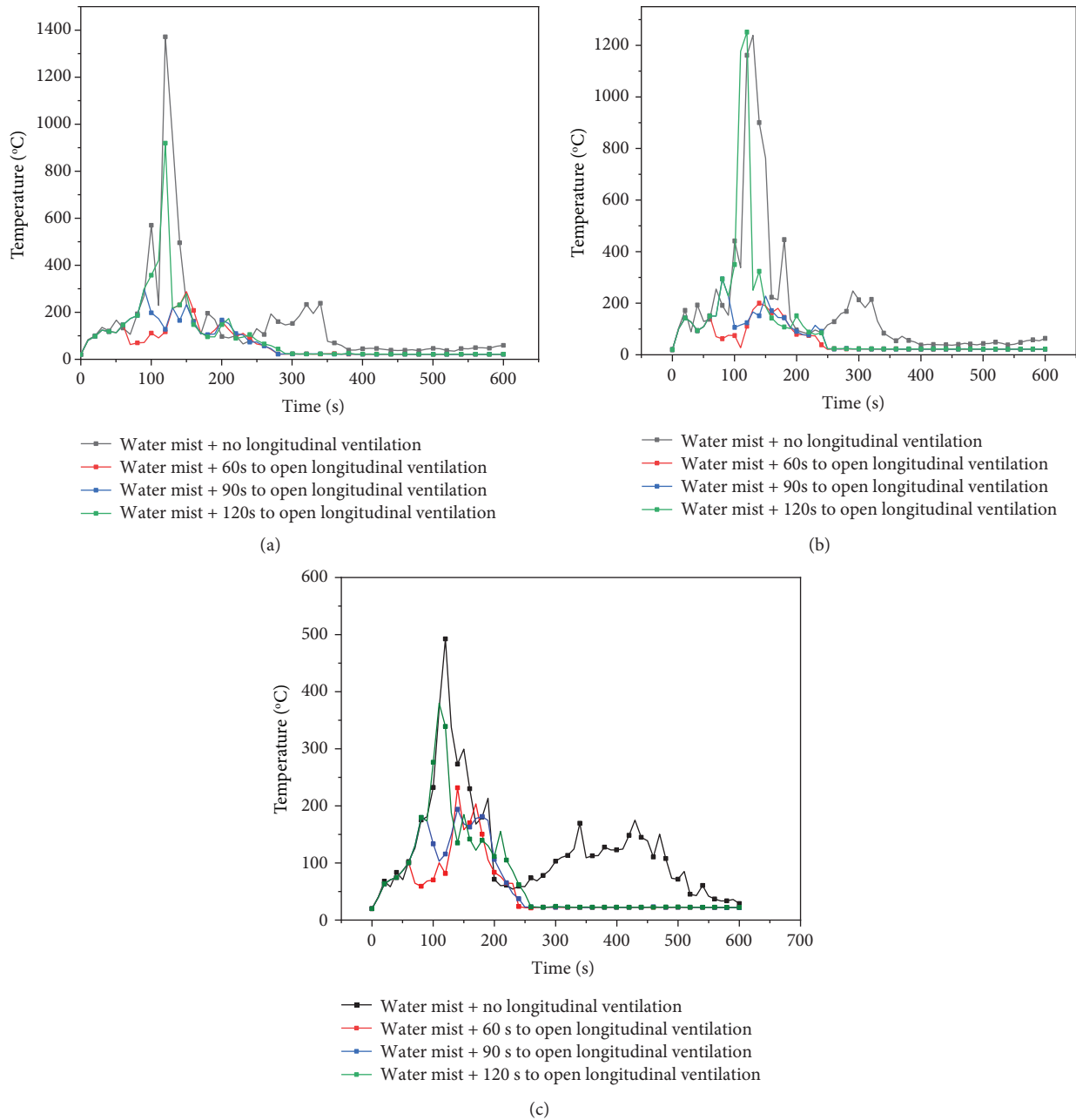


FIGURE 6: Temperature at vault height under different curvatures. (a) Straight tunnel. (b) Curvature 1/500 tunnel. (c) Curvature 1/860 tunnel.

longitudinal wind speed, the effect of longitudinal ventilation on water mist is very small, so the fire extinguishing effect is obvious, as shown in Figure 7. On the contrary, the longitudinal ventilation allows the smoke flow continuously making the droplets entering the flame zone and reducing the heat radiation of the flue gas.

(2) *Temperature Variation at the Height of Human Eyes.* The temperature distribution diagram of each tunnel cross section when the curvature is 1/860 is shown in Figure 8. As shown in Figure 8, the high temperature area is mainly concentrated in the range of 100 m downstream of the fire source, and there is obvious temperature

stratification. The highest temperature is 55°C in the middle of the tunnel, and the temperature in the area below 2 m is close to normal temperature. The hot flue gas velocity upstream of the fire source is relatively slow on account of the resistance of the longitudinal ventilation. Then, the upstream smoke flows back to the downstream part. In this process, the smoke plume gradually loses its buoyancy and sinks to the lower part of the tunnel, causing the cross-sectional temperature of the downstream part of the fire source to reach about 50°C. The earlier the longitudinal ventilation operates, the faster the temperature decreases in the downstream of the fire source.

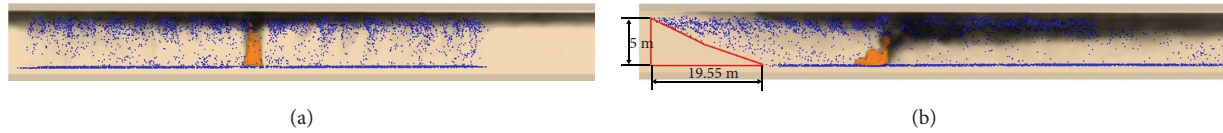


FIGURE 7: Trajectory of water mist droplets in the tunnel. (a) No longitudinal shift. (b) Downstream shift.

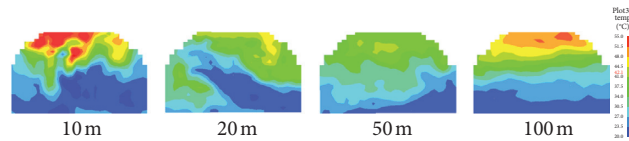


FIGURE 8: Temperature field change in each cross section of calculation condition 11.

3.3.2. Cooling Effect under Different Curvatures.

According to NFPA-15, water spray shall be considered effective for any one of or a combination of the following objectives: (1) extinguishment of fire; (2) control of burning; (3) exposure protection; (4) prevention of fire. Figures 9(a)–9(c) show the change curve of the fire source heat release rate under various simulation conditions. Figure 9(d) shows the time required for fire control under different ventilation operation times.

Through comparative analysis, it is found that, with the advance of fan's starting time, the fire extinguishing time is shortened and the effect is obvious. The starting time of the fan under the straight and curve tunnels has different effects on the time required to extinguish the fire. In the curve tunnel, the fire control time increases with the increase of curvature. In curvature 1/500 tunnel, time required for controlling fire decreases from 220 s to 190 s with the advance opening of longitudinal ventilation of 120 s to 90 s. This is because the wall resistance of the smoke in the tunnel increases with the increase of curvature. The heat release rate of the fire source will increase for a short time after the operation of ventilation in each simulation condition, indicating that the longitudinal ventilation has an accelerating effect on the heat release rate of the oil and fire.

3.4. Velocity of Ventilation System under Different Curvatures.

With the massive production of fire smoke, the smoke contains a large amount of toxic and harmful gases and dust, causing the victims to experience the physiological phenomena of poisoning. The spreading high temperature smoke obscures the sight of people and greatly reduces the speed of evacuation. Relevant research shows that the critical conditions of fire risk in the tunnel are as follows:

- (1) At a height of 2.0 m that is characteristic of human eyes in the tunnel, the flue gas temperature does not exceed 60°C
- (2) At a height of 2.0 m, the visibility of the human eye is less than 10 m

3.4.1. Temperature Variation at the Height of Human Eyes.

Figure 10 shows the velocity field at the height of the human eye in the tunnel under different radius of curvature. As shown in Figure 10, there is a small section of flue gas countercurrent upstream of the fire source. The mixing of hot smoke and cold air forms vortex. Due to the viscosity of the fluid and the increased wall friction at the tunnel bend, a large velocity gradient is formed on the wall surface, and the velocity at the center of the tunnel was about 3 m/s. Meanwhile, affected by the hot smoke, the hot and cold air in the tunnel is strongly convective, resulting in uneven velocity distribution within a certain range downstream the fire source. In the downstream of the remote, the velocity near the wall decreased, and the center velocity increased to about 3.5 m/s due to the influence of curvature.

Compared with the straight tunnel, the smoke velocity at the side wall is reduced as a result of the impact of the side wall in the curve tunnel, and the smoke velocity at the center is higher.

Figure 11(a) is a temperature field at the height of the human eyes in the tunnel under different curvatures. The high temperature zone of a straight tunnel is located within 50 m downstream of the fire source, while the high temperature zone of a curve tunnel fire is mostly concentrated within 100 m downstream of the fire source. The temperature on one side of the tunnel bending direction is higher than the other side in the curve tunnel. Affected by tunnel wall resistance, the greater the curvature of the curve tunnel, the higher the temperature.

As shown in Figure 11(b), comparing the temperature distribution at the height of the human eyes in different curvatures, it can be seen that the greater the curvature, the shorter the length of flue gas reflux. The temperature is closer after 100 m downstream of the fire source. The temperature of the tunnel with large curvature is higher than that with small curvature.

3.4.2. Visibility Variation at the Height of Human Eyes.

Visibility is inversely proportional to the concentration of carbon particles in a fire scenario. Both CO and soot particles

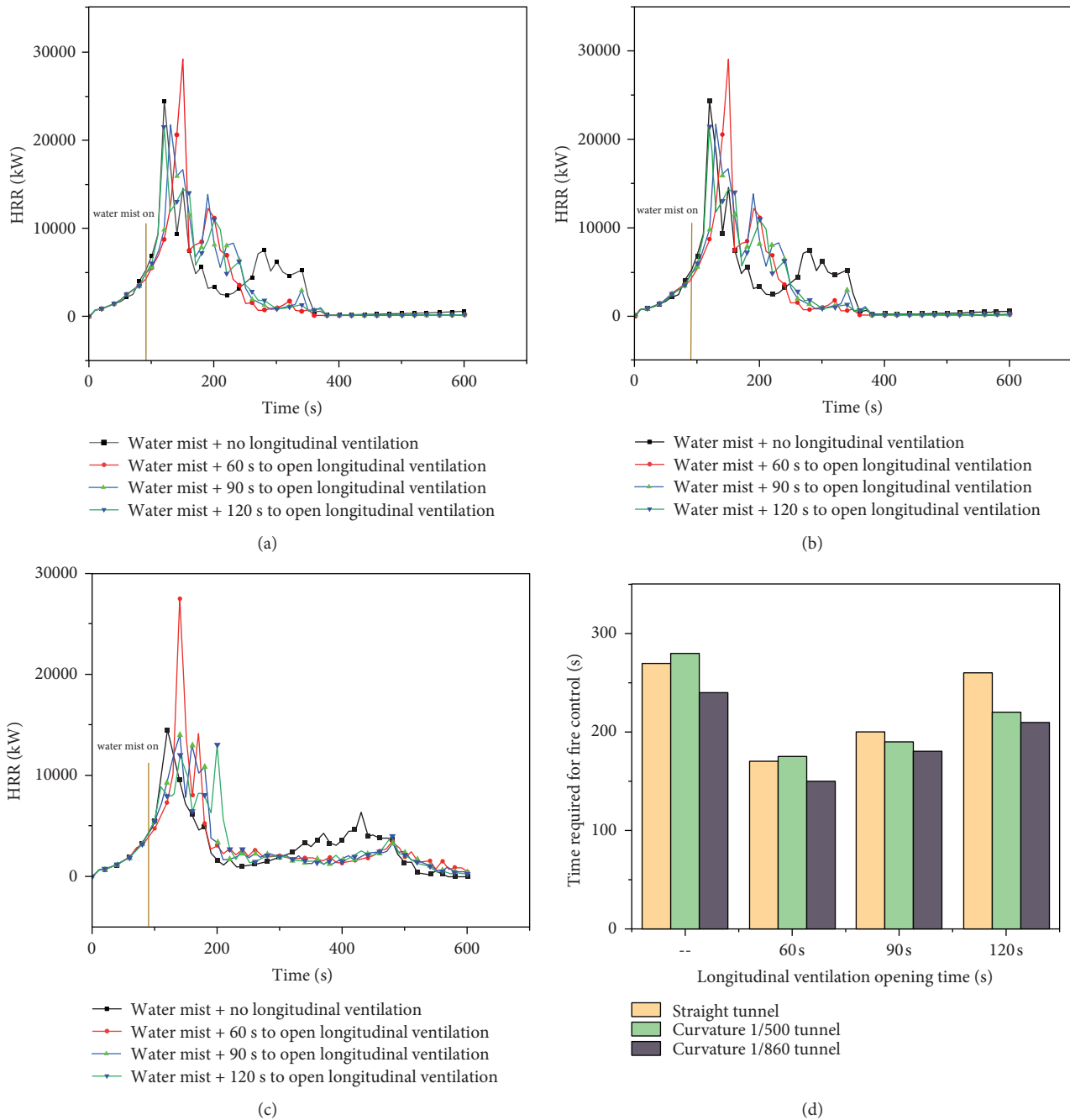


FIGURE 9: Variation of the heat release rate under different curvatures and time required for controlling fire. (a) Straight tunnel. (b) Curvature 1/500 tunnel. (c) Curvature 1/860 tunnel. (d) Time required for controlling fire.

are produced with incomplete combustion. In the process of flue gas diffusion, the concentration of CO and soot particles will be diluted to a stable degree.

As shown in Figure 12, there is no smoke upstream of the fire source at 200 s, and the visibility is 30 m. The early opening of the longitudinal ventilation can significantly improve the visibility of the fire area and reduce the adverse effect of the water mist on the visibility. Visibility

drops to 10 m within 20 m near the fire source, and the greater the curvature is, the lower the visibility is. Due to the stratification of the flue gas in the downstream, soot particles are relatively small, and the visibility is increased to 30 m at a distance of 20 m from the fire source. The variation of visibility at human eye height under different curvatures shows that the greater the curvature, the lower the visibility.

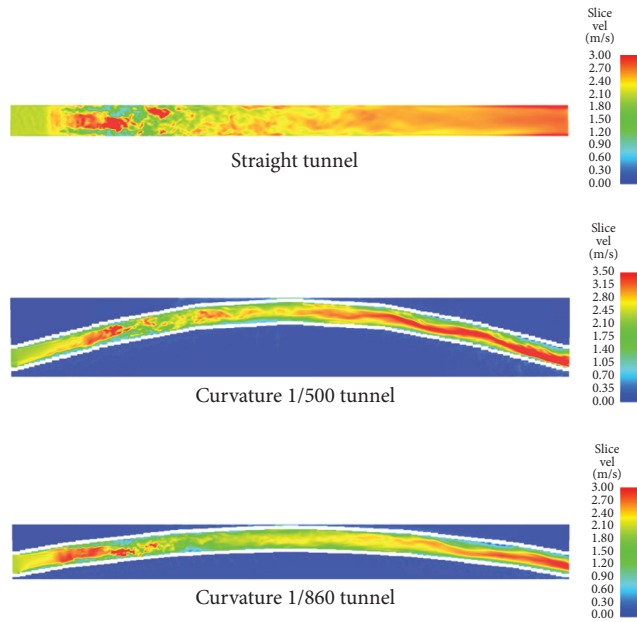


FIGURE 10: Velocity field in the human eye height plane.

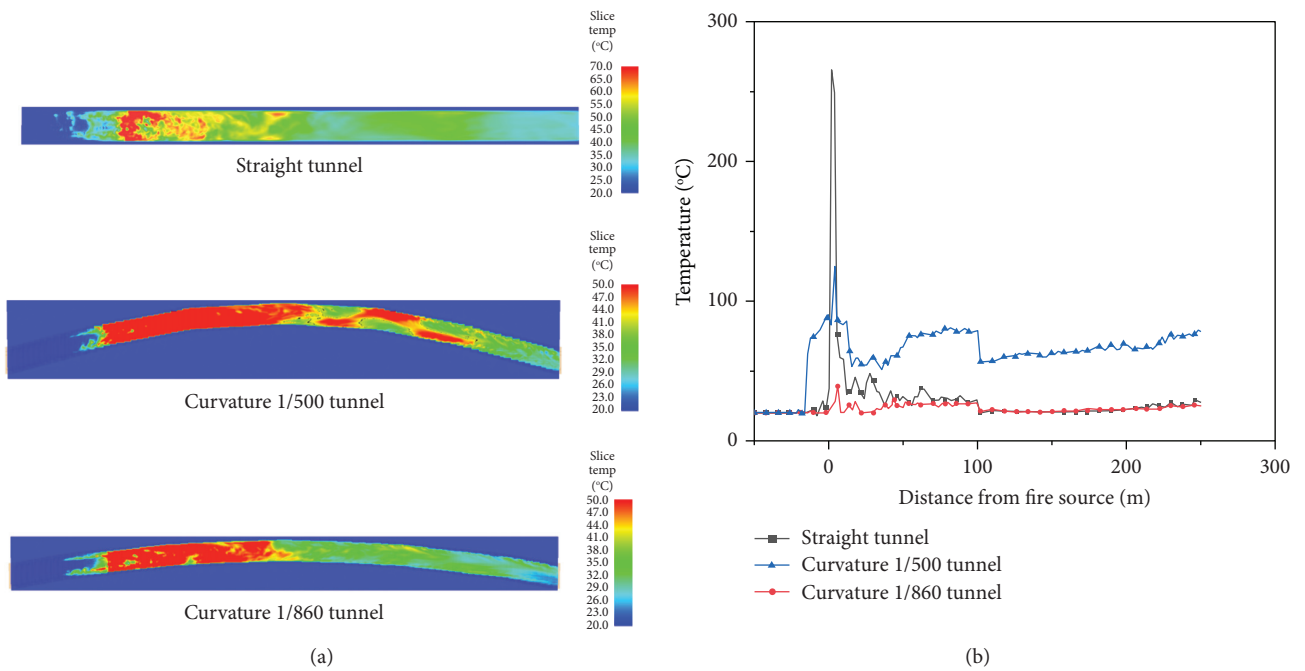


FIGURE 11: Longitudinal distribution of temperature at eye height. (a) Temperature field at the height of the human eye. (b) Temperature curve at eye height of 2 m/s ventilation speed.

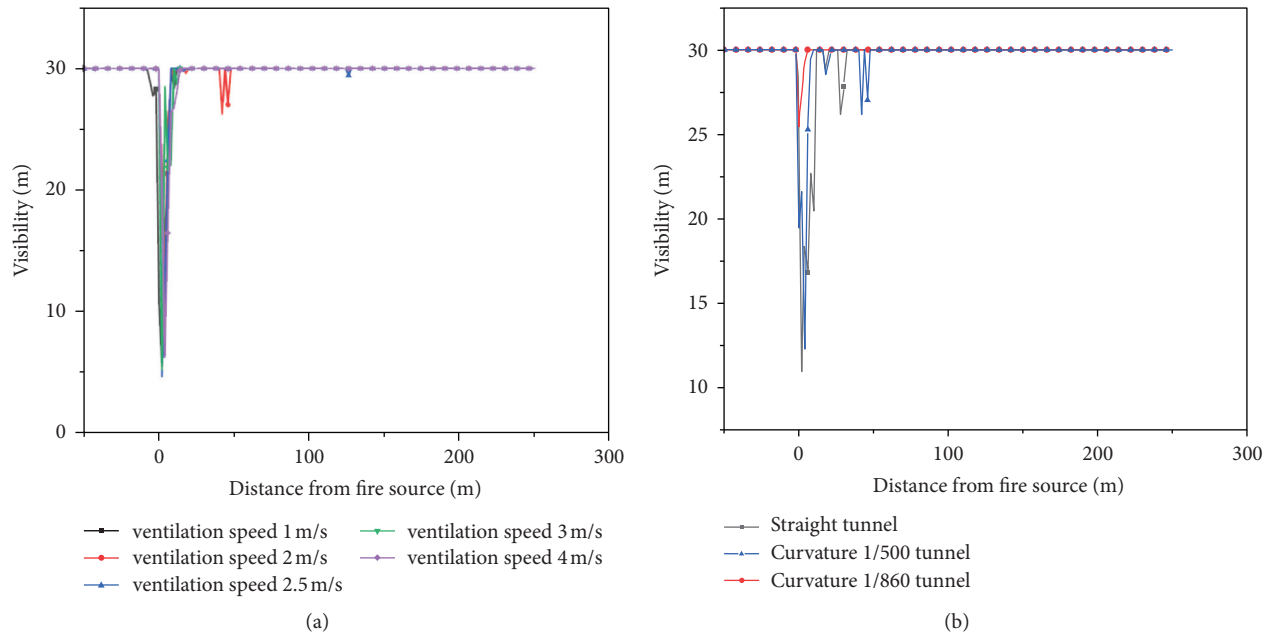


FIGURE 12: Longitudinal distribution of visibility at eye height. (a) Visibility change curve at human eye height under different longitudinal ventilation speeds. (b) Visibility curve at eye height of 2 m/s ventilation speed.

4. Conclusions

The benefit of fire controlling and cooling by water mist in surroundings of a curved tunnel fire is evident and now well analyzed with longitudinal ventilation based on Jinjiazhuang tunnel. A large number of numerical simulations were carried out considering factors of curvature, operation time of longitudinal ventilation system, and longitudinal ventilation speed. The fire extinguishing effects of water mist coupling longitudinal ventilation under different factors were quantitatively analyzed. The conclusions which can be summarized from the study are as follows:

- (1) The simulation result of curvature coupling longitudinal ventilation speed shows that the larger the curvature is, the higher the temperature is and the lower the visibility is, which is not conducive to the safe evacuation of personnel. Under the same curvature, the higher the longitudinal ventilation speed, the lower the temperature in the tunnel. But the high temperature danger zone near the fire source is shorter at ventilation speed of 2 m/s. Therefore, it is suggested that the longitudinal ventilation speed should be 2 m/s when the water mist operates.
- (2) Through comparative analysis of curvature coupling longitudinal ventilation operation time, it can be concluded that the larger the curvature, the more the required fire control time. Under the same curvature, it is recommended to open longitudinal ventilation and water mist simultaneously at 90 s.
- (3) The simulation results for Jinjiazhuang Tunnel with the curve of 1/860 shows that longitudinal ventilation recommended value should be more than 2 m/s for smoke cooling and people evacuation. And, it is

suggested that longitudinal ventilation and water mist system operate at the same time in case of fire.

Data Availability

The data used to support the findings of the study are available from the corresponding author upon request.

Conflicts of Interest

The authors declare that they have no conflicts of interest.

Acknowledgments

This work was financially supported by a grant from the Hebei Provincial Expressway Yan Chong Construction Office (Grant no. YC-201903).

References

- [1] M. Zhong, C. Shi, L. He, J. Shi, C. Liu, and X. Tian, "Smoke development in full-scale sloped long and large curved tunnel fires under natural ventilation," *Applied Thermal Engineering*, vol. 108, pp. 857–865, 2016.
- [2] B. Lou, Q. Rifu, E. Hu, Q. Jiyun, and H. Zhenwen, "Influence of tunnel curvature on smoke spread in a tunnel fire," *Journal of the Chinese Institute of Engineers*, vol. 43, no. 4, pp. 386–396, 2020.
- [3] T. Li and W. Xie, "Numerical simulation study on impact of slope on smoke temperature distribution and smoke spread pattern in curve tunnel fires," *AIP Conference Proceedings*, vol. 1834, pp. 1–11, Article ID 040036, 2017.
- [4] C. Caliendo, P. Ciambelli, M. L. De Guglielmo, M. G. Meo, and P. Russo, "Simulation of fire scenarios due to different vehicle types with and without traffic in a bi-directional road

- tunnel,” *Tunnelling and Underground Space Technology*, vol. 37, pp. 22–36, 2013.
- [5] S. Zhang, H. Yang, Y. Yao et al., “Numerical investigation of back-layering length and critical velocity in curved subway tunnels with different turning radius,” *Fire Technology*, vol. 53, no. 5, pp. 1765–1793, 2017.
- [6] F. Wang, *Research on Key Parameters of Operating Ventilation in Curved Road Tunnels*, Doctor Degree Dissertation, Southwest Jiaotong University, Sichuan, China, 2010.
- [7] W.-Y. Liu, C.-H. Chen, Y.-L. Shu, W.-T. Chen, and C.-M. Shu, “Fire suppression performance of water mist under diverse desmoking and ventilation conditions,” *Process Safety and Environmental Protection*, vol. 133, pp. 230–242, 2020.
- [8] E. Blanchard, P. Boulet, P. Fromy et al., “Experimental and numerical study of the interaction between water mist and fire in an intermediate test tunnel,” *Fire Technology*, vol. 50, no. 3, pp. 565–587, 2014.
- [9] F. Tang, F. Z. Mei, Q. Wang, Z. He, C. G. Fan, and C. F. Tao, “Maximum temperature beneath the ceiling in tunnel fires with combination of ceiling mechanical smoke extraction and longitudinal ventilation,” *Tunnelling and Underground Space Technology*, vol. 68, pp. 231–237, 2017b.
- [10] Q. Li, Z. Tang, Z. Fang, J. Yuan, and J. Wang, “Experimental study of the effectiveness of a water mist segment system in blocking fire-induced smoke and heat in mid-scale tunnel tests,” *Tunnelling and Underground Space Technology*, vol. 88, pp. 237–249, 2019.
- [11] J. P. Garo, J. P. Vantelon, D. Lemonnier, Effect on radiant heat transfer at the surface of a pool fire interacting with a water mist,” *Journal of Heat Transfer*, vol. 133, pp. 1–9, Article ID 023503, 2010.
- [12] Q. Liang, Y. Li, J. Li, H. Xu, and K. Li, “Numerical studies on the smoke control by water mist screens with transverse ventilation in tunnel fires,” *Tunnelling and Underground Space Technology*, vol. 64, pp. 177–183, 2017.
- [13] Y. Cui and J. Liu, “Research progress of water mist fire extinguishing technology and its application in battery fires,” *Process Safety and Environmental Protection*, vol. 149, pp. 559–574, 2021.
- [14] L. Chen, W. Zhu, X. Cai, L. Pan, and G. Liao, “Experimental study of water mist fire suppression in tunnels under longitudinal ventilation,” *Building and Environment*, vol. 44, no. 3, pp. 446–455, 2009.
- [15] W. Zhu, *Simulative Studies on Water Mist Fire Suppression under Longitudinal Ventilation in Long and Narrow Spaces*, University of Science and Technology of China, Hefei, China, 2006.
- [16] Fogtec GmbH&Co.Kg, “Tunnel protection with water mist,” <http://www.fotec.com>.
- [17] J. Sun, Z. Fang, T. Beji, and B. Merci, “Interpretation of flow fields induced by water spray systems in reduced-scale tunnel fire experiments by means of CFD simulations,” *Tunnelling and Underground Space Technology*, vol. 81, pp. 94–102, 2018.
- [18] T. Deng, S. Norris, and R. N. Sharma, “Numerical investigation on the stability of tunnel smoke stratification under the effect of water spray and longitudinal ventilation,” *Tunnelling and Underground Space Technology*, vol. 112, Article ID 103901, 2021.
- [19] Y. F. Li and W. K. Chow, “Study of water droplet behavior in hot air layer in fire extinguishment,” *Fire Technology*, vol. 44, no. 4, pp. 351–381, 2008.
- [20] K. McGrattan, S. Hostikka, J. Floyd et al., *Fire Dynamics Simulator (Version 5)-Technical Reference Guide*, NIST Special Publication 1018-5, National Institute of Standards and Technology, Gaithersburg, MD, 2010.
- [21] P. H. Zhang, F. Rui, W.-b. Xu, and X. L. Tian, “Suppression on the tunnel fire by coupling the longitudinal smoke discharge and high pressure water mist,” *Journal of Northeastern University*, vol. 34, no. 5, pp. 719–722, 2013.
- [22] D. Drysdale, *An Introduction to Fire Dynamics*, pp. 132–138, John Wiley & Sons, United Kingdom, 2011.
- [23] S. L. Hu, *Numerical Simulation Study on Curve Tunnel Fire Ventilation*, Southwest Jiaotong University, Chengdu, Sichuan, China, 2010, in Chinese.

Research Article

Quantitative Characterization of Heterogeneity in Different Reservoir Spaces of Low-Permeability Sandstone Reservoirs and Its Influence on Physical Properties

Fengjuan Dong ^{1,2}, Na Liu,^{3,4} Zhen Sun,⁵ Xiaolong Wei,⁶ Haonan Wang,⁷ Junxiang Nan,^{3,4} and Dazhong Ren^{1,2}

¹Shaanxi Key Laboratory of Advanced Stimulation Technology for Oil & Gas Reservoirs, Xi'an Shiyou University, Xi'an, Shaanxi 710065, China

²College of Petroleum Engineering, Xi'an Shiyou University, Xi'an, Shaanxi 710065, China

³Research Institute of Exploration and Development, PetroChina Changqing Oilfield Company, Xi'an, Shaanxi 710018, China

⁴National Engineering Laboratory for Exploration and Development of Low Permeability Oil and Gas Fields, Xi'an, Shaanxi, 710018, China

⁵The Sixth Natural Gas Plant, PetroChina Changqing Oilfield Company, Yanan, Shaanxi 716000, China

⁶Changqing Downhole Technology Company, PetroChina Chuanqing Drilling Engineering Company Limited, Xi'an, Shaanxi 710018, China

⁷Machine Manufacture Plant Changing Oilfield Company CNPC, Xi'an, Shaanxi 710200, China

Correspondence should be addressed to Fengjuan Dong; dfj_1222@126.com

Received 17 June 2021; Accepted 10 August 2021; Published 21 August 2021

Academic Editor: Xiaohu Zhang

Copyright © 2021 Fengjuan Dong et al. This is an open access article distributed under the Creative Commons Attribution License, which permits unrestricted use, distribution, and reproduction in any medium, provided the original work is properly cited.

The complex pore structure of low-permeability sandstone reservoir makes it difficult to characterize the heterogeneity of pore throat. Taking the reservoir of Sanjianfang formation in QL oilfield as an example, the fractal dimension of different storage spaces is calculated by using fractal theory based on casting thin section, scanning electron microscope, and high-pressure mercury injection, and the correlation between porosity, permeability, and contribution of different storage space permeabilities is analyzed. The results show that the reservoir of Sanjianfang formation in QL oilfield mainly develops small pores, fine pores, and micropores, and the fractal dimension of micropore structure is between 2.6044 and 2.9982, with an average value of 2.8316. The more complex the pore structure is, the stronger the microheterogeneity is. The higher the fractal dimension, the more complex the pore structure and the smaller the porosity and permeability. The fractal dimensions of small pores, fine pores, and micropores increase successively with the decrease in pore radius, and the microstructure heterogeneity of large pores is weaker than that of small pores. It provides a theoretical basis for the exploration and development of low-permeability sandstone reservoirs.

1. Introduction

The pore structure directly controls the reservoir and percolation characteristics and affects the oil/gas production capacity [1]. The pore structure of low-permeability sandstone reservoirs is complex, and the porosity and permeability parameters alone cannot meet the requirements for accurate description and characterization of low-permeability sandstone reservoirs. Therefore, only by studying the

pore structure, can we grasp the accumulation and production rules of reservoir oil and gas from the genetic mechanism and provide technical support for the prediction of high-quality and low-permeability reservoirs and the improvement of oil and gas productivity [2, 3]. Compared with conventional reservoirs, low-permeability sandstone reservoirs are characterized by small pore throat and low dispersion. As a result, pore throat sorting coefficient, mean coefficient, and other parameters cannot accurately reflect

the heterogeneity of micropore structure in low-permeability sandstone reservoirs. In recent years, it is considered that reservoir pores have self-similarity in a certain scale range and belong to fractal structure [4, 5]. The fractal dimension of capillary pressure was used to characterize the complexity of pore structure [6, 7]. A large number of studies have shown that there is obvious heterogeneity of the pore throat structure at the micro/nanometer scale [8–11]. However, there is a lack of quantitative studies on the heterogeneity of pore distribution in porous media, and the mechanism of porous media affected by microscale pore heterogeneity needs to be further understood [12]. Taking the reservoir of Sanjianfang formation in QL oilfield as an example, the fractal dimension of different storage spaces is calculated by using fractal theory based on casting thin section, scanning electron microscope, and high-pressure mercury injection, and the correlation between porosity, permeability, and contribution of different storage space permeabilities is analyzed. It provides theoretical basis for the exploration and development of low permeability sandstone reservoirs.

2. Methods

2.1. Test Method. A 2.5 cm diameter plunger sample is drilled from the core for use in wafer grinding, physical properties, and high-pressure mercury pressure tests.

① Before testing, wash the sample with oil:

The sample was washed with methanol and dichloromethane mixture in the Soxhlet extractor. When the fluorescence of the washing fluid was very low and unchanged, the washing oil was considered to be finished, and the sample was dried continuously by microwave at 100°C for 24 h.

② Casting sheet observation:

After the treatment, the samples were injected into the red casting body, and the thin slices with a thickness of 0.03 mm were ground. Under the polarized light microscope, the statistics and study of petrology and pores were carried out by the point-meter method (300 points were counted for each sample). The experimental methods were strictly carried out in accordance with SY/T 5913–2004 “Rock thin section preparation” [13].

(iv) Petro physical tests:

The experimental methods were strictly carried out in accordance with SY/T6385-1999 “Test method for porosity and permeability of overburden rocks” [14]. FYKS-1 porosity-permeability tester with high temperature and overburden pressure has tested the porosity and permeability. The main technical parameters are as follows: ① the effective pressure of simulated formation is less than 70 MPa; ② the effective temperature of simulated formation is less than 150°C; ③ applicable core is $\Phi 25 \times 25\text{--}80$ mm or $\Phi 38 \times 40\text{--}80$ mm; and ④ measurement precision of permeability is less than 10% for low-permeability

reservoir and is less than 5% for middle and high permeability reservoir; measurement precision of porosity is 0.5%.

(v) High-pressure mercury injection experiment:

The AutoPore IV mercury injection test was conducted under the conditions of 22°C room temperature, 46% to 68% relative humidity, and 0.49 N/m interfacial tension of mercury. The experimental method was strictly carried out in accordance with GB/T29171-2012 “Rock capillary pressure measurement” [15].

2.2. Fractal Theory. Fractal theory was founded in the mid-1970s, and its research object is the disordered and self-similar system widely existing in nature and social activities [16, 17]. Fractal dimension is a reflection of the ability of fractal to fill the embedded space, and most fractal dimensions are fractions. By combining fractal theory with the Laplace equation, the relationship between cumulative pore volume and capillary pressure can be obtained as follows:

$$S_{Hg} = 1 - \left(\frac{P_c}{P_{\min}} \right)^{D-3}, \quad (1)$$

where S_{Hg} is the volume of mercury entering the pores, %, and P_{\min} is the capillary pressure corresponding to the maximum pore throat radius, namely, the mercury inlet pressure, MPa.

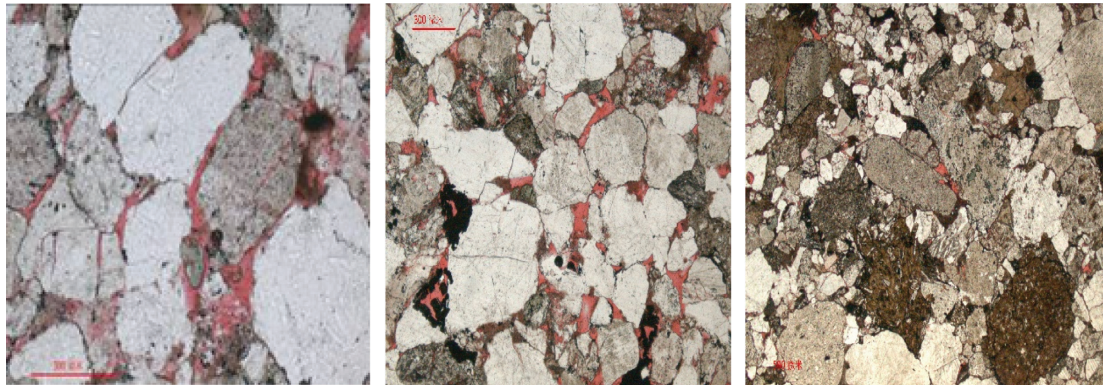
Take the logarithm of both sides of equation (1) to get the following:

$$\lg(1 - S_{Hg}) = (D - 3)\lg P_c - (D - 3)\lg P_{\min}. \quad (2)$$

According to equation (2), the pressure-cumulative mercury intake curve can be drawn, and the fractal dimension (D) can be obtained.

3. Pore Types and Physical Properties of Reservoir

To ensure the representativeness of experimental samples, the selection of rock samples is based on the principle of controlling the whole area, covering reservoirs with different physical properties and selecting more main gas-producing reservoirs. Through the casting thin section analysis and research on the samples taken from the reservoir of Sanjianfang formation in QL oilfield, it is concluded that the main developed reservoir spaces are intergranular pores (63.7%), feldspar dissolution pores (15.4%), cuttings dissolution pores (12.5%), microfractures (6.1%), intercrystalline pores (0.23%), and so on. According to the analysis of reservoir physical properties and pore throat capillary pressure curves, the porosity distribution range of selected rock samples is from 11.6% to 16.7%, the average value is 13.14%, the permeability distribution range is from $0.395 \times 10^{-3} \mu\text{m}^2$ to $87.695 \times 10^{-3} \mu\text{m}^2$, and the average value is $27.513 \times 10^{-3} \mu\text{m}^2$. The selected rock samples represent three types of reservoirs with different permeability levels, as shown in Figure 1. The value radius is more than $2.0 \mu\text{m}$, and



Reservoirs with permeability greater than $50 \times 10^{-3} \mu\text{m}^2$, Sample No.10, 2567.0m, Development of micro fractures, intergranular pores, dissolved pores

Reservoirs with permeability between $10 \times 10^{-3} \mu\text{m}^2$ and $50 \times 10^{-3} \mu\text{m}^2$, Sample No.5, 2480m, Development of dissolution pores, intergranular pores and micro pores

Reservoirs with permeability between $0.1 \times 10^{-3} \mu\text{m}^2$ and $10 \times 10^{-3} \mu\text{m}^2$ Sample No.3, 2712.0m, Development of micro pores and dissolution pores

FIGURE 1: Reservoir spatial characteristics of reservoirs with different permeabilities.

the storage space is mainly composed of microcracks, intergranular pores, and dissolved pores in the reservoirs with permeability greater than $50 \times 10^{-3} \mu\text{m}^2$. The value radius is between $0.5 \mu\text{m}$ and $2.0 \mu\text{m}$, and the storage space is mainly composed of dissolved pores, a few intergranular pores, and micropores in the reservoirs with permeability between $10 \times 10^{-3} \mu\text{m}^2$ and $50 \times 10^{-3} \mu\text{m}^2$. The value radius is between $0.05 \mu\text{m}$ and $0.5 \mu\text{m}$, and the storage space is mainly composed of micropores, a small number of corrosion holes in the reservoirs with permeability between $0.1 \times 10^{-3} \mu\text{m}^2$ and $10 \times 10^{-3} \mu\text{m}^2$.

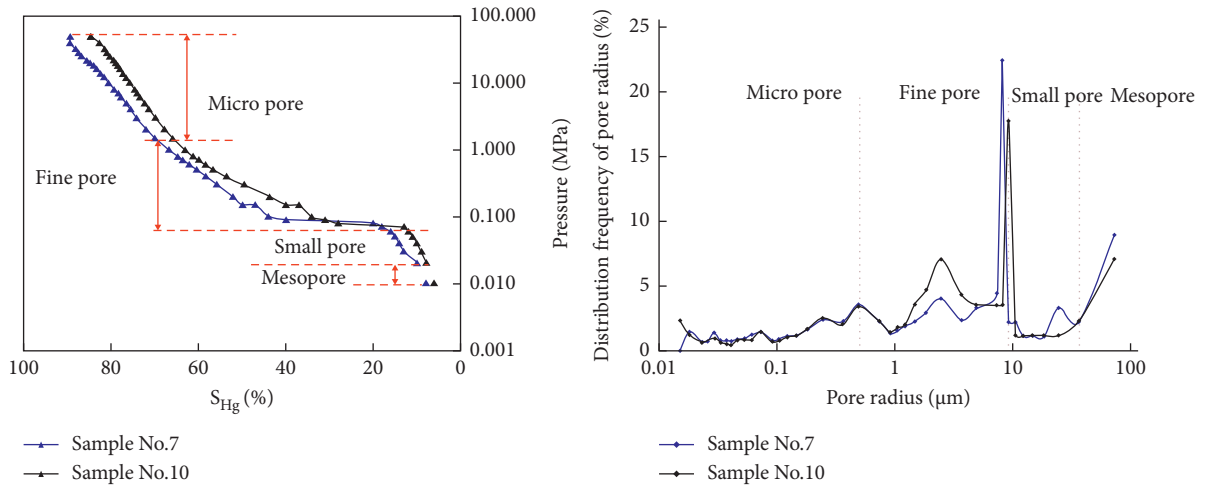
4. Quantitative Characterization of Heterogeneity in Different Reservoir Spaces Based on Fractal Theory

Based on the analysis and test results of ten rock samples of Sanjianfang formation in QL oilfield, the heterogeneity of different reservoir spaces is analyzed and studied by using fractal theory.

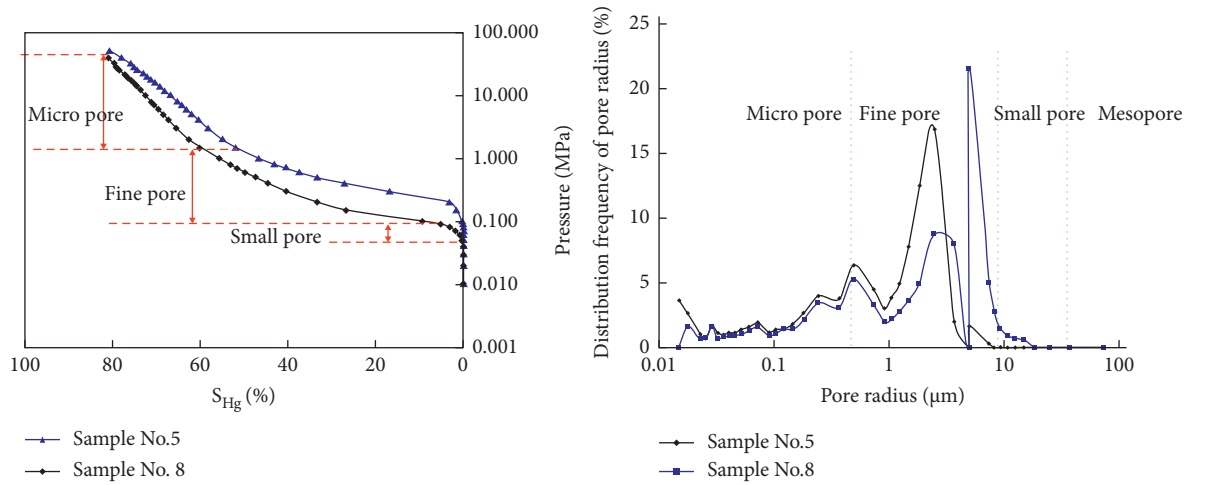
4.1. Characteristics of Capillary Pressure Curves in Different Types of Reservoirs. The permeability of reservoir space composed of different types of pores varies greatly, which leads to significant differences in capillary pressure curves and pore distribution characteristics (Figure 2). In recent years, domestic and foreign scholars usually divide the pores into micropores (0 nm to 2 nm), mesopores (2 nm to 50 nm), and macropores (more than 50 nm) according to their diameters [18]. However, the classification scheme is mainly applicable to shale gas reservoirs. For low-permeability sandstone reservoirs, since the molecular diameter of oil is much larger than that of gas, the pore diameter of this classification scheme is too small to be applicable. Therefore, a new classification scheme is needed to low-permeability sandstone reservoirs.

Through the analysis of the experimental results of mercury injection in ten low-permeability sandstone samples (Figure 2) [19], it can be found that there are three turning points in the mercury injection curve, and the connected pores are divided into four different scales, namely, micropores, fine pores, small pores, and mesopores. In the mercury injection curve, the three turning points occur around the pore radius of $1.0 \mu\text{m}$, $10.0 \mu\text{m}$, and $50.0 \mu\text{m}$, respectively, and the corresponding pressures are 1.0 MPa, 0.08 MPa, and 0.02 MPa, respectively. Figure 2 shows the level of the three kinds of different permeability sandstone samples in mercury porosity distribution with different scales and frequency curve features. Reservoirs with permeability greater than $50 \times 10^{-3} \mu\text{m}^2$ mainly develop intergranular pores but also develop a few microfractures, with mesopores, thick throat, and good connectivity. The discharge pressure is low, and the mercury injection curve is obvious “horizontal platform” in the process of mercury injection. The proportion of mesopore, small pore, fine pore, and micropore in this kind of reservoir is 8.02%, 9.73%, 56.88%, and 25.37%, respectively. Reservoirs with permeability between $10 \times 10^{-3} \mu\text{m}^2$ and $50 \times 10^{-3} \mu\text{m}^2$ mainly develop intergranular pores and dissolution pores, which strengthen the connectivity between pores. The displacement pressure is medium, and the mercury injection curve is weak “horizontal platform” in the process of mercury injection. This kind of reservoir is mainly composed of fine pores and micropores with a few small pores, accounting for 63.06%, 35.64%, and 1.3%, respectively. Reservoirs with permeability between $0.1 \times 10^{-3} \mu\text{m}^2$ and $10 \times 10^{-3} \mu\text{m}^2$ mainly develop micropores and a few dissolved pores, with narrow pores and often open “dead end pores” at one end [20], which contribute little to the permeability, and the discharge pressure is high, and the curve of mercury injection is steep in the process of mercury injection. This kind of reservoir is mainly composed of fine pores and micropores, accounting for 39.16% and 60.84%, respectively.

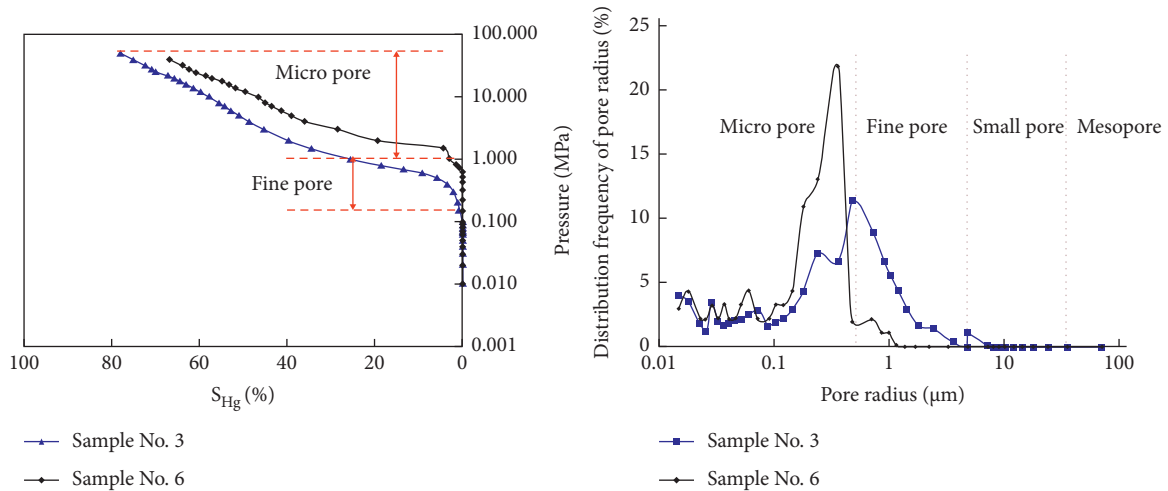
On the whole, as the permeability decreases, the main peak of pore throat distribution shifts to the left, the



Reservoirs with permeability greater than $50 \times 10^{-3} \mu\text{m}^2$



Reservoirs with permeability between $10 \times 10^{-3} \mu\text{m}^2$ and $50 \times 10^{-3} \mu\text{m}^2$



Reservoirs with permeability between $0.1 \times 10^{-3} \mu\text{m}^2$ and $10 \times 10^{-3} \mu\text{m}^2$

FIGURE 2: Capillary pressure curves and pore distribution characteristics of different types of reservoirs.

TABLE 1: Proportions and fractal dimensions of different pores.

Pore of different scales	Proportion (%)	Fractal dimension
Small pore	3.74	2.8109
Fine pore	45.595	2.8211
Micropore	49.295	2.8504

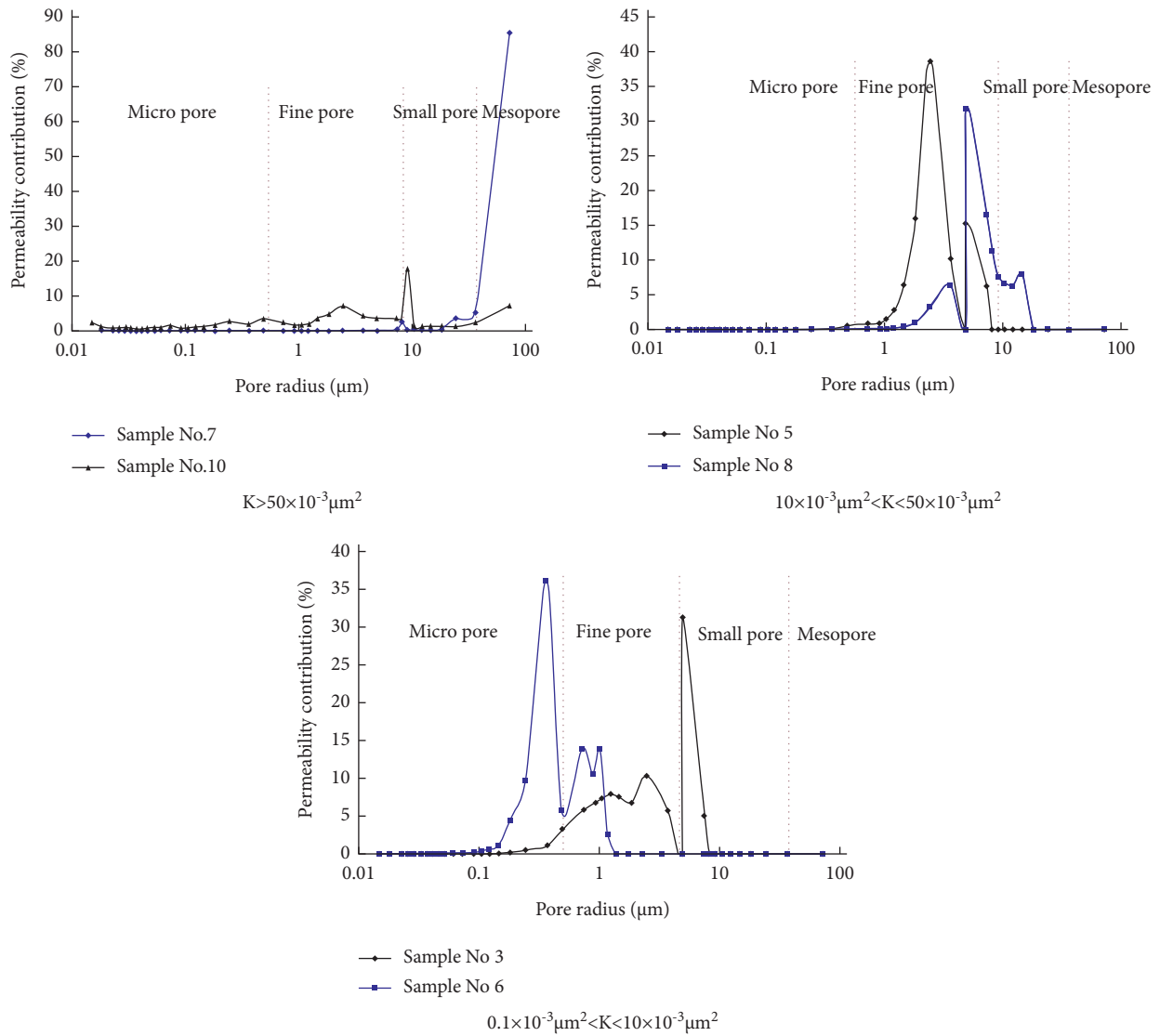


FIGURE 3: The permeability contribution of different pores.

distribution becomes narrower, and the morphological fluctuation of tail peak increases, which indicates that the distribution of pore throat is complex and highly heterogeneous, and various types of pore throat exist in low-permeability sandstone reservoirs [21, 22].

4.2. Quantitative Characterization of Heterogeneity in Different Storage Spaces. Fractal theory is generally used to study irregular shapes with complex structure and self-similarity, which is represented by fractal dimension. For low-permeability sandstone reservoirs, the pores are only in

a certain scale range, and the pore structure has fractal characteristics [23]. There are only two samples with macropores, and the distribution frequency of macropores is low, accounting for only 1.37%. Therefore, macropores are not considered in this study. By statistics and analysis of the fractal dimensions of pores of different scales in ten sandstone samples, it can be seen that the fractal dimensions of small pores, fine pores, and microholes increase successively. Among them, the fractal dimension of small pores is from 2.8454 to 2.9969, with an average of 2.8109. The fractal dimension of fine pores is from 2.2044 to 2.9982, with an average of 2.8211. And the structure of micropores is relatively

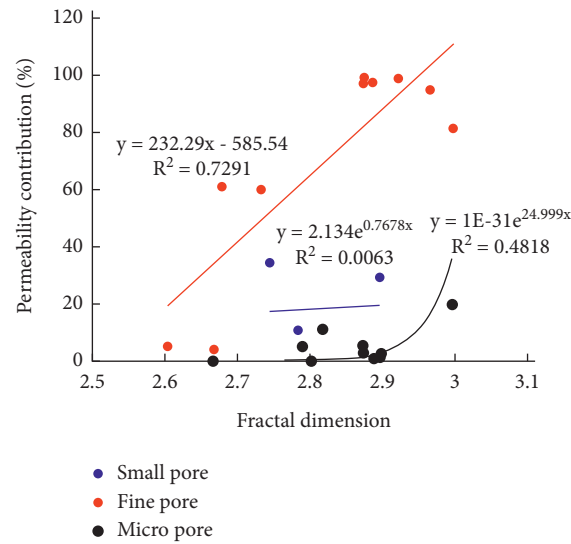


FIGURE 4: The relationship between permeability contribution and fractal dimension of different pores.

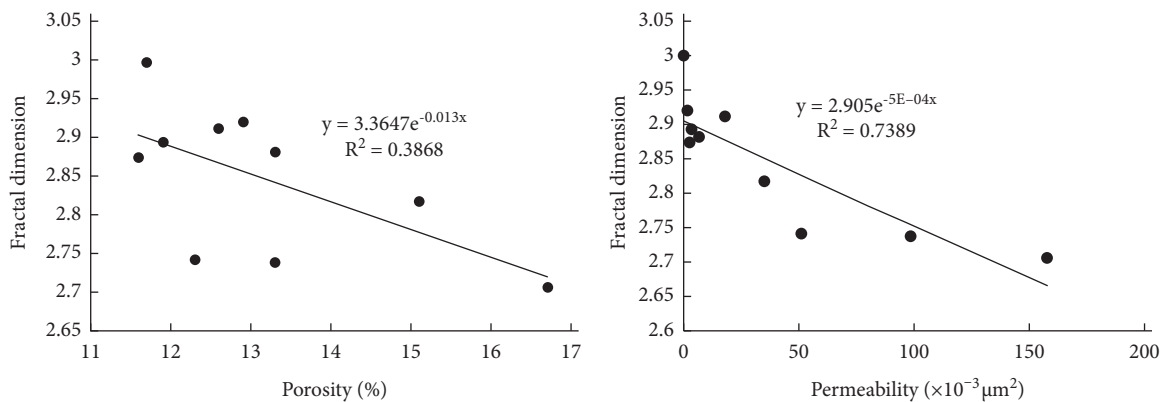


FIGURE 5: Relationship between reservoir properties and fractal dimension.

homogeneous, and the fractal dimension is from 2.666 to 2.9961, with an average of 2.8504. According to statistics on the relationship between the proportion of pores in different scales and the fractal dimension (Table 1), the proportion of small pores, fine pores, and micropores develop in the reservoir of the Sanjianfang formation in the study area increases successively and the fractal dimension increases which agrees with the fact that the pore structure is more complex and heterogeneous in the small pore development zone than in the large pore development zone [24, 25].

5. Effects of Different Reservoir Space Heterogeneities on Reservoir Physical Properties

5.1. Permeability Contribution of Different Reservoir Spaces. The size and distribution of pore throat are the key factors to control the properties of low-permeability sandstone reservoirs. For low-permeability sandstone reservoirs with different permeabilities, a small number of relative macropores develop to control the permeability, but relatively small pores have little

effect on permeability (Figure 3). However, the contribution of relatively small pores to the reservoir property of low-permeability sandstone reservoirs cannot be ignored. For example, the maximum Hg saturation of sample no. 10 is 84.59%. Under the control of mesopores and small pores, the permeability contribution rate reaches 95.1%, but cumulative Hg saturation is only 13.1%. Relatively small pores and micropores control the mercury saturation of 71.49%, and the cumulative mercury saturation of micropores reaches 21.45%.

5.2. Influence of Spatial Heterogeneity of Different Reservoirs on Permeability Contribution. By analyzing the relationship between the permeability contribution of pores at different scales and the fractal dimension (Figure 4), it can be found that the permeability contribution of small pores, fine pores, and micropores is positively correlated with the fractal dimension, and the correlation coefficient (R^2) is 0.0051, 0.7291, and 0.4818, respectively. That is to say, the positive correlation between permeability contribution of fine pores and micropores and fractal dimension is better than that of small pores. The main reason may be that the dissolution

pores and intercrystalline pores develop in the fine pores and micropores scale interval, whose irregular shape makes the heterogeneity of pore structure stronger but may form dominant channels that play a leading role in fluid flow and have good seepage characteristics. A small number of solution holes develop in the small pore size interval which enhance the microscopic heterogeneity but are not the main controlling factor of dominant seepage channel.

5.3. *Effects of Reservoir Heterogeneity on Physical Properties.* By analyzing the relationship between porosity, permeability, and fractal dimension of pore structure (Figure 5), it is found that the reservoir physical property is negatively correlated with the fractal dimension. The larger the fractal dimension is, the more complex the pore structure is and the smaller the porosity and permeability are. There is no significant linear correlation between porosity and fractal dimension, and the correlation coefficient (R^2) is only 0.3868. However, the negative correlation between permeability and fractal dimension is obvious, and the correlation coefficient (R^2) is 0.7847.

6. Conclusion and Understanding

- (1) Micropore structure of low-permeability sandstone reservoirs has fractal characteristics, and its heterogeneity can be characterized by fractal theory. The fractal dimension of micropore structure of Sanjianfang formation in QL oilfield is between 2.6044 and 2.9982, and the average value is 2.8316. The more complex the pore structure is, the stronger the microheterogeneity is.
- (2) Pore as the main reservoir space, the distribution characteristics of microheterogeneity at different scales can reflect the variation of reservoir space. The fractal dimensions of small pores, fine pores, and micropores increase successively with the decrease in pore radius, and the microstructure heterogeneity of large pores is weaker than that of small pores.
- (3) Microscale heterogeneity is the key factor to determine the physical property and percolation mechanism of low-permeability sandstone reservoirs. The higher the fractal dimension, the more complex the pore structure and the smaller the porosity and permeability. The irregular shape of dissolution pores and intercrystalline pores develops in the fine pores and micropores scales which makes the heterogeneity of pore structure stronger but may form dominant channels, play a leading role in fluid flow, and show good seepage characteristics. A small number of solution holes develop in the small pore size interval that enhance the microscopic heterogeneity but are not the main controlling factor of dominant seepage channel. As a result, the positive correlation between permeability contribution of fine pores and micropores and the fractal dimension is better than that of small pores.

Data Availability

The data supporting the results of our study are included within the manuscript.

Conflicts of Interest

The authors declare that they have no conflicts of interest.

Acknowledgments

This work was financially supported by the National Natural Science Foundation of China (41802166), Shaanxi Provincial Key Research and Development Program (2021GY-140), Opening Foundation of Shaanxi Key Laboratory of Advanced Stimulation Technology for Oil and Gas Reservoirs (20JS120), and Open Foundation of Key Laboratory of Coal Resources Exploration and Comprehensive Utilization, Ministry of Natural Resources (KF2021-3).

References

- [1] Z. T. Luo and Y. C. Wang, *The Pore Structure of Reservoir*, Science Press, Beijing, China, 1986.
- [2] Y. N. Qiu and S. H. Xue, *Appraisal Technology of Hydrocarbon Reservoirs*, Petroleum Industry Press, Beijing, China, 1997.
- [3] P. Luo, Y. N. Qiu, A. L. Jia, and X. S. Wang, "The present challenges of Chinese petroleum reservoir geology and research direction," *Acta Sedimentologica Sinica*, vol. 21, no. 1, pp. 142–147, 2003.
- [4] K. W. Li and R. N. Home, "Fractal modeling of capillary pressure curves for the geysers rocks," *Geothermics*, vol. 35, no. 2, pp. 198–207, 2006.
- [5] P. Li, M. Zheng, B. He, S. Wu, and X. Wang, "Pore throat structure and fractal characteristics of tight oil sandstone: a case study in the Ordos Basin, China," *Journal of Petroleum Science and Engineering*, vol. 149, pp. 1–10, 2016.
- [6] S. H. Xue and S. P. Wang, "Fractal feature about the microstructure in sandstone reservoir: taking the paleogene shahejie formation in shengtuo oilfield as an example," *Natural Gas Geoscience*, vol. 24, pp. 886–893, 2013.
- [7] L. Q. Zhang, Y. L. Ji, W. J. Ma, and H. Zhang, "Characteristics of fractional geometry and reservoir evaluation of fore mountain belt at begedashan," *Journal of the University of Petroleum, China*, vol. 22, no. 5, pp. 31–33, 1998.
- [8] Y. Wang, W. K. Feng, R. L. Hu, and C. H. Li, "Fracture evolution and energy characteristics during marble failure under triaxial fatigue cyclic and confining pressure unloading (FC-CPU) conditions," *Rock Mechanics and Rock Engineering*, vol. 54, no. 2, pp. 799–818, 2021.
- [9] Z. Zhu, M. C. He, M. Karakus, X. H. Zhang, and Z. Guo, "The collision experiment between rolling stones of different shapes and protective cushion in open-pit mines," *Journal of Mountain Science*, vol. 8, no. 5, pp. 1391–1403, 2021.
- [10] F. Wu, R. Gao, J. Liu, and C. Li, "New fractional variable-order creep model with short memory," *Applied Mathematics and Computation*, vol. 380, Article ID 125278, 2020.
- [11] F. Wu, H. Zhang, Q. Zou, C. Li, J. Chen, and R. Gao, "Viscoelastic-plastic damage creep model for salt rock based on fractional derivative theory," *Mechanics of Materials*, vol. 150, Article ID 103600, 2020.
- [12] Q. X. Meng, W. Y. Xu, H. L. Wang, X. Y. Zhuang, W. C. Xie, and T. Rabczuk, "DigiSim - an open source software package

- for heterogeneous material modeling based on digital image processing,” *Advances in Engineering Software*, vol. 148, Article ID 102836, 2020.
- [13] National Development and Reform Commission, *Rock Thin Section Preparation: SY/T 5913-2004*, Petroleum industry press, Beijing, China, 2004.
- [14] State Bureau of Petroleum and Chemical Industry, *The Porosity and Permeability Measurement of Core in Net Confining Stress: SY/T6385-1999*, Petroleum industry press, Beijing, China, 1999.
- [15] Standardization Administration of China, *Rock Capillary Pressure Measurement: GB/T29171-2012*, Petroleum industry press, Beijing, China, 2012.
- [16] R. F. Angulo, V. Alvarado, and H. Gonzalez, “Fractal dimensions from mercury intrusion capillary tests,” in *Proceedings of the SPE-23695, Society of Petroleum Engineering Conference*, pp. 255–264, Caracas, Venezuela, March 1992.
- [17] W. I. Friesen and R. J. Mikula, “Fractal dimensions of coal particles,” *Journal of Colloid and Interface Science*, vol. 20, no. 1, pp. 263–271, 1987.
- [18] D. H. Everett, “Manual of symbols and terminology for physicochemical quantities and units, appendixII: definitions, terminology and symbols in colloid and surface chemistry,” *Pure and Applied Chemistry*, vol. 31, no. 4, p. 558, 1972.
- [19] F. J. Dong, *A Study on Reservoir Evaluation and Oil-Water Distribution at Water Cut Stage: A Case from Sanjianfang Formation of Qiuling Oilfield*, Northwest University, Xi’an, China, 2010.
- [20] S. Y. Xu and H. N. Li, “Evolvement of reservoir pore-throatnet and remaining oil distribution,” *Acta Petrolei Sinica*, vol. 24, no. 4, pp. 48–53, 2003.
- [21] K. L. Xi, Y. C. Cao, B. G. Haile et al., “How does the pore-throat size control the reservoir quality and oiliness of tight sandstones? The case of lower Cretaceous Quantou Formation in the southern Songliao Basin, China,” *Marine and Petroleum Geology*, vol. 76, pp. 263–271, 2016.
- [22] Y. B. Yao, D. M. Liu, Y. Che, D. Z. Tang, S. H. Tang, and W. H. Huang, “Petrophysical characterization of coals by low-field nuclear magnetic resonance (NMR),” *Fuel*, vol. 89, no. 7, pp. 1371–1380, 2010.
- [23] K. Li, “More general capillary pressure and relative permeability models from fractal geometry,” *Journal of Contaminant Hydrology*, vol. 111, no. 1-4, pp. 13–24, 2010.
- [24] Y. H. Guo and D. F. Zhao, “Analysis of micro-scale heterogeneity characteristics in marine shale gas reservoir,” *Journal of China University of Mining & Technology*, vol. 44, no. 2, pp. 300–307, 2015.
- [25] J. J. Li, Y. Liu, Y. J. Gao, B. Y. Cheng, F. L. Meng, and H. M. Xu, “Effects of microscopic pore structure heterogeneity on the distribution and morphology of remaining oil,” *Petroleum Exploration and Development*, vol. 45, no. 6, pp. 1043–1052, 2018.

Research Article

Experimental Study on the Influence of Freezing Pressure on the Uniaxial Mechanical Properties of Ice

Baosheng Wang ^{1,2}, Weihao Yang,² Peixin Sun,² Xin Huang ², Yaodan Zhang,³ and Fengjun Chen¹

¹Shanghai Construction Group Co., Ltd., Shanghai 200080, China

²State Key Laboratory for Geomechanics and Deep Underground Engineering, China University of Mining and Technology, Xuzhou 221116, China

³State Key Laboratory of Coastal and Offshore Engineering, Dalian University of Technology, Dalian 116024, China

Correspondence should be addressed to Baosheng Wang; wangbs@scg.cn

Received 15 July 2021; Accepted 9 August 2021; Published 20 August 2021

Academic Editor: Xiaohu Zhang

Copyright © 2021 Baosheng Wang et al. This is an open access article distributed under the Creative Commons Attribution License, which permits unrestricted use, distribution, and reproduction in any medium, provided the original work is properly cited.

In this study, a test technique that enables continuous control of the sample stress state from freezing to testing is proposed to investigate the influence of freezing pressure on the mechanical properties of ice under uniaxial compression. In this method, the water is frozen into the standard cylindrical ice specimen under high hydraulic pressure in a triaxial pressure chamber, and then, the temperature field and stress field of the ice specimens are adjusted to the initial state of the test; finally, an in situ mechanical test is conducted in the triaxial chamber. The uniaxial compression test of ice specimens with temperature of -20°C and freezing pressure of 0.5–30 MPa is performed in the strain rate range of 5×10^{-5} – $1.5 \times 10^{-6} \text{ s}^{-1}$. The results show that, as the freezing pressure increases, the ductile-to-brittle transition zone of the ice specimen during failure moves to the low strain rate range, and the failure mode of the specimen changes from shear failure to splitting failure. Further, the brittleness index of the ice specimen first increases, then decreases, and then again increases with the increase in freezing pressure. The brittleness index reaches the maximum (minimum) when the freezing pressure is 30 MPa (20 MPa). The peak stress of the ice specimen also increases first, then decreases, and then increases with the increase in freezing pressure. The maximum value is also at the freezing pressure of 30 MPa, but the minimum value is obtained at the freezing pressure of 0.5 MPa. The failure strain of the ice specimen first decreases and then increases with the increase in freezing pressure, and the maximum (minimum) value is achieved at the freezing pressure of 0.5 MPa (10 MPa). When the ice specimen exhibits brittle failure, the relationships between the residual stress and the freezing pressure and between the peak stress and freezing pressure are the same, but when the ice specimen exhibits ductile failure, there is no obvious relationship between the residual stress and the freezing pressure.

1. Introduction

Artificial ground freezing method is the most important construction method to stabilize the ground and prevent groundwater ingress during excavation. It allows the penetration of deep, unstable, and water-bearing strata containing sands, silts, and clays. Presently, the depth of artificially frozen topsoil and water-rich strata has reached 750 m [1] and 950 m [2], respectively. The measured data show that the static [3] and dynamic [4] mechanical responses of deep frozen wall are quite different from the

theoretical expectations due to the lack of understanding of the formation mechanism of deep frozen soil and rock mass. At present, the deepest proven natural permafrost layer is more than 1 km deep [5]. Due to the influence of high pressure in the deep environment, there are still many difficulties in drilling and coring in deep permafrost layer [6]. To solve these problems, the mechanical properties of deep frozen soil [7–9] and frozen rock [10, 11] have been experimentally investigated, but the research on the coupling problems of ice-soil and ice-rock, which are based on the mechanical properties of deep-environment ice, is not

mature. Compared with the shallow layer conditions, the deep formation pressure increases significantly [12–14], and the freezing pressure of the deep groundwater can exceed 10 MPa due to the high pressure and the limit on the formation of frost heaving. Therefore, it is of great significance to examine the influence of freezing pressure on the mechanical properties of ice.

Vostok subglacial lake in Antarctica is the deepest lake on the Earth. The thickness of the overlying ice sheet is nearly 4 km [15]. Due to its long history and complete isolation from the outside world, the water of this lake water has significant research value. To obtain lake water specimens, a Russian research team has started the drilling project of huge thick ice sheet since the beginning of this century. However, due to the lack of understanding of the mechanical response of the bottom ice layer, sudden lake water gushing frequently occurs while drilling the bottom of the ice sheet, which brings great difficulties to the sampling process [16]. Isotopic studies have shown that the bottom ice layer is frozen by the high-pressure lake water [17]. Therefore, revealing the mechanical properties of ice frozen at high pressure can boost the applications of drilling technology of thick ice sheet. In addition, there is a high-pressure freezing phenomenon in hydrous exoplanets. For example, the liquid water of Europa is stored under a 150 km thick ice shell, and the high-pressure water is constantly frozen into ice at the bottom of the ice shell [18]. As the observation of ice shell rheology is one of the principal means to explore the extraterrestrial liquid water resources, whether freezing pressure affects the rheological characteristics of ice is worth to be studied.

The uniaxial compression test is a simple method that has been widely used to study the mechanical properties of ice. Using this test, the enhancement effect of negative temperature on the ice strength [19, 20] and stiffness [21, 22], the influence of the loading rate on the failure characteristics [23, 24] and its mechanism [25, 26], and the ductile-brittle transition of ice failure under different conditions [27, 28] have been investigated. However, the ice used in the above studies was frozen without any pressure. There are few reports on mechanical properties of ice frozen under pressure. Furthermore, in the existing technique to form ice by freezing pure water, the water is slowly and unidirectionally frozen to form a large ice body by controlling the heat flow gradient in a large volume, low temperature tank [29–31], and then, the core is taken and processed into a cylindrical ice specimen. This method can realize pressure freezing by improving the equipment, but the ice specimen needs pressure relief, drilling, and grinding. In this process, the stress state of the ice specimen is uncontrollable, and nonideal condition such as instantaneous removal of freezing pressure will inevitably be produced, leading to microcracks and other defects in the ice specimen [32], which cannot fully reflect the effect of pressure freezing.

To address the above issues, in this study, an effective method is proposed to freeze the cylindrical water specimen in a triaxial pressure chamber to form a standard cylindrical ice specimen. Then, the temperature field and stress field of the ice specimen are adjusted to the initial condition of the

test, and the in situ mechanical test is performed to realize the continuous control of the stress state of the specimen during the entire process of freezing and testing. The proposed method is used to prepare ice specimens with freezing pressure from 0.5 MPa to 30 MPa, and uniaxial compression tests are conducted at a constant strain rate and temperature of -20°C . Furthermore, the effects of freezing pressure on the constitutive laws and strength characteristics of the ice specimens are investigated.

2. Experimental Method

2.1. Testing Equipment. The test method prepared in this study is based on the in situ test method of high-pressure frozen geotechnical materials. The entire process of pressure freezing and mechanical test is conducted in a triaxial pressure chamber. The experimental equipment is TAS-LF400 low-temperature triaxial system, which is jointly developed by China University of Mining and Technology and Xi'an KTL Instruments Co., Ltd., as shown in Figure 1. The ultimate axial force of the loading frame is 400 kN, the maximum confining pressure of the pressure/volume controller is 64 MPa, and the control accuracy is 0.05%. The temperature field of the specimen is controlled by the three circulation channels at the top, side, and bottom of the triaxial pressure chamber and the constant, low-temperature circulation grooves A, B, and C connected with them, respectively. The minimum temperature is 60°C , and the temperature control accuracy is 0.1°C . Two lead holes are arranged on the side wall of the pressure chamber to install the sealed lead connector of the sensor.

2.2. Preparation Technique of Ice Specimens

2.2.1. Freezing Process. The ice specimen was prepared by freezing the cylindrical water specimen in the triaxial pressure chamber [33]. The size of the water specimen was $\Phi 61.8 \times 114.7 \text{ mm}^2$. Using the control technology, the freezing expanded by 9% [34] would be forced to develop along the height direction, and the ice specimen with the target size of $\Phi 61.8 \times 125 \text{ mm}^2$ was obtained. The controlled freezing process was divided into two stages: specimen pressurization and stable pressure freezing. During the pressurization, the height of the water specimen was kept constant by the load frame to avoid concave folds due to axial compression, and the confining pressure was increased to the target pressure value by the pressure volume controller. In the period of stable pressure freezing, the quantity of the confining medium in the triaxial chamber was locked by the pressure volume controller to force the freezing expansion to develop along the height direction of the specimen, and the specimen pressure is then controlled by the load frame, which is set to apply a constant axial pressure. The water specimen froze in a gradient temperature field of cold in the lower and hot in the upper generated by circulation thermostats A and C. The radial deformation of the specimen is restricted by the stable volume of the confining medium, and the freezing expansion develops along the height direction as the expansion pressure releases.

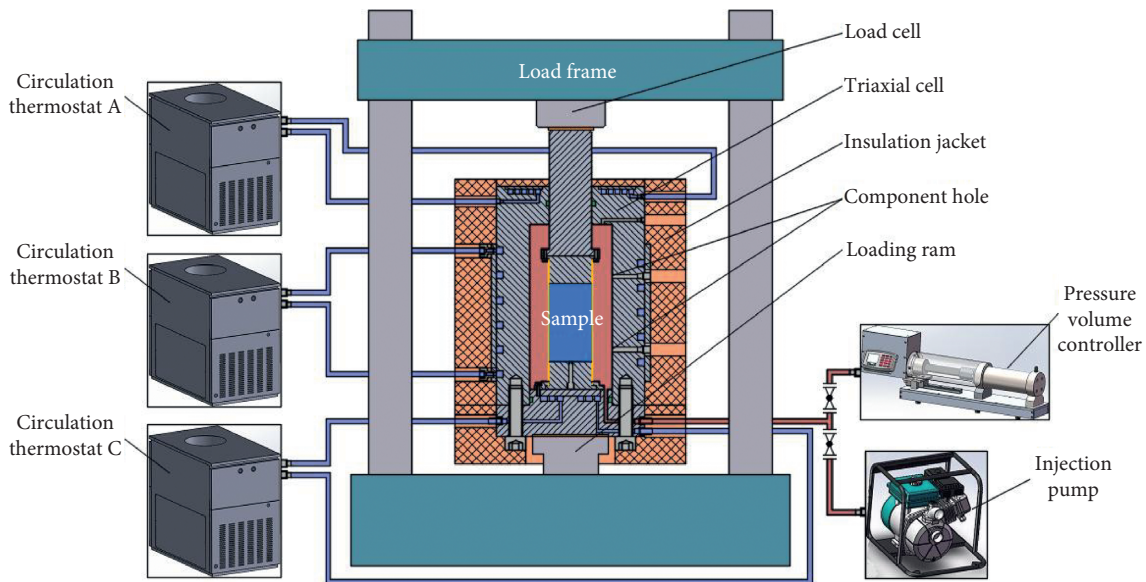


FIGURE 1: Sketch of the TAS-LF400 low-temperature triaxial testing system.

The ice specimen after freezing is shown in Figure 2. The diameter is measured three times from the bottom of the ice specimen along the upward axis, and each measurement is taken along the specimen's circumferential interval of 120° (Figure 3(a)). The measurement results (Figure 3(b)) indicate that the maximum and minimum diameters of the ice specimen are 62.01 and 61.68 mm, respectively, and the maximum absolute error and the maximum relative error of the radial size are 0.33 mm and 0.5%, respectively, which meet the test specifications for geometric accuracy [35].

2.2.2. Temperature Field Adjustment. Ice is a temperature-sensitive material, and its temperature distribution has a significant effect on the mechanical properties. To obtain the real temperature field of the ice specimen, the joint temperature measurement of distributed optical fiber and thermal resistance was employed, and the corresponding layout is shown in Figure 4.

The fiber was sealed in a carbon fiber tube with a diameter of 3 mm and placed along the axis of the specimen. The tube prevented the disturbance of pressure circumstance on the test results. The thermal conductivity of the carbon fiber material is relatively low, meaning that the original temperature distribution of the ice specimen would not be interfered [36]. The distributed optical fiber test equipment was the ODiSI Measurement System, LUNA Company, which could measure the temperature distribution along the whole fiber length, and the temperature measurement accuracy was 0.1°C . Three thermal resistors were arranged along the axial direction outside the insulation film of the specimen, and the temperature measurement accuracy was 0.05°C . The radial temperature distribution of the specimen could be simultaneously analyzed with the measurement results of the optical fiber and the thermal resistors.

Since the ice specimen was formed by one-way freezing from bottom to top, the temperature distribution at the

completion of freezing was cold in the lower and hot in the upper. Before the test, the temperature field needed to be adjusted to uniform distribution according to the design temperature. The design temperature of the test was -20°C , and the temperature field was adjusted by using the three constant low-temperature circulation tanks A, B, and C (Figure 1). In the adjustment process, seven temperature measuring points with equal spacing were set on the distributed optical fiber (Figure 4) to monitor the variation in the temperature field of the ice specimen. The measurement results (Figure 5) indicate that the temperature field of the ice specimen reaches a stable state after approximately 8 h. The measured temperature values of the distributed optical fiber and thermistor in the steady state are shown in Figure 6. The final temperature of the ice specimen is slightly higher in the center and slightly lower at both the ends and sides. The difference between the internal maximum temperature and the minimum temperature is 0.51°C , and the average temperature is -20.08°C , which meets the test specifications.

2.2.3. Stress Field Adjustment. Before the test, the stress state of ice specimen should be changed from the pressure freezing state to the initial state. It is necessary to limit the stress state and variation rate in the conversion process to avoid cracks [37, 38]. According to the triaxial test conclusion of Kalifa et al. [39], when the loading rate is lower than 1 MPa/s , ice begins to crack when the deviatoric stress reaches 0.25–0.5 times the ultimate deviatoric stress. The unloading experiments of Couture and Schulson [40] suggested that the unloading rate should not be greater than $0.17\text{ MPa}\cdot\text{s}^{-1}$ to ensure that cracks do not appear in the ice specimen. In this study, a more conservative constraint is adopted, i.e., the deviatoric stress should not be greater than 0.2 times the ultimate deviatoric stress during the process of stress state transformation, and the adjustment rates of axial pressure and confining pressure should not be greater than $0.05\text{ MPa}\cdot\text{s}^{-1}$.

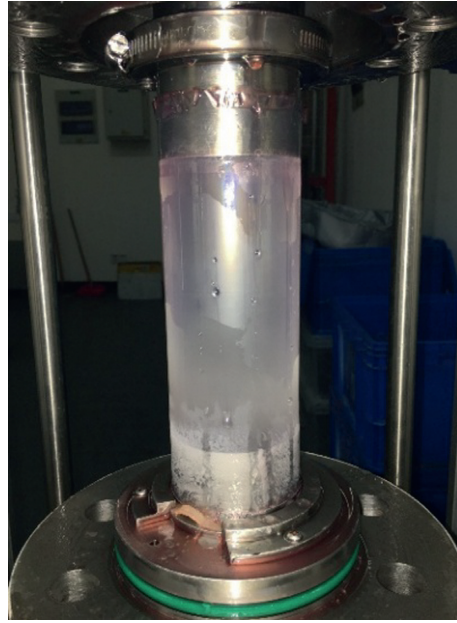


FIGURE 2: An ice sample frozen by the pressurized freezing technique.

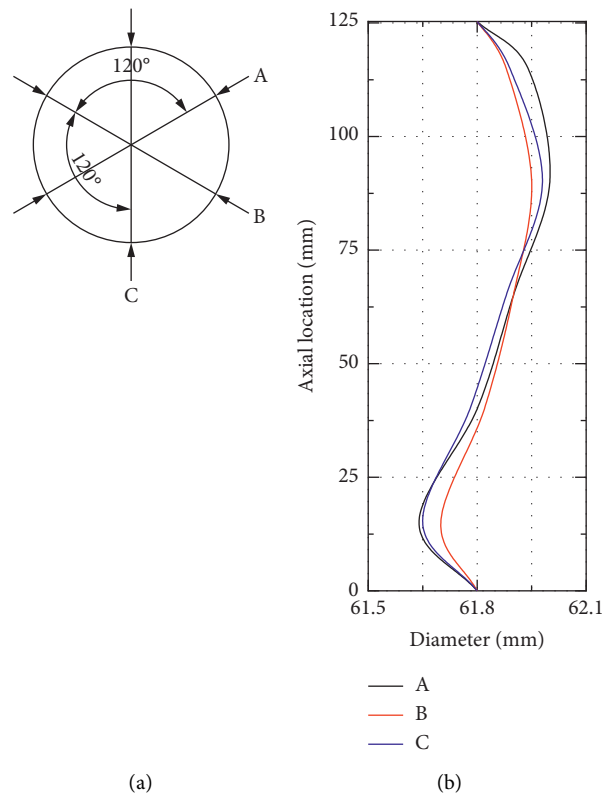


FIGURE 3: Ice sample diameter: (a) measurement intervals and (b) measurement results.

2.3. Experimental Procedures. Using the above specimen preparation technique, in situ uniaxial compression tests of pressurized freezing ice were conducted at -20°C under the constant strain rate. The strain rates considered were 5×10^{-5} , 1.5×10^{-5} , 5×10^{-6} , and $1.5 \times 10^{-6} \text{ s}^{-1}$. Since the

radial accuracy of the ice specimen relies on the interaction between the specimen and the confining medium during freezing, the pressure applied in the freezing process cannot be less than 0.5 MPa. Therefore, the freezing pressure of ice specimens was set to 0.5, 10, 20, and 30 MPa. The test was

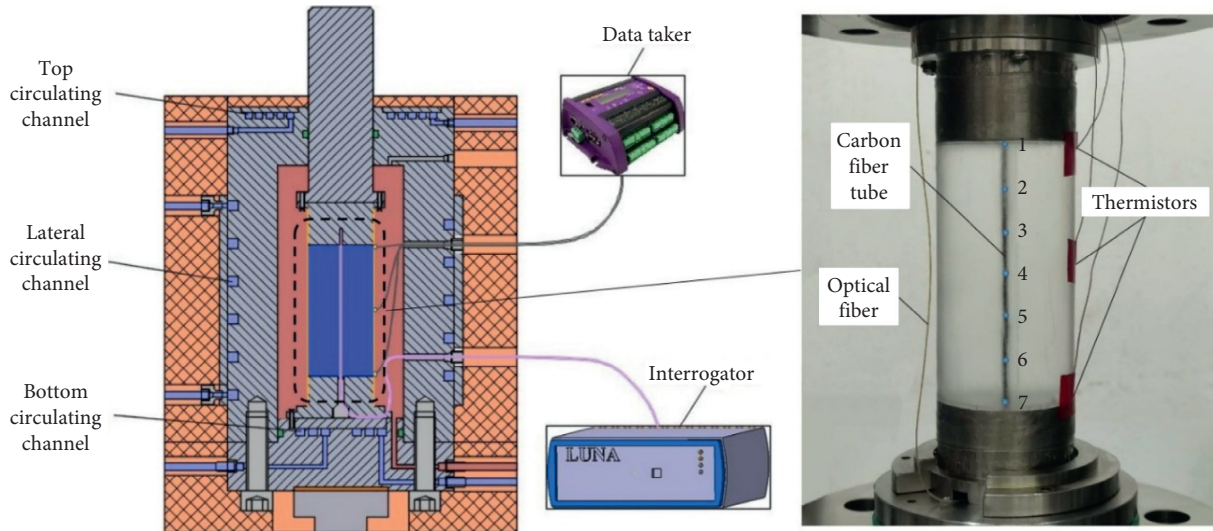


FIGURE 4: Arrangement of temperature sensors.

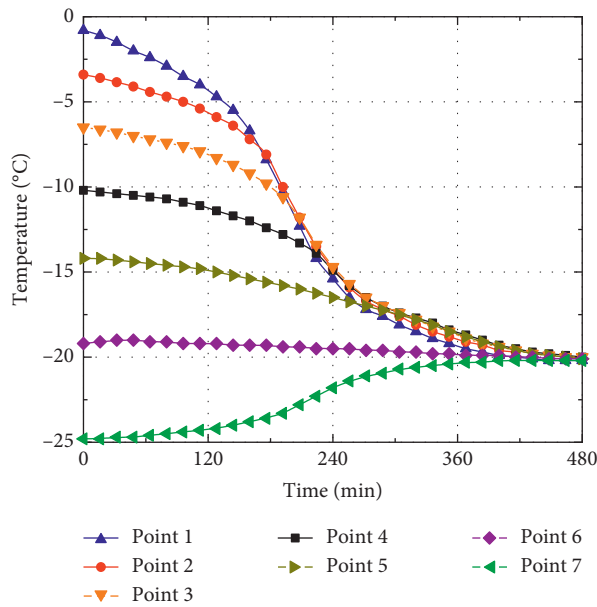


FIGURE 5: Variation in the temperature of seven measurement points on the optical fiber with time.

conducted using all the combinations of the above parameters. Each group contained two specimens, and a total of 32 specimens were tested.

The specific test process is as follows: firstly, the ice specimen was frozen under the pressure environment by using the controlled freezing process. Then, keeping the freezing stress field unchanged, the temperature field of the ice specimen was adjusted to a uniform value of -20°C . After the temperature field of the ice specimen became stable, the freezing pressure of the ice specimen was removed at the rate of $0.05\text{ MPa}\cdot\text{s}^{-1}$ under the condition that the three-dimensional pressures are equal. The uniaxial compression test with the constant strain rate was immediately conducted after the unloading process.

3. Results and Discussion

The stress-strain curves for all the 32 groups of tests are classified and summarized according to the freezing pressure in Figure 7. The test conditions and characteristic results corresponding to each curve are shown in Table 1. The curves with the same test conditions are represented in the same color, and the two repetitions are distinguished by different markers (circles and triangles). According to Table 1, the repeated errors of peak stress, failure strain, and residual stress of the test under the same conditions are 4–14%, 0–14%, and 0–8%, respectively, which are lower than most of the earlier reported values for ice uniaxial compression tests [41–44] and are close to the repeated errors of

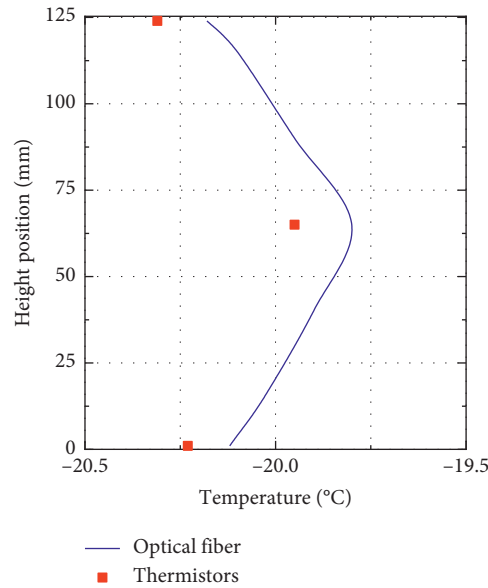


FIGURE 6: Measurement results of the optical fiber and thermistor under the stable temperature field of the ice specimen.

precise tests carried out by Ramseier [45]. The above results prove that the proposed test technique is reliable with high control precision and strong repeatability.

3.1. Stress-Strain Behavior

3.1.1. Failure Characteristics. Due to the rheological properties of ice, the failure characteristics after loading deformation are closely related to the strain rate. When the strain rate is slow, there is sufficient time for dislocation sliding between the ice crystals, so the stress-strain relationship of ice is elastoplastic, leading to ductile failure. When the strain rate is fast, the dislocation sliding between the ice crystals cannot occur, resulting in the dominant internal cracking and crushing. The stress-strain curve drops suddenly after reaching the peak, and brittle failure occurs. In Figure 7(a), when the strain rate is $5 \times 10^{-5} \text{ s}^{-1}$, the failure characteristics of ice specimens with freezing pressure of 0.5 MPa exhibit one brittle and one ductile, while the ice specimens with high pressure freezing all show brittle failure, which indicates that the influence of freezing pressure on the failure characteristics of ice is similar to that of low temperature, leading to the ductile-to-brittle transition zone move to a slow strain rate range.

The specific failure pattern is shown in Figure 8. After the test was completed, hydraulic oil was discharged while maintaining the low temperature in the pressure chamber, and then, the ice specimen was taken out, which took nearly 1 h. In the above process, the side of the ice specimen was tightly wrapped by a heat shrink tube, and the internal cracks were healed to a certain extent under the effect of recrystallization, resulting in self-repair of the ice specimen that might have been disintegrated due to compression failure. Therefore, all the damaged ice specimens were still continuous after the heat shrink tube was removed. The typical failure images of each specimen were processed using

Photoshop software to make the internal cracks clearer. These images are shown in Figures 8(a)–8(d), which reveal the variation in the failure mode of ice specimens under freezing pressure of 0.5–30 MPa and different strain rates. When the freezing pressure is low, there are fewer cracks inside the ice specimen, forming a vertical or inclined main crack (see Figure 8(b) for 0.5 MPa and Figure 8(d) for 0.5 MPa). As the freezing pressure increases, the number of cracks in the specimen gradually increases (see Figure 8(a) for 10 MPa), forming a certain fracture zone in the specimen (see Figure 8(c) for 20 MPa). In addition, with the increase in the freezing pressure, the crack concentration at the top and bottom of the specimen becomes increasingly obvious (see Figure 8(c) for 30 MPa). At a low strain rate, the specimens with high freezing pressure show lateral bulging failure (see Figure 8(d) for 30 MPa), and at high strain rate, the specimens with high freezing pressure still tend to exhibit shear failure (see Figure 8(a) for 30 MPa). In general, as the freezing pressure increases, the failure mode of the ice specimen changes from shear failure to splitting failure, and as the strain rate increases, this phenomenon becomes more and more obvious.

3.1.2. Brittleness Index. The test specimens with strain rates of 1.5×10^{-5} – $1.5 \times 10^{-6} \text{ s}^{-1}$ all showed ductile failure, and all the constitutive curves revealed strain-softening characteristics, but the rates of prepeak rise and postpeak decline of the curves were significantly affected by the freezing pressure. The stress variation rate of the constitutive curve is closely related to the brittleness of the material, which can be quantitatively evaluated by the brittleness index [46, 47]. There are four ways to extract the brittleness index according to the total stress-strain curve (Table 2), and the greater the index, the more significant the brittleness of the material. The index B_1 was proposed by Bishop [48], who suggested that the brittleness of the material can be characterized by

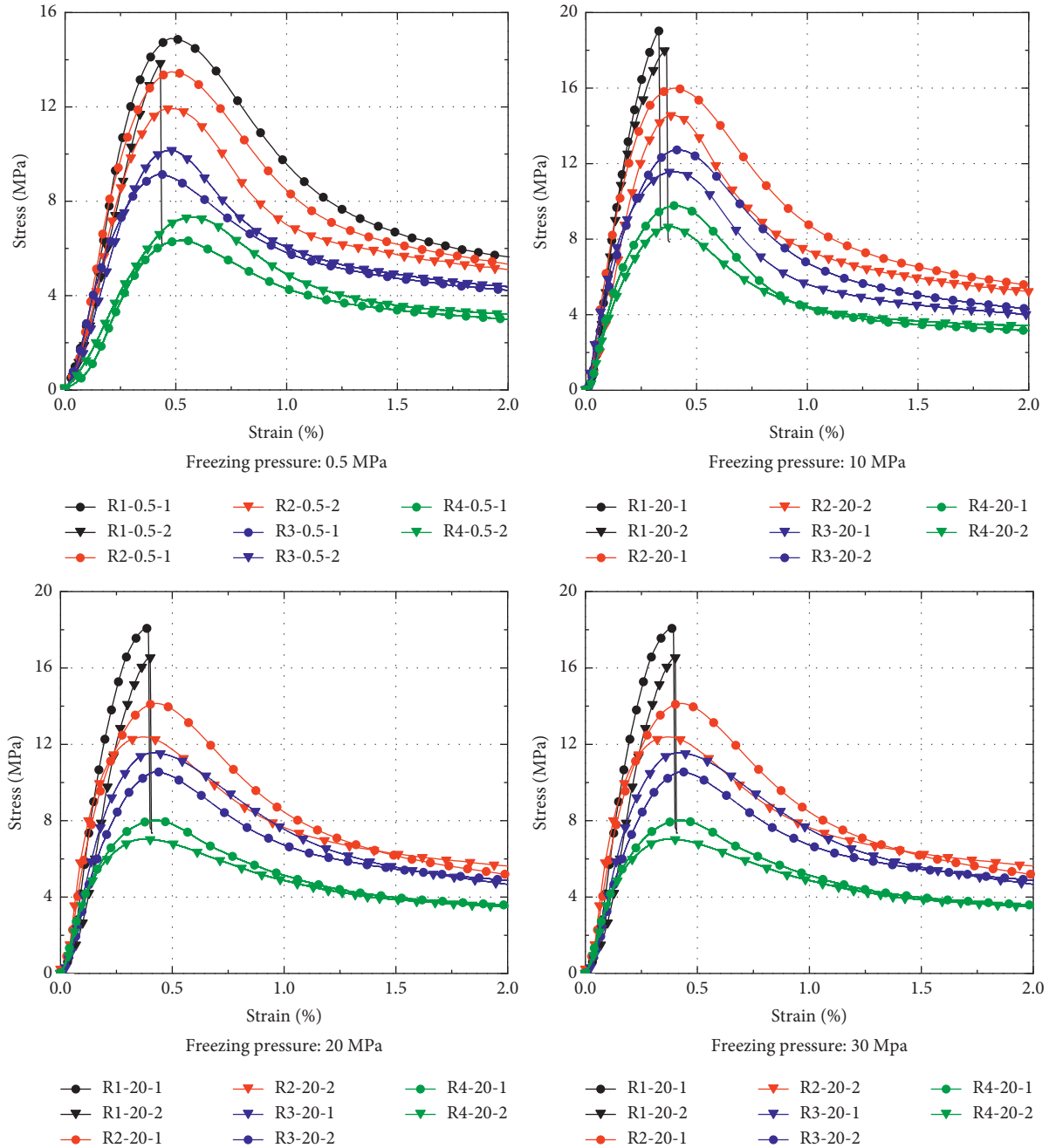


FIGURE 7: Stress-strain curves of all experiments.

the stress drop amplitude after the failure of the specimen, namely, the ratio of the postpeak drop of the stress to the peak stress. Subsequently, Zhou et al. [49] considered the absolute deceleration based on the relative magnitude of the postpeak stress drop and took its logarithm value as the coefficient to propose another brittleness index B_2 . Xia et al. [50] considered the influence of the prepeak stress-strain state on the brittleness characteristics; they used the ratio of the elastic energy released during the specimen failure to the total deformation energy stored before the peak to characterize the brittleness index. Based on the deformation energy calculation method of Tarasov and Potvin [51], the

index B_3 was derived. Tarasov and Potvin [51] believed that the brittleness degree should be reflected by the relative relationship between the deformation energy of the specimen before and after the peak of the constitutive curve, and the index can be expressed by the relationship between the modulus parameters before and after the peak, namely, B_4 .

The brittleness indices are calculated according to Table 2, where the modulus parameters are shown in Table 3. The calculated brittleness index is shown in Figure 9. Under all the strain rates, the variation in the four brittleness indexes with the freezing pressure is similar: the indexes increase first, then decrease, and then again increase. The mean

TABLE 1: Experimental conditions and results.

Group	Strain rate (s ⁻¹)	Freezing pressure (MPa)	Peak stress (MPa)	Failure strain	Residual stress (MPa)	Failure types
R1-0.5-1	5 × 10 ⁻⁵	0.5	14.90	0.48	5.63	Ductile
R1-0.5-2		0.5	13.85	0.43	6.13	Brittle
R1-10-1		10	19.00	0.33	8.48	Brittle
R1-10-2		10	18.12	0.36	7.83	Brittle
R1-20-1		20	18.10	0.39	7.52	Brittle
R1-20-2		20	16.54	0.40	7.59	Brittle
R1-30-1		30	19.55	0.41	9.65	Brittle
R1-30-2		30	20.33	0.40	10.07	Brittle
R2-0.5-1	1.5 × 10 ⁻⁵	0.5	13.50	0.48	5.33	Ductile
R2-0.5-2		0.5	11.92	0.46	5.16	Ductile
R2-10-1		10	16.00	0.40	5.54	Ductile
R2-10-2		10	14.55	0.38	5.23	Ductile
R2-20-1		20	14.14	0.42	5.17	Ductile
R2-20-2		20	12.39	0.37	5.62	Ductile
R2-30-1		30	17.21	0.45	5.51	Ductile
R2-30-2		30	16.10	0.43	5.80	Ductile
R3-0.5-1	5 × 10 ⁻⁶	0.5	9.14	0.43	4.22	Ductile
R3-0.5-2		0.5	10.17	0.48	4.25	Ductile
R3-10-1		10	12.73	0.40	4.14	Ductile
R3-10-2		10	11.58	0.40	4.31	Ductile
R3-20-1		20	10.55	0.41	4.88	Ductile
R3-20-2		20	11.57	0.43	4.66	Ductile
R3-30-1		30	14.03	0.45	4.88	Ductile
R3-30-2		30	13.02	0.43	4.84	Ductile
R4-0.5-1	1.5 × 10 ⁻⁶	0.5	6.35	0.53	2.99	Ductile
R4-0.5-2		0.5	7.33	0.51	3.04	Ductile
R4-10-1		10	9.79	0.40	3.15	Ductile
R4-10-2		10	8.65	0.37	3.43	Ductile
R4-20-1		20	8.02	0.42	3.57	Ductile
R4-20-2		20	7.04	0.36	3.78	Ductile
R4-30-1		30	10.62	0.45	3.43	Ductile
R4-30-2		30	9.92	0.42	3.42	Ductile

value of the four brittleness indexes increases in the following order of the freezing pressure:

$$\bar{B}(20 \text{ MPa}) < \bar{B}(0.5 \text{ MPa}) < \bar{B}(10 \text{ MPa}) < \bar{B}(30 \text{ MPa}), \quad (1)$$

where \bar{B} is the arithmetic average value of $B_1 - B_4$. The number in the brackets represent the freezing pressure.

The brittleness index calculated according to the constitutive relation can reflect the deformation law of ice under static load, which provides a basis for engineers to predict the deformation trend of frozen wall. In addition, the brittleness index is an important parameter to evaluate the dynamic response. The material with the higher brittleness index is easier to be cracked under dynamic action.

When the freezing method is used to construct the shaft in deep water-rich strata, the drilling and blasting method is needed to excavate the inner space of the shaft. Figure 9 shows that according to the hydrostatic head difference, the brittleness of ice at a depth of 1000 meters is significantly greater than that at the shallow part, which should be cautious in the design of the blasting process; particularly, the layout of the surrounding holes should be optimized to avoid the potential safety hazards caused by the cracking and

leakage of the frozen wall. The variation in the ice brittleness with the depth can also play a role in effective drilling of thick ice cover. Engineers can improve the bit form according to the variation in the brittleness index, and the drilling pressure, rotation speed, and other parameters in the drilling process can be optimized to improve the ice breaking efficiency.

3.2. Mechanical Properties

3.2.1. Peak Stress. According to the test, the variation in the peak stress as a function of the freezing pressure is shown in Figure 10. The scattered points are the measured values of each group of tests. The fold lines represent the change in the average value of the repeated test results. The colors of the points and lines correspond to the strain rate. Under the same freezing pressure, the peak stress of ice specimen increases with the increase in the strain rate, which is consistent with the test results of nonpressure freezing ice within the same strain rate range [28, 52]. Under the four strain rates, the variation laws of the peak stress of ice specimens are similar, and the peak stress does not monotonically change with the increase in the freezing

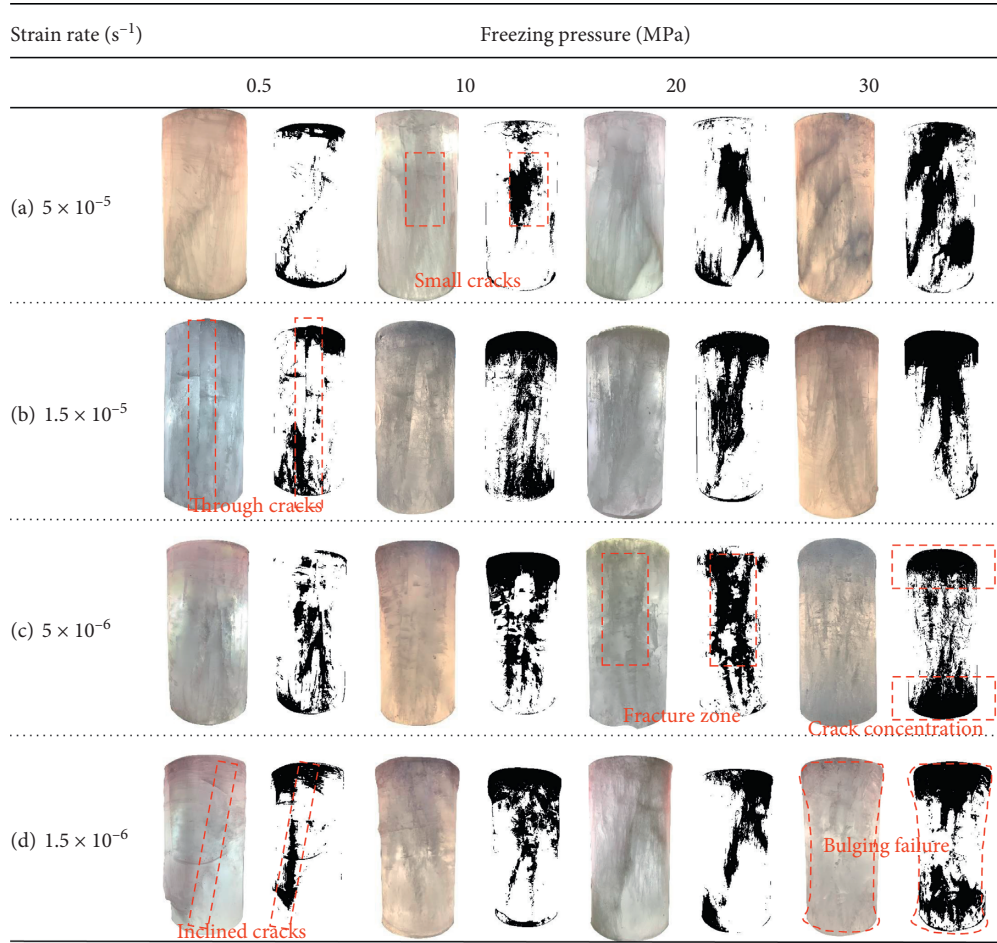


FIGURE 8: Failure pattern of representative specimens. (a) 5×10^{-5} . (b) 1.5×10^{-5} . (c) 5×10^{-6} . (d) 1.5×10^{-6} .

TABLE 2: Summary of calculation methods for the brittleness index.

Formula	Meaning of parameters
$B_1 = \sigma_p - \sigma_r / \sigma_p$	B is the brittleness index; the lower number represents different representation; σ_p and σ_r are peak stress and residual stress, respectively
$B_2 = \sigma_p - \sigma_r / \sigma_p \lg k_{ac} / 10$	k_{ac} is the absolute deceleration after peak, that is, $k_{ac} = \sigma_p - \sigma_r / \varepsilon_r - \varepsilon_p$
$B_3 = \sigma_p - \sigma_r / \varepsilon_r - \varepsilon_p + (\sigma_p - \sigma_r)(\varepsilon_r - \varepsilon_p) / \sigma_p \varepsilon_p$	ε_p and ε_r are failure strain and residual strain, respectively
$B_4 = E_{tb} - E_{td} / E_{tb}$	E_{tb}, E_{td} are maximum tangent modulus before and after peak

pressure, but it increases first, then decreases, and then again increases. When the freezing pressure increases from 0.5 MPa to 10 MPa, the average peak stress increases by 2.50–4.19 MPa, and the relative increase is 20–38%. When the freezing pressure rises to 20 MPa, the peak stress does not continue to rise, and its average value decreases by 1.10–2.01 MPa with a relative decrease of 6–20%. When the freezing pressure increases to 30 MPa, the peak stress increases again, and the average value is 2.47–3.39 MPa higher than that at 20 MPa, and the relative increase is 15–36%.

The freezing pressure interval selected in this experiment is large, and the freezing pressures of 10 MPa and 20 MPa are not necessarily the inflection points of the continuous variation curve of uniaxial compressive strength of ice specimens. It is necessary to conduct more detailed research

by narrowing the interval to obtain comprehensive and accurate variation law. However, the dashed line rule of Figure 10 is still valuable for engineering applications and scientific research. Taking the artificial freezing project as an example, the groundwater pressure is calculated according to the head difference. The test results show that the strength of artificial freezing ice increases significantly with the increase in depth in the depth range of 0–1000 m. These results can provide a basis for decreasing the thickness of pure ice bearing wall of artificial freezing engineering in deep karst [53] and deep water [54], which can reduce energy consumption and shorten the construction period. In addition, ice, as an important part of rock and soil frozen wall, largely determines the mechanical properties of frozen wall. Therefore, the variation law of compressive strength of

TABLE 3: Summary of the maximum tangent modulus before and after the peak of stress-strain curves.

Group	Strain rate (s^{-1})	Freezing pressure (MPa)	Prepeak maximum tangent modulus E_{tb} (GPa)	Maximum tangent modulus after peak E_{ta} (GPa)
R2-0.5-1	1.5×10^{-5}	0.5	6.06	1.36
R2-0.5-2		0.5	6.00	1.28
R2-10-1		10	8.16	1.92
R2-10-2		10	7.95	2.11
R2-20-1		20	8.02	1.28
R2-20-2		20	7.75	1.01
R2-30-1		30	8.78	1.70
R2-30-2		30	8.42	1.52
R3-0.5-1	5×10^{-6}	0.5	5.06	1.01
R3-0.5-2		0.5	4.55	0.79
R3-10-1		10	7.53	1.67
R3-10-2		10	7.80	1.50
R3-20-1		20	6.28	0.89
R3-20-2		20	5.26	0.89
R3-30-1		30	8.80	1.49
R3-30-2		30	7.39	1.60
R4-0.5-1	1.5×10^{-6}	0.5	3.60	0.89
R4-0.5-2		0.5	3.04	0.57
R4-10-1		10	5.07	1.37
R4-10-2		10	4.88	1.13
R4-20-1		20	4.03	0.77
R4-20-2		20	4.33	0.58
R4-30-1		30	5.16	1.25
R4-30-2		30	5.05	1.30

frozen ice can play a crucial role in the study of ice-rock or ice-soil coupling problems and improving the utilization rate of bearing capacity of deep frozen wall.

3.2.2. Residual Stress. The variation in the residual stress of ice specimens with freezing pressure at different strain rates is shown in Figure 11. At the high strain rate, the variation in the residual stress with freezing pressure is consistent with that of the peak stress because the ice specimen exhibits brittle failure in this condition (Figure 7). The value of residual stress is the fall point of the stress-strain curve, and the mechanism through which the freezing pressure affects the stress value is still the same as that for the peak stress. When the strain rate decreases, the failure mode of the ice specimen transforms into ductile failure, and the residual stress is changed to the stable stress value dropping from the peak of the stress-strain curve. In this case, the residual stress of the ice specimen does not change significantly with the increase in freezing pressure.

In artificial freezing construction in thick alluvium, the frozen wall is often in a low-speed rheological state, and the deformation is large, which can reach more than 5% in severe cases [3]. In this case, the bearing capacity of the frozen wall is reflected in its residual strength. Combined

with the variation law of peak stress (Figure 10) and residual stress (Figure 11) of ice with the freezing pressure, it can be seen that, under the condition of small deformation, the resistance of freezing wall increases significantly with the increase in depth, which is conducive to reducing the thickness of freezing wall. However, after entering the stage of large deformation, the bearing capacity advantage of deep frozen wall disappears, resulting in accelerated deformation under high ground pressure, which is unfavorable to the construction safety. Therefore, in the deep topsoil freezing project, it may be useful to adjust the height of the construction section and shorten the exposure time of the frozen wall to limit the deformation of the frozen wall, which may facilitate the bearing capacity advantage.

3.2.3. Failure Strain. The variation in the failure strain with freezing pressure is shown in Figure 12. Different from the change law of stress strength, there is no obvious relationship between the failure strain and the strain rate, which is consistent with the experimental results for nonpressure freezing ice in the same strain rate range [28, 51]. Under the four strain rates, the failure strain decreases first and then increases with the increase in the freezing pressure. When the freezing pressure is 0.5 MPa, the failure strain is the maximum, and its value

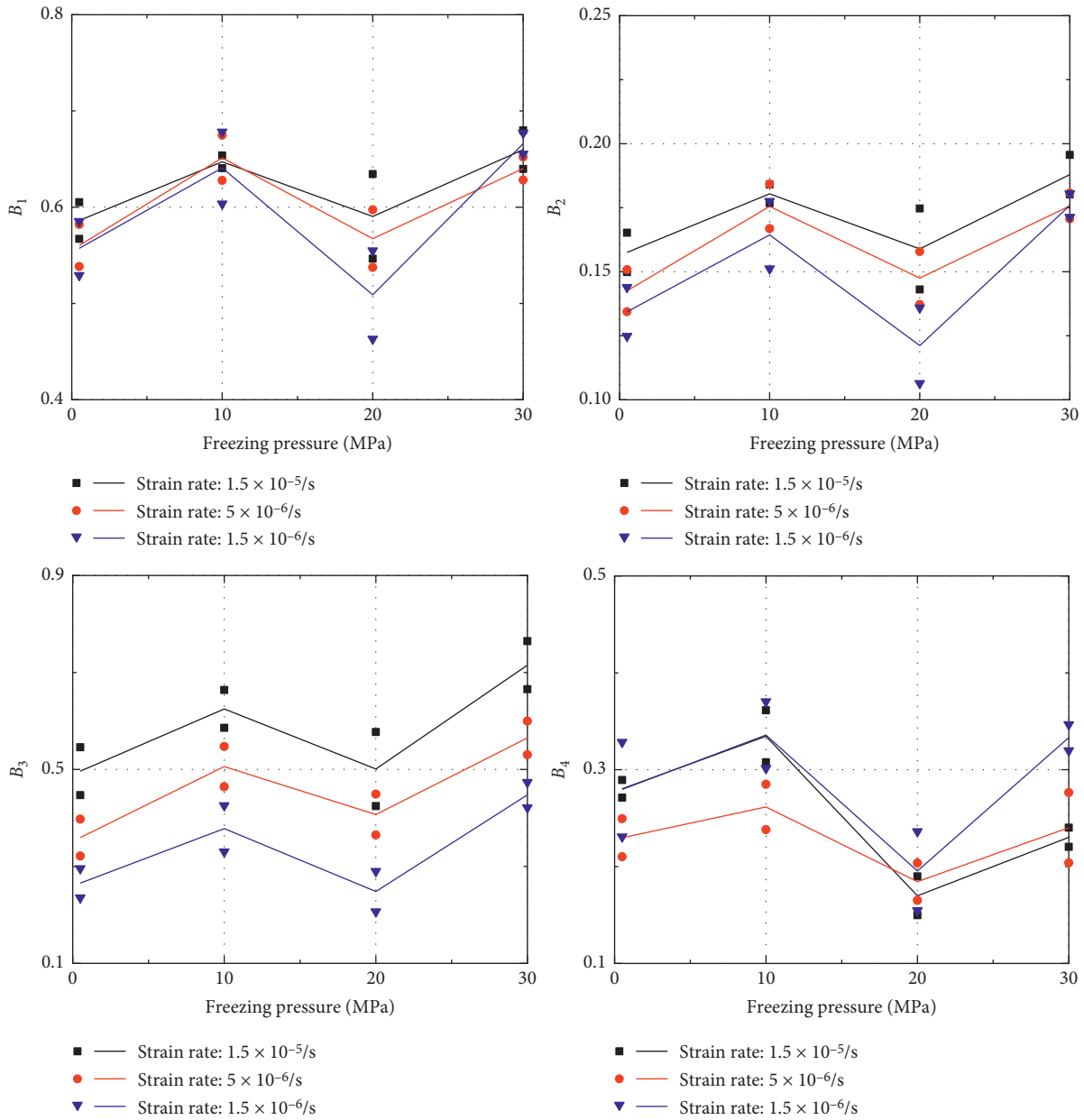


FIGURE 9: Variation in the brittleness indexes with freezing pressure under different strain rates.

is between 0.43% and 0.53%, which is consistent with the failure strain of pressureless frozen ice [28, 51, 55]. When the freezing pressure rises to 10 MPa, the failure strain decreases to a minimum of 0.33–0.4%. Then, the failure strain increases to 0.36–0.43% and 0.40–0.45% when the freezing pressure rises to 20 MPa and 30 MPa, respectively, but it is still lower than the test results of ice specimen frozen under the pressure of 0.5 MPa.

As mentioned in Section 3.2.1, the freezing pressure of 10 MPa is not necessarily the lowest point of the continuous variation curve of failure strain, but the fold line law of failure strain is still worthy of attention of engineers. Since the freezing pressure significantly reduces the failure strain of ice, it is likely that the deformation of the frozen wall formed under high pressure enters the plastic stage too early. Especially, when the groundwater pressure reaches 10 MPa,

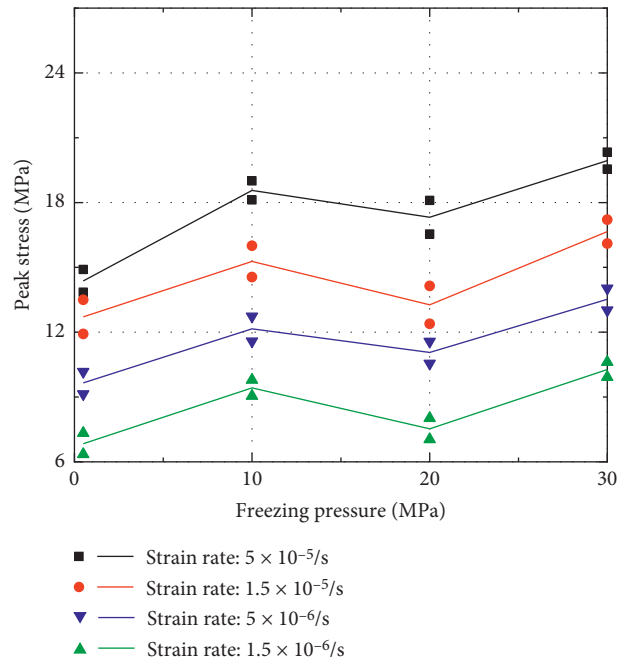


FIGURE 10: Variation in the peak stress with freezing pressure under different strain rates.

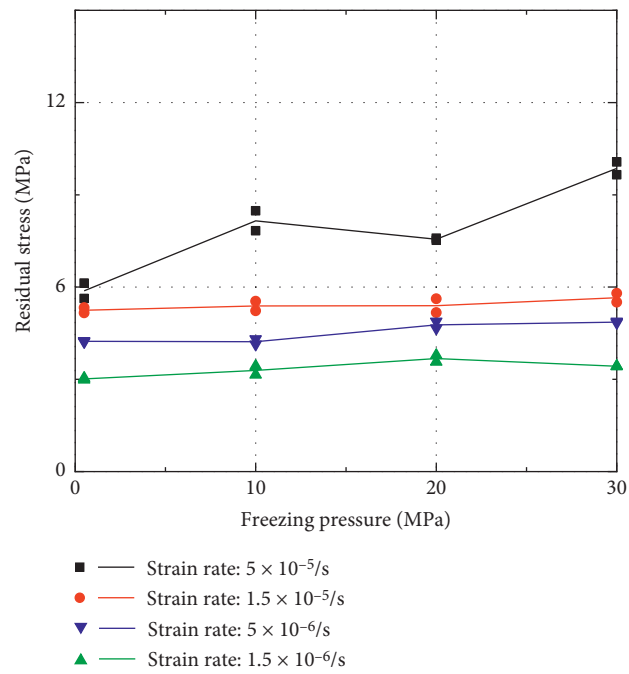


FIGURE 11: Variation in the residual stress with freezing pressure under different strain rates.

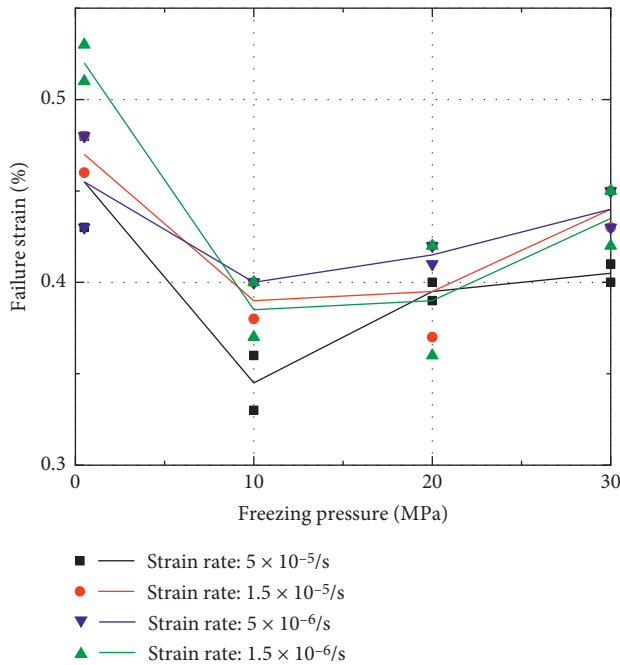


FIGURE 12: Variation in the failure strain with freezing pressure under different strain rates.

the failure strain of deep ice can be reduced by 26% as compared to that of shallow ice. The convergence deformation of the frozen wall should be strictly limited to prevent the rapid decline of its bearing capacity.

4. Conclusion

In this study, an effective method was proposed to prepare standard ice specimens under high hydraulic pressure in a triaxial pressure chamber. Using this technique, the in situ uniaxial compression test of ice specimens with temperature of 20°C and freezing pressure range of 0.5–30 MPa was carried out. The strain rate range was 5×10^{-5} – $1.5 \times 10^{-6} \text{ s}^{-1}$. The main results of the study are summarized as follows:

- (1) The proposed specimen preparation technique continuously controls the stress state of the specimen during the entire process of freezing and testing, which was suitable for the in situ mechanical test of pressurized freezing ice. The geometric accuracy and temperature distribution of the prepared specimens met the test specifications.
- (2) The failure modes of ice specimens changed from shear failure to splitting failure with the increase in the freezing pressure. The influence of freezing pressure on the failure characteristics of ice specimens was similar to that of low temperature, and the ductile-brittle transition zone moved to a slow strain rate range.
- (3) The variation trends of brittleness index and peak stress of ice specimens with the freezing pressure were similar: both increased first, then decreased, and then again increased. However, the locations of extreme points are different. The values of brittleness

index increased in the following order: (20 MPa) < (0.5 MPa) < (10 MPa) < (30 MPa), while the value relation of the peak stress is σ_p (0.5 MPa) < σ_p (20 MPa) < σ_p (10 MPa) < σ_p (30 MPa).

- (4) When the ice specimen exhibited brittle failure, the influence of freezing pressure on residual stress is consistent with that of the peak stress. When the ice specimen exhibited ductile failure, there was no obvious relationship between the residual stress and freezing pressure.
- (5) The failure strain of ice specimen first decreased and then increased with the increase in the freezing pressure, and the values increased in the following order: ε_p (10 MPa) < ε_p (20 MPa) < ε_p (30 MPa) < ε_p (0.5 MPa).

Data Availability

The data used to support the findings of the study are available from the corresponding author upon reasonable request.

Conflicts of Interest

The authors declare that they have no conflicts of interest.

Authors' Contributions

Baosheng Wang, Peixin Sun, and Yaodan Zhang performed the experiments; Baosheng Wang and Xin Huang analyzed the test data; Baosheng Wang and Fengjun Chen wrote the manuscript; Weihao Yang conceived the experiment and provided the guidance and suggestion.

Acknowledgments

This research was supported by the National Natural Science Foundation of China (Grant no. 51874286).

References

- [1] T. Wang, H. Zhang, G. Q. Zhou, and X. Liu, "Evaluation of variability characteristics of mechanical parameters of artificially frozen clay in deep alluvium," *Cold Regions Science and Technology*, vol. 171, 2020.
- [2] J. P. Wang, W. M. Liu, and H. Wang, "Comparisons on ground freezing constructions in 1000 m depth mine shafts," *Mine Construction Technology*, vol. 38, no. 4, pp. 34–37, 2017.
- [3] B. Zhang, W. H. Yang, and B. S. Wang, "Elastoplastic design theory for ultra-deep frozen wall considering large deformation features," *Chinese Journal of Geotechnical Engineering*, vol. 41, no. 7, pp. 1288–1295, 2019.
- [4] R. L. Shan, Y. Bai, L. Song et al., "Experimental study of blasting vibration and damage characteristics on frozen shaft wall," *Chinese Journal of Rock Mechanics and Engineering*, vol. 34, pp. 3732–3741, 2015, S3 in Chinese.
- [5] R. Margesin, *Permafrost Soils*, Springer, New York, NY, USA, 2008.
- [6] R. Atlasov, M. Nikolaeva, and V. Karamzin, *Drilling and Installation of Boreholes for Permafrost Thermal Monitoring on Livingston Island in the Maritime Antarctic*, 2019.

- [7] D.-y. Wang, W. Ma, X.-x. Chang, and A. g. Wang, "Study on the resistance to deformation of artificially frozen soil in deep alluvium," *Cold Regions Science and Technology*, vol. 42, no. 3, pp. 194–200, 2005.
- [8] Y. Yang, Y. Lai, and X. Chang, "Laboratory and theoretical investigations on the deformation and strength behaviors of artificial frozen soil," *Cold Regions Science and Technology*, vol. 64, pp. 39–45, 2010.
- [9] D. Li, C. Zhang, G. Ding et al., "Fractional derivative-based creep constitutive model of deep artificial frozen soil," *Cold Regions Science and Technology*, vol. 170, 2020.
- [10] Y. Bai, R. Shan, Y. Jua, Y. Wu, P. Sun, and Z. Wang, "Study on the mechanical properties and damage constitutive model of frozen weakly cemented red sandstone," *Cold Regions Science and Technology*, vol. 171, 2020.
- [11] L. Wang, N. Li, J. Qi, Y. Tian, and S. Xu, "A study on the physical index change and triaxial compression test of intact hard rock subjected to freeze-thaw cycles," *Cold Regions Science and Technology*, vol. 160, pp. 39–47, 2019.
- [12] C. Zhu, M. C. He, X. H. Zhang, Z. G. Tao, Q. Lin, and L. f. Li, "Nonlinear mechanical model of constant resistance and large deformation bolt and influence parameters analysis of constant resistance behavior," *Rock and Soil Mechanics*, vol. 42, no. 7, pp. 1911–1924, 2021, in Chinese.
- [13] Q. Yin, J. Y. Wu, C. Zhu, M. He, Q. Meng, and H. Jing, "Shear mechanical responses of sandstone exposed to high temperature under constant normal stiffness boundary conditions," *Geomechanics and Geophysics for Geo-Energy and Geo-Resources*, vol. 7, no. 35, 2021.
- [14] F. Wu, H. Zhang, Q. L. Zou, C. Li, J. Chen, and R. Gao, "Viscoelastic-plastic damage creep model for salt rock based on fractional derivative theory," *Mechanics of Materials*, vol. 150, 2020.
- [15] M. J. Siegert, K. Kwok, and C. Mayer, "Water exchange between subglacial Lake Vostok and the overlying ice sheet," *Nature*, vol. 403, pp. 643–646, 2000.
- [16] V. Lukin and S. Bulat, "Vostok subglacial lake: details of Russian plans/activities for drilling and sampling," *Geophysical Monograph Series*, vol. 192, pp. 187–197, 2011.
- [17] J. Jouzel, J. R. Petit, R. Souchez et al., "More than 200 meters of lake ice above subglacial lake vostok, Antarctica," *Science*, vol. 286, no. 5447, pp. 2138–2141, 1999.
- [18] M. H. Carr, M. J. S. Belton, C. R. Chapman et al., "Evidence for a subsurface ocean on Europa," *Nature*, vol. 391, pp. 363–365, 1998.
- [19] S. J. Jones, "A review of the strength of iceberg and other freshwater ice and the effect of temperature," *Cold Regions Science and Technology*, vol. 47, pp. 256–262, 2007.
- [20] L. W. Gold, "Some observations on the dependence of strain on stress for ice," *Canadian Journal of Physics*, vol. 36, no. 10, pp. 1265–1275, 1958.
- [21] L. W. Gold, "The elastic modulus of columnar-grain freshwater ice," *Annals of Glaciology*, vol. 19, pp. 13–18, 1994.
- [22] A. Traelleberg, L. W. Gold, and R. Frederking, *The Strain Rate and Temperature Dependence of Young's Modulus of Ice*, U.S. Army Cold Regions Research and Engineering Laboratory, Hanover, NH, USA, 1975.
- [23] N. K. Sinha, "Rate sensitivity of compressive strength of columnar-grained ice," *Experimental Mechanics*, vol. 21, no. 6, pp. 209–218, 1981.
- [24] G. A. Kuehn and M. S. E. "The mechanical properties of saline ice under uniaxial compression," *Annals of Glaciology*, vol. 19, pp. 39–48, 1994.
- [25] J. R. Rice and R. Thomson, "Ductile versus brittle behaviour of crystals," *Philosophical Magazine*, vol. 29, no. 1, pp. 73–97, 1974.
- [26] E. M. Schulson and S. E. Buck, "The ductile-to-brittle transition and ductile failure envelopes of orthotropic ice under biaxial compression," *Acta Metallurgica et Materialia*, vol. 43, no. 10, pp. 3661–3668, 1995.
- [27] G. Timco and R. Frederking, "Comparative strengths of fresh water ice," *Cold Regions Science and Technology*, vol. 6, no. 1, pp. 21–27, 1982.
- [28] M. Arakawa and N. Maeno, "Mechanical strength of polycrystalline ice under uniaxial compression," *Cold Regions Science and Technology*, vol. 26, no. 3, pp. 215–229, 1997.
- [29] W. F. Weeks and G. F. N. Cox, *Laboratory Preparation of Artificial Sea and Salt Ice*, Cold Regions Research and Engineering Laboratory, Hanover, NH, U.S.A, 1974.
- [30] T. R. Smith and E. M. Schulson, "The brittle compressive failure of fresh-water columnar ice under biaxial loading," *Acta Metallurgica et Materialia*, vol. 41, no. 1, pp. 153–163, 1993.
- [31] G. A. Kuehn, R. W. Lee, W. A. Nixon, and E. M. Schulson, "The structure and tensile behavior of first-year sea ice and laboratorygrown saline ice," *Journal of Offshore Mechanics and Arctic Engineering*, vol. 112, no. 4, pp. 357–363, 1990.
- [32] I. L. Meglis, R. E. Gagnon, and R. P. Young, "Microcracking during stress-relief of polycrystalline ice formed at high pressure," *Geophysical Research Letters*, vol. 22, no. 16, pp. 2207–2210, 1995.
- [33] B. S. Wang, P. X. Sun, T. T. Luo et al., *Freezing Pressurized Water into a Standard Cylindrical Ice Sample in a Triaxial Cell*, Geofluids, 2021.
- [34] V. Petrenko and R. Whitworth, *Physics of Ice*, Oxford University Press, Oxford, England, 2002.
- [35] R. Ulusay, *The ISRM Suggested Methods for Rock Characterization, Testing and Monitoring: 2007-2014*, Springer International Publishing, New York, NY, USA, 2015.
- [36] S. Snyder and J. S. Franks, "Quantifying the effects of sensor coatings on body temperature measurements," *Animal Biotelemetry*, vol. 4, 2016.
- [37] Q. Wang, M. C. He, S. C. Li et al., "Comparative study of model tests on automatically formed roadway and gob-side entry driving in deep coal mines," *International Journal of Mining Science and Technology*, vol. 31, no. 4, pp. 591–601, 2021.
- [38] Q. Wang, Y. Wang, M. C. He et al., "Experimental research and application of automatically formed roadway without advance tunneling," *Tunnelling and Underground Space Technology*, vol. 114, 2021.
- [39] P. Kalifa, G. Ouillon, and P. Duval, "Microcracking and the failure of polycrystalline ice under triaxial compression," *Journal of Glaciology*, vol. 38, no. 128, pp. 65–76, 1992.
- [40] M. L. Couture and E. M. Schulson, "The cracking of ice during rapid unloading," *Philosophical Magazine Letters*, vol. 69, no. 1, pp. 9–14, 1994.
- [41] S. J. Jones, "Comparison of the strength of iceberg and other freshwater ice and the effect of temperature," National Research Council of Canada. NRC Institute for Ocean Technology, Newfoundland, Canada, 2006.
- [42] S. J. Jones, "The confined compressive strength of polycrystalline ice," *Journal of Glaciology*, vol. 28, no. 98, pp. 171–178, 1982.
- [43] D. M. Cole, "Strain-rate and grain-size effects in ice," *Journal of Glaciology*, vol. 115, no. 33, pp. 274–280, 1987.

- [44] I. Meglis, *High Speed Testing of Freshwater Granular Ice*, Institute for Marine Dynamics, National Research Council of Canada, Ottawa, Canada, 1998.
- [45] R. O. Ramseier, *Growth and Mechanical Properties of River and lake Ice*, Laval University, Quebec, Canada, 1976.
- [46] G. Feng, Y. Kang, X. C. Wang, Y. Wu, and X. Li, "Investigation on the failure characteristics and fracture classification of shale under Brazilian test conditions," *Rock Mechanics and Rock Engineering*, vol. 53, no. 7, pp. 3325–3340, 2020.
- [47] G. Feng, X. C. Wang, M. Wang, and Y. Kang, "Experimental investigation of thermal cycling on fracture characteristics of granite in a geothermal-energy reservoir," *Engineering Fracture Mechanics*, vol. 235, 2020.
- [48] A. W. Bishop, *Progressive Failure with Special Reference to the Mechanism Causing it*, Oslo, Oslo, Norway, 1967.
- [49] H. Zhou, F. Z. Meng, C. Q. Zhang, R. Xu, and J. Lu, "Quantitative evaluation of rock brittleness based on stress-strain curve," *Chinese Journal of Rock Mechanics and Engineering*, vol. 33, no. 6, pp. 1114–1122, 2014, in Chinese.
- [50] Y. J. Xia, L. C. Li, C. A. Tang et al., "Rock brittleness evaluation based on stress dropping rate after peak stress and energy ratio," *Chinese Journal of Rock Mechanics and Engineering*, vol. 35, no. 6, pp. 1141–1154, 2016, in Chinese.
- [51] B. Tarasov and Y. Potvin, "Universal criteria for rock brittleness estimation under triaxial compression," *International Journal of Rock Mechanics and Mining Sciences*, vol. 59, pp. 57–69, 2013.
- [52] M. Mellor and D. M. Cole, "Deformation and failure of ice under constant stress or constant strain-rate," *Cold Regions Science and Technology*, vol. 5, no. 3, pp. 201–219, 1982.
- [53] Z. C. Duan, "Deep and ultra-deep karst," *Geological Science and Technology Information*, vol. S1, pp. 122–124, 1982, in Chinese.
- [54] Y. K. Yang, J. J. Zheng, and Q. H. Fang, "Application of freezing method in pile foundation of bridge," *Bridge Construction*, vol. 2, pp. 54–56, 2002, in Chinese.
- [55] R. Frederking, "Plane-strain compressive strength of columnar-grained and granular-snow ice," *Journal of Glaciology*, vol. 18, no. 80, pp. 505–516, 1977.

Research Article

Research on Dynamic Stability Optimization of Rock Spreader considering Prevention of Geological Subsidence and Local Collapse in Reclamation Area

Baofu Kou ¹, Pengliang Huo,² and Xin Shi¹

¹School of Mechanical Engineering, Taiyuan University of Science and Technology, Taiyuan 030024, China

²Shijiazhuang Coal Mining Machinery Co., Ltd., Shijiazhuang 050033, China

Correspondence should be addressed to Baofu Kou; koubaofu2004@163.com

Received 15 July 2021; Accepted 29 July 2021; Published 7 August 2021

Academic Editor: Xiaohu Zhang

Copyright © 2021 Baofu Kou et al. This is an open access article distributed under the Creative Commons Attribution License, which permits unrestricted use, distribution, and reproduction in any medium, provided the original work is properly cited.

The uneven stacking of waste rock materials caused by the dynamic instability of rock spreaders cannot be ignored for geological subsidence and local collapse in reclamation areas. Based on the dynamic stability of the existing rock spreader, combined with the actual application conditions, the load conditions of the rock spreader are analyzed. The static and dynamic analysis and optimization of the key structures such as the receiving arm, the discharging arm, and the main tower are carried out by using the topology optimization method. The optimized virtual prototype of the whole machine is established to verify its rationality. The research results show that the total weight of key parts such as receiving boom, discharging boom, and the main tower is reduced by about 4.5% (4650 kg), the lower-order vibration frequencies below the fifth order of those parts are not within the resonance range, and the stability of the whole machine is greatly improved, which fundamentally solves the problem of uneven rock stacking caused by impact stability. And, the maximum stress and deflection of the whole machine under the worst working conditions meet the actual requirements. The research ideas and conclusions can provide solutions to prevent the subsidence or local collapse of reclamation areas caused by uneven stacking materials.

1. Introduction

A self-moving rock spreader is a kind of equipment that can orderly discharge the rock and other materials except mineral resources to the fixed dump in the process of open-pit mining, which provides the basic conditions for the reclamation of the mining area after mining [1, 2]. The development of open-pit mining toward high-speed, large capacity, and automation puts forward not only higher requirements for mining technology but also higher requirements for operating machinery and equipment [3, 4]. In the early stage, the technology of loading and unloading waste materials by truck and long-distance transportation between mining area and dump has many problems, such as many potential safety hazards, low degree of automation, high emission of waste gas pollution, large consumption of gasoline, and chaotic dump. With the development of mining technology, most open-pit mines

combine the rock spreader and belt conveyor to form the rock exhausting system of open-pit mines [5, 6]. The combination of the two has the advantages of long conveying distance, high conveying efficiency, and good stability [7, 8]. Therefore, the self-moving rock spreader has become one of the indispensable types of equipment for continuous or semicontinuous high-efficiency mining technology of open-pit mines.

At present, under the action of continuous rainfall, weathering, and human disturbance, the phenomenon of uneven settlement or local collapse often occurs in the reclamation area of waste rock and soil [9–11]. However, the uneven stacking of rock materials by rock spreaders will make this phenomenon more serious and even lead to geological disasters and pollution [12–14]. There are two main reasons for uneven rock materials piled up by rock spreaders. The first is the unreasonable position of lining and line technology. The second is the uneven rock stacking

caused by the instability of the rock spreader. With the rapid development of intelligent control, accurate control has been achieved in the layout position and line technology [15]. However, the problem of dynamic stability of rock spreaders is easy to be ignored. Therefore, it is urgent to prevent the subsidence or local collapse of reclamation area caused by uneven stacking materials due to the instability of the rock exhauster structure.

Although the research on the rock spreader has achieved phased results, the design of the rock spreader mostly adopts the way of analogy design, and there is a technical bottleneck in the structure refinement design of the rock spreader [16, 17]. Yang and Pu [18] optimized the limit device of the PL-2400 rock spreader support truck, which improved the reliability of the rock spreader. Dong and Wang [19] proposed the stacking and discharging process design of rock spreaders based on the scale parameters of waste dump and equipment parameters of rock spreader. Han [20] and Meng et al. [21] optimized the cab and control interface of the rock spreader according to the problems existing in the working environment and control room of the rock spreader. Hu et al. [22] and Zhang [23] have made a new design for the lubrication system of the rock spreader, which improves the working efficiency and service life of the rock spreader. Yao et al. [24] put forward a method to limit the vibration of the discharging boom of the rock spreader. Therefore, on the basis of the existing research results of the rock exhauster, the formation of a more perfect calculation method for the structure optimization of the rock spreader can not only shorten the design cycle of the rock spreader and promote the standardization and serialization of the rock spreader but also improve the uniformity of the material of the rock spreader and prevent the serious subsidence or landslide in the reclamation area to a certain extent.

Structural topology optimization is an effective lightweight design method to solve complex working conditions [25–27]. In the field of mine engineering, relevant scholars have studied different types of structural parts by using topology optimization theory and achieved good results [28, 29]. Wu et al. [30] applied the variable density method to optimize the topology of the main arm and the small arm of the hydraulic chisel loader. The result shows that the weight is reduced by 8%, but the stress is reduced and the safety factor is improved. Tang et al. [31] established the topology optimization model of the key structural parts of the feeder by using the variable density method and the substructure method and carried out the optimization. After the optimization, the natural frequency of the structure was increased by 4.17% and 6.30%, respectively, and the maximum dynamic stress was reduced by 46.4%, which improved the overall stiffness and structural reliability of the feeder. Pang et al. [32] used the topology optimization method to study the lightweight of the track frame of the WK-75 excavator based on multibody dynamics. After topology optimization, the thickness of the main support plate and rib plate of the track frame is reduced, and the material utilization efficiency is improved.

To sum up, relevant scholars have made some progress in structural stability and topology optimization of rock spreaders [33], but they have not formed a complete

optimization design method and theory for the dynamic stability of key structures of rock spreaders. According to the field investigation and theoretical analysis, it is easy to produce large impact vibration due to the large self-weight of the key structure of the rock spreader and its low-order frequency is close to the natural frequency. This not only leads to the short service life of the rotary bearing of the receiving boom and the counterweight boom but also causes the failure of the hydraulic cylinder connecting the discharging boom from time to time [34]. More importantly, it will cause the uniform discharge of geotechnical materials by the rock spreader. In view of the above problems, firstly, the actual load conditions of rock spreaders are analyzed, based on this, a static and dynamic analysis of the existing structure was made, and the problems existing in its dynamic stability were discussed. Then, the topology optimization analysis of the three main structural parts of the discharge arm, the receiving arm, and the main tower is carried out by using the variable density topology theory. And then, based on the topology results and combined with the field application conditions, the new design of each structure is carried out. Finally, the static and dynamic verification of the key structural parts after topology optimization is carried out, and the whole machine joint simulation is carried out to verify the correctness of the topology optimization results. Here, it is aimed to explore a set of topology optimization design theories and methods suitable for the key main structural parts of a large rock spreader, so as to improve the dynamic stability of its main structural parts, and make the stress on the structural parts uniform and give full play to the mechanical efficiency of materials. The research conclusion can provide an important guarantee for solving the discharge uniformity of rock spreaders and indirectly curb or prevent the serious settlement or local landslide in the reclamation area of waste rock and soil.

2. Analysis of Load Characteristics of Rock Spreader

The rock spreader is mainly composed of receiving system, discharging system, pitching system, counterweight system, main tower, and crawler walking device. The schematic diagram of the whole machine is shown in Figure 1. Taking a certain type of rock spreader as the research object, the main design parameters of this type of rock spreader are shown in Table 1.

In the process of discharging rock, the rock spreader will be subjected to the complex load, which is accompanied by the process of full load starting and braking, sudden unloading, and climbing with a load. In the calculation process, the load value is determined according to the comprehensive consideration of the material conveying capacity and the external environmental load [35, 36]. According to the code for the design of steel structure of mobile continuous bulk material handling equipment, the load of rock spreader is quantified. Then, it is designed and checked according to the following working conditions [37, 38]:

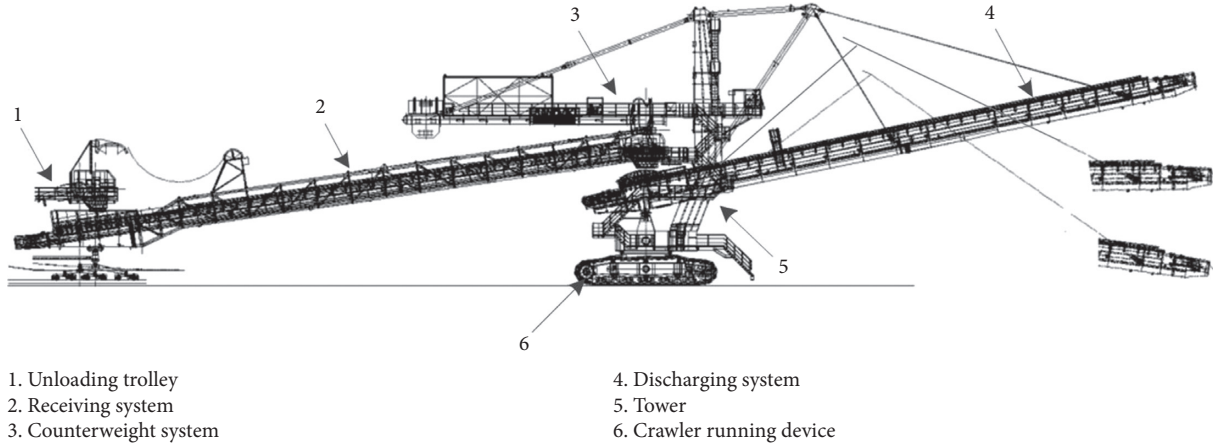


FIGURE 1: Structure diagram of the spreader. 1: unloading trolley; 2: receiving system; 3: counterweight system; 4: discharging system; 5: tower; 6: crawler running device.

TABLE 1: Main design parameters of rock spreader.

Main design parameters	Value
Rated conveying capacity	4500 t/h
Average grounding voltage under normal operation	≤ 110 kPa
Radius of gyration	50 m
Length of discharging boom	50 m
Maximum upward angle of discharging boom	13°
Maximum downward angle of discharging boom	4°
Length of the receiving boom	50 m
Width of conveyor belt	1.4 m
Speed of conveyor belt	4 m/s
Speed of travel	0~8 m/ min
Working gradient	1:20
Walking gradient	1:10

Condition I: the rock spreader is only subjected to self-weight load (no-load working condition)

Condition II: normal operation of rock spreader (rated load with wind load)

Condition III: abnormal operation (rated load with wind load and seismic load)

To alleviate the impact of the rock spreader on the receiving boom in the working process, the left end of the receiving boom is connected with the receiving boom support trolley through the guide wheel group and guide rail. The length of the guide wheel group is 2500 mm, and the length of the guide rail at the left end of the receiving boom is 7500 mm. In the working process, the position of the guide wheel group determines the three typical working positions of the receiving boom. The three positions are as follows: the guide wheel of the support car of the unloading car is located in the left limit position, the middle position, and the right limit position of the guide rail. There are three typical working positions for the discharging boom of rock discharging machine: the discharging boom is horizontal, the discharging boom is upward 13° , and the discharging boom is downward 4° .

Influence analysis of each part: ① The receiving boom of the rock spreader supports the whole receiving conveyor to complete the receiving operation. The left end of the receiving boom is connected with the receiving boom support trolley through the guide wheel guide rail, and the right end is suspended on the counterweight boom through the slewing bearing. The weight of the receiving boom directly affects the service life of the slewing bearing. ② The discharging boom supports the whole discharging conveyor to complete the discharging operation. The discharging boom mainly realizes the pitching movement of the discharging boom through the hydraulic cylinder. The quality of the discharging boom directly affects the service life of the hydraulic cylinder and other parts. ③ The main tower is used to fix the discharging boom and the counterweight boom. The above three key structural parts occupy a very important position in the upper structure of the rock spreader, and their structural rationality directly affects the working flexibility and energy consumption of the whole machine.

The load and working condition combination of receiving boom are shown in Table 2. The load and working condition combination of the discharging boom are shown in Table 3.

3. Static and Dynamic Characteristics Analysis of Key Structure of Rock Spreader

3.1. Finite Element Analysis of Structure

3.1.1. Finite Element Analysis Theory of Structure [39]. The dynamic equation of the structure is as follows:

$$[M]\{\ddot{x}\} + [C]\{\dot{x}\} + [K]\{x\} = \{F(t)\}, \quad (1)$$

where $[M]$ is the structural mass matrix, $[C]$ is the damping matrix, $[K]$ is the stiffness matrix, $\{x\}$ is the displacement vector, and $\{F(t)\}$ is the force vector.

TABLE 2: The load and working condition combination of receiving boom.

Load type	Name	Size (N)	Type of working condition		
Basic load	Deadweight of receiving boom	359170	I	II	III
	Conveyor belt	75000	✓	✓	✓
	Roller	77700	✓	✓	✓
	Materials	158500		✓	✓
	Walking platform and railings	128800	✓	✓	✓
	Buffer bed and receiving chute	87390	✓	✓	✓
	Discharging chute	37990	✓	✓	✓
	Head roller and driving device	69830	✓	✓	✓
	Tail roller and tightening device	29830	✓	✓	✓
Additional load	Wind load	10428		✓	✓
Special loads	Seismic load				✓

TABLE 3: The load and working condition combination of discharging boom.

Load type	Name	Size (N)	Type of working condition		
Basic load	Deadweight of receiving boom	263030	I	II	III
	Conveyor belt	65000	✓	✓	✓
	Roller	55000	✓	✓	✓
	Materials	158500		✓	✓
	Walking platform and railings	112930	✓	✓	✓
	Buffer bed and receiving chute	48180	✓	✓	✓
	Discharging chute	25000	✓	✓	✓
	Head roller and driving device	96720	✓	✓	✓
	Tail roller and tightening device	66260	✓	✓	✓
Additional load	Wind load	9870		✓	✓
Special loads	Seismic load				✓

For the static analysis of linear structure, the influence of time is ignored. The following relationship can be deduced by combining (1):

$$[K]\{x\} = \{F\}, \quad (2)$$

where $\{F\}$ is the static load without considering the time effect.

The stress and strain values of the structure under load can be obtained by solving equation (2). According to the deformation value and stress value, we can check whether the structure meets the user requirements under different working conditions.

The structural strain can be expressed as

$$\{\varepsilon\} = \partial\{f\} = \partial[N]\{\delta\}^e = [B]\{\delta\}^e, \quad (3)$$

where $\{\varepsilon\}$ is the strain matrix, $\{f\}$ is the concentrated load matrix, $[N]$ is the shape function matrix, $\{\delta\}^e$ is the node displacement matrix, and $[B]$ is the constant strain element matrix.

The structural stress can be expressed as

$$\{\sigma\} = [D]\{\varepsilon\} = [D][B]\{\delta\}^e = [S]\{\delta\}^e, \quad (4)$$

where $\{\sigma\}$ is the stress matrix, $[D]$ is the elastic matrix, $\{\varepsilon\}$ is the strain matrix, $\{\delta\}^e$ is the node displacement matrix, and $[S]$ is the constant stress element matrix.

Q345E is mainly used as the boom material of the rock spreader. In view of the complexity of the loads, the third strength theory or the fourth strength theory is needed to check the strength of the rock spreader structure. Because the fourth strength theory mainly considers the influence of the principal stress σ_2 , it is closer to reality than the third strength theory. Therefore, the static strength of the rock spreader structure is checked according to the stress value σ_e calculated by the fourth strength theory.

The von Mises stress can be expressed as

$$\sigma_e = \sqrt{\frac{1}{2} [(\sigma_1 - \sigma_2)^2 + (\sigma_2 - \sigma_3)^2 + (\sigma_3 - \sigma_1)^2]}, \quad (5)$$

where σ_1 , σ_2 , and σ_3 are the three principal stresses of any particle, and $\sigma_1 > \sigma_2 > \sigma_3$.

The strength check standard is as follows:

$$\sigma_e \leq [\sigma], \quad (6)$$

where σ_e is the maximum equivalent stress and $[\sigma]$ is the allowable stress.

The structural stiffness can be expressed as

$$[K]^e = [B]^T [D] [B] V, \quad (7)$$

where $[K]^e$ is the element stiffness matrix and V is the unit tetrahedral volume.

TABLE 4: Allowable stress under different working conditions.

Parameter name	Working condition I	Working condition II	Working condition III
Safety coefficient	1.5	1.33	1.2
Q345E (MPa)	230	259	288

The allowable tensile stress of Q345E used in the boom structure of the rock spreader is $[\sigma] = 345$ MPa, but the allowable safety factor is clearly different under different working conditions. According to the “code for the design of steel structure of mobile continuous bulk handling equipment,” different safety factors should be selected for the structure of rock spreader under different working conditions [36], and the allowable stress table is shown in Table 4.

According to “the code for design of steel structures,” the allowable deflection value of the boom of rock spreader is $L/250$ [39]. The length of the receiving boom is 50 m, so the allowable deflection is 250 mm. The length of discharging boom is 21.6 m, so the allowable deflection is 86.4 mm. The height of the main tower is 20 m, so the allowable deflection is 80 mm.

3.1.2. Establishment of the 3D Solid Model of the Key Structure. The assignment of structural material properties is as follows: elastic modulus $E = 210$ GPa, Poisson’s ratio $\mu = 3$, density $\rho = 7850$ kg/m³, and yield strength $\sigma = 345$ MPa. To improve the efficiency of simulation, on the basis of not affecting the accuracy of the key object, some secondary structural parts are simplified as follows [40]:

- (1) Some features such as threaded holes, fillets, and chamfers are simplified
- (2) The receiving conveyor, walking platform railing, driving device, and reversing device are added to the relevant boom in the form of load
- (3) The influence of the connecting plate on the structure is ignored
- (4) The weld and bolt connection are ignored
- (5) The wire rope is established by using the line body in the submodule “Geometry” of “ANSYS Mechanical”

The models of receiving boom, discharging boom, and main tower are shown in Figure 2.

3.1.3. Finite Element Solution and Analysis of Key Parts

(1) Finite Element Analysis of Receiving Boom. The guide rail at the left end of the receiving boom is supported by the guide wheel of the supporting trolley, so the translational degrees of freedom along the direction of the guide rail are released, and the degrees of freedom in other directions are limited. The right end lug is hinged with the fixed end lug of the unloading boom, so the degree of freedom of rotation around the hanging shaft is released at the hinge, and the degree of freedom in other directions is limited.

As shown in Figure 3, under working condition III, the maximum deformation of the receiving boom is 66.74 mm, which occurs in the center of the receiving boom span; the

maximum stress is 190.67 MPa, which occurs on the vertical steel plate at the left end of the receiving boom.

(2) Finite Element Analysis of Discharging Boom. According to the matching condition of the discharging boom and the rotary platform, its abutments can be set as a hinge joint; that is, it can limit the movement degree of freedom in XYZ direction and the rotation degree of freedom around X- and Z-axis and release the rotation degree of freedom around Y-axis. The connection between the strut and the hydraulic cylinder is hinged; that is, the movement degree of freedom in XYZ direction and the rotation degree of freedom around the X- and Z-axis are limited, and the rotation degree of freedom around the Y-axis is released.

When adding a load, in order to better simulate the load of walking platform railings and conveyors, the model is processed by the design modeler in ANSYS Workbench, and the imprint surface is added at the position where the load needs to be applied in the model, so as to apply the load more accurately [41].

It can be seen from Figure 4 that the total deformation displacement of the discharging boom under condition III is the largest, which occurs between the second and third hanging points, and the maximum deformation is 48.259 mm. Under condition III, the maximum stress of the discharging boom is 168.77 MPa, which occurs at the connection between the diagonal web member and the main chord between the two groups of suspension points, and the stress distribution in most other areas is about 90 MPa or less.

(3) Finite Element Analysis of Main Tower. It can be seen from Figure 5 that the maximum deformation of the tower under adverse conditions is 56.685 mm, and the maximum deformation occurs at the top of the main tower. The maximum stress value of the main tower is 218.06 MPa, and the maximum stress position occurs at the connection between the counterweight boom and the main tower. Because there is no stiffener at the junction of the original tower, the structure is relatively weak.

To sum up, by comparing the allowable values of stress in Table 4 and the allowable values of deflection and deformation mentioned above and analyzing Figures 3–5, it can be seen that the maximum stress value and maximum deflection and deformation value of key parts such as receiving boom, discharging boom, and main tower are within the safe range, but they are all abundant and have large optimization space. In addition, the distribution of stress and deflection in different parts is uneven, and the stress and deflection in many parts are very small, so it is difficult to play the maximum utility of materials.

3.2. Modal Analysis of Boom. The receiving boom and discharging boom are equipped with belt conveyors, driving

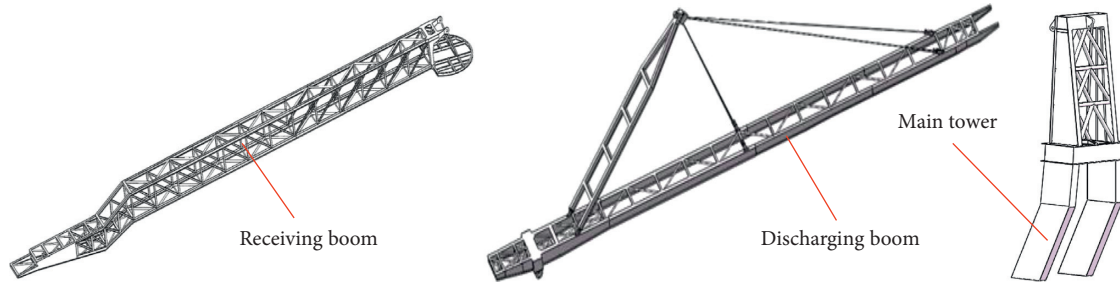
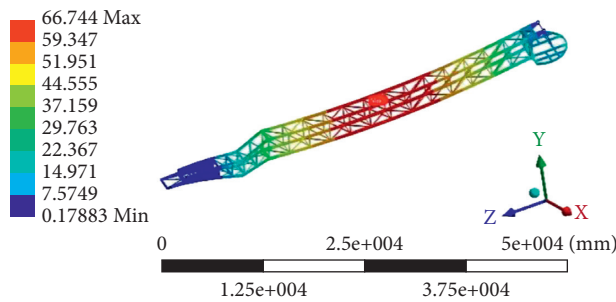


FIGURE 2: The models of receiving boom, discharging boom, and main tower.

I: gongkuang III
Total Deformation
Type: Total Deformation
Unit: mm
Time: 1



I: gongkuang III
Equivalent Stress
Type: Equivalent (von-Mises) Stress
Unit: MPa
Time: 1

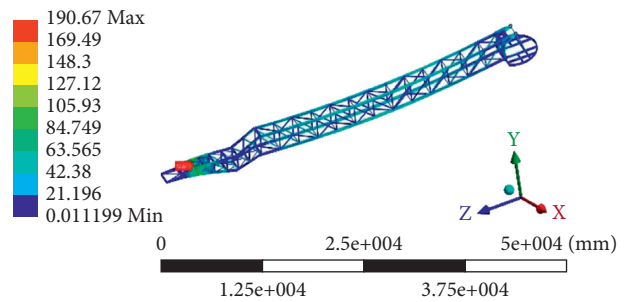
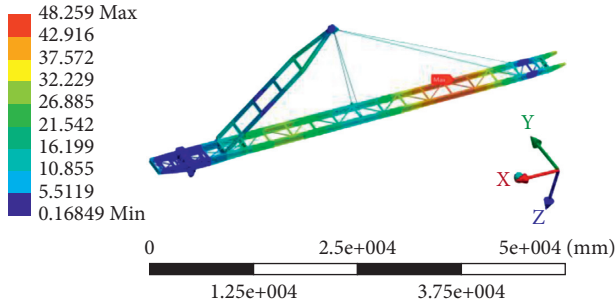


FIGURE 3: Deformation and stress nephogram of receiving boom under working condition III.

I: gongkuang III
Total Deformation
Type: Total Deformation
Unit: mm
Time: 1



I: gongkuang III
Equivalent Stress
Type: Equivalent (von-Mises) Stress
Unit: MPa
Time: 1

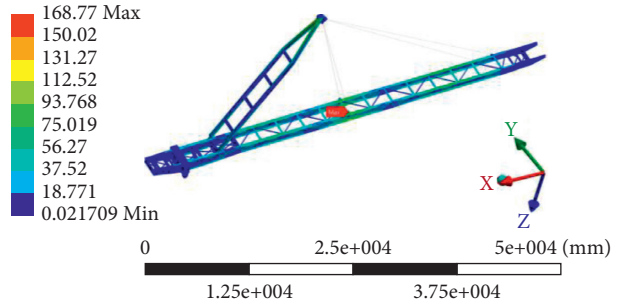


FIGURE 4: Deformation and stress nephogram of discharging boom under working condition III.

motors, idlers, etc. The periodic work of these parts will inevitably bring the excitation sources to the boom and affect the dynamic performance of the boom. The boom will produce complex vibration and deformation under the excitation of idler and motor, so the research on the dynamic characteristics of boom has a great impact on the safety and service life of boom. As the basis of dynamic analysis, modal analysis is a common method of structural dynamic characteristics analysis. Modal analysis can be used to solve the natural frequency and main mode of vibration of the boom of the rock spreader [42], and the frequency and resonance position of the boom of the rock spreader can be obtained.

According to the analysis results, the optimal design of the rock spreader can be carried out, which provides a theoretical basis for improving the dynamic characteristics of the boom.

When the speed of the driving motor is 1485 r/min, the excitation frequency of the driving motor is $f = 1485 / 60 = 24.75$ Hz. The roller rotation excitation should be calculated according to the belt speed. Under the rated working condition of the rock spreader, the belt speed $v = 4$ m/s, so the excitation frequency $f = 1000v / \pi d = 4000 / 159\pi = 8$ Hz. If the $\pm 15\%$ resonance band is selected [43], the resonance band caused by the idler is in the range of 6.8 Hz ~ 9.2 Hz.

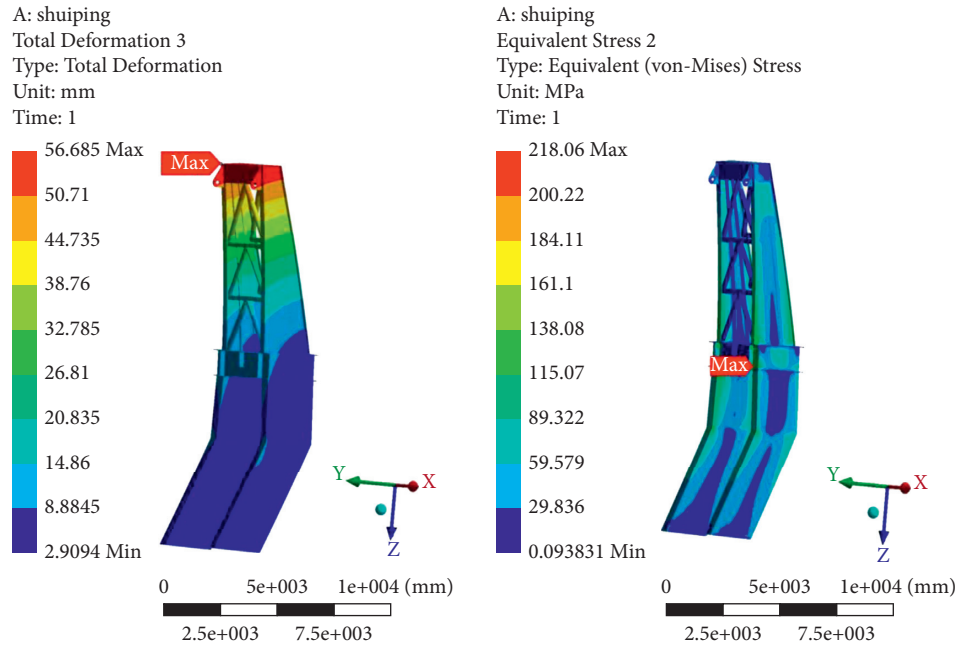


FIGURE 5: Deformation and stress nephogram of the main tower under severe working conditions.

3.2.1. Modal Analysis of Receiving Boom. Modal calculation of the receiving boom is carried out by the modal module in ANSYS Workbench. The degree of freedom around the x -axis is released at the hanging point of the right end of the receiving boom, and the other degrees of freedom are limited. The degrees of freedom of the left end of the boom along the z -axis are released, and all degrees of freedom in other directions are constrained. The first six modes of the boom can be obtained by solving the mode of the boom, as shown in Figure 6.

The frequency of the receiving boom is far from that of the motor, so it will not be affected by the vibration frequency of the motor. The fifth-order natural frequency of the receiving boom is 7.60 Hz, which is easy to cause resonance in the resonance band of the idler.

According to the vibration mode diagram of the first six modes in Figure 6 and the vibration mode description in Table 5, it can be seen that the stiffness of the head of the receiving boom is weak, and the multistage vibration modes show the maximum vibration mode at the head of the receiving boom. The first natural frequency of the receiving boom is low, so it is necessary to optimize the structure of the receiving boom, so as to improve the low natural frequency of the receiving boom, improve its dynamic performance, and reduce the risk of resonance.

3.2.2. Modal Analysis of Discharging Boom. In the same way, constraints are imposed on the discharging boom and modal analysis is carried out to obtain the first six modes. The calculation results are shown in Figure 7.

It can be seen from the above Figure 7 and Table 6 that the natural frequencies of each order of the discharging boom are far different from the excitation frequency of the motor, so the motor excitation will not cause resonance. However, the fifth- and sixth-order natural frequencies of

the discharging boom are 8.36 Hz and 8.93 Hz, respectively, which are all within the resonance band of the idler and are easy to cause resonance.

4. Lightweight of Key Parts of Rock Spreader

4.1. Basic Theory of Topology Optimization

4.1.1. Topology Optimization Based on the Variable Density Method [44, 45]. The topology optimization module of ANSYS Workbench uses the variable density method to optimize the structure topology. Firstly, the continuum structure is discretized by the finite element method, and the relationship between relative density and elastic modulus is expressed in the form of the density interpolation function of continuous variables. Then, taking the relative density of the elements as the optimization variable, each element corresponds to an optimization variable in the optimization process. By changing the value of each optimization variable, the elastic modulus of each element and the stiffness matrix of the structure are changed, so that the material is redistributed in the matrix model, and finally, the optimal structure meeting the stress, deformation, and other constraints is obtained.

4.1.2. Mathematical Algorithm for Topology Optimization [44–46]. The Lagrange multiplier method is an important method to solve the extremum problem and conditional stationary value problem. Its central idea is to transform the extremum problem of original function under constraint condition into the extremum problem of the functional under unconstrained conditions, that is, to complete the transformation from a constrained optimization problem to an unconstrained optimization problem. Since the

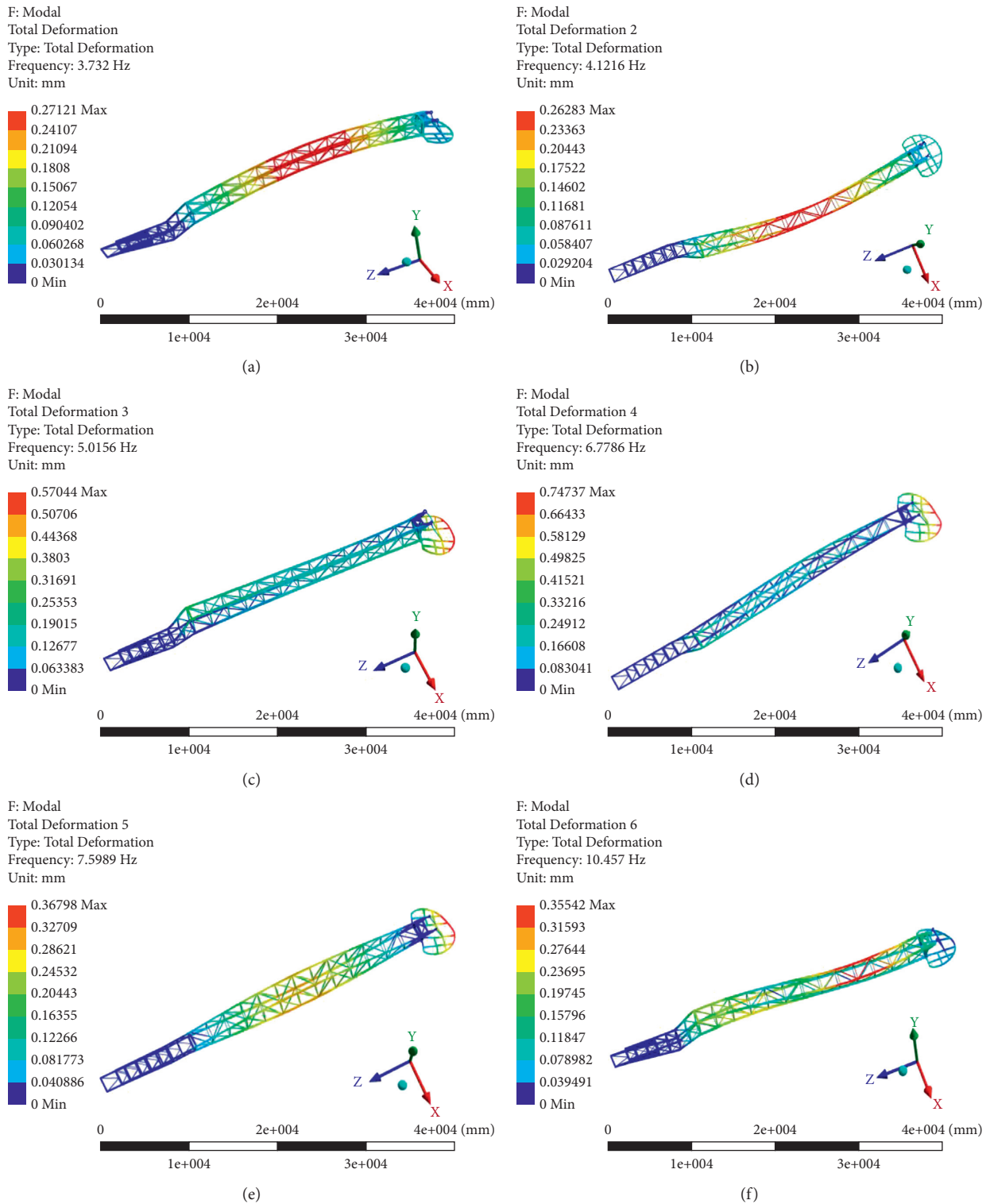


FIGURE 6: The vibration mode diagram of the first six modes of the receiving boom before optimization. (a) The first mode. (b) The second mode. (c) The third mode. (d) The fourth mode. (e) The fifth mode. (f) The sixth mode.

introduction of the Lagrange multiplier method simplifies the mathematical calculation process, the Lagrange multiplier method is selected to solve the variable density topology optimization problems.

It is assumed that the density of each virtual cell in the topology optimization space is ρ_i , and the actual density of the optimized space is ρ_0 . The relationship between the virtual density ρ_i and actual density ρ_0 can be expressed as follows:

TABLE 5: Description of the first six natural frequencies and vibration modes of receiving boom.

Order	Natural frequency (Hz)	Total amplitude (mm)	Mode shapes
1	3.73	0.27	The midspan is bent in the positive direction of the y-axis
2	4.12	0.27	The midspan is bent in the positive direction of the x-axis
3	5.02	0.58	The whole boom is slightly twisted, and the head of the receiving boom is twisted along the x-axis
4	6.78	0.75	The tail of the boom turns to the positive direction of the x-axis, and the head of the boom turns around the y-axis
5	7.60	0.37	The middle of the boom is twisted around the z-axis, and the head is about the x-axis
6	10.46	0.36	The position near the tail of the boom turns to the negative direction of the x-axis, and the position near the head turns to the positive direction of the x-axis

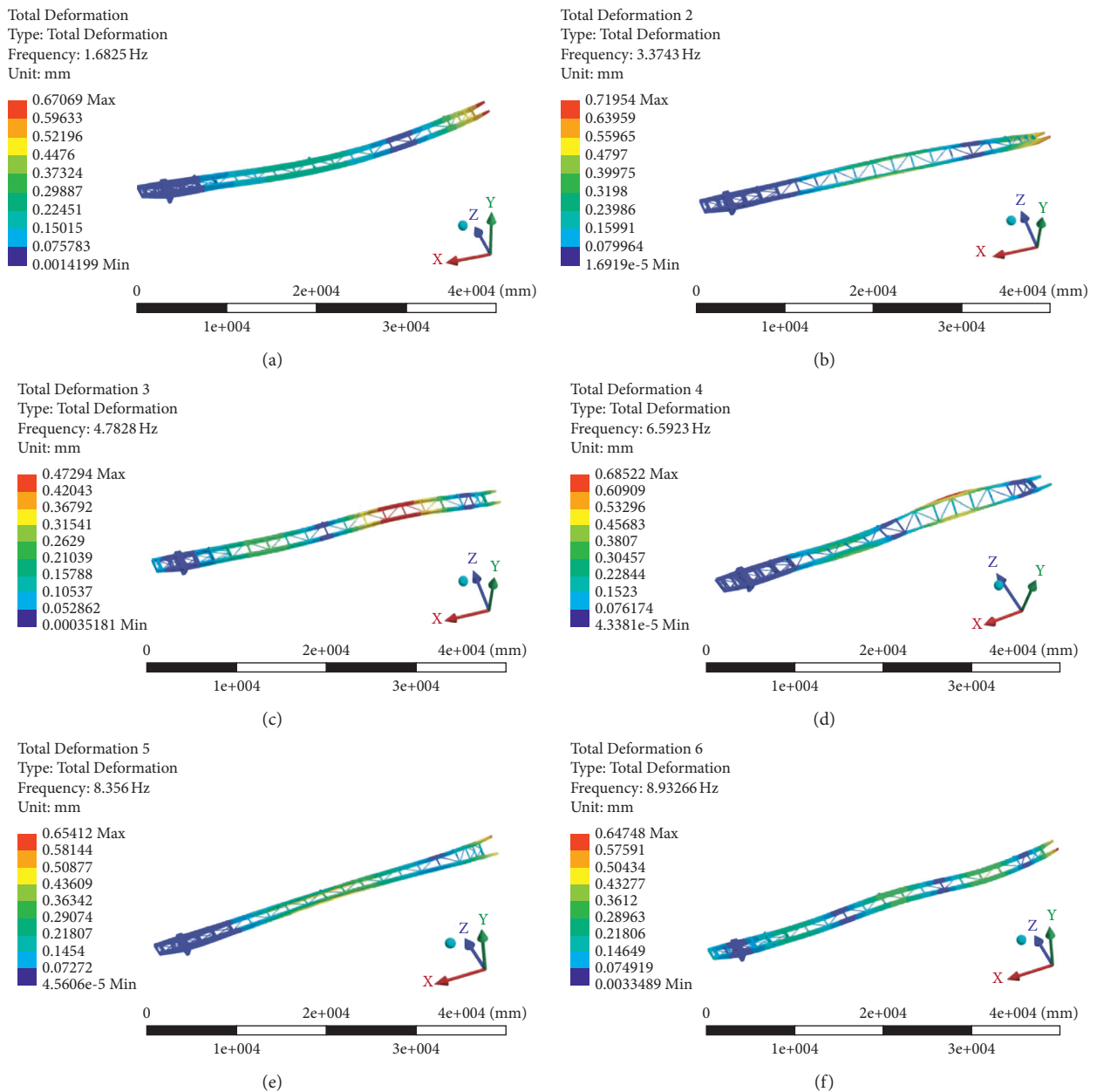


FIGURE 7: The vibration mode diagram of the first six modes of the discharging boom before optimization. (a) The first mode. (b) The second mode. (c) The third mode. (d) The fourth mode. (e) The fifth mode. (f) The sixth mode.

TABLE 6: Description of first six natural frequencies and vibration modes of receiving boom.

Order	Natural frequency/ Hz	Total amplitude/ mm	Mode shapes
1	1.68	0.67	The middle span is around the Z-axis and bending in the positive direction of the y-axis
2	3.37	0.72	The head of the boom is twisted around the x-axis
3	4.78	0.47	Bending occurs between two groups of hanging points of boom
4	6.59	0.69	The two groups of hanging points of the boom are twisted in the opposite direction around the x-axis
5	8.36	0.65	The midspan and the head of the boom twist in the opposite direction of the x-axis
6	8.93	0.65	The whole boom is bent around Z-axis in the XY plane

$$\rho_i = x_i \rho_0, \quad (8)$$

$$C = F^T U = U^T K U. \quad (12)$$

where x_i is the relative density of elements and i is the total number of all elements in the optimization space.

Then, when the relative density $x_i = 1$, it means that the entity is here; when the relative density $x_i = 0$, it means that the hole is hollowed out. The relative density x_i is defined as the threshold value in the software. Setting different threshold values, the topological results are different. Of course, it is necessary to ensure that $0 \leq x_i \leq 1$. To make the relative density x_i converge to 0 or 1, a penalty factor p is introduced. K_i is used to represent the relative stiffness of the i -th element, and K_0 represents the inherent stiffness of the topological space. The relationship between relative stiffness and inherent stiffness is as follows:

$$K_i = (x_i)^p K_0. \quad (9)$$

According to Hooke's Law,

$$F = K U, \quad (10)$$

where F is the load, K is the stiffness matrix, and U is the displacement.

The flexibility and stiffness are reciprocal to each other. If the flexibility is C , that is,

$$C = \frac{1}{K}. \quad (11)$$

Substituting equation (11) into equation (10), we can obtain the following results:

$$L = C + \lambda_0 (V - fV_0 - V_1) + \lambda_1^T (K U - F) + \sum_{i=1}^n \lambda_2^i (x_{\min} - x_i) + \sum_{i=1}^n \lambda_3^i (x_i - x_{\min}). \quad (14)$$

When the function takes the extremum,

$$\frac{\partial L}{\partial x_i} = 0, \quad i = 1, 2, \dots, n. \quad (15)$$

By deriving x_i from both sides of equation (14) and simplifying it, the following equation can be obtained:

$$\frac{\partial L}{\partial x_i} = \frac{\partial U^T}{\partial x_i} K U + U^T \frac{\partial K}{\partial x_i} + U^T K \frac{\partial U}{\partial x_i} + \lambda_0 V_i + \lambda_1^T \left(\frac{\partial K}{\partial x_i} U + K \frac{\partial U}{\partial x_i} \right). \quad (16)$$

The objective of topology optimization is to minimize the flexibility of the structure, that is, to maximize the material stiffness. The volume ratio before and after optimization is taken as the constraint condition. The relative density of each unit in the topology optimization space is taken as the design variable. On the basis of the above, the mathematical model of topology optimization can be obtained as follows:

$$\begin{aligned} \text{Design variable: } X &= \{x_1, x_2, \dots, x_n\}^T \\ \text{Objective function: } C &= \min F(X) = F^T U \\ \text{Constraints: } k &\geq V_1/V_0 \end{aligned}$$

$$\begin{aligned} 0 < x_{\min} \leq x_i \leq x_{\max} \leq 1 \\ F &= K U, \end{aligned} \quad (13)$$

where k is the set ratio of surplus material, which is the decisive parameter to be set before topology optimization, and v_1 is the total volume before topology optimization; x_{\min} and x_{\max} are the minimum value and the maximum value of the relative density value x_i of the element, respectively. Limiting the value range of x_i can ensure that the structure will not produce a singular total stiffness matrix.

Based on the mathematical model of topology optimization and Lagrange multiplier method, the constructed function can be expressed as follows:

By deriving x_i from both sides of equation (10), the following equation can be obtained:

$$\frac{\partial F}{\partial x_i} = \frac{\partial F}{\partial x_i} U + K \frac{\partial U}{\partial x_i} = 0. \quad (17)$$

Taking equation (17) into equation (16), the following equation can be obtained:

$$\frac{\partial L}{\partial x_i} = U^T \frac{\partial K}{\partial x_i} U + \lambda_0 V_i + \lambda_1^T \frac{\partial K}{\partial x_i} + \frac{\partial U}{\partial x_i} (2U^T + \lambda_1^T K), \quad (18)$$

where λ_1^T takes any value. From equations (9) and (18), when function (14) takes the extreme value, that is, $\partial L/\partial x_i = 0$, the following can be obtained:

$$P(x_i)^{P-1} U_i^T K_0 U_i = \lambda_0 V_i. \quad (19)$$

Taking equation (9) into equation (19) and multiplying x_i^m at both ends of the equation, the following is obtained:

$$P(x_i)^{m-1} U_i^T K U_i = \lambda_0 V_i x_i^m. \quad (20)$$

Let $\varepsilon_i = (x_i)^{m-1} U_i^T K U_i$, and substitute it into equation (20):

$$x_i = \left(\frac{P\varepsilon_i}{\lambda_0 V_i} \right)^{\frac{1}{m}} (x_{\min} < x_i \leq 1),$$

$$x_i = \left(\frac{\varepsilon_i}{V_i} \right)^{1/m} \left\{ \frac{fV_0 + \sum_{j=1}^k V_j x_{\min}}{\sum_{j=1}^n V_j (\varepsilon_j/V_j)^{1/m}} \right\} (x_{\min} < x_i \leq 1). \quad (21)$$

Here, k represents the number of elements $x_i \leq 1$ and the iterative equation of x_i can be expressed as follows:

$$\text{When } x_{\min} < x_i \leq 1, \quad x_i = (\varepsilon_i/V_i)^{1/m} \left\{ (fV_0 + \sum_{j=1}^k V_j x_{\min}) / (\sum_{j=1}^n V_j (\varepsilon_j/V_j)^{1/m}) \right\}$$

When $x_i > 1$, it is not in line with the actual situation, so $x_i^{z+1} = 1$

When $x_i \leq x_{\min}$, the relative density exceeds the lower limit, so $x_i^{z+1} = x_{\min}$

The above list is the mathematical calculation process of applying the Lagrange multiplier method to solve topology optimization problems based on the variable density method. As long as the volume ratio before and after topology optimization is limited, the virtual density of each unit in the design space can be calculated through a certain number of iterations. If the density of a place is 1, it means that it is reserved; if the density is zero, it means that it is set as a hole; if the density is between the two, it means that part of it is reserved, so the topology optimization problem can be solved.

The topology optimization process in ANSYS Workbench is shown in Figure 8.

4.2. Topology Optimization Analysis

4.2.1. Topological Matrix Model. Before topology optimization of structures, it is necessary to establish a reasonable matrix model for topology optimization. In general, the initial model should be larger than or equal to the outer dimension of the original structure. According to the design input of receiving boom, discharging boom, and main tower overall shape and actual working condition, the topology optimization matrix model of key parts as shown in Figure 9 is established by using SolidWorks software.

4.2.2. Topology Optimization Calculation. Topology optimization is completed on the premise that the strength and stiffness meet the requirements. In ANSYS Workbench, the

design variables, objective functions, and constraints are defined, and the value of residual material proportion k is set, which is consistent with the value of residual material proportion k set by the Lagrange multiplier method in the previous theory. The topology optimization module can iterate the relative density according to the input percentage of retained materials and finally remove the region of materials with a relative density of less than 1. After the previous calculation, the percentage of retained material is in the range of 70%~90%, and the convergence effect is good. Five groups of topology optimization calculations with material removal percentages of 15%, 16%, 17%, 18%, 19%, and 20% are carried out for receiving boom and discharging boom structure. The topology structure diagram is shown in Figures 10 and 11.

Five groups of topology optimization calculation with material removal percentages of 17%, 18%, 19%, 20%, 21%, and 22% are carried out for the main tower structure. The topology structure is shown in Figure 12.

According to the uniformity and rationality of the structure distribution obtained by topology optimization of different k values, and combined with the particularity of field application conditions, $k=0.18$ is adopted for the receiving arm, discharging arm, and the main tower as the basis for subsequent reconstruction.

4.2.3. Model Reconstruction after Optimization. There are many irregular parts in the model after topology optimization, so we need to follow the principle of manufacturability when reconstructing the model:

- (1) In the process of repairing the model, we need to consider manufacturability. We need to use the straight bar instead of the bending part in the topology optimization results. On the one hand, the bending web member is not easy to produce, which will increase the production cost; on the other hand, the bent web member may affect the installation of other parts. Therefore, under the condition of keeping the whole structure unchanged, the bending web members after topology optimization are changed into straight web members
- (2) Because not all cell densities are 0 or 1 after topology optimization, there are some unreasonable local positions that need to be modified in the topology optimization results. When repairing the model, it should be noted that the color lighter part is the middle density unit, which is the removable unit
- (3) To ensure the lightweight of the boom, we try to use the bar to replace the plate, which can also maximize the lightweight of the boom
- (4) In the reconstruction process, we try to make the members form a triangle connection, because more triangles will make the boom structure more stable and the stiffness of the boom will be improved
- (5) The original structure of the connection part between the two ends of the boom and the rest of the rock spreader should not be changed as far as possible, so as to ensure the normal assembly of the parts

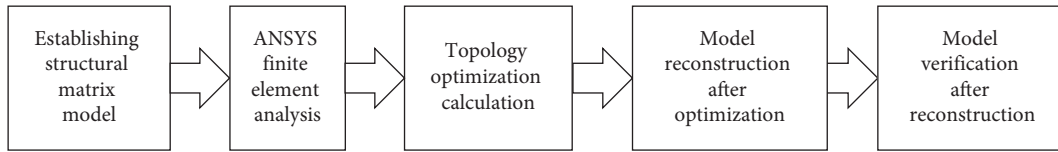


FIGURE 8: Topology optimization process.

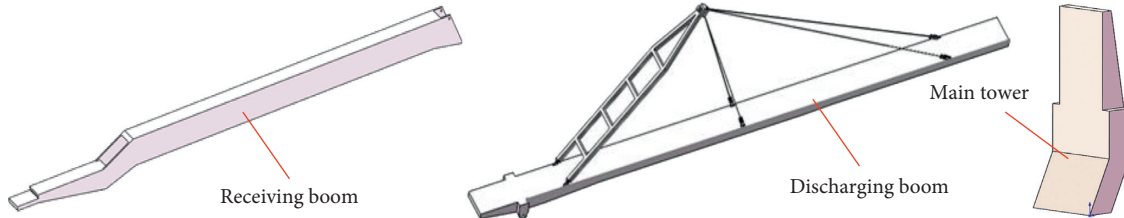


FIGURE 9: Topological matrix model.

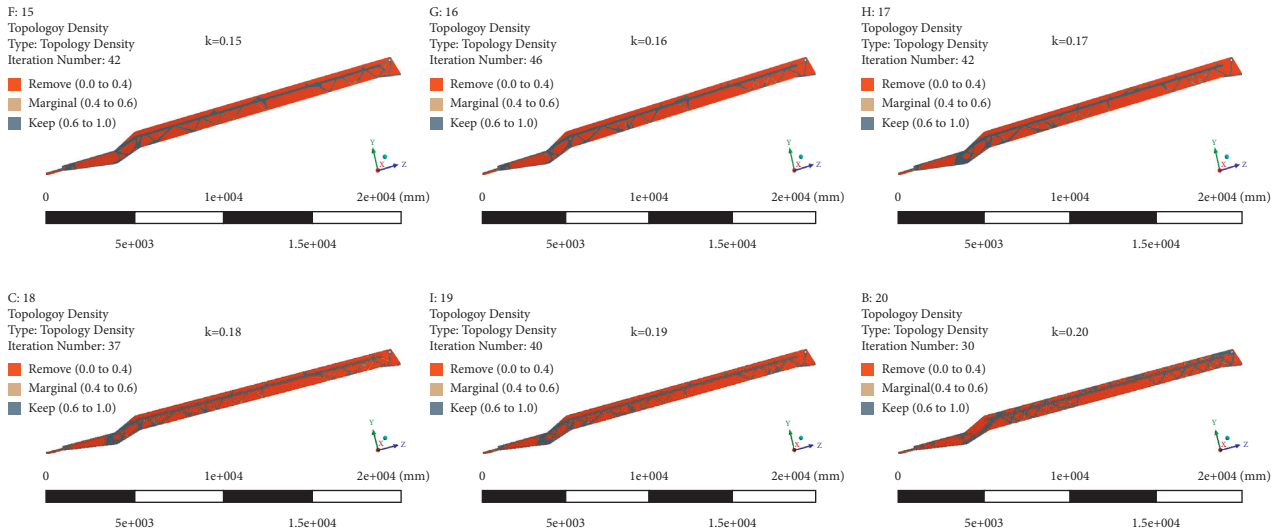


FIGURE 10: Topological structure of receiving boom.

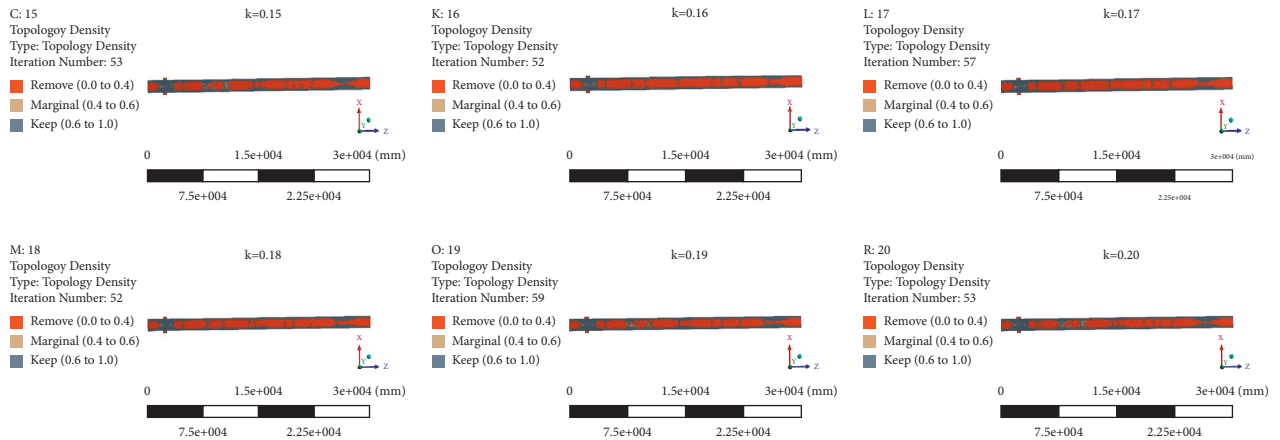


FIGURE 11: Topological structure of discharging boom.

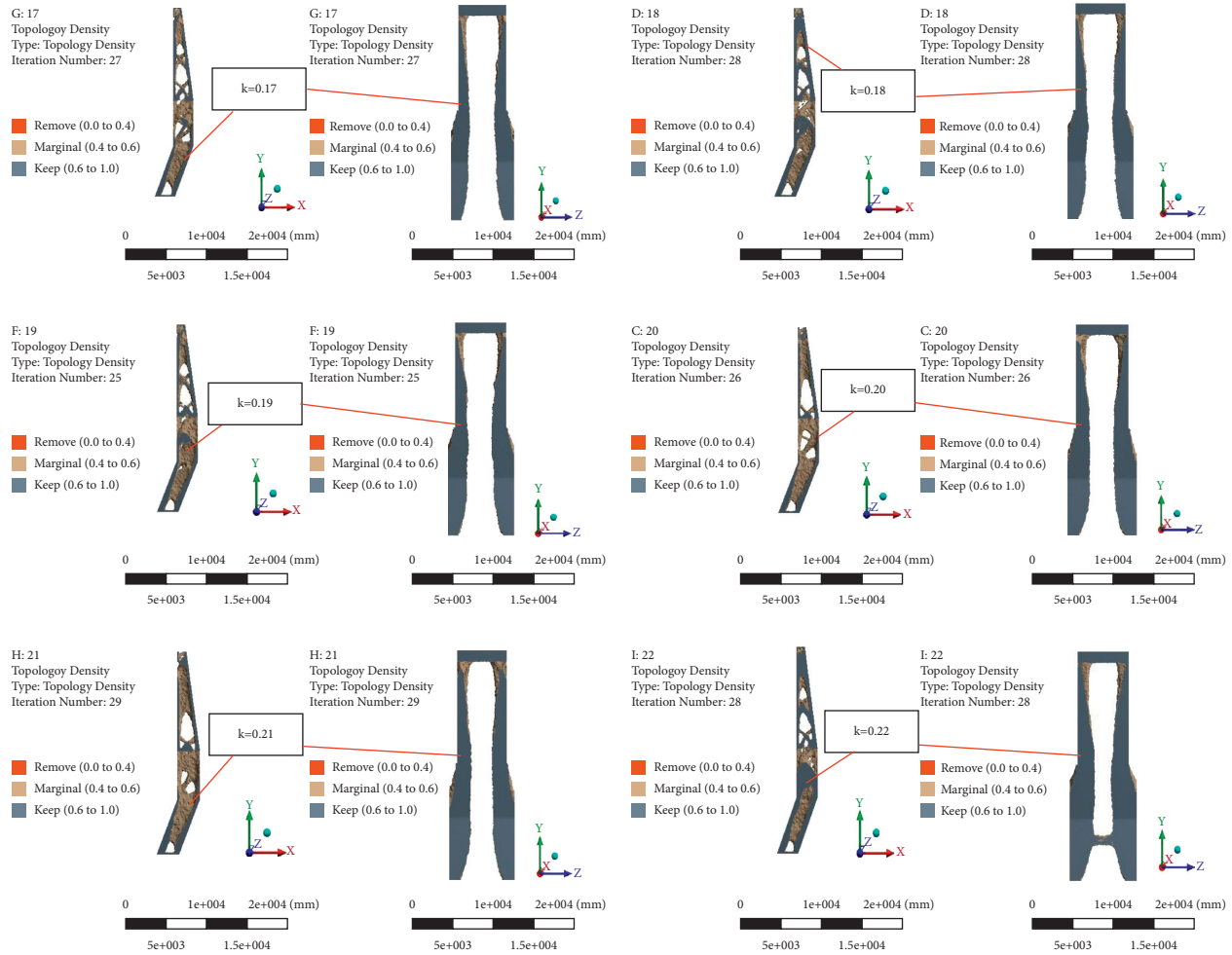


FIGURE 12: Topological structure of the main tower.

The optimized models of receiving boom, discharging boom, and main tower are shown in Figure 13. The weight comparison of key parts before and after optimization is shown in Table 7.

4.2.4. Model Verification after Optimization

(1) *Verification of Receiving Boom after Optimization.* Referring to the previous method and the process of calculating the static and dynamic characteristics of the receiving boom, the static simulation and modal analysis of the optimized receiving boom are carried out. The deformation and stress distribution of the receiving boom under optimized condition III are shown in Figure 14; the comparison of deformation and stress before and after optimization is shown in Table 8. The low-order modal shapes of the optimized boom are shown in Figure 15, and the dynamic performance comparison before and after optimization is shown in Table 9.

It can be seen from Figure 14 and Table 8 that, under the worst condition III, the maximum deformation of the receiving boom after optimization is reduced by 10.8% compared with that before optimization. The maximum

stress is increased by 6.2%, but it is still in the safe range, and the stress of the optimized boom tends to be uniform, so it is obvious that the new structure is more reasonable.

According to Figure 15 and Table 9, after optimization, the multistage amplitude of the receiving boom decreases, and its stiffness is improved to a certain extent. After optimization, all low-order natural frequencies of the boom are improved to a certain extent, especially the 5th-order frequency is changed from 6.78 Hz to 9.32 Hz, which is 38.68% higher than that before optimization, avoiding the resonance band caused by the idler. The improvement of the natural frequency of the receiving boom means the improvement of the overall stiffness of the boom, which makes the operation of the rock spreader more stable.

(2) *Verification of Discharging Boom after Optimization.* Referring to the previous method and the process of calculating the static and dynamic characteristics of the discharging boom, the static simulation and modal analysis of the optimized discharging boom are carried out. The deformation and stress distribution of the discharging boom under optimized condition III are shown in Figure 16. The comparison of deformation and stress before and after



FIGURE 13: Model reconstruction after topology optimization.

TABLE 7: Weights comparison of key parts before and after optimization.

Parameter name	Before optimization	After optimization	Changes (%)
Receiving boom (kg)	35917	34125	-5
Discharging boom (kg)	26303	25222	-4.1
Main tower (kg)	41429	39652	-4.5

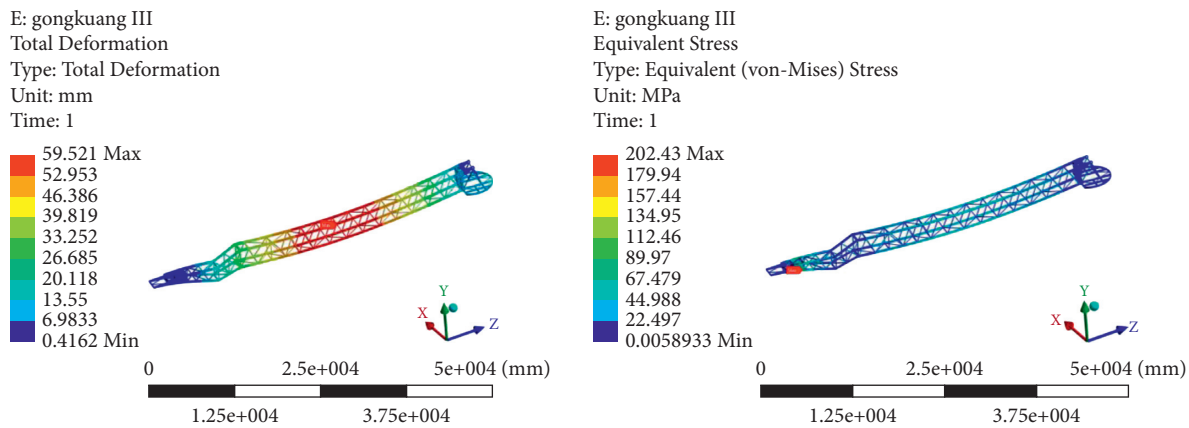


FIGURE 14: Deformation and stress nephogram of the optimized receiving boom under condition III.

TABLE 8: Comparison of maximum stress and deflection before and after optimization of receiving boom.

Parameter name	Before optimization	After optimization	Changes (%)
Maximum deflection deformation (mm)	66.74	59.52	-10.8
Maximum stress (MPa)	190.67	202.43	+6.2

optimization is shown in Table 9. The low-order modal shapes of the optimized discharging boom are shown in Figure 17, and the dynamic performance comparison before and after optimization is shown in Table 10.

It can be seen from Figure 16 and Table 10 that under the worst condition III, the maximum deformation of the optimized discharging boom increases by 12.7%, and the maximum stress increases by 16.8%, but they are within the safe range. It is worth noting that the maximum stress and deformation of the new structure are more evenly distributed and the design is more reasonable.

It can be seen from Figure 17 and Table 11 that the fifth-order frequency of the discharging boom before the optimization is within the resonant frequency range of the idler, while the first five order modes after optimization avoid the resonant frequency of the idler, which improves the dynamic characteristics of the discharging boom to a certain extent.

(3) *Verification of the Whole Machine Virtual Prototype.* To verify whether the structure of the rock spreader meets the overall load requirements after optimization, the optimized receiving boom, discharging boom, and main tower are reconstructed and verified by finite element analysis.

The action of the receiving boom is the most frequent during the operation of the rock spreader. This section mainly focuses on the stress and deformation of the receiving boom of the rock spreader under the rated load, wind load, and seismic load at the upper, horizontal, and lower positions. Finite element analysis is carried out for the whole machine model assembled after topology optimization, in which the material properties, loads, and boundary conditions are set the same as those for single part analysis, and the finite element model is shown in Figure 18.

The simulation analysis is carried out for the three main positions of the upper row, the lower row, and the horizontal row of the rock spreader under dangerous working

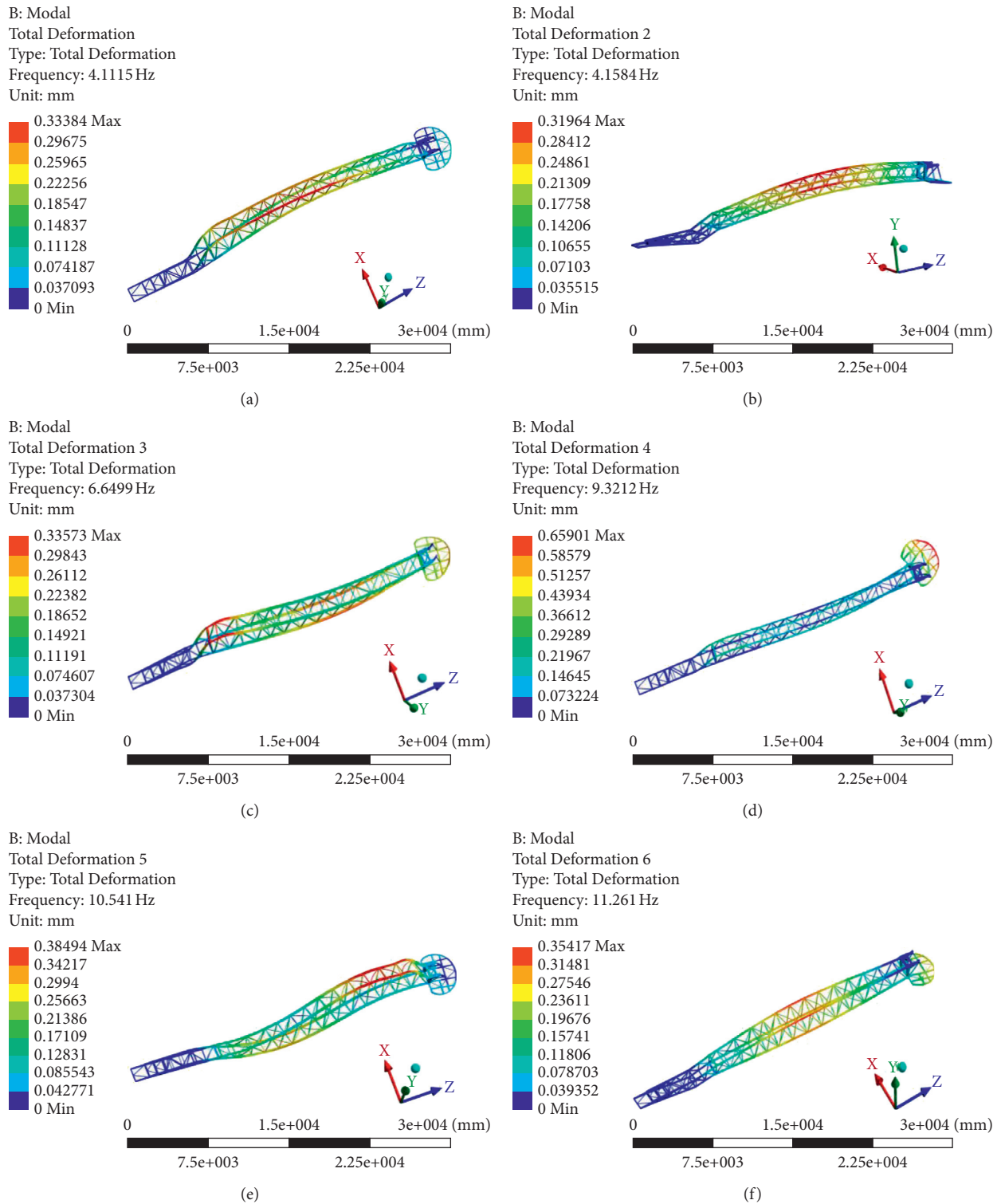


FIGURE 15: The vibration mode diagram of the first six modes of the receiving boom after optimization. (a) The first mode. (b) The second mode. (c) The third mode. (d) The fourth mode. (e) The fifth mode. (f) The sixth mode.

conditions. The deformation and stress nephogram of three different working positions are shown in Figure 19–21.

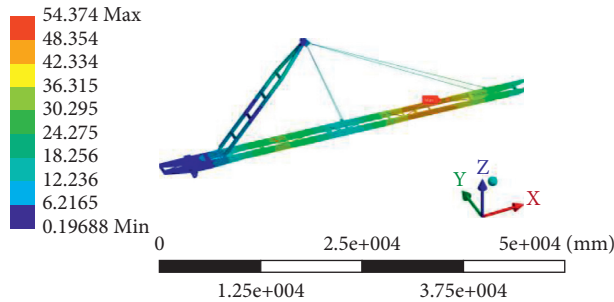
It can be seen from Figures 19–21 and Table 12 that the maximum deformation under three different working conditions occurs at the midspan position of the receiving

boom. The maximum stress occurs at the vertical steel plate on the left side of the receiving boom. Among them, the maximum deflection and maximum stress of the rock spreader under the upper discharge condition are larger, which are 57.72 mm and 218.41 MPa, respectively, but both

TABLE 9: Comparison of the dynamic performance of receiving boom before and after optimization.

Frequency order	Before optimization	After optimization	Changes (%)
1	3.73	4.11	+10.19
2	4.12	4.16	+0.97
3	5.02	6.65	+32.47
4	6.78	9.32	+37.46
5	7.60	10.54	+38.68
6	10.46	11.26	+7.65

U: gongkuang III
 Total Deformation
 Type: Total Deformation
 Unit: mm
 Time: 1



U: gongkuang III
 Equivalent Stress
 Type: Equivalent (von-Mises) Stress
 Unit: MPa
 Time: 1

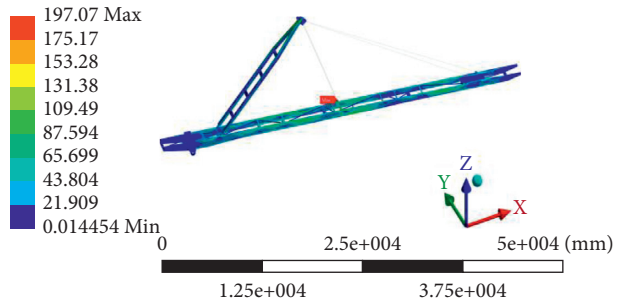
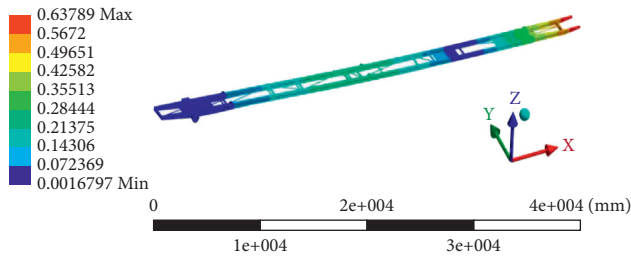


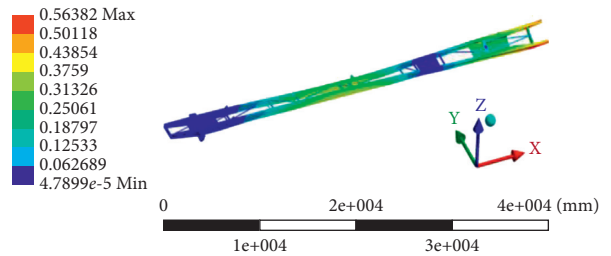
FIGURE 16: Deformation and stress nephogram of the optimized discharging boom under condition III.

Total Deformation
 Type: Total Deformation
 Frequency: 1.4377 Hz
 Unit: mm



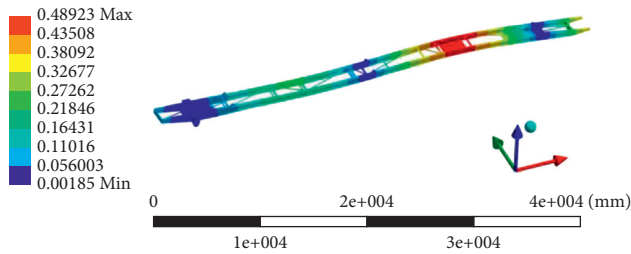
(a)

Total Deformation 2
 Type: Total Deformation
 Frequency: 3.2319 Hz
 Unit: mm



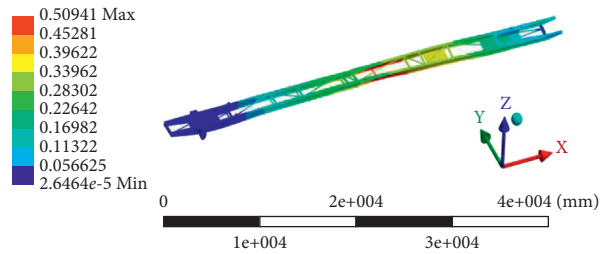
(b)

Total Deformation 3
 Type: Total Deformation
 Frequency: 4.681 Hz
 Unit: mm



(c)

Total Deformation 4
 Type: Total Deformation
 Frequency: 5.0944 Hz
 Unit: mm



(d)

FIGURE 17: Continued.

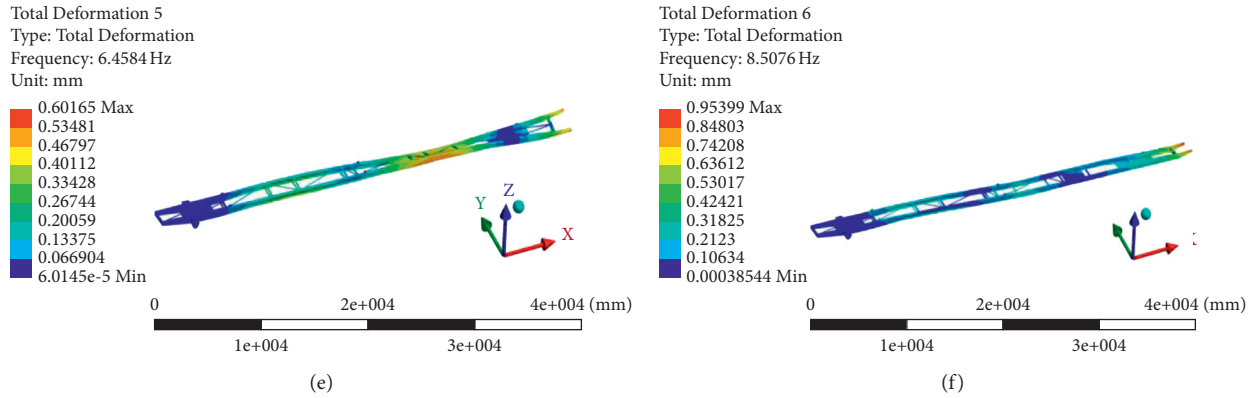


FIGURE 17: The vibration mode diagram of the first six modes of the discharging boom after optimization. (a) The first mode. (b) The second mode. (c) The third mode. (d) The fourth mode. (e) The fifth mode. (f) The sixth mode.

TABLE 10: Comparison of maximum stress and deflection before and after optimization of discharging boom.

Parameter name	Before optimization	After optimization	Changes (%)
Maximum deflection deformation (mm)	48.26	54.37	+12.7
Maximum stress (MPa)	168.77	197.07	+16.8

TABLE 11: Comparison of dynamic performance of discharging boom before and after optimization.

Frequency order	Before optimization	After optimization	Changes (%)
1	1.68	1.44	-14.28
2	3.37	3.23	-4.15
3	4.78	4.68	-2.09
4	6.59	5.09	-22.76
5	8.36	6.46	-22.73
6	8.93	8.51	-4.70

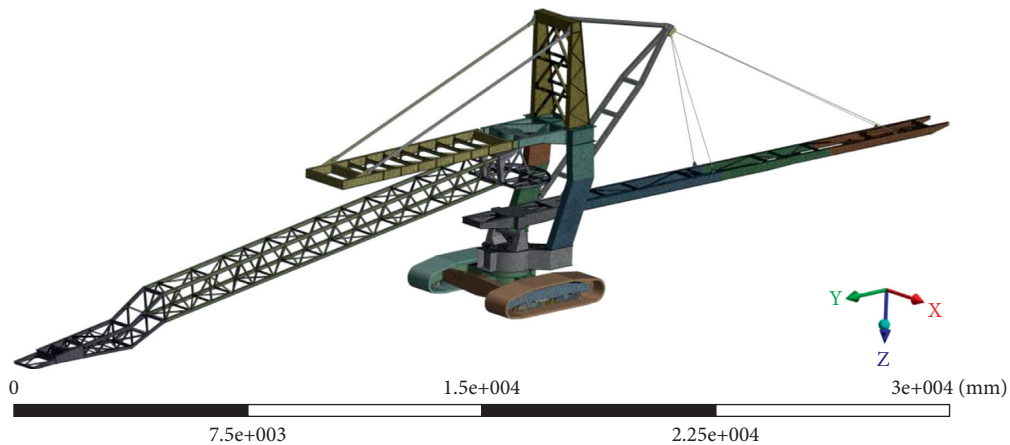


FIGURE 18: Assembly machine model after topology optimization.

are within the safe range and meet the engineering requirements. It can be seen from Table 7 that the weight of the receiving boom, discharging boom, and main tower is reduced by 5%, 4.1%, and 4.5%, respectively. It can be seen that the topology lightweight of each key structural part

not only reduces the weight of the whole machine and reduces the production cost and power of the equipment but also reduces the grounding pressure of the rock spreader to a certain extent and improves the safety of the rock spreader.

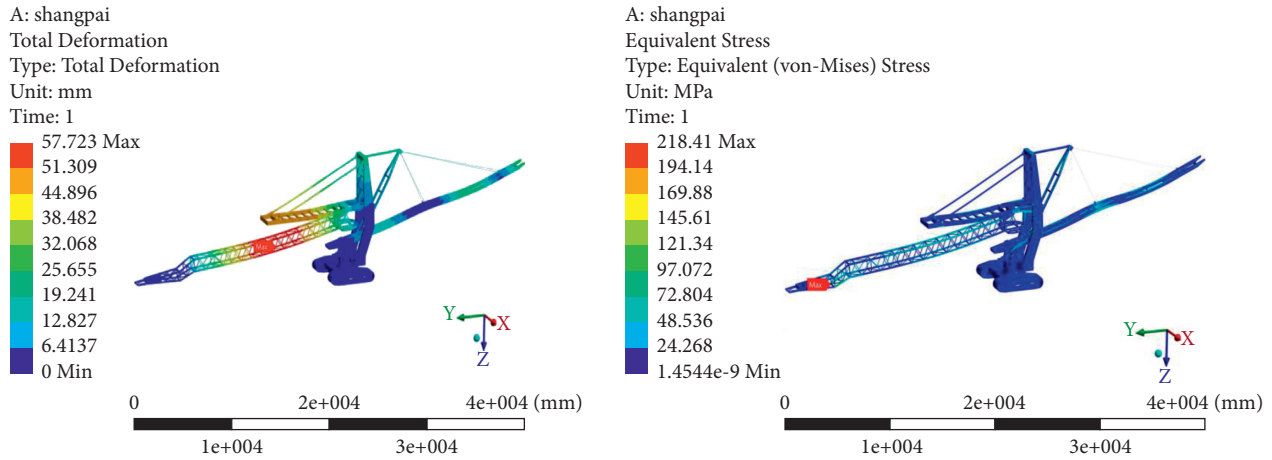


FIGURE 19: Deflection deformation and stress nephogram of the whole machine structure under the upper position.

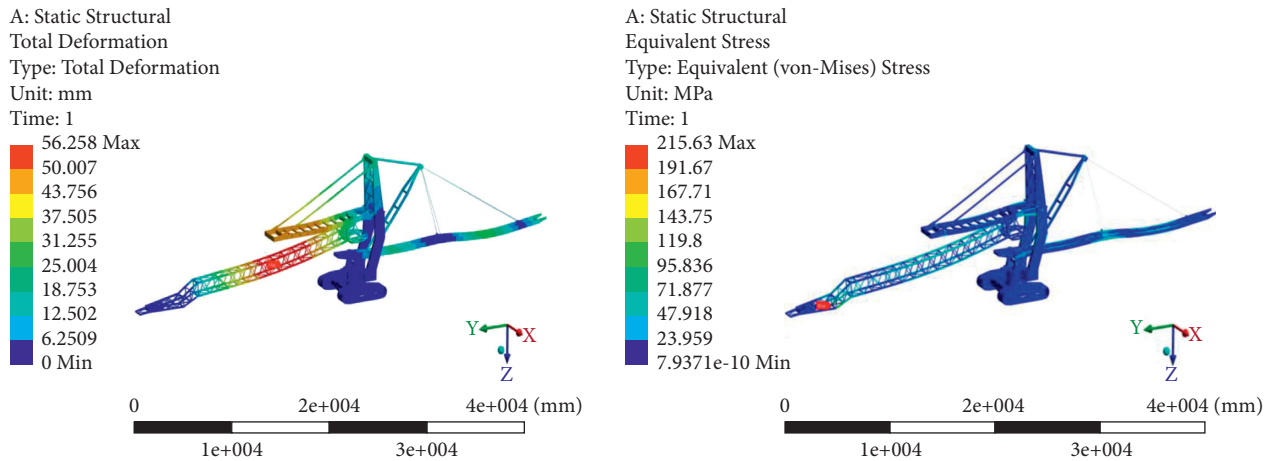


FIGURE 20: Deflection deformation and stress nephogram of the whole machine structure under the horizontal position.

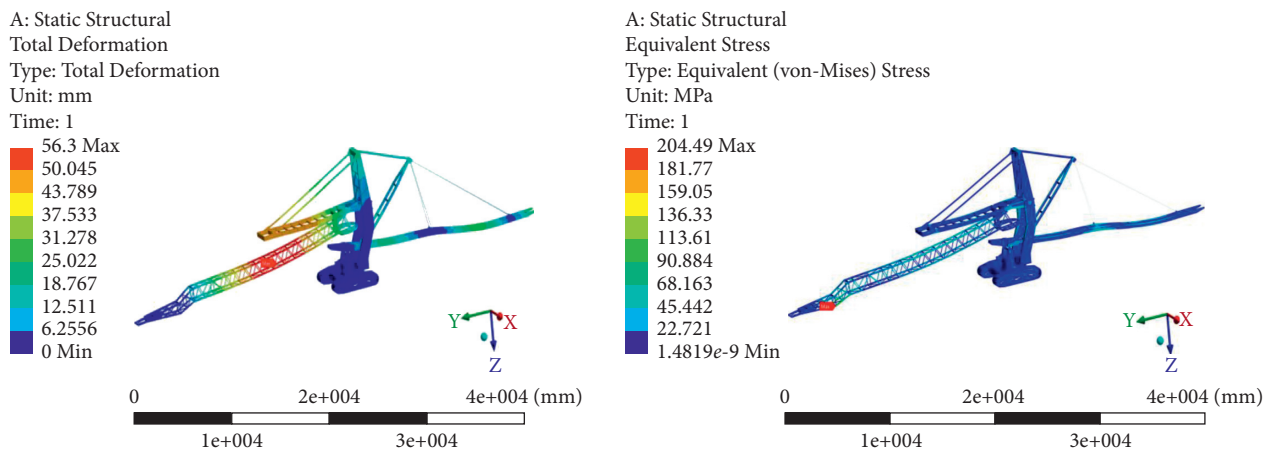


FIGURE 21: Deflection deformation and stress nephogram of the whole machine structure under the lower position.

TABLE 12: Maximum deformation and stress values of rock spreader at different working positions.

Parameter name	Maximum deflection deformation (mm)	Maximum stress (MPa)
The upper position	57.72	218.41
The horizontal position	56.26	215.63
The lower position	56.30	204.49

5. Conclusion

- (1) The actual load characteristic analysis, structural topology optimization and reconstruction, static and dynamic simulation of each optimized part, and static and dynamic performance analysis of the whole machine verify the correctness of the optimization of the key structure of the rock spreader. A set of topology optimization design theories and methods suitable for the key main structural parts of a large rock spreader is formed, which solves the problems of its large vibration and poor discharge uniformity
- (2) After the topology optimization of the key parts, the following conclusions are obtained in terms of stability. ① The multistage amplitude of the receiving boom decreases, which improves its stiffness to a certain extent. And its low-order natural frequencies are improved, avoiding the resonance band caused by the idler. ② The first five modes of the discharging boom avoid the resonance frequency of the idler, which improves the dynamic characteristics of the boom to a certain extent. ③ Compared with before optimization, the weight of receiving boom, discharging boom, and main tower can be reduced by 5.0%, 4.1%, and 4.5%, respectively, but their stress distributions are more uniform and their structures are more reasonable
- (3) The optimized key structures of the rock spreader are assembled and the virtual prototype is established. Under the worst working conditions, the maximum deflection deformation and the maximum equivalent stress of the receiving boom, discharging boom, and main tower after optimization are in the safe range, which can meet the working requirements of the rock spreader. The correctness of topology optimization lightweight design is verified.

Data Availability

The data used to support the findings of this study are available from the corresponding author upon request.

Conflicts of Interest

The authors declare that they have no conflicts of interest.

Acknowledgments

This work was supported by the Foundations of Key R&D Projects of Shanxi Province (International Scientific and Technological Cooperation), China (Grant no.

201803D421041), Major Science and Technology Projects of Shanxi Province, China (Grant no. 20181101017), and Applied Basic Research Project of Shanxi Province, China (Grant no. 201701D121017).

References

- [1] C. G. Gong, Z. F. Bian, H. F. Bian et al., "Key technology of DEM model construction based on UAV and vegetation index in dump soil field," *Journal of China Coal Society*, vol. 44, no. 12, pp. 3849–3858, 2019.
- [2] Y. Zhou, "Dynamic analysis of statically determinate portal structure of double-crawler spreader," Master's Thesis, Tsinghua University, Beijing, China, 2012.
- [3] L. F. Ma, Z. Yang, Y. Zhang, Z. X. Wang, F. B. Wu, and Z. Q. Yao, "Technical development and application of heavy spreader," *Heavy Machinery*, vol. 2020, no. 5, pp. 14–18, 2020.
- [4] Z. Z. Zhang, "Study on mining technology in the second mining area of weijiamao open-pit coal mine," master's thesis, Inner Mongolia University of Science & Technology, Inner Mongolia, Baotou, China, 2014.
- [5] H. Zhong, "Application of semi continuous mining technology in open pit mine," *Coal Engineering*, vol. 42, no. 10, pp. 7–9, 2012.
- [6] T. M. Han, "Selection and design of related equipment for production system in Apartak Open -pit Coal Mine," *Open pit mining technology*, vol. 36, no. 3, pp. 84–86, 2021.
- [7] J. Chang, T. Hu, X. Liu, and X. Ren, "Construction of green infrastructure in coal-resource based city: a case study in Xuzhou urban area," *International Journal of Coal Science & Technology Technology*, vol. 5, no. 1, pp. 92–104, 2018.
- [8] N. D. Rose and O. Hungr, "Forecasting potential rock slope failure in open pit mines using the inverse-velocity method-Case examples," in *Proceedings of the 1st Canada-US Rock Mechanics Symposium-Rock Mechanics Meeting Society's Challenges and Demands*, Vancouver, Canada, May 2007.
- [9] W. Zhu, Y. Zhang, Z. K. Liu, and Q. Zhu, "Pre- and post-collapse ground deformation revealed by sar interferometry: a case study of foshan (China) ground collapse," *Journal of Sensors*, vol. 2020, Article ID 8899054, 17 pages, 2020.
- [10] X. T. Ai, G. J. Wang, C. Zhang et al., "Stability analysis of high dump with wide graded waste rock," *Rock and Soil Mechanics*, vol. 41, no. 11, pp. 3777–3788, 2020.
- [11] G. Baer, Y. Magen, R. N. Nof, E. Raz, V. Lyakhovskiy, and E. Shalev, "InSAR measurements and viscoelastic modeling of sinkhole precursory subsidence: implications for sinkhole formation, early warning, and sediment properties," *Journal of Geophysical Research: Earth Surface*, vol. 123, no. 4, pp. 678–693, 2018.
- [12] G. Chen, Y. Zhang, R. Zeng et al., "Detection of land subsidence associated with land creation and rapid urbanization in the Chinese loess plateau using time series InSAR: a case study of Lanzhou New District," *Remote Sensing*, vol. 10, no. 2, p. 270, 2018.

- [13] X. W. Yang, Y. M. Chen, Y. L. Zhao, L. L. Gao, and Y. F. Jing, "Experimental study on seepage in No.2 dump of dapo iron mine," *Coal Technology*, vol. 40, no. 6, pp. 150–155, 2021.
- [14] F. Q. Wen, H. Y. Dong, J. Y. Feng, W. W. Yang, X. P. Qu, and L. P. Wang, "Optimizing management of high bench dumping process for dumping site in an open-cast mine," *Metal Mine*, vol. 501, no. 3, pp. 50–56, 2018.
- [15] Z. L. Yang, J. M. Yang, Q. Li, and S. L. Jiang, "Determination of the largest bench height of belt dumping conveyor and the safety distance," *Metal Mine*, vol. 465, no. 3, pp. 63–67, 2015.
- [16] S. F. Lu, Z. G. Liu, X. G. Zhang, and Y. M. Guan, "Design and optimization of the scalable feeding arm for dumping machine," *Mining Research and Development*, vol. 34, no. 1, pp. 85–88, 2014.
- [17] M. Dong and Q. Luo, "Research and application on energy saving of port belt conveyor," *Procedia Environmental Sciences*, vol. 10, no. 10, pp. 32–38, 2011.
- [18] W. K. Yang and W. L. Pu, "Optimization of limit device of PL-2400 dumping machine supporting vehicle," *Opencast Mining Technology*, vol. 32, no. 10, pp. 53–55, 2017.
- [19] H. Y. Dong and Y. M. Wang, "Stacking and discharging process design of rock extractor in a mine in Bayan Obo," *Modern Mining*, vol. 564, no. 4, pp. 263–265, 2016.
- [20] X. Han, "Design and research on the cab of the dumping machine based on ergonomics," Master's Thesis, Taiyuan University of Technology, Taiyuan, China, 2020.
- [21] H. N. Meng, J. J. Ren, A. F. Li, J. L. Li, and Y. K. Wang, "Research on layout optimization design of operation interface layout in spreader," *Machine Design and Research*, vol. 36, no. 6, pp. 159–165, 2020.
- [22] Q. L. Hu, J. H. Li, and S. J. Guo, "Design and reconstruction of dry oil concentrated lubrication system for tanker transportation system," *Chemical Engineering Design Communications*, vol. 43, no. 5, p. 246, 2017.
- [23] Y. S. Zhang, "Discussion on the lubrication for the external tooth of slewing bearing in dumping plough," *Science-technology Innovation and Productivity*, vol. 298, no. 11, pp. 100–101, 2018.
- [24] Z. Q. Yao, L. F. Ma, F. B. Wu, and W. Q. Pan, "Research and analysis on vibration of discharging arm conveyor of spreader," *Coal Mine Machinery*, vol. 41, no. 1, pp. 75–77, 2020.
- [25] M. Ding, D. Geng, M. D. Zhou, and M. X. Lai, "Topology optimization strategy of structural strength based on variable density method," *Journal of Shanghai Jiaotong University*, vol. 55, no. 6, pp. 764–773, 2021.
- [26] N. Pollini and O. Amir, "Mixed projection- and density-based topology optimization with applications to structural assemblies," *Structural and Multidisciplinary Optimization*, vol. 61, no. 2, pp. 687–710, 2020.
- [27] R. Picelli, S. Townsend, C. Brampton, J. Norato, and H. A. Kim, "Stress-based shape and topology optimization with the level set method," *Computer Methods in Applied Mechanics and Engineering*, vol. 329, no. 2, pp. 1–23, 2018.
- [28] F. Y. Huang, "The topology optimization design of liner replacement manipulator on mill," Master's Thesis, Jiangxi University of Science and Technology, Ganzhou, China, 2017.
- [29] J. Fu, "Structural optimization and lightweight design of a dump truck frame," Master's Thesis, Jiangsu University, Zhenjiang, China, 2020.
- [30] W. D. Wu, Z. X. Yang, J. Li, and J. T. Dai, "Load analysis and structure optimization of rock scraping operation of driving arm of hydraulic excavating machine," *Coal Mine Machinery*, vol. 42, no. 3, pp. 85–88, 2021.
- [31] H. P. Tang, H. X. Li, Y. Z. Jiang, and J. Liu, "Structural design of key components of feeder based on topology optimization and multi-objective optimization," *Journal of Mechanical Strength*, vol. 42, no. 4, pp. 842–848, 2020.
- [32] Y. M. Pang, Y. B. Wang, X. H. Li, W. H. Li, and J. J. Ren, "Finite element analysis and structure optimization on track frame of WK-75 mine excavator," *Mining Research and Development*, vol. 39, no. 1, pp. 100–105, 2019.
- [33] X. X. Liu, "Feasibility Analysis and Technical Scheme Study on Land Loss Mining in Baoli Open-Pit Coal Mine," Master's Thesis, China University of Mining and Technology, Xuzhou, China, 2019.
- [34] P. Xue, "The design and analysis of the discharge arm based on the quality control," Master's Thesis, Northeastern University, Shenyang, China, 2014.
- [35] J. J. Xiao, "The dynamic simulation research on gantry crane based on virtual prototype technology," Master's Thesis, Southwest Jiaotong University, Chengdu, China, 2008.
- [36] L. Wang, "Finite element analysis for bucket wheel stacker-reclaimer and optimal design for the structure of forearm," Master's Thesis, Wuhan University of Technology, Wuhan, China, 2014.
- [37] W. J. Zhang, *Mobile Equipment for Continuous Handling of Bulk Materials Rules for the Design of Steel Structures*, China Standards Press, Beijing, China, 2005.
- [38] L. Wan, G. N. Xu, D. M. Gu et al., *Design Rules of Cranes*, China Standards Press, Beijing, China, 2008.
- [39] S. Shi, L. J. Wang, H. Q. Yu et al., *Code for Design of Steel Structures*, China Standards Press, Beijing, China, 2017.
- [40] L. Daryl and Logan, *Fundamentals of Finite Element Method*, Publishing House of Electronics Industry, Beijing, China, 3rd edition, 2003.
- [41] A. Mmtm, H. L. Chen, and J. Wang, *Introduction and Application of ANSYS Workbench 18.0 Finite Element Analysis*, China Machine Press, Beijing, China, 2018.
- [42] Z. J. Wang and L. M. Sun, *ANSYS 18.0 Finite Element Analysis Foundation and Example Course*, China Machine Press, Beijing, China, 2018.
- [43] Y. W. Kang, Q. T. Guo, J. G. Ji, and C. W. Wang, "Finite element dynamic analysis of mill-foundation considering soil-structure interaction," *Mining Machinery*, vol. 41, no. 2, pp. 70–75, 2013.
- [44] J. S. Liu, G. T. Parks, and P. J. Clarkson, "Topology/shape optimization of axisymmetric continuum structures metamorphic development approach," *Structural and Multi-disciplinary Optimization*, vol. 29, pp. 73–83, 2005.
- [45] G. Z. Yu, "The finite element analysis and research on topology optimization technology for vehicle frame base on ANSYS workbench," Master's Thesis, Harbin Institute of Technology, Harbin, China, 2014.
- [46] Y. S. Yin, "Topology optimization methods of continuum structure based on variable density method," Master's Thesis, Northeastern University, Shenyang, China, 2014.

Research Article

Microscale Mineral and Pore Structure Characterization of the Low-Permeability Sandstone in the Ordos Basin, China

Jie Gao ¹, Zhen Sun,² Jianping Liu,³ Chenyang Zhao,³ Dazhong Ren,⁴ Rongjun Zhang,⁴ Tingting Li,¹ and Dengke Liu ⁵

¹School of Civil Engineering & Geodesy, Shaanxi College of Communication Technology, Xi'an 710018, China

²No. 6 Gas Production Plant, Changqing Oilfield Company, PetroChina, Yanan 716000, China

³Exploration and Development Research Institute, PetroChina Changqing Oilfield Company, Xi'an 710018, China

⁴Xi'an Key Laboratory of Tight Oil (Shale Oil) Development, Xi'an Shiyou University, Xi'an 710065, China

⁵School of Human Settlement and Civil Engineering, Xi'an Jiaotong University, Xi'an 710049, China

Correspondence should be addressed to Dengke Liu; liudengke02@126.com

Received 27 May 2021; Revised 22 June 2021; Accepted 1 July 2021; Published 10 July 2021

Academic Editor: Xiaohu Zhang

Copyright © 2021 Jie Gao et al. This is an open access article distributed under the Creative Commons Attribution License, which permits unrestricted use, distribution, and reproduction in any medium, provided the original work is properly cited.

Given the insufficient understanding of the characteristics and controlling factors of the low-permeability sandstone reservoir in the Heshui area, the Ordos Basin, the present study examined the microscale mineral and pore structure of Chang 2 reservoir. It analyzed its major controlling factors using a series of methods, including imaging and indirect methods. The results show that the rocks of Chang 2 reservoir in the study area are dominated by lithic arkose and feldspathic detritus quartz sandstone. The reservoir space develops intragranular pores, feldspar dissolved pores, lithic dissolved pores, and intercrystallite pores. Microcracks can occasionally be found. The average porosity is 10.5%, and the average permeability is 2.2 mD, featuring a low-porosity-ultralow-permeability reservoir. During the reservoir development, traps formed by small-scale nose-shaped uplifts resulting from the tectonic effects provide opportunities for good reservoir space. Sedimentation and diagenetic processes control the degree of development and direction of the evolution of reservoir porosity to a certain degree. Multisegment capillary pressure curve and long missing zone were corresponding to relatively good pore-throat structures. Illite was the predominant diagenetic clay minerals that determine the reservoir quality. These three effects all contribute to the overall development of the reservoir.

1. Introduction

The recent waterflooding and chemical flooding advancements have significantly increased the low-permeability sandstone reservoirs [1, 2]. The low-permeability sandstone reservoir in the Heshui area, located in the Ordos Basin in China, is now one of the China's most significant hydrocarbon reservoirs [3]. In recent years, through the exploration and evaluation of the Heshui area, scholars have found that the yield of Chang 2 reservoir in oil tests was relatively high. This finding is vital for increasing China's oil production and reserve, demonstrating the vast potential for future prospecting and development [4, 5]. However, compared with massive studies of other areas, the Heshui area study is still limited and is in the primary stages [4].

Previous studies in this area were primarily concerned with the oil groups from Chang 8 to Chang 6. A lack of systematic investigations of the characteristics, formation, and controlling factors in Chang 2 significantly restrained the target evaluation and optimization analysis [6, 7].

Consequently, the mineralogical, diagenetic, tectonic, and pore structure characterization of Chang 2 sandstones are still poorly understood. Mineral composition, physical properties, and pore size distributions are the most significant parameters in sandstones that affect the mechanical, storage, and transport properties of the sandstones [8–10]. Compared to conventional reservoirs, the pore networks in sandstone reservoirs are more complicated because of the abundance of microscale heterogenetic distributions of minerals [11].

Composition, proportion, and distribution are the essential characteristics of the minerals [12]. Pores could be divided into different groups based on various category criteria, and the criterion proposed by the IUPAC is the most common one [13]. Many scholars have applied this criterion to analyze the pore networks. In contrast, this criterion is not a generally accepted way for each research, and the pore network classification needs to base on actual demand. Thin section (TS) and scanning electron microscopy (SEM) are the image analysis methods to determine the mineralogical characteristics qualitatively and quantitatively [14]. Pressure-controlled mercury intrusion and rate-controlled mercury intrusion (PCMI/RCMI) are the standard techniques to quantify the pore size distributions [15, 16]. Combining PCMI and RCMI can give us information about the whole pore size distributions of more than 3.6 nm [17].

Based on the development status of low- (ultralow-) permeability reservoirs and the characteristics of Chang 2 in the Heshui area, the present research aims to provide a comprehensive and systematic study of its physical properties and the microscopic pore structure, utilizing copious experimental methods, including core observation, TS, SEM, PCMI, and RCMI methods. Besides, the present research also examined the main controlling factors affecting the reservoir, which is of great significance for future research on the Yanchang Formation and further expansion of the domains in oil-gas exploration in the central basin [18, 19].

2. Methodology

2.1. Geological Background. Heshui area is located in the southern part of the Shaanbei Slope (Northern Shaanxi Slope) and the Tianhuan Depression in the Ordos Basin. Its tectonic evolution is inseparable from the overall tectonic background of the Ordos block. The general structure of the Heshui area features a gentle monocline oriented on an east-west axis, without any faults or large-scale basement uplifts. The monoclinic slope is generally less than 1° , and the average gradient is about 6 m/km. Small nose-shaped uplifts with an amplitude of 10 to 20 m were formed in local areas due to differential compaction [20]. These uplifts tend to have graduate tilts at the two ends and are largely axisymmetric. The closed areas generally do not exceed 10 km^2 in size. The angle is directional in specific ways and is regularly distributed [21]. Although the structures above in the study area affect the distribution of oil pools, their influence is only marginal.

The Chang 2 oil group has undergone a certain degree of denudation on the southern and southwestern margins of the basin, but it is still preserved. The lithological features of the oil group tend to be roughly coarse-grained in the north and fine-grained in the south, with an average thickness of 110 to 120 m (Figure 1). The overall petrological characteristics are as follows: light gray and brown and fine- and medium-fine-grained sandstone intercalated with dark shales in typology. Typically, the rocks are massive, with trivial and thin stratification, dominated by argillaceous and calcareous cementation.

2.2. Experimental Procedures. An optical microscope is applied to identify the mineral types and quantify the mineral's composition and proportion. Before the tests, the rocks were sliced to pieces and covered by glass. The *E-c* system was applied to analyze the mineral characteristics quantitatively.

Zeiss GeminiSEM 500 was used to analyze the mineralogical distributions of the samples. Before the tests, the samples were first polished as a cube, milled via argon ion. After those steps, the samples were finally coated with carbon.

Micromeritics AutoPore 9420 mercury porosimeter was used to perform the PCMI experiments. The samples were first dried for 12 h and then saturated by lipophilic remover. Finally, the samples were put into the apparatus and the relationship between capillary pressure and mercury saturation was tested.

Automated System for Pore Examination ASPE-730 was used to conduct the RCMI tests. The pre-exam procedures were the same as that of PCMI. However, in this test, the maximum pressure was not over 6.2 MPa, corresponding to the pore radius of $0.12 \mu\text{m}$.

3. Results and Discussion

3.1. Petrological Characteristics. According to the statistics collected from core observation, thin-section casting, and other analytical processes, rocks in the study area are mainly medium gray, fine-grained sandstones, fine-grained sandstones, and fine siltstones, with an average particle size between 0.1 and 0.35 mm and a maximum of 0.5 mm. The rocks are dominated by lithic arkose and feldspathic detritus quartz sandstones (Figure 2).

The total amount of debris is between 74.6% and 90%, with an average of 84.4%. Among the debris, the content of quartz is 24.6% to 60%, with an average of 44.9%; the range of feldspar is 12% to 39%, with an average of 22.8%; the content of cuttings is 10% to 34.2%, with an average of 19.2% (Table S1).

The degree of sorting is good to medium. The degree of rounding is mainly subangular to subcircular; the main types of cementing are enlarged-porous cementing, porous cementing, pore-increasing cementing, and pore-film cementing.

The overall content of interstitials is not high, mainly composed of cement ranging from 10% to 24.5%, with an average of 16.2%. Most of the cementations are authigenic clay materials, followed by feldspathic components and pyrites. Matrix only takes up a deficient composition (Table S2).

3.2. Diagenesis and Diagenetic Stages. Chang 2 reservoir in the study area contains relatively high plastic debris such as phyllite, schist, and mica. Feldspar dissolved pores and lithic dissolved pores are fairly developed, in which diagenetic fractures can be found occasionally. Kaolinite, illite, and chlorite in the authigenic clay minerals are ubiquitous, with high carbonate content. Quartz is secondarily enlarged and contains authigenic quartz grains. This shows that the effect of compaction and pressure solution was strong in this period. The cement mainly comprises authigenic clay

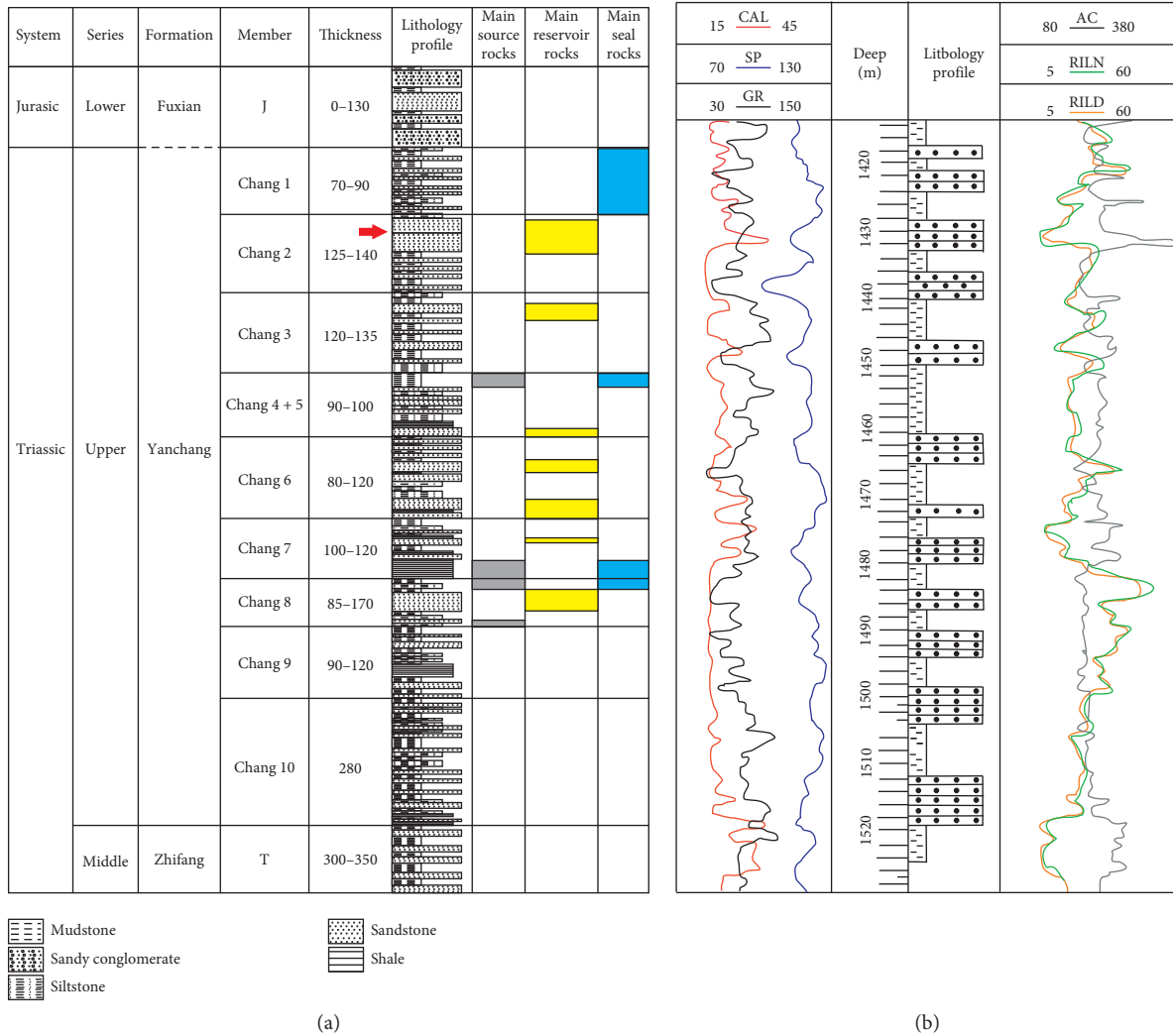


FIGURE 1: (a) Lithology profile of the Yanchang Formation and (b) well-logging data of Chang 2 reservoir in the study area [22].

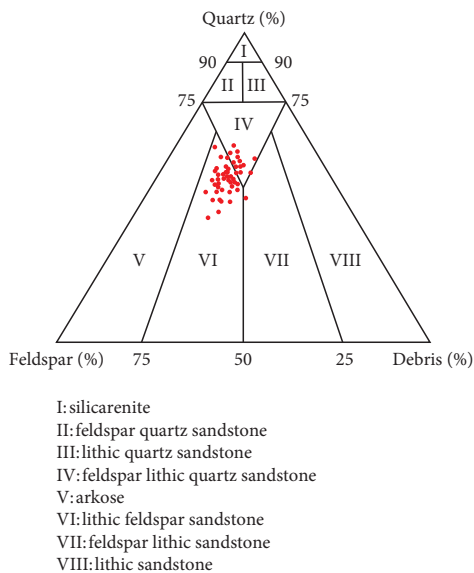


FIGURE 2: Ternary diagram of mineralogy in Chang 2 sandstone.

minerals and carbonate minerals, and the content of kaolinite in sandstone is relatively high. Carbonate and siliceous cementation are common, while metasomatism and fracturing are relatively common (Figure 3). Among the aforementioned diagenetic processes, the dissolution of feldspar and debris and the metasomatism of kaolinite are beneficial to forming good reservoirs.

In contrast, other kinds of processes are likely to cause damage to the reservoirs. The diagenetic sequence of the reservoir is compaction → chloritization → quartz enlargement → calcite precipitation → organic acid generation → feldspar, debris, and calcite dissolution → iron calcite precipitation → oil emplacement. The above characteristics indicate that the diagenetic stage of the sandstones in the study area is amidst stages A to B of the middle diagenetic stage.

3.3. *Physical Characteristics of the Reservoir.* The statistical analysis (Figure 4(a)) show that the reservoir porosity is mainly between 7% and 13% with an average of 10.5%, the

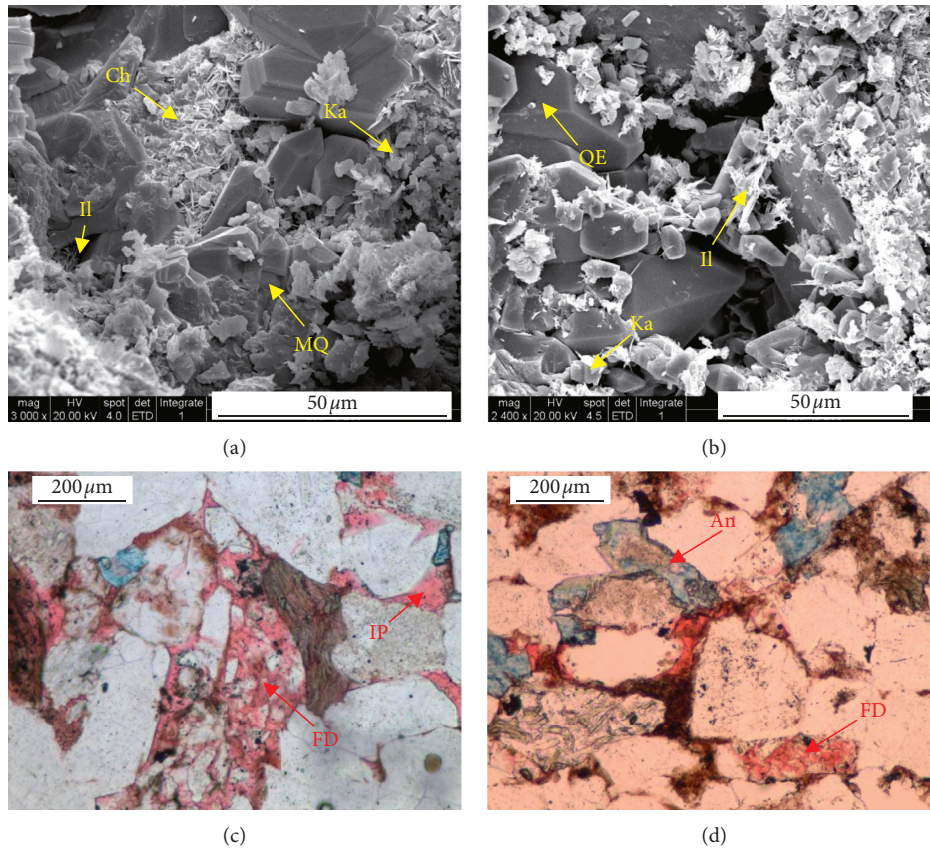


FIGURE 3: Diagenesis of Chang 2 reservoir in the study area. (a) Cementation of microcrystalline quartz (MQ), kaolinite (Ka), illite (Il), and chlorite (Ch) (N39, 1218.6 m); (b) quartz enlargement (QE), intergranular kaolinite (Ka), and illite cementation (Il) (Z140, 1473.9 m); (c) feldspar dissolution (FD) and intergranular pores (IP) (N9, 1210 m); (d) ankerite (An) and feldspar dissolution (FD) (Z140, 1473.9 m).

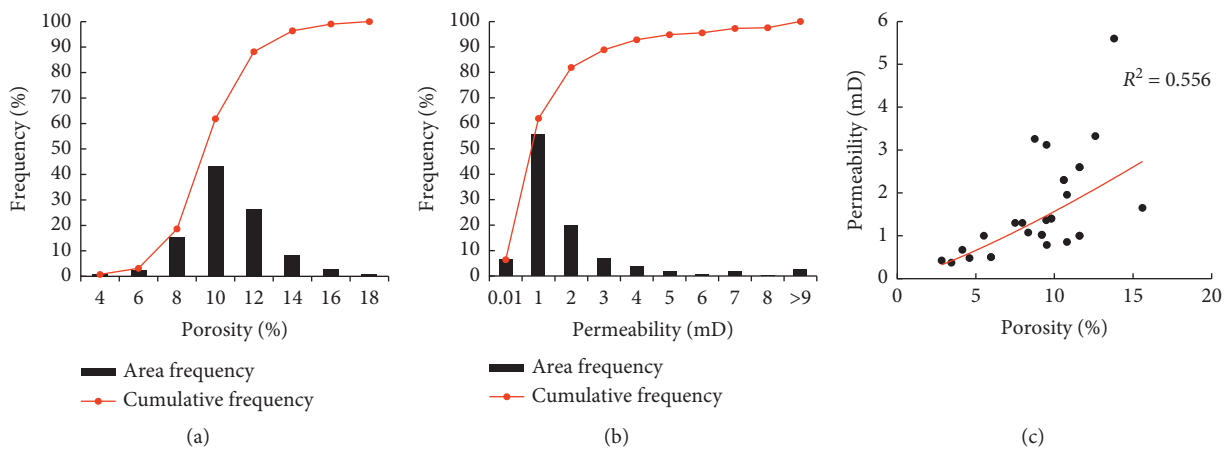


FIGURE 4: The distribution of (a) porosity, (b) permeability, and (c) the porosity-permeability relationship of Chang 2 reservoir in the study area.

main frequency is distributed in the 5% to 15% section, accounting for 76% of the total distribution. The permeability is mainly distributed between 0.15 and 3 mD, and the average is 2.2 mD. The frequency distribution is mainly between 0.5 and 5 mD, accounting for 56.7% of the total

distribution. The above results suggest that the target reservoir in Heshui area belongs to low-porosity-ultralow-permeability reservoirs [23]. Figure 4(c) shows a positive correlation between the porosity and permeability ($R^2 = 0.556$), indicating good physical characteristics.

3.4. Microstructure and Characteristics of the Reservoir.

The sandstones in the study area mainly develops intergranular pores with an average content of 1.8%, followed by feldspar dissolved pores with an average content of 0.9%, then by lithic dissolved pores of 0.2%, and then by intercrystalline pores of 0.1%. Microcracks can occasionally be found. The average aperture ratio is 3.2%. The average pore diameter mainly falls between 30 and 80 μm . The main types of pore combination are dissolved pore-intergranular pore type, microporous type, intergranular pore-dissolved pore type, and intergranular pore type (Figure 5). The main types of throats are lamellar throats, and a small number of constricted throats also exist. The tortuosity of the mainstream throat is relatively low-relatively high (Figure 6), and the average throat radius is 0.93 μm . The sorting coefficient is 1.49, and the relative sorting coefficient is 0.14. The type of pore-throat combination is mainly mesopore-fine pore-fine throat type, and the coordination number of throats mainly falls between 2 and 6, and the connectivity between throat and pore is poor.

The high-pressure mercury intrusion experiment (see Table S3 for mercury intrusion parameters) shows that the pore-throat radius of the reservoir is relatively small, and the pore-throat volume is relatively large. Besides, the throat is relatively thin and small. The degree of sorting is moderate to low. The residual mercury saturation is relatively high, and the displacement pressure is relatively low. The maximum mercury saturation is average. This shows that the storage ability of the study area is average, the filtration capacity is relatively poor, and the connected storage space is relatively small. Besides, we also conducted an oil-water phase permeability experiment, which shows that rocks in the study area are neutral-weakly hydrophilic, and the oil-water displacement efficiency is low.

3.5. Major Controlling Factors. Based on the formation and distribution characteristics of the reservoirs, it is believed that the development and spatial distribution of Chang 2 reservoir in the study area are comprehensively controlled by tectonics, sedimentation, and diagenetic effects.

The study area is in the Shaanbei Monocline. Since it was affected by denudation and differential compaction, small-scale nose-shaped uplifts are developed in local areas. These nose-like uplifts and the belt-like sandstone reservoirs distributed in the up-dip direction near NE-SW (Figure 7), together with the interriver argillaceous lithology, are mutually configured to form a good trap [24]. Chang 2 reservoir in the study area is controlled by lithology and tectonism, and the types of reservoirs are mainly lithology-tectonism composite reservoirs. In the up-dip direction of the structure, a good trap is easily formed due to the compaction of the sand body. However, we also need to point out that not all reservoirs in high structural positions can become good oil layers. The reasons for this need to be analyzed in conjunction with sedimentation and diagenesis.

Sedimentation controls the spatial distribution of various sedimentary environments and their products on the

macroscopic level and the physical properties of rocks on the microscopic level. According to the sedimentary facies analysis and sand distribution characteristics of Chang 2 reservoir in the study area, it is found that the target layer in this area belongs to the delta front deposit, and the sand body extends far, running through the role area [25, 26]. Large-area underwater distributary channels, braided channels, and estuary bar sand bodies with larger thickness and better physical properties provide the possibility of forming oil layers. We also found that the microfacies sand bodies of the estuary bar have more refined grains and uniform structure, with the primary intergranular pores accounting for about 80%. The dissolved pores were developed, which accounts for about 15%. The physical properties data show that the study area is a favorable reservoir facies zone, but the spread area is small and cannot be used as the main force zone. The sand body in the microfacies at the estuary dam is fine-grained, well-sorted, with primary intergranular pores accounting for 60% to 80%. Dissolved pores area developed, accounting for about 20% of pores. Porosity is greater than 10%. Permeability value is greater than 1 mD, and the oil-bearing characteristic is generally good. These regions can serve as favorable reservoir facies belts. Due to strong reservoir heterogeneity, the physical properties change, resulting in poor oil content and storage performance in the flanks of the underwater distributary channel and the distributary bays.

We were taking two samples from different sedimentary facies belts as an instance (Figure 8). There are two platforms and a low missing zone for the samples from underwater distributary channels, while single long platforms and short, a missing zone for the samples from estuary bar. A heterogeneous hydrodynamic environment led to high heterogeneous grain distributions and then caused the complex pore-throat structures. However, due to the strong hydrodynamic condition, the larger pores were relatively developed (Figures 8(a) and 8(c)). Compared to underwater distributary channels, the sands from the estuary bar have more homogeneous grain distributions. The long platform indicates the relatively uniformly distributed grain sizes, and the short missing zone suggested the stable hydrodynamic condition. However, weak hydrodynamic streams generally could not carry large grains, leading to poor physical properties and simple pore-throat networks with low average radius (Figures 8(b) and 8(d)).

Diagenesis controls the evolution direction of pores in the process of burial diagenesis and is of great significance to reservoir evaluation and prediction [27, 28]. The diagenetic type of the target layer in the study area is very complicated. According to microscopic observation and statistics, the diagenetic processes exhibit strong, compact compaction, dissolution, and cementation effects (Figure 9). Among those processes, the dissolution of feldspar and debris and the metasomatism of kaolinite are beneficial to forming good reservoirs. In contrast, other types are likely to cause damage to the reservoirs.

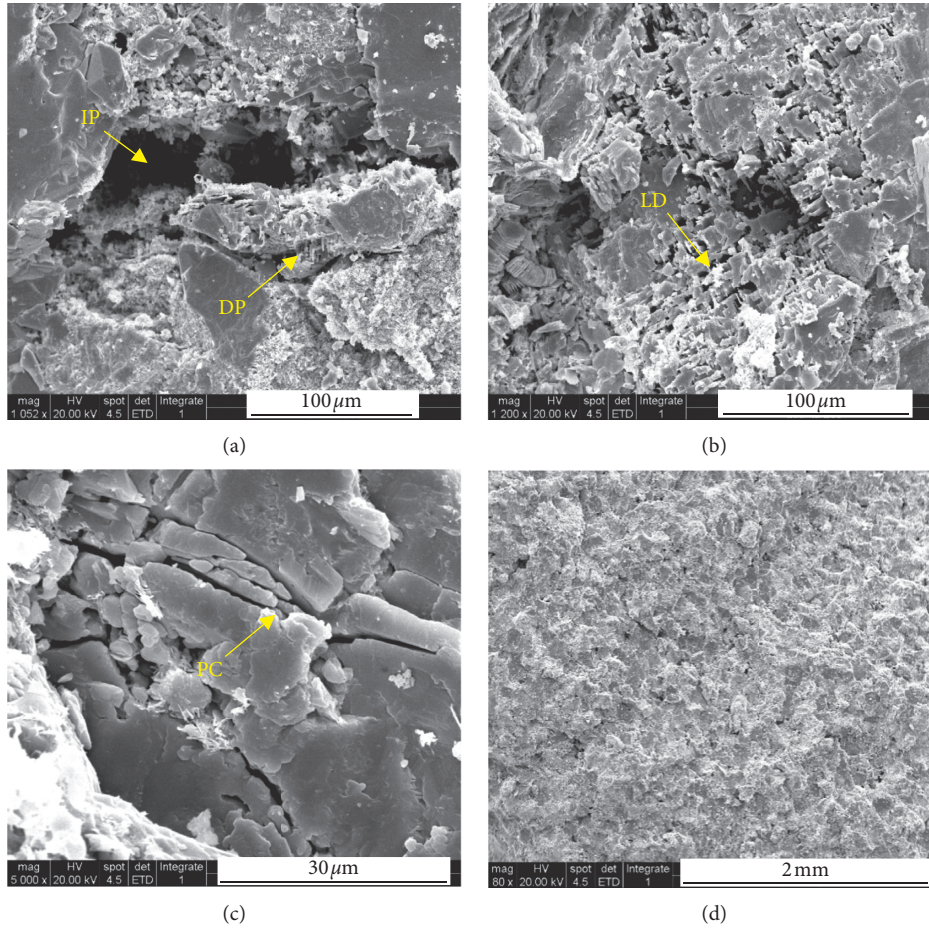


FIGURE 5: Pore types of Chang 2 reservoir in the study area. (a) Residual intergranular pores (IP) and dissolution pores (DP) (Z140, 1473.4 m); (b) particle leaching dissolution pores (LD) (Z140, 1473.4 m); (c) particle cracks (PC) (Z140, 1473.9 m); (d) overall, poor pore development (Z140, 1473.9 m).

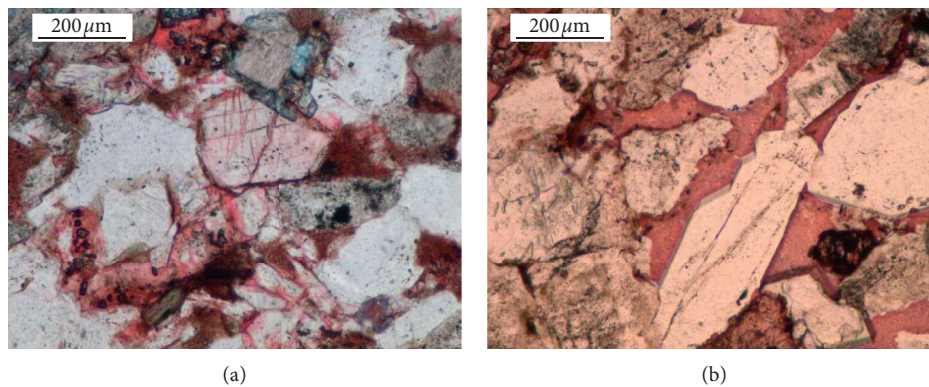


FIGURE 6: Throat types of Chang 2 reservoir in the study area. (a) Flake throat (N39, 1218.6 m) and (b) necking throat (Z48, 1291.1 m).

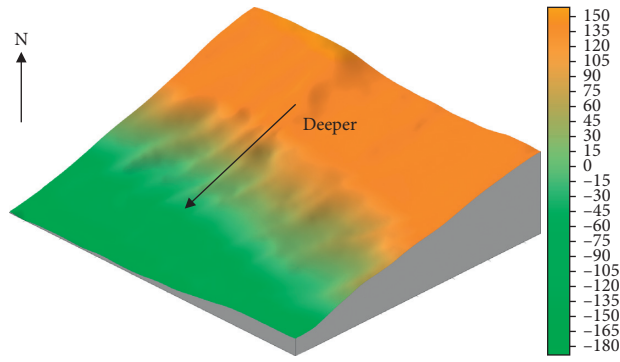


FIGURE 7: Top surface structure of Chang 2.

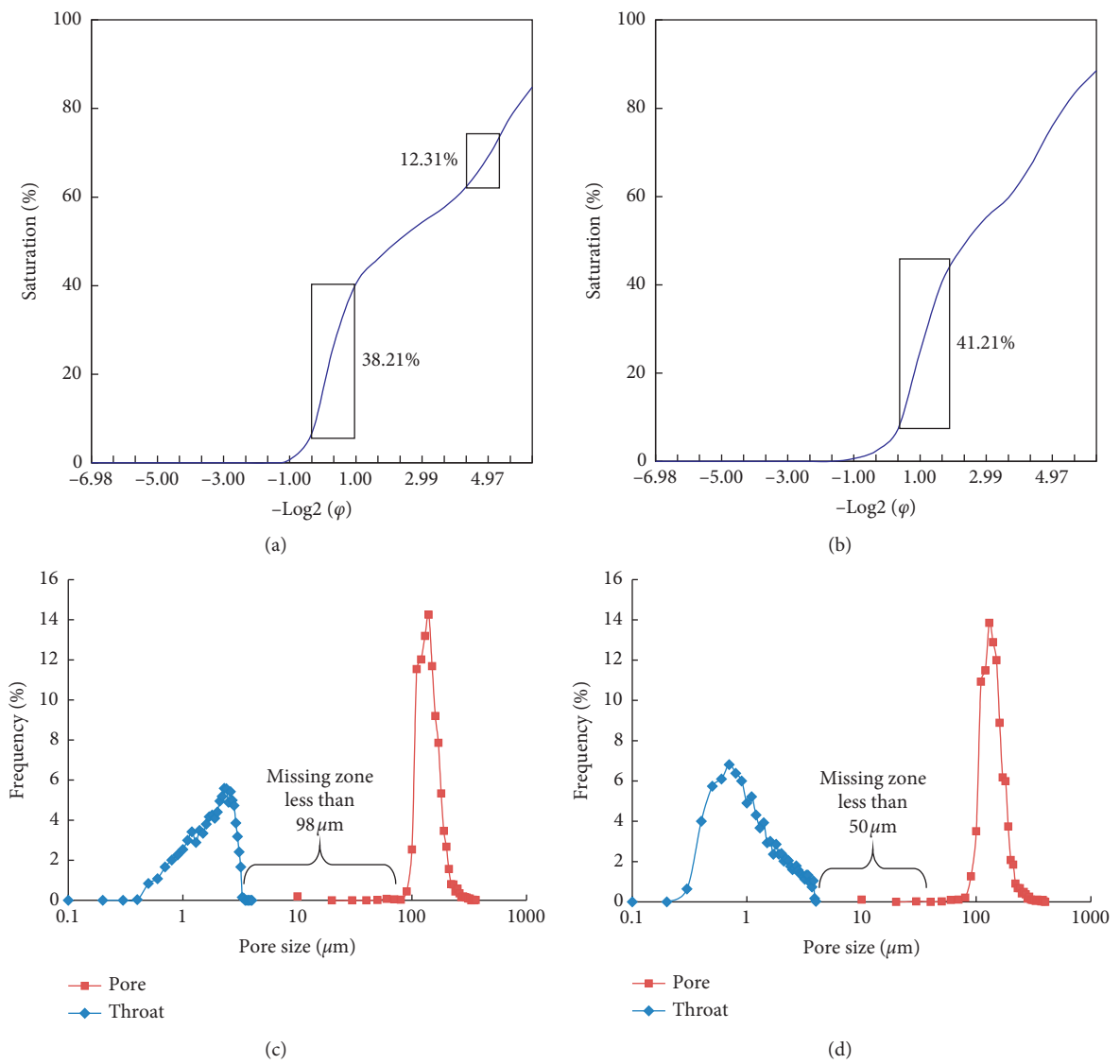


FIGURE 8: Cumulative pore size distributions from PCMI and RCMI.

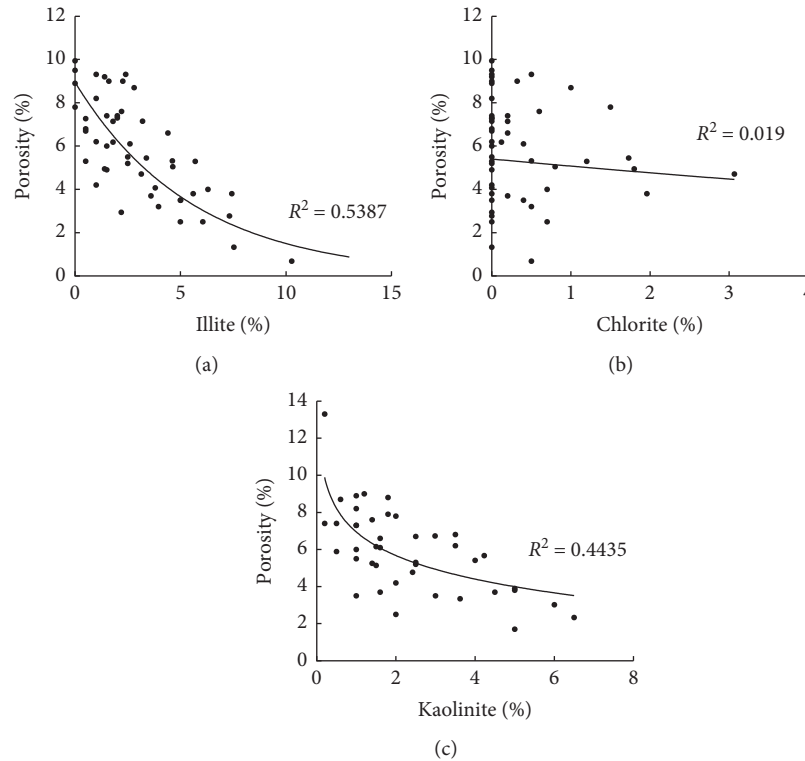


FIGURE 9: The relationships between diagenetic minerals and reservoir quality.

4. Conclusions

- (i) The rock types of research area are mainly lithic arkose and feldspathic detritus quartz sandstone. Clay materials are mainly kaolinite, chlorite, and illite. Detrital components are dominated by quartz, followed by feldspar. The diagenetic stage is amidst stages A to B of the middle diagenetic stage.
- (ii) The aimed sandstones belong to low-porosity-ultralow-permeability reservoirs. The main types of pore combination are dissolved pore-intergranular pore type, microporous type, intergranular pore-dissolved pore type, and intergranular pore type. The main types of throats are lamellar throats, and a small number of constricted throats also exist. The type of pore-throat combination is mainly mesopore-fine pore-fine throat type.
- (iii) The development of Chang 2 reservoir in the Heshui area of the Ordos Basin is influenced by tectonism, sedimentation, and diagenesis. Small-scale nose-shaped uplifts formed by tectonism form a good trap. The sorting of the sedimentary process has significant control over the porosity of the reservoir. The compaction, dissolution, and cementation effects during the diagenetic processes are relatively strong, which controls the evolution direction of the reservoir pores.

Data Availability

The experimental data used to support the findings of this study are included in the manuscript.

Conflicts of Interest

The authors declare that there are no conflicts of interest regarding the publication of this study.

Acknowledgments

The authors would like to acknowledge the financial support from the Shaanxi Natural Science Basic Research Program, China (2021JM-543 and 2021JQ-029), Open Fund of Key Laboratory of Coal Resources Exploration and Comprehensive Utilization, Ministry of Natural and Resources (KF2021-3 and KF2020-2), Shaanxi Provincial Key Research and Development Program (2021GY-140), Open Fund of Shaanxi Key Laboratory of Advanced Stimulation Technology for Oil & Gas Reservoirs (20JS120), National Natural Science Foundation of China (51934005 and 52074226), and Young Science and Technology Talents Foundation of Shaanxi Province (2019KJXX-054). The authors thank Minghua Li from Xi'an Jiaotong University for his contributions to figure drawing.

Supplementary Materials

Supplementary material contains Tables S1 to S3, which show the data of debris components, cement composition, and pore-throat structure parameters, respectively. (*Supplementary Materials*)

References

- [1] A. K. Alhuraishawy, B. Bai, M. Wei, J. Geng, and J. Pu, "Mineral dissolution and fine migration effect on oil recovery factor by low-salinity water flooding in low-permeability sandstone reservoir," *Fuel*, vol. 220, pp. 898–907, 2018.
- [2] Q.-X. Meng, W.-Y. Xu, H.-L. Wang, X.-Y. Zhuang, W.-C. Xie, and T. Rabczuk, "DigiSim—an open source software package for heterogeneous material modeling based on digital image processing," *Advances in Engineering Software*, vol. 148, Article ID 102836, 2020.
- [3] J. Yan, X. He, S. Zhang et al., "Sensitive parameters of NMR T₂ spectrum and their application to pore structure characterization and evaluation in logging profile: a case study from Chang 7 in the Yanchang formation, Heshui area, Ordos basin, NW China," *Marine and Petroleum Geology*, vol. 111, pp. 230–239, 2020.
- [4] Z. L. Zhou, G. W. Wang, Y. Ran, J. Lai, Y. Cui, and X. Zhao, "A logging identification method of tight oil reservoir lithology and lithofacies: a case from Chang 7 member of Triassic Yanchang formation in Heshui area, Ordos basin, NW China," *Petroleum Exploration and Development*, vol. 43, no. 1, pp. 65–73, 2016.
- [5] C. Zhu, M.-c. He, M. Karakus, X.-h. Zhang, and Z. Guo, "The collision experiment between rolling stones of different shapes and protective cushion in open-pit mines," *Journal of Mountain Science*, vol. 18, no. 5, pp. 1391–1403, 2021.
- [6] J. Fan, X. Qu, C. Wang, Q. Lei, L. Cheng, and Z. Yang, "Natural fracture distribution and a new method predicting effective fractures in tight oil reservoirs in Ordos basin, NW China," *Petroleum Exploration and Development*, vol. 43, no. 5, pp. 806–14, 2016.
- [7] C. Zhu, M. He, M. Karakus, X. Zhang, and Z. Tao, "Numerical simulations of the failure process of anacinal slope physical model and control mechanism of negative Poisson's ratio cable," *Bulletin of Engineering Geology and the Environment*, vol. 80, no. 4, pp. 3365–3380, 2021.
- [8] I. H. Falcon-Suarez, K. Amalokwu, J. Delgado-Martin, B. Callow, K. Robert, and L. North, "Comparison of stress-dependent geophysical, hydraulic and mechanical properties of synthetic and natural sandstones for reservoir characterization and monitoring studies," *Geophysical Prospecting*, vol. 67, no. 4, pp. 784–803, 2019.
- [9] Y. Bernabe, "Pore geometry and pressure dependence of the transport properties in sandstones," *Geophysics*, vol. 56, no. 4, pp. 436–446, 1991.
- [10] Q. Wang, Z. Jiang, B. Jiang, H. Gao, Y. Huang, and P. Zhang, "Research on an automatic roadway formation method in deep mining areas by roof cutting with high-strength bolt-grouting," *International Journal of Rock Mechanics and Mining Sciences*, vol. 128, Article ID 104264, 2020.
- [11] K. Zhang, J. Lai, G. Bai et al., "Comparison of fractal models using NMR and CT analysis in low permeability sandstones," *Marine and Petroleum Geology*, vol. 112, Article ID 104069, 2020.
- [12] Y. Wang, W. K. Feng, R. L. Hu, and C. H. Li, "Fracture evolution and energy characteristics during marble failure under triaxial fatigue cyclic and confining pressure unloading (FC-CPU) conditions," *Rock Mechanics and Rock Engineering*, vol. 54, no. 2, pp. 799–818, 2021.
- [13] J. Rouquerol, D. Avnir, C. W. Fairbridge et al., "Recommendations for the characterization of porous solids (technical report)," *Pure and Applied Chemistry*, vol. 66, no. 8, pp. 1739–1758, 1994.
- [14] Q. Wang, Y. Wang, M. He et al., "Experimental research and application of automatically formed roadway without advance tunneling," *Tunnelling and Underground Space Technology*, vol. 114, Article ID 103999, 2021.
- [15] L. M. Anovitz and D. R. Cole, "Characterization and analysis of porosity and pore structures," *Reviews in Mineralogy and Geochemistry*, vol. 80, no. 1, pp. 61–164, 2015.
- [16] A. Li, F. Dai, Y. Liu, H. Du, and R. Jiang, "Dynamic stability evaluation of underground cavern sidewalls against flexural toppling considering excavation-induced damage," *Tunnelling and Underground Space Technology*, vol. 112, Article ID 103903, 2021.
- [17] D. Ren, R. Li, D. Liu, Y. Li, N. Liu, and F. Yang, "Quantifying fractal dimension in integrated experimental data of tight sandstones," *Geofluids*, vol. 2019, Article ID 6463473, 19 pages, 2019.
- [18] E. D. Pittman, "Diagenesis of quartz in sandstones as revealed by scanning electron microscopy," *Journal of Sedimentary Research*, vol. 42, no. 3, pp. 507–19, 1972.
- [19] M. P. Fahy and M. J. Guccione, "Estimating strength of sandstone using petrographic thin-section data," *Environmental & Engineering Geoscience*, vol. 16, no. 4, pp. 467–485, 1979.
- [20] X. Li, J. Yao, H. Liu, X. Liu, L. Wei, and M. Feng, "Tectonic origin type of the low amplitude uplifted structure and its role in the control of the distribution of oil and gas in Mesozoic, the Ordos basin," *Geoscience*, vol. 27, no. 4, pp. 755–65, 2013.
- [21] J.-q. Luo and Z.-m. He, "Tectonic evolution and oil-gas distribution in the Mesozoic Ordos basin," *Geology and Resources*, vol. 2, 2008.
- [22] D. Liu, J. Su, Z. Gu, Y. Qi, F. Yang, and T. Tian, "Geochemical properties and pore structure control on oil extraction of shale," *Lithosphere*, vol. 2021, Article ID 6646791, 2021.
- [23] M. Wang, H. Tang, S. Liu, F. Zhao, L. Li, and H. Lu, "Formation mechanism of differential sandstone densification modes and its impact on reservoir quality: a case study of upper paleozoic Permian in eastern part of Sulige gas field, Ordos basin," *Journal of China University of Mining and Technology*, vol. 6, pp. 1282–300, 2017.
- [24] W. Zhang, L. Xie, W. Yang, Y. Qin, and P. a. Peng, "Micro fractures and pores in lacustrine shales of the upper Triassic Yanchang Chang 7 member, Ordos basin, China," *Journal of Petroleum Science and Engineering*, vol. 156, pp. 194–201, 2017.
- [25] I. Martini and F. Sandrelli, "Facies analysis of a Pliocene river-dominated deltaic succession (Siena basin, Italy): Implications for the formation and infilling of terminal distributary channels," *Sedimentology*, vol. 62, no. 1, pp. 234–265, 2015.
- [26] C. Zou, Z. Yang, H. Wang, D. Dazhong, L. Honglin, and S. Zhensheng, "Exploring petroleum inside source kitchen: Jurassic unconventional continental giant shale oil & gas field in Sichuan basin, China," *Acta Geologica Sinica*, vol. 93, no. 7, pp. 1551–62, 2019.
- [27] C. Zhang, D. Zhu, Q. Luo et al., "Major factors controlling fracture development in the middle Permian Lucaogou formation tight oil reservoir, Junggar basin, NW China," *Journal of Asian Earth Sciences*, vol. 146, pp. 279–295, 2017.
- [28] Y. Zhou, D. Zhenchun, and W. Lihua, "Main factors controlling formation of dolomite reservoir underlying gypsum-salt layer in the 5th member of Ordovician Majiagou formation, Ordos basin," *Oil & Gas Geology*, vol. 39, no. 6, pp. 1214–8, 2018.

Research Article

Optimization of Stope Structure Parameters Based on the Mined Orebody at the Meishan Iron Mine

Mingzhi Sun , Fengyu Ren , and Hangxing Ding 

School of Resources and Civil Engineering, Northeastern University, Shenyang 110819, China

Correspondence should be addressed to Hangxing Ding; dinghangxing@mail.neu.edu.cn

Received 2 June 2021; Accepted 17 June 2021; Published 9 July 2021

Academic Editor: Gan Feng

Copyright © 2021 Mingzhi Sun et al. This is an open access article distributed under the Creative Commons Attribution License, which permits unrestricted use, distribution, and reproduction in any medium, provided the original work is properly cited.

Based on the engineering background of the Meishan iron mine with sublevel caving (SLC) method, in this work, we adopted the method for identifying the shape of mined orebody (the original location in blasted slice), which analyzed and determined reasonable stope structure parameters. In the field test, the markers were arranged in the blasted slice, the mined orebody was measured by in situ tests, and reliable data were achieved. The shape of the mined orebody was obtained through this test when the width of drift was 6 m. The mined orebody's shape was compared with the shape of the isolated extraction zone (IEZ), and the difference increased with increasing height. When the stope structural parameters were determined by the mined orebody, the larger the sublevel height was, the smaller the error was, which was compared with the method using ellipsoid arrangement theory to determine the stope structural parameters. Finally, the reasonable stope structure parameters were optimized. The sublevel height was 22 m, and the drift spacing was 20 m.

1. Introduction

The characteristic of the SLC method is the large contact area between blasted ores and the caved waste from the overlying rock mass. The overall shape of the blasted ores and the residual ores is less consistent with the IEZ's shape if the stope structure parameters mismatch the flow behavior of blasted ores [1–6]. A great deal of waste rock was prone to mix with the ores in the drawing process, which could result in low ore recovery and high dilution.

The key to effectively reduce the ore loss and dilution rate in the SLC method was the reasonable stope structure parameters. The researchers had proposed various optimization methods for stope structure parameters based on IEZ's shape [7–15]. Kvapil et al. [16] conducted many research works on the design and optimization of structural parameters in the SLC method. The result shown that the shape of blasted ores and IEZ followed the consistency principle, which based on the ellipsoid draw theory. According to the empirical formula of our design, blasted ores, and the properties of caved rock as the guidance, an ellipsoid was extracted with certain width

and thickness [17–23]. Castro et al. [24–29] proposed a mining theory of high sublevel and large drift spacing based on the ore drawing theory, adjusted the sublevel height and drift spacing in different mines accordingly, and implemented it. In addition, extensive literature indicated that the decreased ore loss and dilution rate depended on the reasonable stope structure parameters [30–36]. Tan et al. [37] proved that the optimization of stope structural parameters based on ellipsoid arrangement theory was not rigorous and perfect, which did not follow the consistent principle of the blasted ores and IEZ's shape in essence. Further, our research group had obtained the IEZ's shape of the Meishan iron mine in the previous particle flow experiments. The IEZ's shape was arranged by ellipsoid arrangement theory, and the optimized stope structural parameters were obtained. However, the loss and dilution index of ores was unsatisfactory in practical applications. The main reasons are as follows: (1) when the structural parameters of stope before blasting were optimized by the IEZ's shape after blasting, the shape change of ore-rock body was ignored during the blasting process; (2) the structural parameters determined based on the IEZ's shape

deviated from the optimal value, due to the lack of understanding of drawn ores' shape within burden spacing before blasting.

Here, based on the above deficiencies, a new method to determine the shape of the mined orebody by the in situ test was proposed. According to the ellipsoid arrangement theory, the stope structure parameters were optimized by the mined orebody's shape measured in the field test. Therefore, there was a direct correlation between the mined orebody's shape and the structural parameters, but the indirect relationship existed between IEZ's shape and the stope structure. It could avoid the change of the ore-rock body's form during the blasting process. This method has a significant meaning to further reduce the loss and dilution rate of the SLC method and ensure the full use of metal mineral resources.

2. In Situ Mined Orebody Measurement Test

2.1. Meishan Iron Mine SLC Operation. The Meishan SLC iron mine was located at Yuhuatai District, Nanjing city of China, which was one of the first batches of technologically advanced mines to adopt the SLC method in China, and the ore loss and dilution control technology was advanced. Recently, the tests of large drift spacing structural parameters were conducted which are based on the original structural parameter (15 m × 15 m). The test results were not satisfactory; the ore loss and dilution rate were not significantly reduced under the condition that the sublevel height is 15 m and the drift spacing is 20 m. Particularly, the new structural parameter (18 m × 20 m) was adopted in the second stage of the extension of the operation, but the ore loss rate and dilution rate also have not been significantly reduced. Therefore, in situ tests on the mined ore body's shape were employed to optimize the structural parameters of the mining of deep ore body and further reduce the ore loss and dilution rate.

The mined orebody's shape was essential to the determination of stope structural parameters. The shape and size of a single blasted slice and the shape of the blasted ores were determined by the stope structure parameters. The IEZ's shape was consistent with that of the blasted ores and residual ores, which indicated that the mined orebody's shape coincided with the blasted slice and the stope structural parameters were reasonable.

A single blasted slice in drawing drift by the SLC method is shown in Figure 1(a). The holes were drilled in fan rings before blasting for placing the markers and arranged in the middle of the two rows of blast holes. The ores contained markers that would be blasted and drawn. The IEZ's shape came from experiments, as shown in Figure 1(b). According to the drawing theory, the shape of mined orebody was depicted by the method of determining the IEZ's shape [8]. The corresponding quality of drawn ores was measured when the blasted ores containing markers were drawn, and the mined orebody's shape could be obtained. This method was called in situ mined orebody measurement test. The mined orebody was a solid ore block with a particular shape rather than ores. The ideal stope structural parameters could make the blasted ores completely contained by the IEZ, and a directionless drawing was achieved

before the stage of recovery of upper residual ores. Meanwhile, in an ideal situation, the whole of ores that came from the blasted slice should be completely drawn, but it is difficult to achieve in real production. In practice, part of the blasted ores could not be drawn, which led to an obvious difference between the mined orebody and the original blasted slice. The schematic diagram of mined orebody is shown in Figure 1(c).

2.2. Experimental Setup. To determine the mined orebody's shape, the operation is selected in row 10 of S1 drift at -306 m level in the Meishan iron mine. The details of the test location and mining preparation works are shown in Figure 2. The relationship between the position of markers and blast holes is depicted in Figure 3. To determine the rationality of stope structure parameters, the bottom position of the holes should be focused on monitoring. Meanwhile, the original blasted slice must be covered to the fullest degree. The rationality of stope structure parameters could be verified by the shape of the loss dilution index, and the optimized structural parameters could be determined by the mined orebody. The markers that adopted RFID technology are shown in Figure 4(a). RFID was a flexible application technology that is easy to operate, simple and practical, and especially suitable for automatic control. The recognition work needs no manual intervention, which supported both read-only mode and read-write mode, and needs no touch or aim. RFID technology has many advantages, such as convenient and fast reading, more effective recognition distance, fast recognition speed, good penetration, long service life, wide application range, strong resistance to pollution, and durability. Meanwhile, the location of markers was important considerations in depicting the geometry of the mined orebody. Therefore, the markers should be able to actively transmit signals, resist blasting impact, and avail to monitor.

The charge trolley of the Meishan iron mine was employed for the installation of markers; the process is shown in Figure 4(b). It could precisely control the depth of the placement and ensure that the installed markers reach the designed position. The woven bags were used for fixing markers; that is, the gaps during the markers in the drilling holes were filled with woven bags and compacted. As shown in Figure 4(c), the woven bags were used as the interval between the markers, and it played a good role in fixing the interval for the markers. The markers should be stouter enough to survive from the first blasting process and subsequent ore drawing to ensure sufficient data for further analysis.

2.3. Test Process and Data. The positions of each marker are shown in Figure 5, and these markers covered the range of the blasted slice. In Figure 5, 79 markers were installed in the test ore body. Among them, 11 markers were installed in No. 1 hole, 18 markers were installed in No. 2 hole, 23 markers were installed in No. 3 hole, 16 markers were installed in No. 4 hole, and 11 markers were installed in No. 5 hole.

To monitor the markers during the drawing, the layout of each piece of equipment and data lines in the stope drift is shown in Figure 6. Two marker monitors were arranged on the roof of the drift near the drawing point of S1 and next to

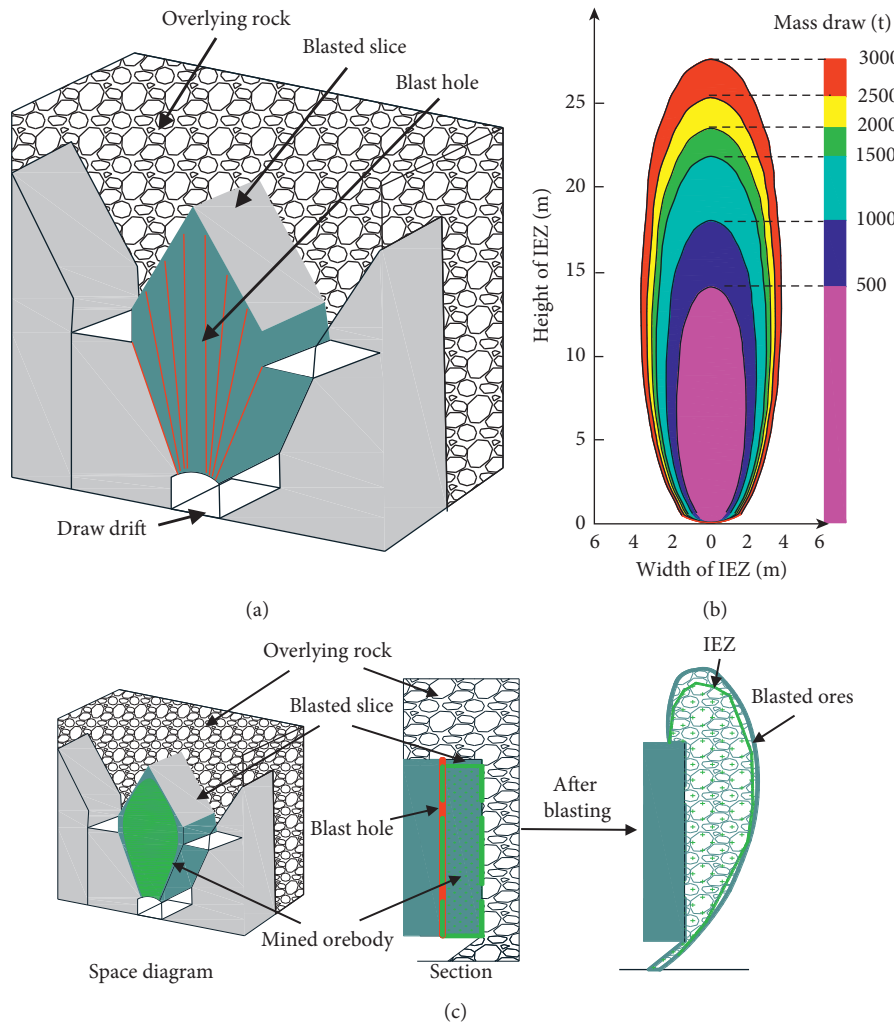


FIGURE 1: (a) A single blasted slice. (b) The IEZ's shape of the end drawing in the direction of vertical drift. (c) Schematic diagram of mined orebody's shape.

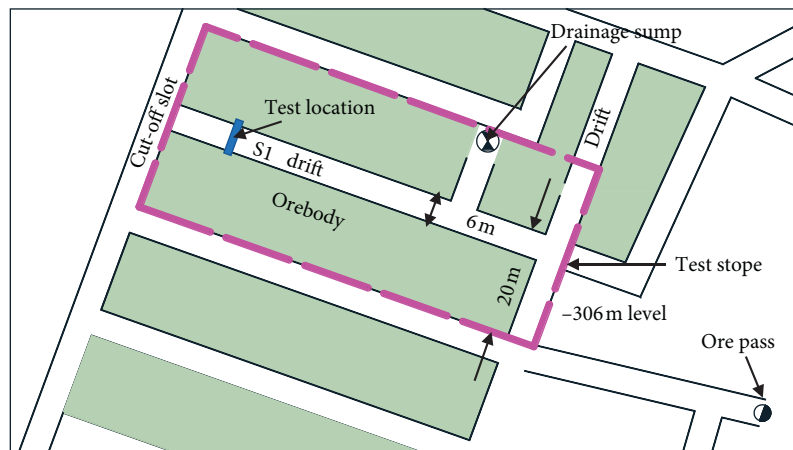


FIGURE 2: The layout of the test location and mining preparation works.

the ore pass, respectively. When the ores flowed from the drawing point, the first monitoring was completed. When the ores were transported to the ore pass by the scraper, the second monitoring was completed. Meanwhile, a monitor

was arranged on the roof of the drift near the drawing point to obtain the ores flow video. The monitoring station was arranged in the S5 extension drift, and the 485 hubs and laptop were placed in it. It is used to observe the running

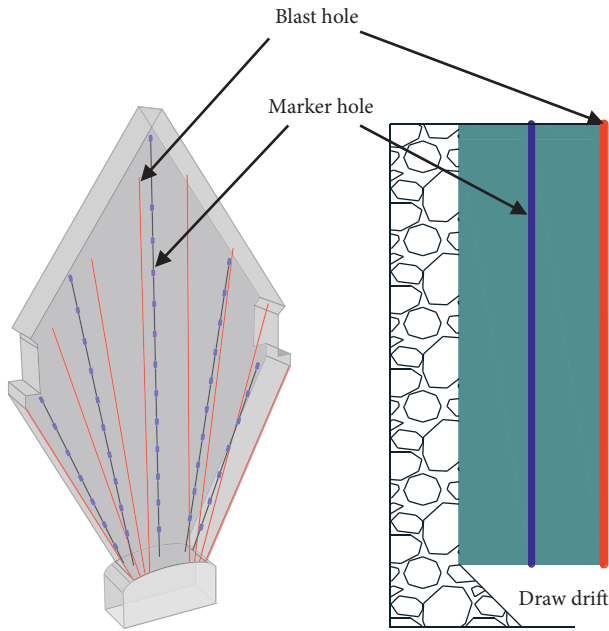


FIGURE 3: The relationship between the position of markers and blast holes.

condition of the system. The data line and power line should be fixed on the roof of the drift to avoid damaging the wire by mining equipment in operation.

The 5.6 m^3 scrapers were employed in the test, with 206 scoop ores being drawn. The average scoop of ores weighed about 15 t, and the quantity of the total ore was about 3090 t. The dilution occurs at about 140 scoops, and before that, it was a nondilution drawing. A total of 54 markers were detected in the test, and the 2, 14, 22, 11, and 5 markers are recycled from the corresponding holes (Nos. 1–5), respectively. As shown in Figure 7, the green solid circle indicates that the markers could be monitored.

2.4. Test Result. Mined orebody in situ measurement test was accomplished by RFID technology, and better test results had been obtained. The number of markers detected in each hole in the test and overall monitoring situation is shown in Figure 8. The comprehensive monitoring rate of the markers was 68.4%, which reached the expected test result. A sufficient number of markers were monitored, which provided abundant data for the determination of the mined orebody's shape.

3. Analysis of the Test Result

3.1. The Determined Shape of a Mined Orebody. According to the above information, the markers with the same quality of drawing ores were selected, and based on the position in the blasted slice of different markers, mined orebodies' shapes with corresponding quality of drawing ores were obtained. The markers recycled in the test and their corresponding quality of drawing ores are shown in Figure 9(a). The mined orebody's shape was depicted by the data from different qualities of drawing ores (500, 1000,

1500, 2000, 2500, and 3000 t), which are displayed in Figure 9(b). The volume of mined orebody increased with the increase of drawing ores, it was not the same as the corresponding IEZ, but the overall shape was roughly the same. The nondilution drawing occurred before 2000 t, and the width and height of the mined orebody increased in this process. When the quality of drawing ores was greater than 2000 t, the waste rock would be mixed, and the width and height of the mined orebody increased slowly, which influence the development speed of mined orebody's shape. It is probably due to the dilution phenomenon that appeared when the quality of drawing ores was greater than 2000 t.

When the quality of drawing ores was 500 t, the volume was calculated as 200 m^3 , and the height of the IEZ was 13.1 m. When the quality of drawing ores was 1000, 1500, 2000, 2500, and 3000 t, respectively, the corresponding heights of the IEZ were calculated as 16.9, 20, 22.2, 22.5, 24.5, and 26.4 m. The development process of the mined orebodies and IEZs is shown in Figure 10(a)–10(f). The magenta and green lines represented the shape of the IEZ and mined orebody. The height of the mined orebodies was calculated as 11.8, 14.8, 18.5, 20.9, 22.3, and 24.9 m, respectively.

It could be seen from the shape comparison diagram of the mined orebody and the IEZ that the height of the IEZ was greater than the height of the mined orebody, and the width of the mined orebody was larger than that of the IEZ. It is indicated that the blasting range of the ores was contained in the IEZ, which was produced through the blasting of the blasted slice. The ores on both sides of the blasted slice tended to squeeze inward during the blasting. According to Figure 10(f), when the quality of the drawing ores was 3000 t, the widths of IEZ and mined orebody were 8.28 and 11.65 m, respectively. In a comparison of the width and height of IEZ and mined orebodies, their relationship could be expressed as $S_m/H_m = 1.49S_d/H_d$ (S_m and H_m were the height and width of mined orebody; S_d and H_d were the height and width of IEZ). It could be seen that the difference in proportion existed between the IEZ and mined orebody. The determination of stope structural parameters according to the IEZ's shape made a certain error.

Owing to the use of cut-off grade drawing ore, the whole drawing process included three stages, which were no dilution, dilution, and up to cut-off grade. The height and corresponding width of the mined orebody at the different quality of drawing (500, 1000, 1500, 2000, 2500, and 3000 t) are listed in Table 1. The above data were imported into the origin software and fitted. Z was the independent variable, Y was the dependent variable, and Z and Y represented the height and width of the mined orebody, respectively.

As shown in Figure 11, it was found that the data followed the first-order equation ($y = 0.47z + 0.81$) after fitting. R^2 was 0.96, which was close to 1 and indicated that the fitting degree is high. In the drawing, with the increased quantity of mined ores, the development width of mined orebody was directly proportional to its height.

According to the fitting results, the mined orebody's was modified, the final shape looks like an inverted water droplet (Figure 12).

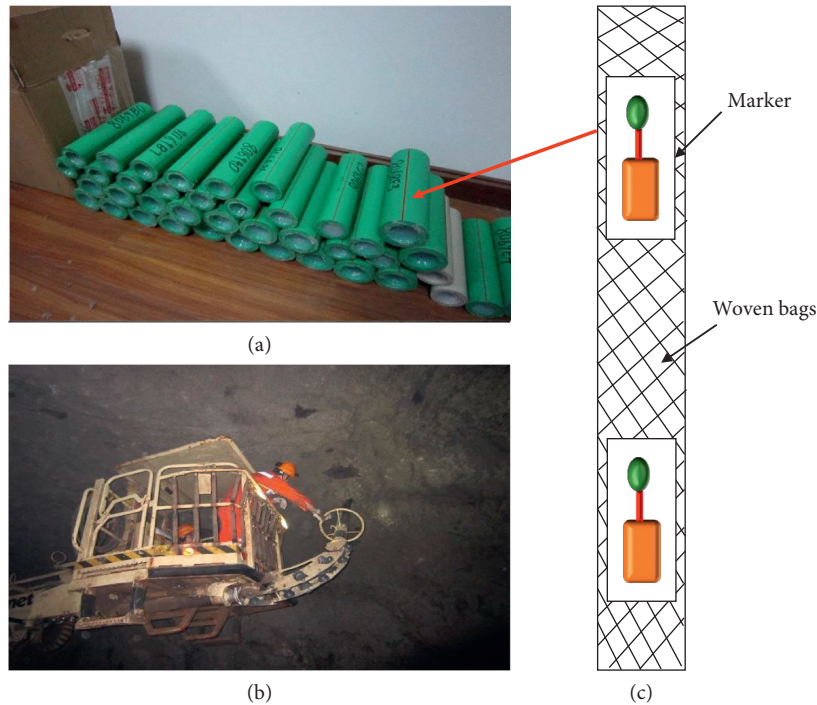


FIGURE 4: Photographs of markers and installing process: (a) markers; (b) installation markers by charge trolley; (c) profile of marker.

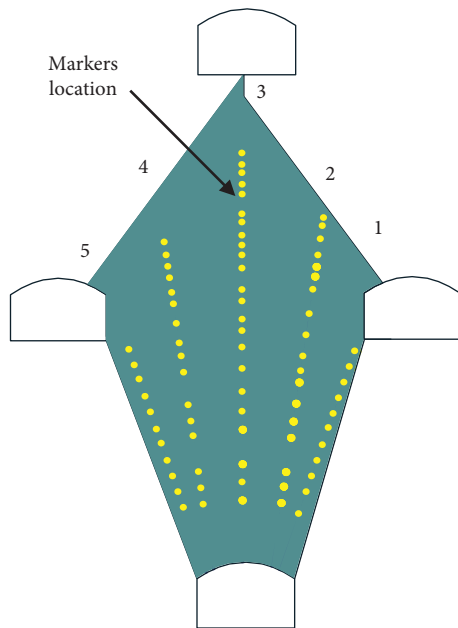


FIGURE 5: The installation structure diagram of markers and the location in fan rings.

3.2. Comparison of Stope Structure Parameters. In the past, the ellipsoid arrangement theory was used to determine the structural parameters of the SLC method. It followed the principle; that is, the shape of blasted ores was consistent with IEZ. The essence of structural parameter optimization was the space arrangement optimization of IEZ. When the 4 ellipsoids were arranged in space, the 5 points were tangent to each other, and the optimal

structural parameters could be obtained. The results of practical application in mine were unsatisfied when the stope structural parameters were determined by IEZ's shape. It is difficult to achieve the ideal index of the ore recovery effect. Analysis of the main reasons is as follows: the theoretical analysis and practical demonstration of this method were insufficient. The shape of the ore block was directly arranged by IEZ's shape, which lacked the necessary correlation analysis. By comparing the IEZ's shape and measured mined orebody's shape, it could be concluded that certain errors existed when the stope structure parameters were determined by ellipsoid arrangement theory.

The viewpoints of used ellipsoid arrangement determined structural parameters are as follows: (1) If the 5 points that were the tangent of IEZ in each stope units could not be achieved, it would cause the loss of ore. If the IEZ in each stope units crossed each other, it would lead to ore dilution due to repeated drawing. (2) "The optimal structural parameters for the high coincidence degree between the blasted ores and IEZ's shape" were equivalent to "the optimal structural parameters which were obtained when the IEZs without waste rock were tangent with each other." (3) According to the IEZ arrangement of 5 points that were tangent to each other for the best, two optimal ellipsoid arrangement models could be obtained. One is the high sublevel structure, and the other is the large spacing structure. According to the shape of the measured mined orebody and IEZ, the specific arrangement is displayed in Figure 13. Figure 13(a) is the large spacing arrangement. When the IEZs were tangent to each other, the overlapping parts occurred among the mined orebodies. Figure 13(b) shows the high sublevel arrangement, the



FIGURE 6: The layout of monitoring system: (a) monitors on the roof of the drift near drawing point; (b) monitors; (c) video on the roof of the drift near drawing point; (d) monitors next to the ore pass; (e) monitoring station.

uncovered areas appeared among mined orebodies. These areas could not be drawn, which was the loss of ores.

Through the above two forms of ellipsoid arrangement models, there was some irrationality existing in the determination of stope structure parameters by this method. Based on the ellipsoid arrangement theory, the IEZ and mined orebody were arranged in the stope, which had the same quality of drawing. The dilution and loss rate of the two forms of mined orebody arrangement were calculated. The results showed that the repeated coverage rate was 6.38% and the noncoverage rate was 10.43%. Repeated coverage means that the ores in this area will be mined twice, resulting in the fact that the waste rock could inevitably be mixed in the drawing process, which would further reduce the recovery rate. Noncoverage means that the ores in this area have not been drawn, resulting in the loss of ores and lower recovery rates.

4. Optimization of Stope Structure Parameters

In the caving process of SLC, the mixed waste rock came from both sides and top of drawing points. The parameters affecting ore loss and dilution indexes mainly include sublevel height and drift spacing. Meanwhile, ore loss and dilution are not affected by the single parameters, but by joint effect. The height and width of mined orebodies corresponding to different qualities of drawing ores are shown in Table 2. These data could be used to analyze the relationship between the height and width of the mined orebody and then determine the reasonable stope structural parameters. Through comparison calculation of the height and width of the mined orebodies in stope structure, the height-width ratios (H/W) were 1.96~2.36. According to the H/W of the mined orebodies, the reasonable stope structural parameters proportion ratios of H and S could be concluded

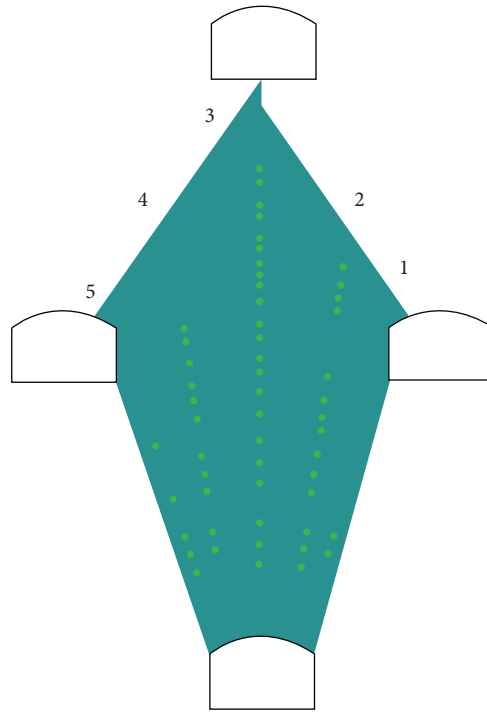


FIGURE 7: The location of monitored markers in the test.

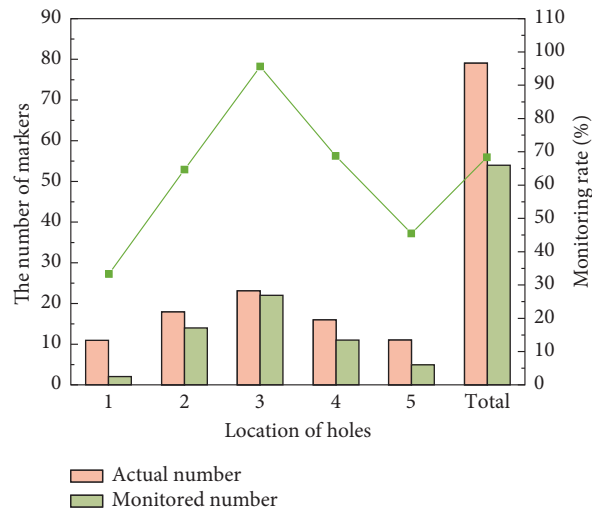


FIGURE 8: The location of monitored markers in the test.

as 0.98~1.18. Presently, the values H and S were 18 and 20 m, which were applied in the Meishan iron mine. These parameters were inconsistent with the proportion of mined orebodies, which led to a poor recovery index. The matching degree between stope structural parameters and flow behavior of ore and rock was low, which led to the dilution increased in the middle and late periods of drawing. Therefore, it was necessary to improve the matching degree between structural parameters and the flow behavior of ores.

According to the results of the mined orebody in situ measurement test, several schemes of stope structural parameters were designed based on the specific situation, which is shown in Table 3. The more reasonable

parameters were selected based on the matching degree between the mined orebody's shape and the stope structure. According to different structural parameters, let the mined orebodies be tangential to the outline of a blasted slice. The mined orebody's shape was matched with different stope structural parameters ($H \times S = 18\text{ m} \times 20\text{ m}$, $20\text{ m} \times 18\text{ m}$, $20\text{ m} \times 20\text{ m}$, $22\text{ m} \times 20\text{ m}$, $24\text{ m} \times 20\text{ m}$, and $24\text{ m} \times 22\text{ m}$, resp.), and the corresponding coverage rate was calculated.

The matching degree between the mined orebody's shape and structural parameter schemes is shown in Figures 14(a)–14(f). Compared with the other five schemes, the mined orebody's shape that was obtained through the current

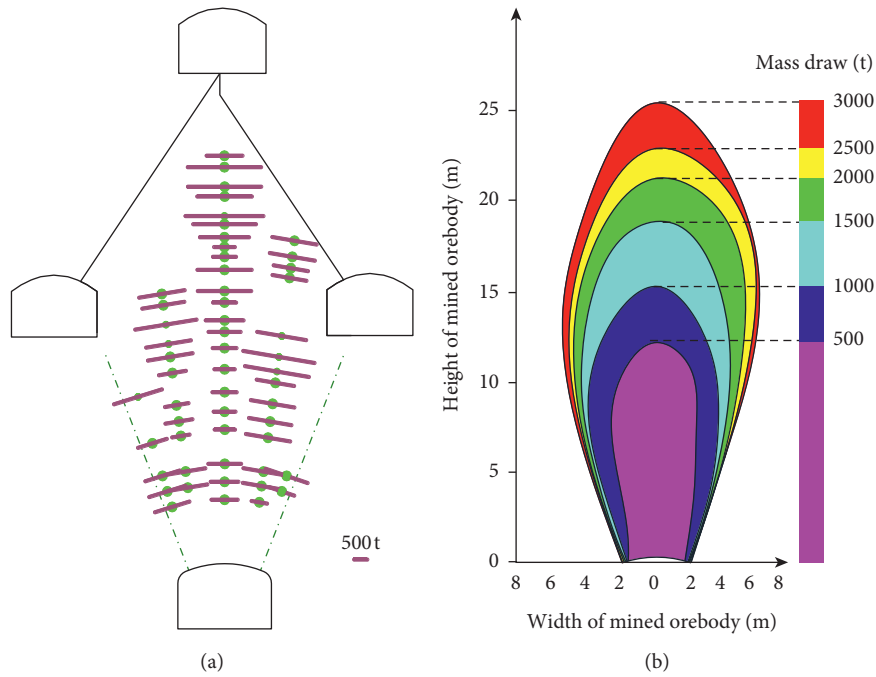


FIGURE 9: (a) Markers monitored in the test and their corresponding quality of drawing ore. (b) Mined orebodies were depicted by the data from the markers.

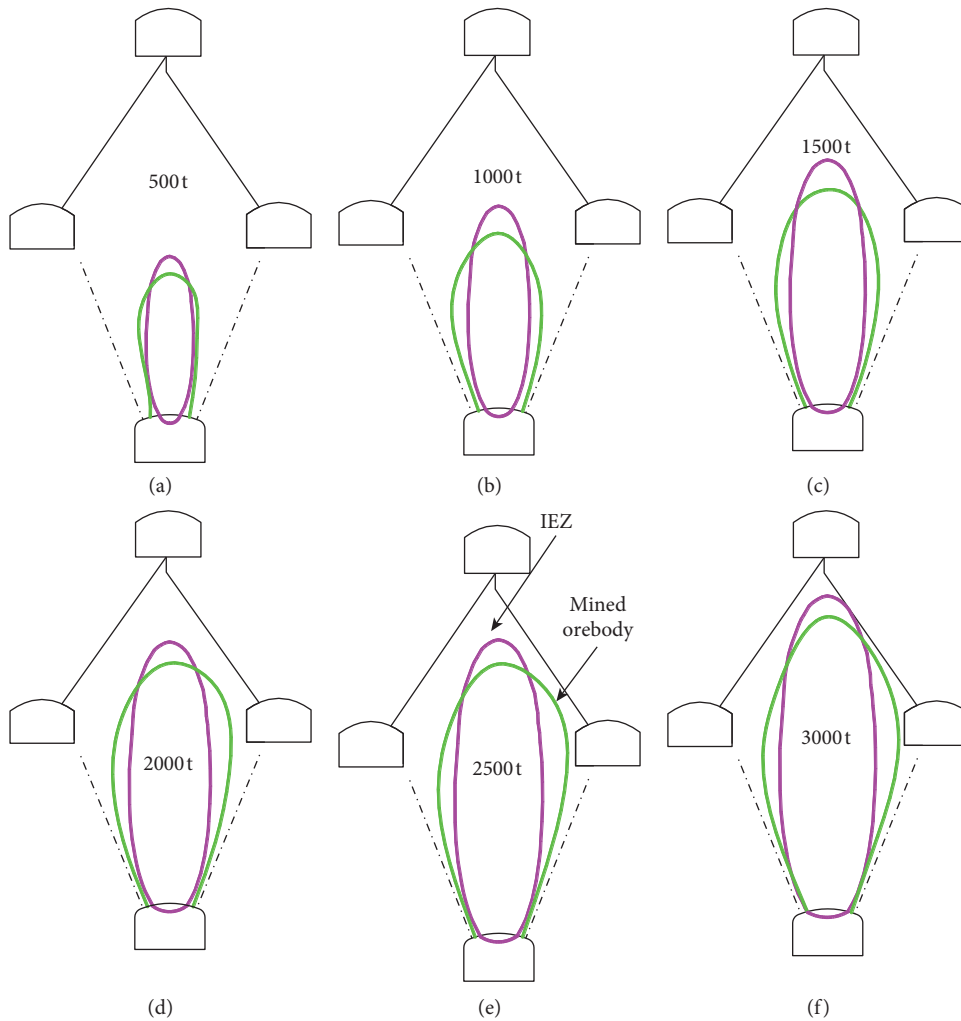


FIGURE 10: Comparison of the mined orebody's shape and the IEZ's shape in the test.

TABLE 1: Data of the height and width of the mined orebody.

Number	Z (m)	Y (m)
1	11.5	5
2	14.5	6.8
3	17.7	8.6
4	20.2	10.2
5	23.2	10.7
6	25.4	11.5

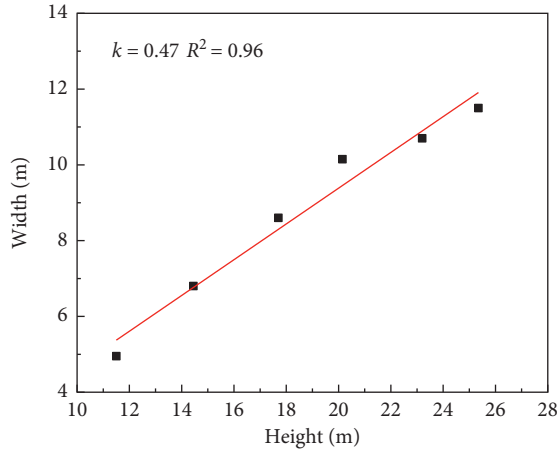


FIGURE 11: The linear relation between height and width of the mined orebody.

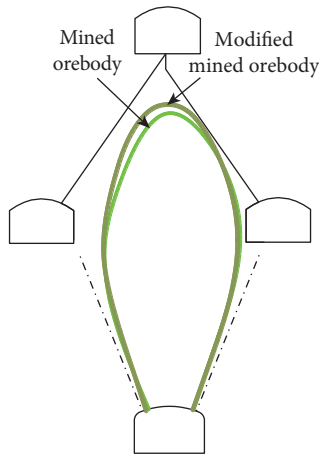


FIGURE 12: The modified mined orebody.

structural parameters scheme ($H \times S = 18 \text{ m} \times 20 \text{ m}$) had a relatively low coverage rate.

The value of coverage rate and uncovered rate of each scheme is listed in Figure 15. The coverage rate could determine the matching degree between each scheme and the mined orebody. The matching degree of scheme 4 was the highest, followed by schemes 2, 5, and 6. The matching degree was higher, and the proportional relationship between stope structural parameters and the mined orebody's shape was closer. The H/S value of scheme 4 was 1.1, which coincided with the reasonable ratio range (0.98~1.18). Here, the structural parameter was $22 \text{ m} \times 20 \text{ m}$. The area of the blasted slice increased from 337 to 417 m^2 , which was

improved by 23.74%. With the improvement of the drawn index, mining efficiency could be significantly increased.

Verification tests were employed on the optimized stope structural parameters in the Meishan iron mine. Alternatively, the mine had introduced a series of advanced drilling equipment and charging trolleys since mining with large structural parameters, which could fully meet the mining requirements of sublevel height ($H = 22 \text{ m}$). Alternatively, the ore body was still thick and had the conditions to further increase the sublevel height under the current mining level of -306 m . Hence, in situ tests with increasing the sublevel height were conducted. The sublevel height was increased from 18 to 22 m as the drift spacing was 20 m. The blasted slice was determined by the optimized structural parameters as displayed in Figure 16.

The specific parameters were $H = 22 \text{ m}$, $L = 20 \text{ m}$, $B = 2.4 \text{ m}$, and $W = 6 \text{ m}$. The in situ tests were selected at the S4 drift of -306 m level, and the plane position of the test stope is shown in Figure 17(a). The blast holes were drilled with the Simba H1354 drilling trolley in a double drilling center mode. The height of the drilling center was 1.9 m, the interval was 1.2 m, and the diameter of the blast hole was 91 mm. The detailed arrangement of blast holes is shown in Figure 17(b).

The geological ore capacity of the test stope was 45,767 t, and the average geological grade was 46.6%. The drawing results are shown in Table 4. According to the calculation formulas of ore loss and dilution (1)–(3), the recovery rate of the new test stope and the dilution rate could be calculated as 90.64% and 9.95%.

$$\text{Waste rock - mixing rate : } Y = \frac{C - C_c}{C - C_y} \times 100, \quad (1)$$

$$\text{ore recovery rate : } H_k = \frac{Q_c}{Q} (100 - Y), \quad (2)$$

$$\text{ore dilution rate : } P = \frac{C - C_c}{C} \times 100. \quad (3)$$

In the formulas, Q was industrial reserves of ore bodies (t), Q_c was the quality of mined ores (t), C was in situ grade of industrial reserves of ore (%), C_c was the grade of recovered mined ore and waste rock (%), and C_y was the grade of mixed waste rock (%). In addition, C_y was a constant; the value was 15%.

The test results indicated that the new sublevel height was beneficial to improve the stability of mining and

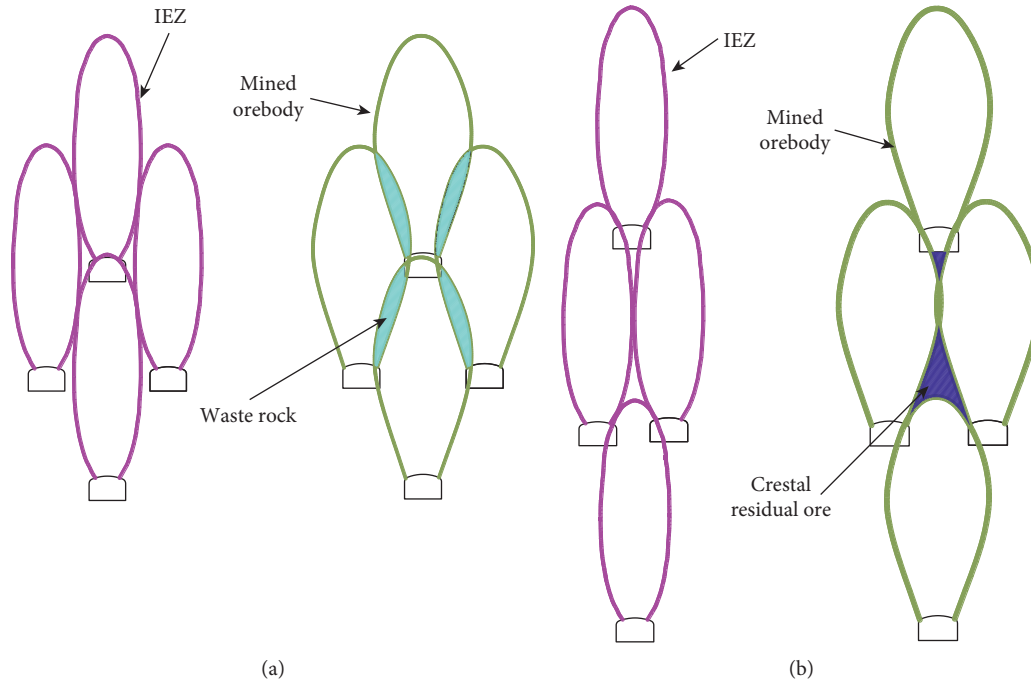


FIGURE 13: The mined orebody and IEZ specific arrangement. (a) Arrangement of IEZs and mined orebodies with large spacing. (b) Arrangement of IEZs and mined orebodies with high sublevel.

TABLE 2: Height and width of mined orebody in the test.

Drawing ores (t)	Height (m)	Width (m)	H/W
500	11.8	5	2.36
1000	14.9	7.6	1.96
1500	18.5	8.7	2.12
2000	20.9	10	2.09
2500	22.5	10.8	2.08
3000	25	11.5	2.17

TABLE 3: Stope structure parameter scheme.

Scheme	Height (m)	Drift spacing (m)
1	18	20
2	20	18
3	20	20
4	22	20
5	24	20
6	24	22

preparatory work as well as production efficiency. The excellent drawing indexes were obtained under the new stope structural parameters, proving that the stope structural

parameters determined by the mined orebody's shape were a reasonable matching relationship. It was helpful to improve the economic benefit of the mine.

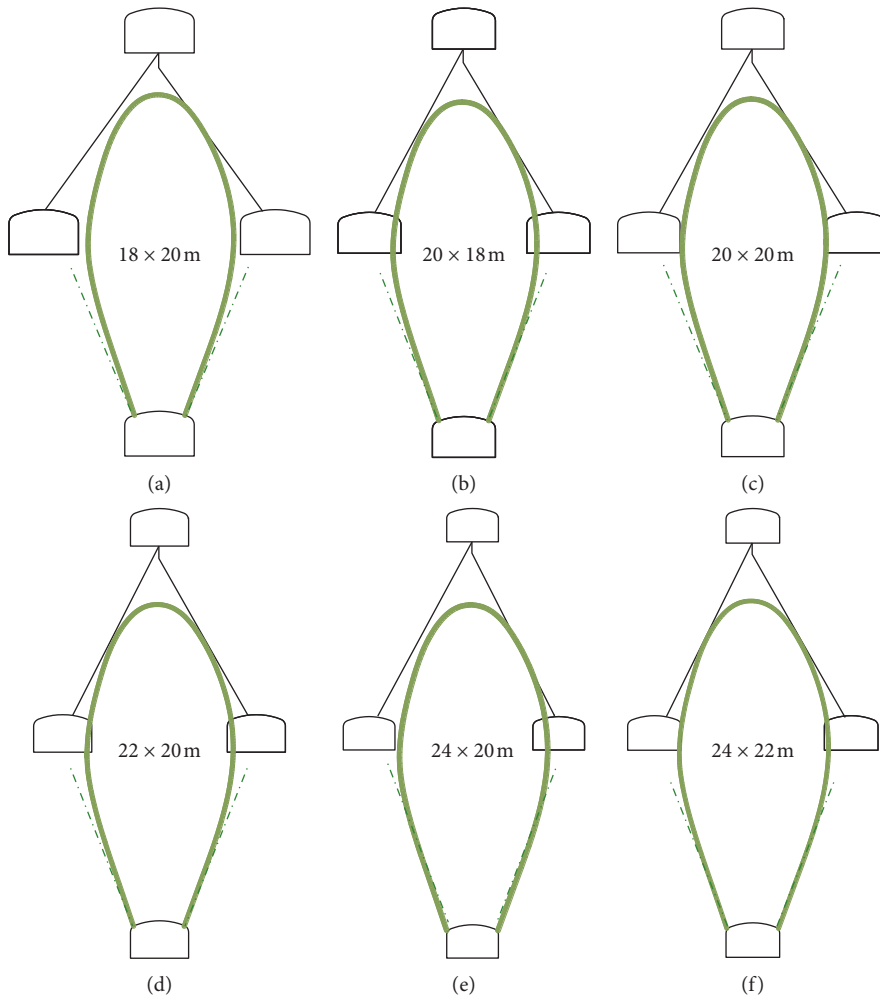


FIGURE 14: The matching degree between the mined orebody's shape and structural parameter schemes.

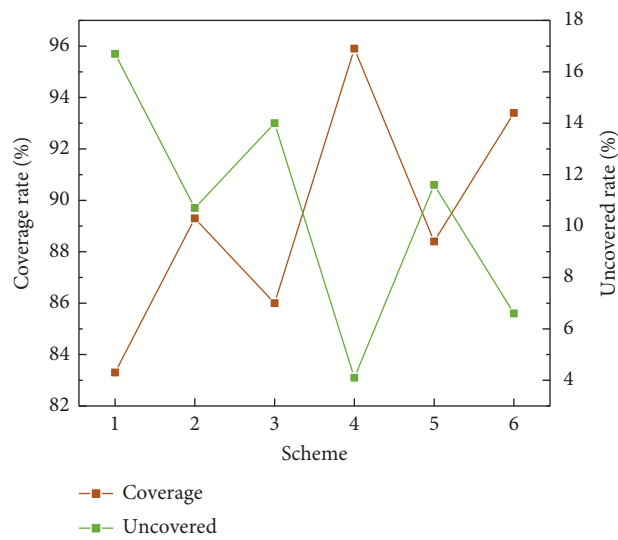


FIGURE 15: Coverage and uncovered rate of mined orebody of each structural parameter scheme.

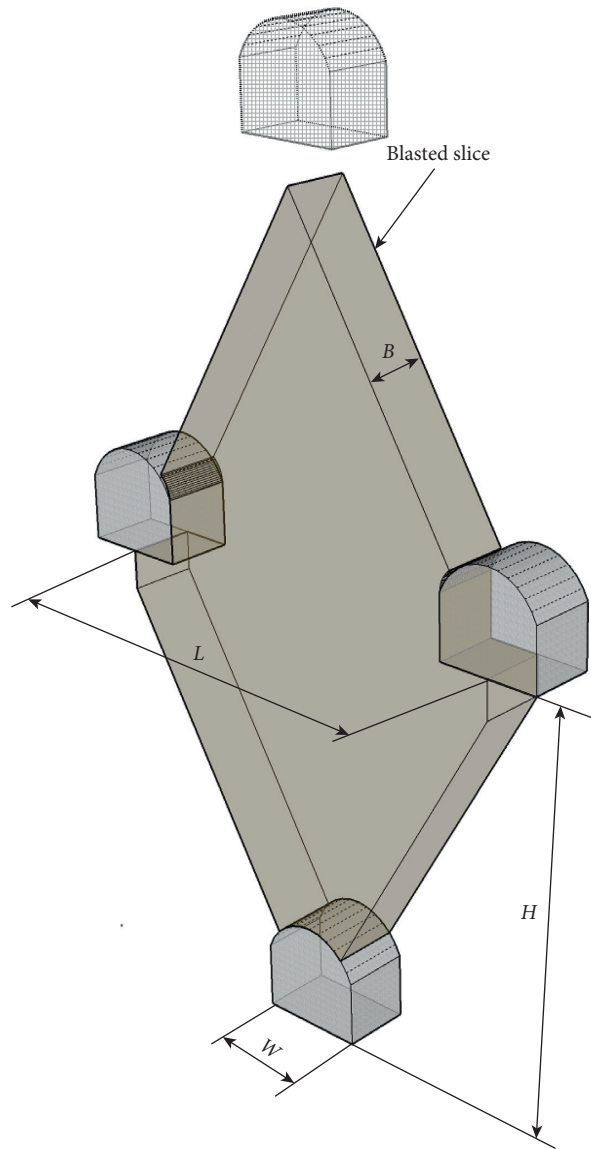


FIGURE 16: The blasted slice determined by the optimized structural parameters.

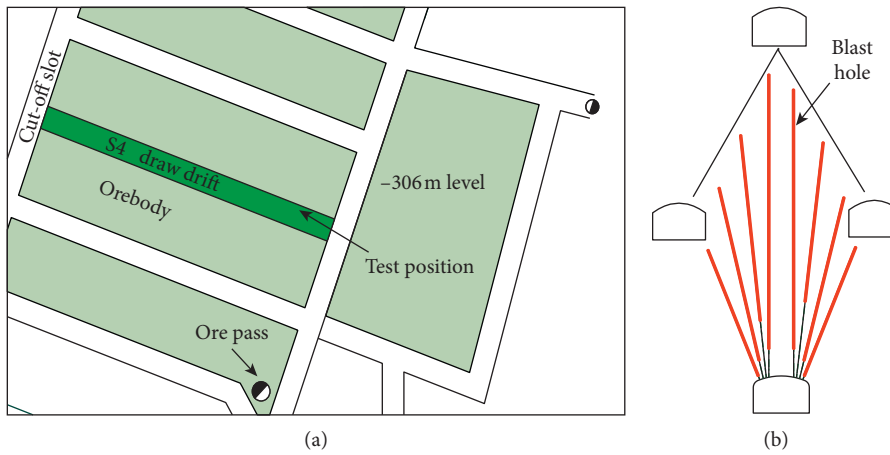


FIGURE 17: (a) The plane position of the test stoppe. (b) The detailed arrangement of blast holes in verification tests.

TABLE 4: The drawing ore date in the test stope.

Number	Q (t)	C (%)	Q _c (t)	C _c (%)
1	3258	45.64	3326	42.1
2	3289	45.72	3196	42.1
3	3313	45.29	3294	42.1
4	3303	46.22	3603	42.1
5	3326	46.88	3104	42.9
6	3347	46.35	3552	42.9
7	3366	46.96	3493	42.9
8	3355	46.64	3679	42.9
9	3372	47.17	3556	42.9
10	3354	47.38	3667	41.39
11	3339	47.37	3594	41.39
12	3328	47.15	3730	41.39
13	3386	47.62	3973	41.39

5. Conclusions

Here, based on the Meishan iron mine with sublevel caving (SLC) method, the mined orebody's shape measurement method and the relationship between mined orebody and IEZ were studied. Meanwhile, the structure parameters of the stope were optimized using the mined orebody's shape. In the field test, the markers were arranged in a single blasted slice, the mined orebody was measured by in situ test method. The monitored recovery rate of markers was 68.4%. The mined orebody's shape was compared with IEZ's shape, and the difference increased with increasing height. The reasonable stope structure parameters were finally optimized through the mined orebody's matched with designed stope structures. The sublevel height (H) was 22 m, and the drift spacing (S) was 20 m. Besides, the verification tests were employed on the optimized stope structural parameters, the recovery rate of the new test stope was 90.64%, and the dilution rate was 9.95%, indicating that the new structural parameters were beneficial to improve production efficiency.

Data Availability

The data used to support the findings of the study are available from the corresponding author upon request.

Conflicts of Interest

The authors declare that they have no conflicts of interest.

Acknowledgments

The study was supported by grants from the National Natural Science Foundation of China (nos. 51534003 and 51404065), the Basic Scientific Research Program funded for Central Universities and Colleges of China (no. 140104008), and the National Key Research and Development Program of China (no. 2016YFC0801601). The authors are grateful for their support.

References

- [1] I. D. Brunton, S. J. Fraser, J. H. Hodgkinson, and P. C. Stewart, "Parameters influencing full scale sublevel caving material recovery at the Ridgeway gold mine," *International Journal of Rock Mechanics and Mining Sciences*, vol. 47, no. 4, pp. 647–656, 2010.
- [2] L. Wang, A. Shao, X. Liu, L. Yang, and H. Ding, "New computational framework for modeling the gravity flow behavior of sublevel caving material," *Computers and Geotechnics*, vol. 125, Article ID 103675, 2020.
- [3] D. S. S. Sandanayake, E. Topal, and M. W. A. Asad, "Designing an optimal stope layout for underground mining based on a heuristic algorithm," *International Journal of Mining Science and Technology*, vol. 25, no. 5, pp. 767–772, 2015.
- [4] K. Yu, F. Ren, G. Chitombo, R. Puscasu, and L. Kang, "Optimum sublevel height and drift spacing in sublevel caving mining based on random medium theory," *Mining, Metallurgy & Exploration*, vol. 37, no. 2, pp. 681–690, 2020.
- [5] R. He and F. Ren, "Stop structure parameters optimization of deep ore body in beiminghe iron mine," *Metal Mine*, vol. 432, no. 6, pp. 16–18, 2012.
- [6] G. Tao, Z. Liu, F. Ren, and Q. Ren, "Optimization research of stope structural parameters in sublevel caving with non-pillar," *China Coal Society*, vol. 35, no. 8, pp. 1269–1272, 2010.
- [7] A. Jin, H. Sun, S. Wu, and Y. Gao, "Confirmation of the upside-down drop shape theory in gravity flow and development of a new empirical equation to calculate the shape," *International Journal of Rock Mechanics and Mining Sciences*, vol. 92, pp. 91–98, 2017.
- [8] F. Ren, *Stochastic Medium Theory for Draw and its Application*, Metallurgical Industry Press, Beijing, China, 1994.
- [9] G. Tao, M. Lu, X. Zhang, R. Zhang, and Z. Zhu, "A new diversion drawing technique for controlling ore loss and dilution during longitudinal sublevel caving," *International Journal of Rock Mechanics and Mining Sciences*, vol. 113, pp. 163–171, 2019.
- [10] G. Tao, S. Yang, and F. Ren, "Experimental research on granular flow characters of caved ore and rock," *Rock and Soil Mechanics*, vol. 30, no. 10, pp. 2950–2954, 2009.
- [11] M. E. Kuchta, "A revised form of the Bergmark-Roos equation for describing the gravity flow of broken rock," *Mineral Resources Engineering*, vol. 11, no. 4, pp. 349–360, 2002.
- [12] Qi Wang, Z. Jiang, B. Jiang, H. Gao, Y. Huang, and P. Zhang, "Research on an automatic roadway formation method in deep mining areas by roof cutting with high-strength bolt-

- grouting,” *International Journal of Rock Mechanics and Mining Sciences*, vol. 128, Article ID 104264, 2020.
- [13] Y. Wang, W. K. Feng, R. L. Hu, and C. H. Li, “Fracture evolution and energy characteristics during marble failure under triaxial fatigue cyclic and confining pressure unloading (FC-CPU) conditions,” *Rock Mechanics and Rock Engineering*, vol. 54, pp. 799–818, 2021.
- [14] Q. Wang, Y. Wang, M. C. He et al., “Experimental research and application of automatically formed roadway without advance tunneling,” *Tunnelling and Underground Space Technology*, vol. 114, no. 3, Article ID 103999, 2021.
- [15] A. Li, F. Dai, Y. Liu, H. B. Du, and R. C. Jiang, “Dynamic stability evaluation of underground cavern sidewalls against flexural toppling considering excavation-induced damage,” *Tunnelling and Underground Space Technology*, vol. 112, Article ID 103903, 2021.
- [16] R. Kvapil, *Underground Mining Methods Handbook*, Society of Mining, Metallurgy and Explorations, Englewood, CO, USA, 1982.
- [17] I. Janelid and R. Kvapil, “Sublevel caving,” *International Journal of Rock Mechanics and Mining Science & Geomechanics Abstracts*, vol. 3, no. 2, pp. 129–132, 1966.
- [18] R. Kvapil, “Underground Mining Methods Handbook,” *The Mechanic Sand Design of Sublevel Caving Systems*, US Department of Energy, New York, NY, USA, 1982.
- [19] Mattson, Stewart, and J. A. Cox, “Sublevel caving and draw control procedures at Granduc,” *Mineral Metallurgy Bulletin*, vol. 66, no. 732, pp. 45–56, 1973.
- [20] D. O’Sullivan and A. Newman, “Optimization-based heuristics for underground mine scheduling,” *European Journal of Operational Research*, vol. 241, no. 1, pp. 248–259, 2015.
- [21] P. O. Sandstrom, “Application and optimization of sublevel caving techniques,” *Engineering and Mining Journal*, vol. 6, pp. 112–125, 1972.
- [22] F. Melo, F. Vivanco, C. Fuentes, and V. Apablaza, “On drawbody shapes: from Bergmark-Roos to kinematic models,” *International Journal of Rock Mechanics and Mining Sciences*, vol. 44, no. 1, pp. 77–86, 2007.
- [23] Q. X. Meng, W. Y. Xu, H. L. Wang, X. Y. Zhuang, W. C. Xie, and T. Rabczuk, “DigiSim-an open source software package for heterogeneous material modeling based on digital image processing,” *Advances in Engineering Software*, vol. 148, Article ID 102836, 2020.
- [24] C. Zhu, M. C. He, M. Karakus, X. H. Zhang, and Z. Guo, “The collision experiment between rolling stones of different shapes and protective cushion in open-pit mines,” *Journal of Mountain Science*, vol. 18, no. 5, pp. 1391–1403, 2021.
- [25] Q. Yin, J. Y. Wu, C. Zhu, M. C. He, and Q. X. Meng, “Shear mechanical responses of sandstone exposed to high temperature under constant normal stiffness boundary conditions,” *Geomechanics and Geophysics for Geo-Energy and Geo-Resources*, vol. 7, no. 35, 2021.
- [26] R. Castro, R. Trueman, and A. Halim, “A study of isolated draw zones in block caving mines by means of a large 3D physical model,” *International Journal of Rock Mechanics and Mining Sciences*, vol. 44, no. 6, pp. 860–870, 2007.
- [27] R. Castro and M. Pineda, “The role of gravity flow in the design and planning of large sublevel stopes,” *Journal of the South African Institute of Mining and Metallurgy*, vol. 115, no. 2, pp. 113–118, 2015.
- [28] Z. Zhang and M. Wimmer, “A case study of dividing a single blast into two parts in sublevel caving,” *International Journal of Rock Mechanics and Mining Sciences*, vol. 104, pp. 84–93, 2018.
- [29] A. Gustafson, H. Schunnesson, J. Paraszczak, G. Shekhar, and P. Brnman, “Operator influence on the loading process at LKAB’s iron ore mines,” *Journal of the South African Institute of Mining and Metallurgy*, vol. 120, no. 3, pp. 191–202, 2020.
- [30] J. Cao, F. Ren, J. Zhang, and Q. Yang, “Experimental study on diversion drawing by stress-relieve sublevel caving method,” *Journal of Northeastern University*, vol. 32, pp. 1186–1189, 2011.
- [31] J. Wu, W. Lin, and H. Hu, “Post-failure simulations of a large slope failure using 3DEC: the Hsien-du-Shan slope,” *Engineering Geology*, vol. 242, pp. 92–107, 2018.
- [32] R. Xia, B. Li, X. Wang, T. Li, and Z. Yang, “Measurement and calibration of the discrete element parameters of wet bulk coal,” *Measurement*, vol. 142, pp. 84–95, 2019.
- [33] R. Castro, F. Gonzalez, and E. Arancibia, “Development of a gravity flow numerical model for the evaluation of drawpoint spacing for block/panel caving,” *Southern African Institute of Mining and Metallurgy*, vol. 109, no. 7, pp. 393–400, 2009.
- [34] D. Qiao, *Research on particle movement rule and draw theory*, PhD thesis, Northeastern University, Boston, MA, USA, 2003.
- [35] Y. Hu, F. Ren, H. Ding, Y. Fu, and B. Tan, “Study on the process and mechanism of slope failure induced by mining under open pit slope: a case study from Yanqianshan iron mine, China,” *Advances in Civil Engineering*, vol. 2019, Article ID 6862936, 26 pages, 2019.
- [36] H. Ding, S. Chen, S. Chang, G. Li, and L. Zhou, “Prediction of surface subsidence extension due to underground caving: a case study of Hemushan iron mine in China,” *Mathematical Problems in Engineering*, vol. 2020, Article ID 5086049, 10 pages, 2020.
- [37] B. Tan, Z. Zhang, R. He, and Q. Zhu, “Discussion on the rationality and experimental research of the ore-drawing ellipsoid arrangement theory,” *Journal of Northeastern University*, vol. 40, no. 7, pp. 1014–1019, 2019.

Research Article

Prediction and Evaluation of Rockburst Based on Depth Neural Network

Jin Zhang , Mengxue Wang, and Chuanhao Xi

College of Civil Engineering, Qingdao University of Technology, Qingdao 26033, China

Correspondence should be addressed to Jin Zhang; zhangjin@qut.edu.cn

Received 13 May 2021; Accepted 27 May 2021; Published 7 June 2021

Academic Editor: Gan Feng

Copyright © 2021 Jin Zhang et al. This is an open access article distributed under the Creative Commons Attribution License, which permits unrestricted use, distribution, and reproduction in any medium, provided the original work is properly cited.

The formation mechanism of rockburst is complex, and its prediction has always been a difficult problem in engineering. According to the tunnel engineering data, a three-dimensional discrete element numerical model is established to analyze the initial stress characteristics of the tunnel. A neural network model for rockburst prediction is established. Uniaxial compressive strength, uniaxial tensile strength, maximum principal stress, and rock elastic energy are selected as input parameters for rockburst prediction. Training through existing data. The neural network model shows that the rockburst risk is closely related to the maximum principal stress. Based on the division of rockburst risk areas, according to different rockburst levels, the corresponding treatment methods are put forward to avoid the occurrence of rockburst disaster. Based on the field measured data and test data, combined with the existing rockburst situation, numerical simulation and neural network method are used to predict the rock burst classification, which is of great significance for the early and late construction safety of the tunnel.

1. Introduction

Deep tunnel rockburst has great harm, and the mechanism and law of rockburst formation have not been fully revealed, which leads to the difficulty of comprehensive, accurate, and complete rockburst prediction and prevention methods. The academic theories related to its formation mainly include strength theory, impact tendency theory, stiffness theory, energy theory, and three-criterion instability theory.

For example, in Feng et al.'s work [1], in the field of coal mining, based on the elastic thin plate theoretical model, the roof deformation deflection equation and surrounding rock deformation energy equation are derived. A method is proposed to reduce the risk of rockburst by quantitatively adjusting the strength of backfill. Li et al. [2] established an elastic-plastic brittle catastrophe rockburst model of rock with structural plane and studied the relationship between energy accumulation and dissipation in the process of dynamic fracture of coal and rock. In the work of Pan et al. [3], based on energy theory and damage mechanics, the quantitative functional relationship between joint density and energy density was derived. Then, the theoretical results are

verified by numerical simulation and uniaxial compression test, and the influence of joint density on rockburst tendency of elastic brittle plastic rock mass is discussed. In the work of Pan et al. [4], based on energy theory and damage mechanics, the quantitative functional relationship between joint density and energy density is derived. In the work of Wang et al. [5], based on the instability theory and cusp catastrophe theory, the instability conditions of pillars under asymmetric mining conditions were determined. According to the complexity and uncertainty of rockburst prediction, Ran et al. [6] established a rockburst classification prediction model based on rough set normal cloud. Xue et al. [7] proposed a method of rockburst evaluation based on rough set theory and extension theory. Ma et al. [8] analyzed several main rockburst theories, including strength theory, energy theory, blasting responsibility theory, stiffness theory, and instability theory. Li et al. [9–11] used neural network inversion technology to analyze the in situ stress distribution characteristics and engineering failure phenomenon of rock mechanics engineering.

In terms of rockburst prediction method and rock mechanics research method, Ji et al. [12] studied the

contribution of multiple MS data (including MS original wave data and MS energy data) to rockburst by using the method of combining support vector machine (SVM) and genetic algorithm (GA). Zhou et al. [13] used the stress type rockburst criterion of Gaoligongshan tunnel to identify the high-risk area and low-risk area of rockburst. Then, acoustic emission (AE) method is used to predict the magnitude and location of rockburst danger area. Cai et al. [14] established membership function in fuzzy model by using Gaussian shape and exponential distribution function in reliability theory. The core of performance measure in confusion matrix is used to determine the weight of each index [15–19]. The principle of maximum membership degree (MMDP) is combined with variable fuzzy pattern recognition (VFPR) to obtain the comprehensive prediction results [20–23]. Other experts have also provided relevant research on rockburst prediction by using rock fractal, indoor experiments and engineering practice [24–26].

As an effective means to study rock mechanics, numerical simulation has been widely used in various fields of rock mechanics. At the same time, relying on the effective analysis of the field data to obtain the relevant physical and mechanical model is also essential for the research [27–31].

In this paper, Yufengsi tunnel is taken as a typical engineering example. Firstly, according to the stratum lithology and rock mass in the study area, the in situ stress parameters and rock strength parameters are obtained through laboratory tests. Then, through numerical simulation, the in situ stress field is inverted, and the main control factors of rockburst are selected. Finally, through the neural network training model, the characteristics of the target rockburst are analyzed, and the preventive measures are put forward. The research can provide an important basis for the division of rockburst area and subsection control.

2. Engineering Geological Conditions

2.1. Geological Characteristics. Yufengsi tunnel is located in the south section of Yulong Snow Mountain in the Sanjiang orogenic belt, northwest of Lijiang, Yunnan Province. The tunnel site belongs to the high mountain area of tectonic denudation. The mountain system is nearly north-south. The main peak of Yulong Snow Mountain is 5596 m above sea level. The tunnel passes through the watershed between Lijiang basin and Jinsha River on the southwest side of Yulong Snow Mountain and runs to 310 km. The total length is about 10.9 km, and the maximum buried depth is more than 1000 m. It is a deep buried tunnel, as shown in Figure 1.

Due to the multistage tectonic process in geological history, the structural deformation in the field area is strong, folds and active faults are developed, and the tunnel passing area is mainly controlled by nearly north-south comb folds and faults. From the entrance of Lijiang basin tunnel to the exit of Renhegou tunnel, the line successively passes through Daju Lijiang fault zone, Wenhai fault zone, Wenhai anticline, Xuehuacun syncline, and other geological structures.

The total length of the tunnel longitudinal section is about 10.96 km. According to the engineering rock mass classification standard (GB 50218-94), the surrounding rock

quality can be divided into several levels, such as II, III, IV and V. Among them, class V surrounding rock is mainly distributed in the loose eluvium section near the tunnel entrance, and the loose eluvium section is about 150 m. The stratum is weak, with high water content and strong heterogeneity. Type IV surrounding rock is mainly distributed in the fault fracture zone and the contact zone of different lithology. The rock mass is broken and is mostly in granular structure, with a total length of about 500 m; class III surrounding rock is mainly distributed in the basalt and medium thick limestone section, with a total length of about 4000 m, of which the basalt section is about 3460 m long, which is distributed near the tunnel entrance to the entry mileage of 3870 m. The tunnel in this section has a large buried depth, the maximum buried depth is about 1000 m, and the rock mass is relatively complete. The limestone section is about 600 m long and is distributed near the tunnel exit. In the range of 4–10 km, the grade of surrounding rock varies greatly.

2.2. Rock Strength. The higher the strength of rock, the greater the elastic energy accumulated before failure, so the higher the possibility of rockburst. The length of Yufengsi tunnel through hard basalt accounts for about 40% of the total length, and thick sandstone and thick limestone account for about 50%. The complete massive basalt is mainly located between 300 and 3800 m of tunnel mileage, the local hard thick sandstone is between 3800 and 10200 m, and the hard thick limestone is mainly located between 10200 and 10900 m near the tunnel exit.

Basalt, sandstone, and limestone samples were collected in the study area, and uniaxial and triaxial stress tests were carried out. The test results show that the three kinds of rock failure are shear failure (Figure 2). The uniaxial strengths of sandstone, limestone, and basalt are 143 MPa, 116 MPa, and 102 MPa, respectively. With the increase of surrounding rock, the strengths of three kinds of rock samples increase sharply; limestone has the largest elastic modulus, followed by sandstone and basalt.

3. In Situ Stress Inversion

The in situ stress is an important factor affecting tunnel rockburst. With the increase of depth, the in situ stress increases, and the number, frequency, and intensity of rockburst increase. At the same time, the structure and strong denudation are easy to produce abnormal distribution and concentration of in situ stress. Therefore, it is very important to use numerical simulation and machine learning method for in situ stress inversion.

3.1. Model Establishment. Taking the tunnel as the central axis, rectangular areas with side lengths of 10889 m and 2500 m are selected, and the bottom surface of the model is taken to 1000 m below the tunnel axis. The establishment of the top surface is based on the contour plane map provided by the geological exploration data, which is imported into surfer software, and the high-precision terrain coordinate

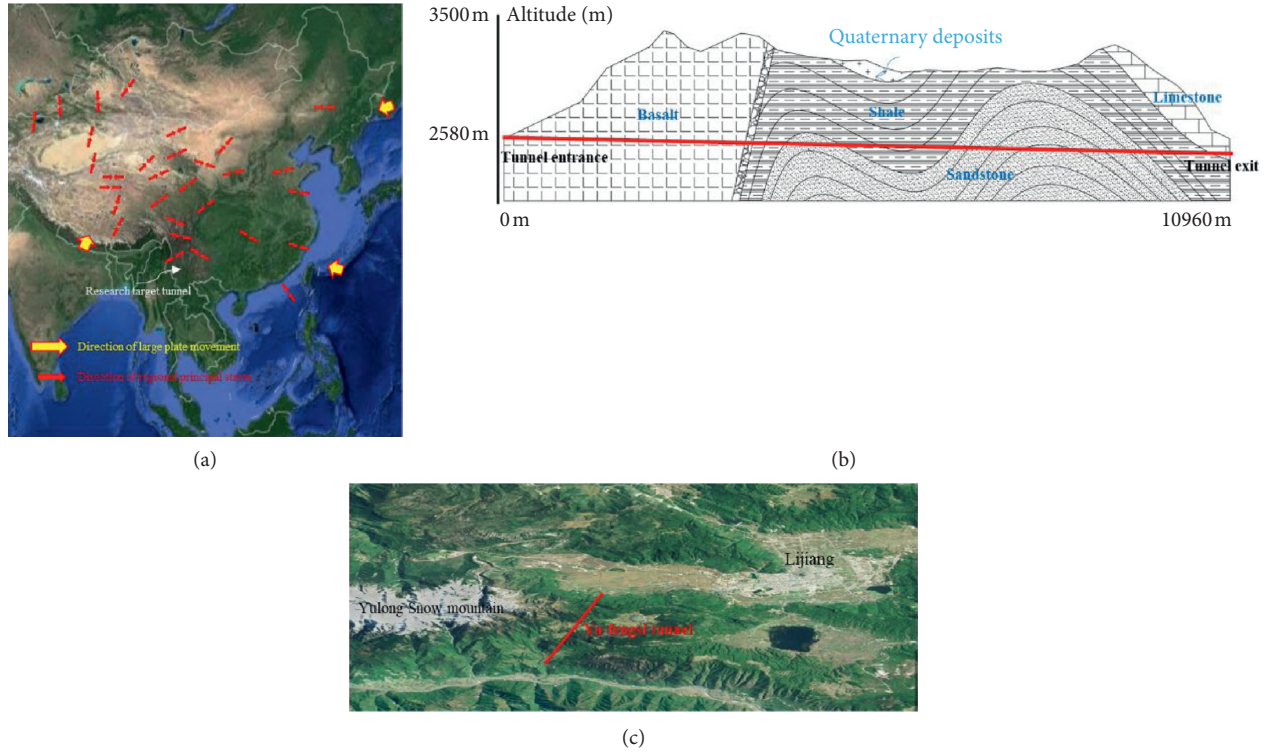


FIGURE 1: Engineering geological characteristics of Yufengsi deep-buried tunnel. (a) Tectonic stress. (b) Geological section. (c) Tunnel location.

value is obtained by Kriging interpolation method. Then, the coordinate value is imported into the discrete element software 3DEC. The specific numerical model is shown in Figure 3. The material parameters of rock mass are shown in Table 1.

3.2. Boundary Conditions. The four basic factors that cause the distribution of in situ stress are vertical stress field, horizontal tectonic stress field in X -direction, horizontal tectonic stress field in Y direction, and shear tectonic stress field, as shown in Figure 4. The method of applying self-weight stress field is to apply vertical constraint to the bottom of the model and normal constraint to the side of the model. According to the properties of rock mass, the density is applied to obtain the gravity load. The application method of X -direction horizontal tectonic stress field is to apply stress on both sides of the model in X -direction to simulate tectonic stress. The application method of horizontal tectonic stress field in Y -direction is to apply stress on both sides of the model in Y -direction to simulate tectonic stress. The shear tectonic stress field is obtained by applying shear stress to four sides.

3.3. Principle and Results of In Situ Stress Inversion Based on Multiple Regression Analysis. In multiple regression analysis, independent variables must have a significant impact on dependent variables and have a close linear correlation. There is a linear correlation between independent variables and dependent variables. There should

be a certain degree of mutual exclusion between independent variables; that is, the degree of correlation between independent variables should not be higher than that between independent variables and dependent variables. Independent variables should have complete statistical data. Therefore, the stress values obtained under the above four boundary conditions are selected as independent variables. The measured in situ stress is taken as the dependent variable, as shown in the following formula:

$$\hat{\sigma}_k = b_0 + \sum_{i=1}^n b_i \sigma_k^i \quad (1)$$

In the above formula, $\hat{\sigma}_k$ is the measured in situ stress value of the measuring point, and k is the mark of the measuring point. b_0 is the free term and b_i is the multiple regression coefficient. n is the number of working conditions. In σ_k^i , k is the numerical solution consistent with the measured point coordinates, and i is the working condition number. In this paper, the first condition is vertical stress, the second condition is X -direction tectonic stress, the third condition is Y -direction tectonic stress, and the fourth condition is shear tectonic stress.

The regression coefficient is solved by the least square method. According to the actual measurement of in situ stress, there are 15 measuring points, and each measuring point has 6 observation components. The sum of squares of the residual error of the least square method is shown in the following formula:

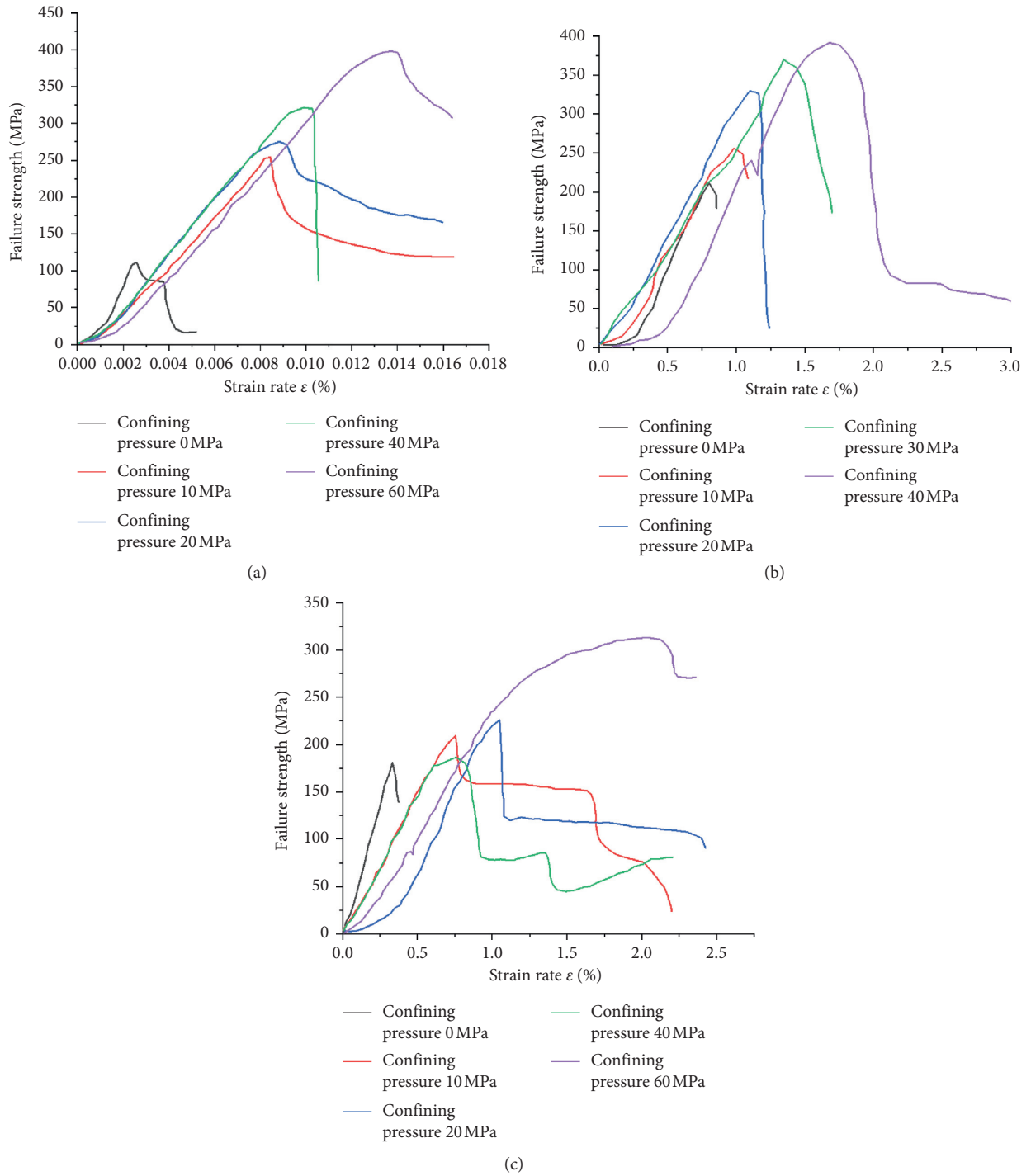


FIGURE 2: Stress-strain curve of tunnel surrounding rock. (a) Limestone. (b) Basalt. (c) Sandstone.

$$Q_{res} = \sum_{k=1}^m \sum_{j=1}^6 \left(\sigma_{jk} - b_0 - \sum_{i=1}^n b_i \sigma_{jk}^i \right)^2. \quad (2)$$

In the above formula, $m = 15$, σ_{jk} is the k th observation point, and j is the stress component obtained by numerical simulation.

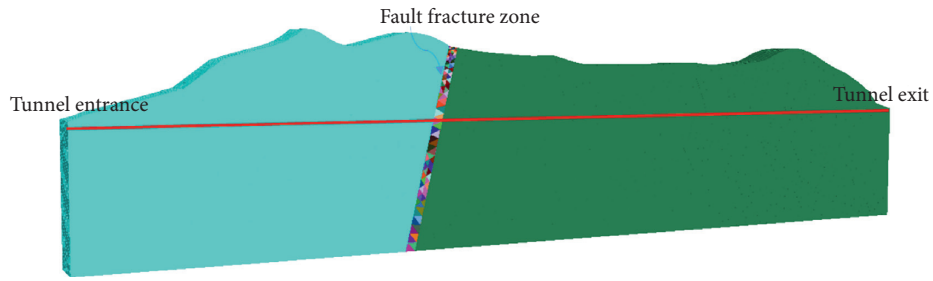


FIGURE 3: Calculation model diagram.

TABLE 1: Physical and mechanical properties of surrounding rock.

Lithology	Density ρ_d	Uniaxial compression test				Triaxial compression test			
		σ_c	E	μ	10 MPa	20 MPa	40 MPa	60 MPa	
Sandstone	2.710	143.58	6.14	0.328	187.63	257.19	265.12	380.00	
Limestone	2.797	116.17	70.64	0.229	270.26	314.68	349.07	468.34	
Basalt	2.965	102.76	52.24	0.129	222.78	307.29	345.94	418.57	

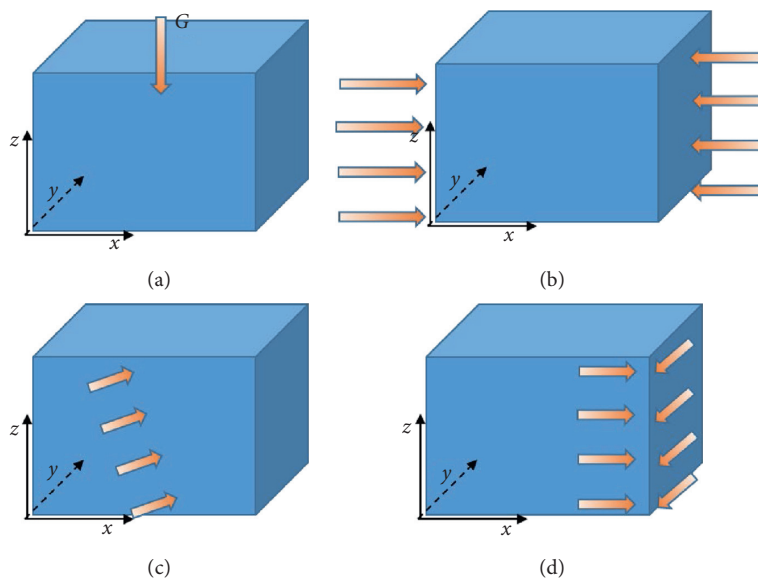


FIGURE 4: Schematic diagram of model boundary conditions. (a) Z-direction load. (b) X-direction structural load. (c) Y-direction structural load. (d) Shear tectonic stress.

According to the principle of the least square method, the optimal solution is obtained when the sum of the squares

of the residuals between the observed value and the regression value reaches the minimum.

$$\begin{bmatrix}
 6m \sum_{k=1}^m \sum_{j=1}^6 \sigma_{jk}^1 & \sum_{k=1}^m \sum_{j=1}^6 \sigma_{jk}^2 & \dots & \sum_{k=1}^m \sum_{j=1}^6 \sigma_{jk}^n \\
 \sum_{k=1}^m \sum_{j=1}^6 (\sigma_{jk}^1)^2 & \sum_{k=1}^m \sum_{j=1}^6 \sigma_{jk}^1 \sigma_{jk}^2 & \dots & \sum_{k=1}^m \sum_{j=1}^6 \sigma_{jk}^1 \sigma_{jk}^n \\
 & \sum_{k=1}^m \sum_{j=1}^6 (\sigma_{jk}^2)^2 & \dots & \sum_{k=1}^m \sum_{j=1}^6 \sigma_{jk}^2 \sigma_{jk}^n \\
 \text{Symmetric} & & & \vdots \\
 & & & \sum_{k=1}^m \sum_{j=1}^6 (\sigma_{jk}^n)^2
 \end{bmatrix}
 \times
 \begin{bmatrix}
 b_0 \\
 b_1 \\
 b_2 \\
 \vdots \\
 b_n
 \end{bmatrix}
 =
 \begin{bmatrix}
 \sum_{k=1}^m \sum_{j=1}^6 \sigma_{jk} \\
 \sum_{k=1}^m \sum_{j=1}^6 \sigma_{jk}^1 \sigma_{jk} \\
 \sum_{k=1}^m \sum_{j=1}^6 \sigma_{jk}^2 \sigma_{jk} \\
 \vdots \\
 \sum_{k=1}^m \sum_{j=1}^6 \sigma_{jk}^n \sigma_{jk}
 \end{bmatrix}. \quad (3)$$

The matrix of undetermined coefficient b is obtained by solving (3), and the distribution of regional geostress is obtained according to equation (1). The results show that the free term b_0 is 1.66, the self-weight stress field regression coefficient b_1 is 1.33, the x -direction tectonic stress field regression coefficient b_2 is 5.31, the y -direction tectonic stress field regression coefficient b_3 is 4.68, and the horizontal shear tectonic stress field b_4 is 9.98.

According to the statistical principle and multiple regression significance experimental analysis, the correlation coefficient $R = 0.996$ indicates that there is a high degree of correlation between the independent variable and the dependent variable, and the F significance statistic is 1.16×10^{-8} , which also indicates that the regression effect is significant.

Stress field inversion regression formula is as follows:

$$\sigma_{\text{inversion value}} = 1.66 + 5.31\sigma_x + 4.68\sigma_y + 1.33\sigma_z + 9.98\sigma_{xy}. \quad (4)$$

In the above formula: $\sigma_{\text{inversion value}}$ is the inversion value of in situ stress, σ_x is the stress produced by the tectonic compression movement in X -direction, σ_y is the stress produced by the tectonic compression movement in Y -direction, σ_z is the in situ stress component produced by the gravity stress, and σ_{xy} is the in situ stress component produced by the plane shear stress.

Through the simulation inversion results, the distribution maps of the maximum, middle, and minimum principal stress fields in Yufengsi tunnel area are obtained (Figures 5–7). The stress distribution of rock mass in tunnel site has the following characteristics.

The in situ stress field is obviously affected by lithology, topography, and faults. The stress concentration is strong in the valley. On steep ridges and isolated hilltops, the stress relaxes and decreases. The contour of the maximum principal stress is basically consistent with the topographic change on the profile, and the value is high in the mountain area, but the contour of the basin is shifted downwards. With

the increase of buried depth, the stress value increases. Near the tunnel exit, the difference between the maximum principal stress and the minimum principal stress reaches 40 MPa, and the tunnel is obviously affected by the bias stress environment.

4. Prediction and Analysis of Rockburst Based on Deep Neural Network

4.1. Evaluation Index and Sample Data. There are external and internal reasons for rockburst. The external reason is that rockburst usually occurs in underground rock mass with high ground stress. Due to the excavation of caverns in the rock mass, the spatial environment of rock mass is changed, and the stress redistribution and stress concentration around the caverns are caused. The internal reason is that rockburst usually occurs in hard rock, and its mineral structure is dense and hard. The brittle failure of surrounding rock due to excavation unloading leads to the sudden release of elastic strain energy stored in rock mass, which eventually leads to the failure of surrounding rock, such as burst loosening, spalling, and ejection, resulting in rockburst. At the same time, it is found that the stress level of rockburst is higher, and the intensity of rockburst is closely related to the degree of stress concentration. Considering the main factors affecting the occurrence and intensity of rockburst, the four indexes are selected.

The factors that affect the rockburst in tunnel are more complex, which is particularly important for the selection of the indexes to evaluate the occurrence of rock burst. Through the mechanism of rockburst and investigation statistics, this paper holds that rockburst usually occurs in the area with high stress concentration, so the maximum principal stress is selected as one of the evaluation criteria. Rockburst is a result of energy accumulation and instantaneous explosion of rock. Therefore, the rock hardness, namely, uniaxial strength and tensile strength, is also an

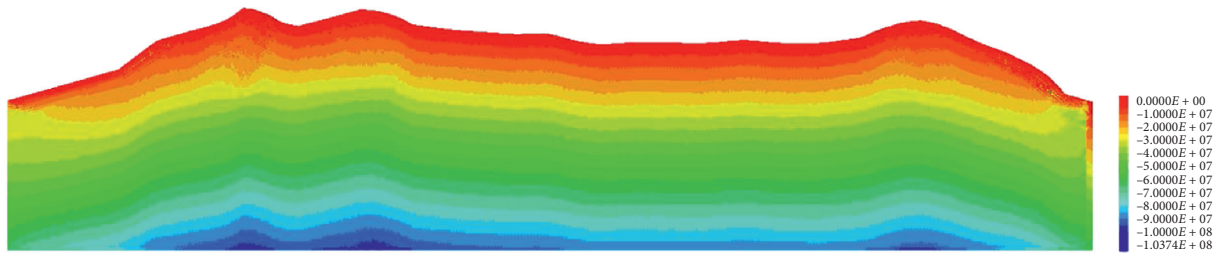


FIGURE 5: Distribution characteristics of maximum principal stress.

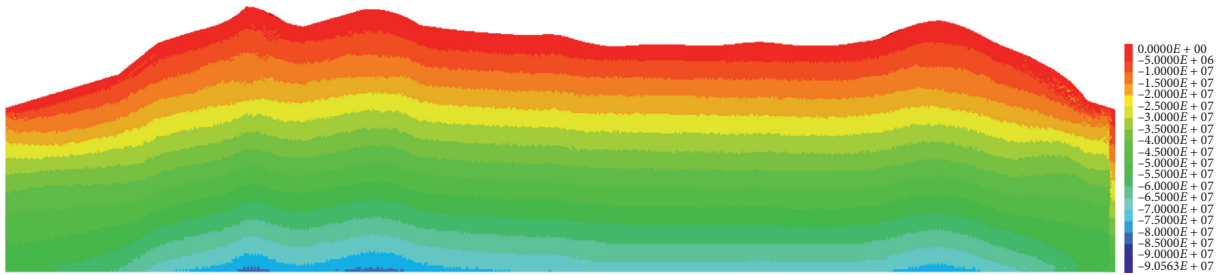


FIGURE 6: Distribution characteristics of intermediate principal stress.

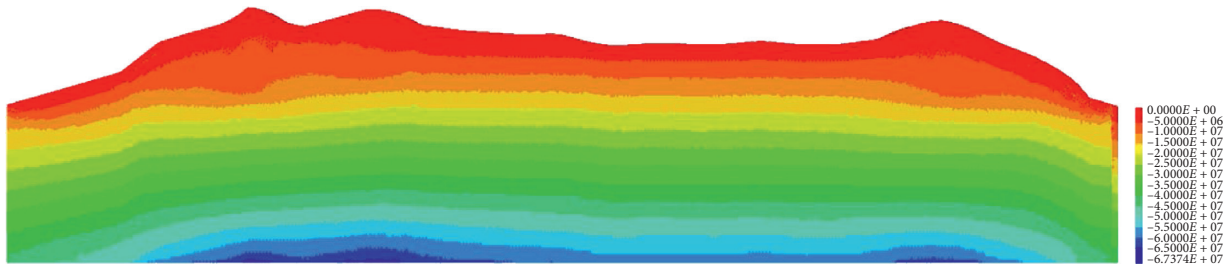


FIGURE 7: Distribution characteristics of minimum principal stress.

important index. The higher the index, the greater the energy stored between the occurrence and failure of rock, and the elastic energy index of rock is also regarded as one of the evaluation indexes.

Through the analysis of rockburst at home and abroad, the sample data are obtained by taking the maximum principal stress, uniaxial strength, tensile strength, and elastic energy index as the rating indexes in Table 2.

4.2. BP Neural Network Model Based on Genetic Algorithm Optimization. BP neural network optimized by genetic algorithm is divided into three parts: BP neural network structure determination, genetic algorithm optimization, and BP neural network prediction. The structure of BP neural network is determined according to the number of input and output parameters of the fitting function, and then the individual length of genetic algorithm is determined. Genetic algorithm optimization uses genetic algorithm to optimize the weights and thresholds of BP neural network. Each individual in the population contains a network

ownership value and threshold. Individual fitness value is calculated by fitness function. Genetic algorithm finds the corresponding individual with the optimal fitness value through selection, crossover, and mutation operation. BP neural network prediction uses genetic algorithm to get the optimal individual, assign the initial weights and thresholds of the network, and output the prediction function after training.

The nonlinear function to be fitted in this paper has four input parameters and one output parameter, so the structure of BP neural network is set as 4-6-1; that is, there are four nodes in the input layer, six nodes in the hidden layer, and one node in the output layer $4 \times 6 + 6 \times 1 = 30$ weights, $6 + 1 = 7$ thresholds, so the individual coding length of genetic algorithm is $30 + 7 = 37$. 20 groups of rock burst data are selected as input data and 10 groups are selected as test data. The sum of absolute prediction errors of training data is taken as individual fitness value. The smaller the individual fitness value is, the better the individual is. The flow chart of BP neural network optimized by genetic algorithm is shown in Figure 8.

TABLE 2: Rockburst sample data of typical hard rock tunnel.

Project name	Maximum principal stress σ_1 (MPa)	Uniaxial compressive strength of rock σ_c (MPa)	Uniaxial tensile strength of rock σ_t (MPa)	Elastic energy index w_{et}	Rockburst grade
Diversion tunnel of Yuzixi hydropower station	90.0	170.0	11.3	9.0	Medium rockburst
Vietas hydropower station in Sweden	80.0	180.0	6.7	5.5	Slight rockburst
Guanyue tunnel, Japan	89.0	236.0	8.3	5.0	Medium rockburst
Qinling tunnel	60.7	111.5	7.9	6.2	Strong rockburst
Kuocangshan tunnel	13.9	124.0	4.2	2.0	No rockburst
Jinping II hydropower station	30.6	160.8	11.1	3.6	Strong rockburst
Erlangshan highway tunnel	53.7	62.29	6.7	5.9	Medium rockburst
Qinling railway tunnel	40	98	7.6	4.6	Slight rockburst

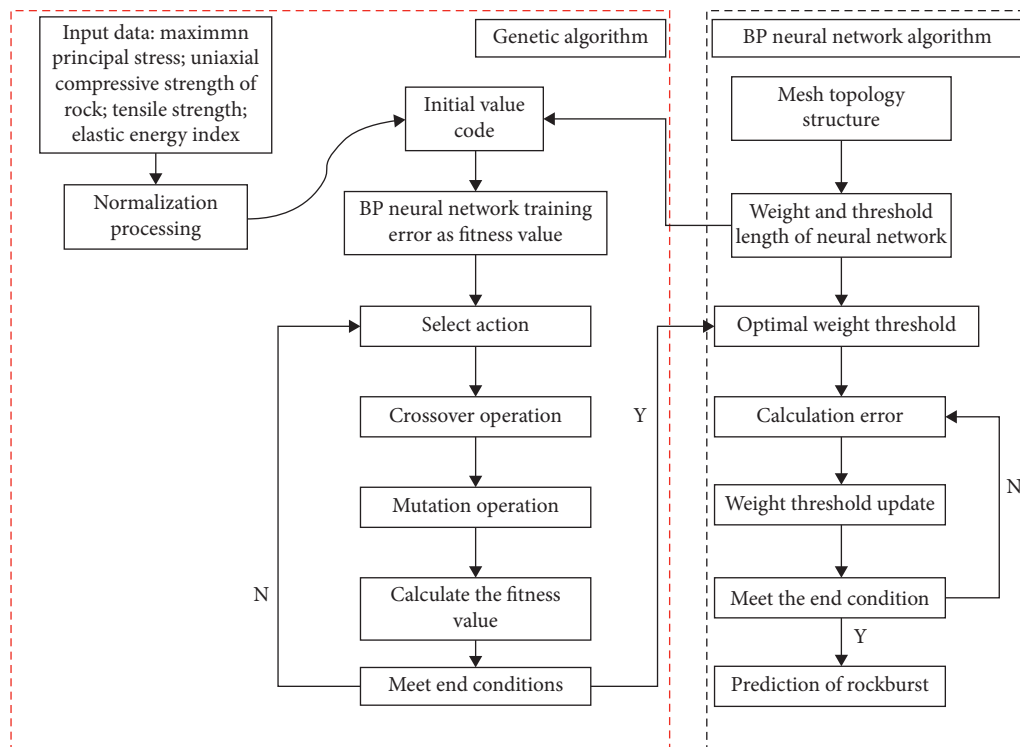


FIGURE 8: Flow chart of BP neural network optimized by genetic algorithm.

4.3. Rockburst Prediction. According to the neural network inversion results, the first section 0~500 m belongs to the basalt slight rockburst section. The second section is the basalt serious rockburst section, from the tunnel entrance mileage of 500 m to 3750 m. The third section is a slight rockburst section, from the tunnel entrance mileage of 3750 m to 5500 m. The fourth section is a medium rockburst section, with the mileage from 5500 m to 9200 m. The fifth section is a serious rockburst section, from 920 m to 11000 m. It can be seen from Figure 9 that the risk degree of rockburst is highly correlated with the maximum principal stress.

5. Advanced Treatment of Rockburst Danger Area

According to the harm of rockburst to engineering construction, rockburst can be divided into three different levels: "slight rockburst," "medium rockburst," and "strong rockburst." Through the above research, the risk characteristics of rockburst in different areas are obtained. The prevention methods of rockburst with different intensity are described below.

In the section of slight rockburst, the excavation footage shall be controlled within 3 m. The water gel explosive with

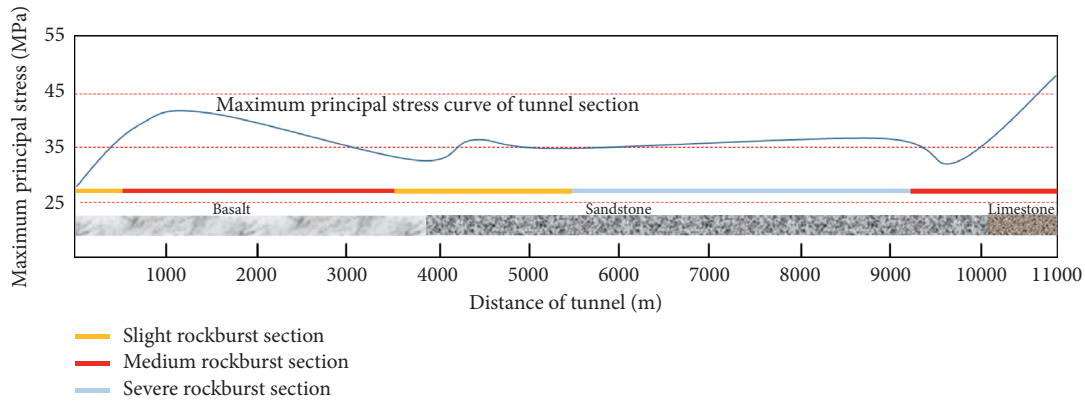


FIGURE 9: Maximum principal stress variation and rockburst risk zoning.

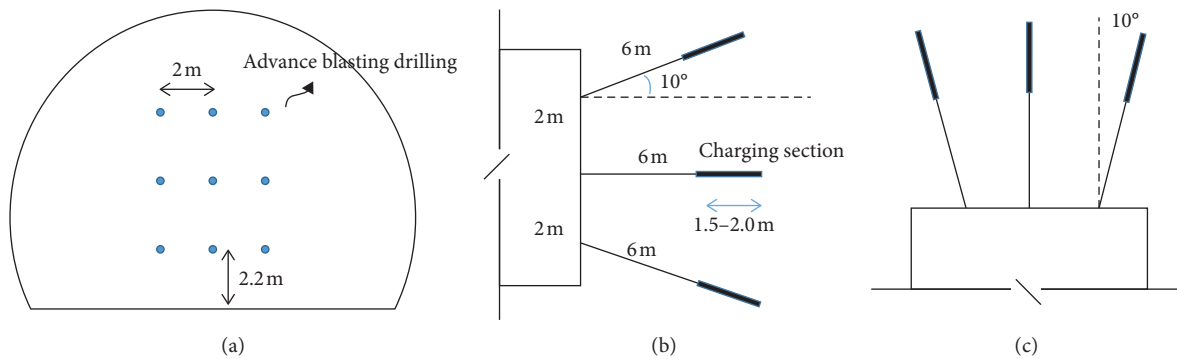


FIGURE 10: Stress release of advance blasting. (a) Front view. (b) Side view. (c) Vertical view.

high fierceness and high power matching with hard rock is selected. The surrounding hole spacing is increased to reduce the impact of blasting on surrounding rock. Strengthen the management of smooth blasting technology, so as to achieve smooth excavation contour and avoid stress concentration caused by uneven surface. Water is added to soften the surrounding rock surface, and high-pressure water is sprayed directly on the excavation exposed surface to soften the surface.

In medium strength rockburst section, advanced in situ stress relief blasting is adopted: the main construction technology of stress adjustment blasting includes the layout of advanced stress relief holes and the design of charge quantity. Generally speaking, the blastholes are required to be evenly arranged on the working face, and the distance between blastholes is about 2 m. The drilling depth is controlled by 2 times of single cycle footage, and the angle is controlled within 5~10°. The length of the hole charge is 1.5~2.0 m, and the charge quantity is 1~2 kg. In actual construction, it is appropriate that the rock mass can be formed by blasting without breaking, and it is prior to the hole blasting, as shown in Figure 10. Combined with advanced blasting, the excavation footage should be controlled within 2 m, with smooth blasting and high-pressure water spraying.

In the strong rockburst section, the same advanced in situ stress relief blasting technology as the medium

rockburst section is adopted, and the vault is properly densified. Two-bench method is adopted for excavation, and the excavation step is controlled within 2 m. At the same time, smooth blasting technology is adopted. High-pressure water spraying softens the surrounding rock on the tunnel surface. The stress release holes are constructed on the side wall of the tunnel with the depth of 3~5 m and the spacing of 0.8 m.

6. Conclusion

Based on the inversion of the initial geostress field in the study area, combined with the neural network calculation model optimized by genetic algorithm, a rockburst prediction model is established:

- (1) It is considered that the main controlling factors of rock burst prediction are uniaxial compressive strength, uniaxial tensile strength, maximum principal stress, and elastic energy index. Based on this, a neural network model based on genetic algorithm optimization is established.
- (2) By collecting and training the existing rockburst data, the analysis shows that the rockburst risk is closely related to the maximum principal stress characteristics, uniaxial strength, tensile strength,

and elastic energy index of rockburst. At the same time, although the buried depth of the tunnel exit section is shallow, the risk of rockburst is high due to the stress concentration in the valley area and the large deviatoric stress.

- (3) The rockburst prediction model based on in situ stress field inversion and neural network is applied to the rockburst prediction analysis, and the results are basically consistent with the actual engineering situation. At the same time, based on the division of rockburst risk areas, according to different rockburst levels, the corresponding treatment methods are proposed to avoid the occurrence of rockburst disasters.

Data Availability

The data are available and explained in this article; readers can access the data supporting the conclusions of this study.

Conflicts of Interest

The authors declare that there are no conflicts of interest.

Authors' Contributions

The manuscript was approved by all authors for publication.

Acknowledgments

This research was supported by the National Natural Science Foundation of China Youth Fund Project (41702320).

References

- [1] X. Feng, Q. Zhang, and M. Ali, "3d modelling of the strength effect of backfill-rocks on controlling rockburst risk: a case study," *Arabian Journal of Geosciences*, vol. 13, no. 3, 2020.
- [2] X. Li, S. Chen, E. Wang, and Z. Li, "Rockburst mechanism in coal rock with structural surface and the microseismic (ms) and electromagnetic radiation (emr) response," *Engineering Failure Analysis*, vol. 124, no. 3, Article ID 105396, 2021.
- [3] Y. Pan, Z. Yong, and M. Y. Guang, "Mechanism and catastrophe theory analysis of circular tunnel rockburst," *Applied Mathematics and Mechanics*, vol. 27, no. 6, pp. 841–852, 2006.
- [4] J. Pan, F. Ren, and M. Cai, "Effect of joint density on rockburst proneness of the elastic-brittle-plastic rock mass," *Shock and Vibration*, vol. 2021, Article ID 5574325, 9 pages, 2021.
- [5] X. Wang, K. Guan, T. Yang, and X. Liu, "Instability mechanism of pillar burst in asymmetric mining based on cusp catastrophe model," *Rock Mechanics and Rock Engineering*, vol. 54, no. 3, pp. 1463–1479, 2021.
- [6] L. Ran, Y. Ye, N. Hu, C. Hu, and X. Wang, "Classified prediction model of rockburst using rough sets-normal cloud," *Neural Computing and Applications*, vol. 31, no. 6, 2019.
- [7] Y. Xue, Z. Li, S. Li et al., "Prediction of rock burst in underground caverns based on rough set and extensible comprehensive evaluation," *Bulletin of Engineering Geology and the Environment*, vol. 78, no. 1, pp. 417–429, 2019.
- [8] T. H. Ma, C. A. Tang, S. B. Tang et al., "Rockburst mechanism and prediction based on microseismic monitoring," *International Journal of Rock Mechanics and Mining Sciences*, vol. 110, pp. 177–188, 2018.
- [9] G. Li, Y. Hu, Q. B. Li, T. Yin, J. X. Miao, and M. Yao, "Inversion method of in-situ stress and rock damage characteristics in dam site using neural network and numerical simulation—a case study," *IEEE Access*, vol. 8, Article ID 46701, 2020.
- [10] L. Gan, M. Weibin, T. Siming, and Z. Wenhao, "Effects of high-pre-tension support system on soft rock large deformation of perpendicularly crossing tunnels," *Advances in Civil Engineering*, vol. 2020, Article ID 6669120, 18 pages, 2020.
- [11] G. Li, W. Ma, S. Tian, Z. Hongbo, F. Huabin, and W. Zou, "Groundwater inrush control and parameters optimization of curtain grouting reinforcement for the jingzhai tunnel," *Geofluids*, vol. 2021, Article ID 6634513, 10 pages, 2021.
- [12] B. Ji, F. Xie, X. Wang, S. He, and D. Song, "Investigate contribution of multi-microseismic data to rockburst risk prediction using support vector machine with genetic algorithm," *IEEE Access*, vol. 8, Article ID 58817, 2020.
- [13] X. P. Zhou, S. L. Peng, J. Z. Zhang, Q. H. Qian, and R. C. Lu, "Predictive acoustical behavior of rockburst phenomena in Gaoligongshan tunnel, Dulong River highway, China," *Engineering Geology*, vol. 247, 2018.
- [14] W. Cai, L. Dou, M. Zhang, W. Cao, J. Q. Shi, and L. Feng, "A fuzzy comprehensive evaluation methodology for rock burst forecasting using microseismic monitoring," *Tunnelling & Underground Space Technology*, vol. 80, pp. 232–245, 2018.
- [15] L. Mo-Xiao, S. Ying-Hua, and Z. Guang, "Study on the fractal characteristics of rock in the prediction of rockburst," *RSC Advances*, vol. 7, no. 68, Article ID 43073, 2017.
- [16] W. Gao, "Forecasting of rockbursts in deep underground engineering based on abstraction ant colony clustering algorithm," *Natural Hazards*, vol. 76, no. 3, pp. 1625–1649, 2015.
- [17] F. Essrich, "Quantitative rockburst hazard assessment at elandsrand gold mine," *The Journal of The South African Institute of Mining and Metallurgy*, vol. 52, no. 7, pp. 107–109, 1997.
- [18] Q. Huang, S. Liu, G. Wang, and W. Cheng, "Evaluating the changes of sorption and diffusion behaviors of Illinois coal with various water-based fracturing fluid treatments," *Fuel*, vol. 283, Article ID 118884, 2021.
- [19] Y. Wang, W. K. Feng, R. L. Hu, and C. H. Li, "Fracture evolution and energy characteristics during marble failure under triaxial fatigue cyclic and confining pressure unloading (FC-CPU) conditions," *Rock Mechanics and Rock Engineering*, vol. 54, pp. 799–818, 2021.
- [20] K. Wu, Z. Shao, and S. Qin, "An analytical design method for ductile support structures in squeezing tunnels," *Archives of Civil and Mechanical Engineering*, vol. 20, no. 3, p. 91, 2020.
- [21] K. Wu, Z. Shao, M. Sharifzadeh, S. Hong, and S. Qin, "Analytical computation of support characteristic curve for circumferential yielding lining in tunnel design," *Journal of Rock Mechanics and Geotechnical Engineering*, vol. 13, pp. 1–13, 2021.
- [22] K. Wu, Z. Shao, S. Qin, W. Wei, and Z. Chu, "A critical review on the performance of yielding supports in squeezing tunnels," *Tunnelling and Underground Space Technology*, vol. 114, Article ID 103815, 2021.
- [23] N. Zhao, Z. Shao, K. Wu, Z. Chu, and S. Qin, "Time-dependent solutions for lined circular tunnels considering rockbolts reinforcement and face advancement effects," *International Journal of Geomechanics*, vol. 21, p. 10, 2021.

- [24] B. Li, R. Bao, Y. Wang, R. Liu, and C. . Zhao, "Permeability evolution of two-dimensional fracture networks during shear under constant normal stiffness boundary conditions," *Rock Mechanics and Rock Engineering*, vol. 54, no. 3, pp. 1–20, 2021.
- [25] Q. Wang, H. Gao, B. Jiang, S. Li, and Q. Qin, "In-situ test and bolt-grouting design evaluation method of underground engineering based on digital drilling," *International Journal of Rock Mechanics and Mining Sciences*, vol. 138, Article ID 104575, 2021.
- [26] Q. Wang, Q. Qin, B. Jiang, S. Xu, and H. Zhang, "Mechanized construction of fabricated arches for large-diameter tunnels," *Automation in Construction*, vol. 124, no. 3, Article ID 103583, 2021.
- [27] A. Li, F. Dai, Y. Liu, H. Du, and R. Jiang, "Dynamic stability evaluation of underground cavern sidewalls against flexural toppling considering excavation-induced damage," *Tunneling and Underground Space Technology*, vol. 112, no. 4, Article ID 103903, 2021.
- [28] X. Yang, J. Wang, C. Zhu, M. He, and Y. Gao, "Effect of wetting and drying cycles on microstructure of rock based on sem," *Environmental Earth Sciences*, vol. 78, no. 6, pp. 1–10, 2019.
- [29] Q. X. Meng, W. Y. Xu, H. L. Wang, X. Y. Zhuang, and T. Rabczuk, "Digisim -an open source software package for heterogeneous material modeling based on digital image processing," *Advances in Engineering Software*, vol. 146, no. 9, p. 16, 2020.
- [30] Q. Yin, J. Wu, C. Zhu, M. He, and H. Jing, "Shear mechanical responses of sandstone exposed to high temperature under constant normal stiffness boundary conditions," *Geomechanics and Geophysics for Geo-Energy and Geo-Resources*, vol. 7, no. 2, pp. 1–17, 2021.
- [31] W. Qi, B. Zja, J. Bei, B. Hga, B. Yha, and Z. Peng, "Research on an automatic roadway formation method in deep mining areas by roof cutting with high-strength bolt-grouting," *International Journal of Rock Mechanics and Mining Sciences*, vol. 128, 2020.

Research Article

Study on the Mixed Materials Proportion of Stratum Based on the Modelling Experiment

Yijun Zhou¹ and Tao Xu² 

¹College of Architecture and Engineering, North China University of Science and Technology, Tangshan 063210, China

²School of Civil Engineering, Southeast University, Nanjing 211189, China

Correspondence should be addressed to Tao Xu; xu-tao@seu.edu.cn

Received 4 May 2021; Accepted 19 May 2021; Published 26 May 2021

Academic Editor: Xiaohu Zhang

Copyright © 2021 Yijun Zhou and Tao Xu. This is an open access article distributed under the Creative Commons Attribution License, which permits unrestricted use, distribution, and reproduction in any medium, provided the original work is properly cited.

It is highly significant to select similar materials as well as the proportion of mixed materials in the model test. The mixed materials are used to simulate the stratum of the model test, including the iron ore powder, natural sands, gypsum, and lime. The stratum contains silty clay and silt soil. First of all, the symmetry coefficient of model mechanics parameters are calculated by the equation, and the symmetry ratio is 16:1. Second, calculate the proportion of compositions in mixed materials by the orthogonal test. The deviation method is used to analyze the mixed materials and how to influence the elastic modulus, cohesion, and friction angle. Finally, get the mixed materials which meet the symmetry theory and control factors.

1. Introduction

The model test is a method that uses the symmetry theory to reduce the size of the prototype. The symmetrical material is highly significant to the model test, and it usually contains some kinds of materials called mixed materials. Choosing suitable mixed materials can determine the model test whether success or not [1–3].

The mixed materials have been researched by some researchers. In abroad, Fumagalli [4] researched the model test of engineering geology initially in the 1960s. He used gypsum, powder of PbO, expansive soil, and water to simulate the stratum. Han et al. [5] researched the materials of MIB to study the rock and soil. Wang [6] selected the barite, quartz, and vaseline to study proportion of mixed materials in the model test. He found that different proportions of mixed materials lead to different results of the test. Chen and Zuo [7, 8] introduced several materials to study the influence for proportion of stratum, including PbO, gypsum, expansive soil, sands, starch, hardener, and so on.

The symmetry theory is mainly used to guide the model test to determine the proportion for the model and prototype [9–12].

The geology model test is highly complex and is affected by lots of factors, such as density of soil, cohesion of soil, friction angle of soil, elastic modulus of soil, and so on. Therefore, the much more important factor must be controlled, ignoring the less important factors [13–17].

To measure the proportion of mixed materials, some kinds of methods are introduced, including the direct shear test, orthogonal test, deviation analysis method, three axes test, and so on [18–26].

2. Materials and Methods

2.1. Determination of Symmetry Coefficient of Stratum

2.1.1. Symmetry Ratio. In the process of the model test, the symmetry ratio is a crucial step and also determines the model test whether it can correctly react to objective laws or not. The symmetry ratio is the ratio between the prototype and the model and marked C . The definitions of model test parameters are as follows: L is the length, r is the density, δ is the displacement, σ is the stress, ε is the strain, σ^t is the tensile strength, σ^c is the compressive strength, c is the cohesion, ϕ is the friction angle, μ is Poisson's ratio, and f is

the coefficient of friction. All of the parameters of symmetry ratio are given in Table 1.

2.1.2. *Establishment of Symmetry Equation.* According to the symmetry theory, establish the equation of the prototype

and model, including the equilibrium equation, geometric equation, and physical equation.

(1) Establish a symmetrical condition by the equilibrium equation:

$$\text{Equilibrium equation of prototype: } \left\{ \begin{array}{l} \left(\frac{\partial \sigma_x}{\partial x} \right)_p + \left(\frac{\partial \tau_{yx}}{\partial y} \right)_p + \left(\frac{\partial \tau_{zx}}{\partial z} \right)_p + X_p = 0 \\ \left(\frac{\partial \sigma_y}{\partial y} \right)_p + \left(\frac{\partial \tau_{zy}}{\partial z} \right)_p + \left(\frac{\partial \tau_{xy}}{\partial x} \right)_p + Y_p = 0 \\ \left(\frac{\partial \sigma_z}{\partial z} \right)_p + \left(\frac{\partial \tau_{xz}}{\partial x} \right)_p + \left(\frac{\partial \tau_{yz}}{\partial y} \right)_p + Z_p = 0 \end{array} \right. \quad (1)$$

$$\text{Equilibrium equation of model: } \left\{ \begin{array}{l} \left(\frac{\partial \sigma_x}{\partial x} \right)_m + \left(\frac{\partial \tau_{yx}}{\partial y} \right)_m + \left(\frac{\partial \tau_{zx}}{\partial z} \right)_m + X_m = 0 \\ \left(\frac{\partial \sigma_y}{\partial y} \right)_m + \left(\frac{\partial \tau_{zy}}{\partial z} \right)_m + \left(\frac{\partial \tau_{xy}}{\partial x} \right)_m + Y_m = 0 \\ \left(\frac{\partial \sigma_z}{\partial z} \right)_m + \left(\frac{\partial \tau_{xz}}{\partial x} \right)_m + \left(\frac{\partial \tau_{yz}}{\partial y} \right)_m + Z_m = 0 \end{array} \right. \quad (2)$$

Substitute the symmetry coefficient c_σ, c_L, c_X into formula (1), and the following formula is obtained:

$$\left\{ \begin{array}{l} \left(\frac{\partial \sigma_x}{\partial x} \right)_m + \left(\frac{\partial \tau_{yx}}{\partial y} \right)_m + \left(\frac{\partial \tau_{zx}}{\partial z} \right)_m + \frac{c_\gamma c_L}{c_\sigma} X_m = 0 \\ \left(\frac{\partial \sigma_y}{\partial y} \right)_m + \left(\frac{\partial \tau_{zy}}{\partial z} \right)_m + \left(\frac{\partial \tau_{xy}}{\partial x} \right)_m + \frac{c_\gamma c_L}{c_\sigma} Y_m = 0 \\ \left(\frac{\partial \sigma_z}{\partial z} \right)_m + \left(\frac{\partial \tau_{xz}}{\partial x} \right)_m + \left(\frac{\partial \tau_{yz}}{\partial y} \right)_m + \frac{c_\gamma c_L}{c_\sigma} Z_m = 0 \end{array} \right. \quad (3)$$

According to formulas (2) and (3), we can get the equation for c_γ, c_L, c_σ .

$$\frac{c_\gamma c_L}{c_\sigma} = 1. \quad (4)$$

(2) Establish a symmetrical condition by the geometry equation:

TABLE 1: Symmetry coefficient calculation formula.

Parameter	Length	Strain	Density	Volume force	Displacement	Stress	Elastic modulus	Poisson's ratio	Friction angle	Cohesion
Symmetry ratio	$C_L = (L_p/L_m)$	$C_\epsilon = (\epsilon_p/\epsilon_m)$	$C_\gamma = (\gamma_p/\gamma_m)$	$C_X = (X_p/X_m)$	$C_\delta = (\delta_p/\delta_m)$	$C_\sigma = ((\sigma^t)_p/(\sigma^t)_m) = ((\sigma^t)_p/(\sigma^t)_m)$	$C_E = (E_p/E_m)$	$C_\mu = (\mu_p/\mu_m)$	$C_\phi = (\phi_p/\phi_m)$	$C_c = (c_p/c_m)$

$$\text{Geometry equation of prototype: } \left\{ \begin{array}{l} (\varepsilon_x)_p = \left(\frac{\partial u}{\partial x} \right)_p \\ (\varepsilon_y)_p = \left(\frac{\partial v}{\partial y} \right)_p \\ (\varepsilon_z)_p = \left(\frac{\partial w}{\partial z} \right)_p \\ (\gamma_{xy})_p = \left(\frac{\partial u}{\partial y} \right)_p + \left(\frac{\partial v}{\partial x} \right)_p \\ (\gamma_{yz})_p = \left(\frac{\partial v}{\partial z} \right)_p + \left(\frac{\partial w}{\partial y} \right)_p \\ (\gamma_{zx})_p = \left(\frac{\partial u}{\partial z} \right)_p + \left(\frac{\partial w}{\partial x} \right)_p \end{array} \right\}. \quad (5)$$

$$\text{Geometry equation of model: } \left\{ \begin{array}{l} (\varepsilon_x)_m = \left(\frac{\partial u}{\partial x} \right)_m \\ (\varepsilon_y)_m = \left(\frac{\partial v}{\partial y} \right)_m \\ (\varepsilon_z)_m = \left(\frac{\partial w}{\partial z} \right)_m \\ (\gamma_{xy})_m = \left(\frac{\partial u}{\partial y} \right)_m + \left(\frac{\partial v}{\partial x} \right)_m \\ (\gamma_{yz})_m = \left(\frac{\partial v}{\partial z} \right)_m + \left(\frac{\partial w}{\partial y} \right)_m \\ (\gamma_{zx})_m = \left(\frac{\partial u}{\partial z} \right)_m + \left(\frac{\partial w}{\partial x} \right)_m \end{array} \right\}. \quad (6)$$

Substitute the symmetry coefficient $c_\varepsilon, c_\delta, c_L$ into formula (5), and the following formula is obtained:

$$\left\{ \begin{array}{l} (\varepsilon_x)_m \left(\frac{c_\xi c_L}{c_\delta} \right) = \left(\frac{\partial u}{\partial x} \right)_m \\ (\varepsilon_y)_m \left(\frac{c_\xi c_L}{c_\delta} \right) = \left(\frac{\partial v}{\partial y} \right)_m \\ (\varepsilon_z)_m \left(\frac{c_\xi c_L}{c_\delta} \right) = \left(\frac{\partial w}{\partial z} \right)_m \\ (\gamma_{xy})_m \left(\frac{c_\xi c_L}{c_\delta} \right) = \left(\frac{\partial u}{\partial y} \right)_m + \left(\frac{\partial v}{\partial x} \right)_m \\ (\gamma_{yz})_m \left(\frac{c_\xi c_L}{c_\delta} \right) = \left(\frac{\partial v}{\partial z} \right)_m + \left(\frac{\partial w}{\partial y} \right)_m \\ (\gamma_{zx})_m \left(\frac{c_\xi c_L}{c_\delta} \right) = \left(\frac{\partial u}{\partial z} \right)_m + \left(\frac{\partial w}{\partial x} \right)_m \end{array} \right\}. \quad (7)$$

According to formulas (6) and (7), we can get the equation for c_ξ, c_δ, c_L .

$$\frac{c_\xi c_L}{c_\delta} = 1. \quad (8)$$

(3) Establish a symmetrical condition by the physical equation:

$$\left. \begin{array}{l} \text{Physical equation of prototype :} \\ (\varepsilon_x)_p = \frac{1}{E_p} [\sigma_x - \mu(\sigma_y + \sigma_z)]_p \\ (\varepsilon_y)_p = \frac{1}{E_p} [\sigma_y - \mu(\sigma_x + \sigma_z)]_p \\ (\varepsilon_z)_p = \frac{1}{E_p} [\sigma_z - \mu(\sigma_x + \sigma_y)]_p \\ (\gamma_{xy})_p = \left[\frac{2(1+\mu)}{E_p} \tau_{xy} \right]_p \\ (\gamma_{xz})_p = \left[\frac{2(1+\mu)}{E_p} \tau_{xz} \right]_p \\ (\gamma_{yz})_p = \left[\frac{2(1+\mu)}{E_p} \tau_{yz} \right]_p \end{array} \right\} \quad (9)$$

$$\left. \begin{array}{l} \text{Physical equation of model :} \\ (\varepsilon_x)_m = \frac{1}{E_p} [\sigma_x - \mu(\sigma_y + \sigma_z)]_m \\ (\varepsilon_y)_m = \frac{1}{E_p} [\sigma_y - \mu(\sigma_x + \sigma_z)]_m \\ (\varepsilon_z)_m = \frac{1}{E_p} [\sigma_z - \mu(\sigma_x + \sigma_y)]_m \\ (\gamma_{xy})_m = \left[\frac{2(1+\mu)}{E_p} \tau_{xy} \right]_m \\ (\gamma_{xz})_m = \left[\frac{2(1+\mu)}{E_p} \tau_{xz} \right]_m \\ (\gamma_{yz})_m = \left[\frac{2(1+\mu)}{E_p} \tau_{yz} \right]_m \end{array} \right\} \quad (10)$$

Substitute the symmetrical coefficient $c_\varepsilon, c_\sigma, c_\mu, c_E$ into formula (9), and the following formula is obtained.

$$\left. \begin{aligned} (\varepsilon_x)_m &= \frac{c_\sigma}{c_\varepsilon c_E} \frac{1}{E_m} [\sigma_x - c_\mu \mu (\sigma_y + \sigma_z)]_m \\ (\varepsilon_y)_m &= \frac{c_\sigma}{c_\varepsilon c_E} \frac{1}{E_m} [\sigma_y - c_\mu \mu (\sigma_x + \sigma_z)]_m \\ (\varepsilon_z)_m &= \frac{c_\sigma}{c_\varepsilon c_E} \frac{1}{E_m} [\sigma_z - c_\mu \mu (\sigma_x + \sigma_y)]_m \\ (\gamma_{xy})_m &= \frac{c_\sigma}{c_\varepsilon c_E} \left[\frac{2(1+\mu)}{E_p} \tau_{xy} \right]_m \\ (\gamma_{xz})_m &= \frac{c_\sigma}{c_\varepsilon c_E} \left[\frac{2(1+\mu)}{E_p} \tau_{xz} \right]_m \\ (\gamma_{yz})_m &= \frac{c_\sigma}{c_\varepsilon c_E} \left[\frac{2(1+\mu)}{E_p} \tau_{yz} \right]_m \end{aligned} \right\}. \quad (11)$$

According to formulas (10) and (11), we get the equation for $c_\sigma, c_\varepsilon, c_E$. The symmetry coefficient of Poisson's is $c_\mu = 1$.

$$\frac{c_\sigma}{c_\varepsilon c_E} = 1. \quad (12)$$

2.1.3. Symmetry Ratio Determination. According to the symmetry theory and the size of model box, finally the symmetry ratio in the model test is $C_L = 16:1$. It is assumed that the symmetry ratio of density is $1:1$, and the dimensionless parameter is $1:1$. Therefore, all of the parameters of symmetry ratio in the model test are given in Table 2.

3. Testing

3.1. Selecting of Stratum Symmetry Materials

3.1.1. Prototype Stratum Parameters. In the model test, selecting the soil of Shanghai is considered as the prototype stratum. The information of prototype stratum in Shanghai is given in Table 3. According to formula (13), the relationship between compression modulus and elastic modulus is

$$E = E_S \left(1 - \frac{2\mu^2}{1-\mu} \right), \quad (13)$$

where E is the elastic modulus of soil, kPa; E_S is the compression modulus of soil, kPa; μ is Poisson's ratio of soil.

Based on the exiting conclusion of research, finally, it selected mixed materials to research stratum in the model test, including iron ore powder, natural sands, gypsum, and lime. The iron ore powder and natural sands are aggregate, which have a great density. The gypsum and lime is the adhesive, which has better sticky property and great tension. In addition, the mixed materials are no harm for beings, easily available, low cost, and so on.

3.1.2. Determination of Mixed Materials Ratio Initially. According to the direct shear test for many times, rely on the density of symmetry ratio. The mixed materials ratio is obtained initially, as given in Table 4. The mixed materials are made to simulate each stratum, as given in Table 5.

From what has been researched above, it just studies about the mixed materials ratio for silty clay and silt soil.

3.2. Determination of Mechanics Parameters for Stratum Symmetry Materials

3.2.1. Design of the Orthogonal Test. The orthogonal test is used to research the proportion of mixed materials, design three factors and three levels, a total of nine tests, according to the purpose of the test, considering the density, cohesion, friction angle, elastic modulus, and Poisson's ratio as the control index, as given in Table 6.

3.2.2. Parameters of the Orthogonal Test. In order to get the five parameters, that is, density, cohesion, friction angle, elastic modulus, and Poisson's ratio, the research adopts, respectively, the density test, the direct shear test, elastic modulus test, and Poisson's ratio test.

(1) Density test

In the density test, the formula of density is given in the following equation, and the instruments are given in Table 7.

$$\rho = \frac{m_1 - m_2}{V_2}, \quad (14)$$

ρ is the density of soil, g/cm³; m_1 is the total quality of soil and ring knife, g; m_2 is the quality of ring knife, g; V_2 is the volume of ring knife, cm³.

(2) Direct shear test

The direct shear test is a common method to measure the shear strength of soil. There is about four times to measure the shear strength in one direct shear test, under different vertical pressures, measuring the shear stress when soil is destroyed. The formula is given as follows:

$$\tau_f = c + \sigma \tan \phi, \quad (15)$$

τ_f is the shear strength of soil, kPa; c is the cohesion of soil, kPa; ϕ is the friction angle of soil; σ is the vertical stress, kPa.

(3) Poisson's ratio and the elastic modulus test

The value of Poisson's ratio is measured by two steps:

- (a) The lateral pressure coefficient K_0 of soil samples is obtained by the static pressure coefficient test
- (b) Getting the value of Poisson's ratio according to the generalized Hooker's law

The elastic modulus is measured from the lateral compression test of similar materials, as shown in Figure 1, and the formula is derived as follows:

TABLE 2: Each of parameter for symmetry ratio.

Parameter	Geometry	Displacement	Stress	Strain	Cohesion	Friction angle	Elastic modulus	Poisson's ratio	Bending moment
Prototype	16	16	16	1	16	1	16	1	16 ⁴
Model	1	1	1	1	1	1	1	1	1

TABLE 3: The physical quantity of prototype stratum in Shanghai.

Stratum	Density (kN/m ³)	Cohesion (kPa)	Friction angle (°)	Elastic modulus (MPa)	Poisson's ratio	Thickness of stratum (m)
Fill the soil	18.5	0	15	11	0.33	0.64
Silty clay	19.2	20	17	38	0.36	1.92
Silt soil	17.5	13	11	10	0.31	17.6
Silty clay	18.4	27	14	42	0.34	6.24

TABLE 4: Mixed materials finished initially.

Proportion of iron and sand in mixture (%)	Quality ratio between iron and sand	Quality ratio between gypsum and lime	Volume ratio between water and gypsum
85	1.5:3.5	1:1	2:8

TABLE 5: Simulation materials of each stratigraphic.

Stratum	Thickness of prototype (m)	Thickness of the model (cm)	Mixed materials
Fill the soil	0.64	4	Natural sands
Silty clay	1.92	12	Iron ore powder, natural sands, gypsum, and lime
Silt soil	17.6	110	Iron ore powder, natural sands, gypsum, and lime
Silty clay	6.24	39	Iron ore powder, natural sands, gypsum, and lime

TABLE 6: Value of control index.

Factors	Proportion of iron and sand in mixture (%)	Quality ratio between iron and sand	Quality ratio between gypsum and lime
Level 1	80	2:3	2:1
Level 2	85	1.5:3.5	1:1
Level 3	90	1:4	1:2

TABLE 7: Instrument of the density test.

Name	Ring knife	Balance	Vernier caliper	Compaction meter
Parameters	Internal diameter, 6–8 cm; height 2 cm	Accuracy, 0.1 g	Accuracy, 0.02 mm	Diameter, 100 mm; height, 127 mm; volume, 997 cm ³

According to generalized Hooke's law,

$$\varepsilon_x + \varepsilon_y = 0, \quad (16)$$

$$\varepsilon_x = \frac{\sigma_x}{E} - \frac{\mu(\sigma_y + \sigma_z)}{E}, \quad (17)$$

$$\varepsilon_y = \frac{\sigma_y}{E} - \frac{\mu(\sigma_x + \sigma_z)}{E}. \quad (18)$$

Substituting formulas (17) and (18) into formula (16), the following equation is obtained:

$$K_0 = \frac{\sigma_x}{\sigma_z} = \frac{\mu}{1 - \mu}, \quad (19)$$

where μ is Poisson's ratio; K_0 is the side pressure coefficient; E is the elastic modulus, kPa.

According to generalized Hooke's law, the strain of Z axis is given in the following formula:

$$\varepsilon_z = \frac{\sigma_z}{E} - \frac{\mu(\sigma_x + \sigma_y)}{E}. \quad (20)$$

Substituting $\sigma_z = p$, $\sigma_x = \sigma_y = (\mu/(1 - \mu))p$ into formula (20), the following equation is obtained:

$$E = \frac{P}{\varepsilon_z} \left(1 - \frac{2\mu^2}{1 - \mu} \right), \quad (21)$$

$$\varepsilon_z = \frac{\Delta H}{H} = \frac{(e_0 - e_1)}{(1 + e_0)}. \quad (22)$$

Compression coefficient under confinement conditions is

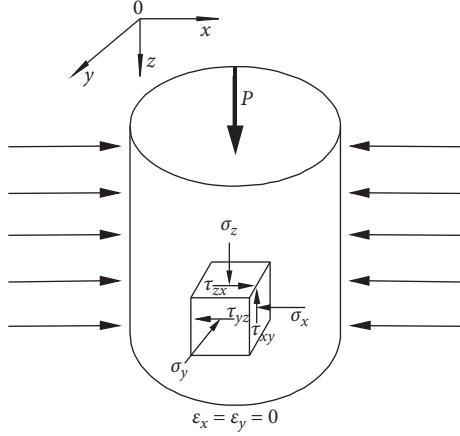


FIGURE 1: Stress condition of the confined compress test.

$$a = \frac{\Delta e}{\Delta \sigma} = \frac{(e_0 - e_1)}{P}. \quad (23)$$

Finally, formula (21) is given as follows:

$$E = \frac{1 + e_0}{a} \left(1 - \frac{2\mu^2}{1 - \mu} \right). \quad (24)$$

Compression modulus under confinement conditions is

$$E_S = \frac{1 + e_0}{a}, \quad (25)$$

$$E = E_S \left(1 - \frac{2\mu^2}{1 - \mu} \right),$$

where E_S is the compression modulus under confinement conditions, kPa; e_0 is the porosity ratio; a is the compression coefficient under confinement conditions, kPa^{-1} ; Δe is the change of the amount porosity ratio; $\Delta \sigma$ is the change of the amount vertical stress, kPa.

4. Results and Analysis

According to design and the performed orthogonal test, the results of the orthogonal test obtained are given in Table 8.

Because the value of density almost has no change, as well as Poisson's ratio, they are out of consideration in the following test.

First of all, to produce the mixed materials, select the cohesive force, the friction angle, and the elastic modulus as the control factor.

4.1. Analysis of Cohesive Force as the Control Factor. According to the results of the orthogonal test for nine group data, calculate the relative error of nine group cohesive data. The smaller the value of relative error, the more accurate the results, as given in Table 9.

According to the orthogonal test and relative error of cohesive, the dispersion of factors for A , B , and C is

$$\begin{aligned} A: & (I_A - \delta)^2 + (II_A - \delta)^2 + (III_A - \delta)^2 = 112.92, \\ B: & (I_B - \delta)^2 + (II_B - \delta)^2 + (III_B - \delta)^2 = 14.82, \\ C: & (I_C - \delta)^2 + (II_C - \delta)^2 + (III_C - \delta)^2 = 35.25. \end{aligned} \quad (26)$$

From the test results analysis and Figure 2, we can see that

- The relationship between the A , B , and C is $A > C > B$
- The factor 2 point is inflection point, and the line changes suddenly when through the factor 2 point.
- $A1, B2, C2$ is the closest value, respectively, in each factor compared with the prototype cohesion value

4.2. Analysis of Friction Angle as the Control Factor. According to the results of the orthogonal test for nine group data, calculate the relative error of nine group friction angle data. The smaller the value of relative error, the more accurate the results, as given in Table 10.

According to the orthogonal test and relative error of friction angle, the dispersion of factors for A , B , and C is

$$\begin{aligned} A: & (I_A - \delta)^2 + (II_A - \delta)^2 + (III_A - \delta)^2 = 0.0481, \\ B: & (I_B - \delta)^2 + (II_B - \delta)^2 + (III_B - \delta)^2 = 0.0065, \\ C: & (I_C - \delta)^2 + (II_C - \delta)^2 + (III_C - \delta)^2 = 0.0099. \end{aligned} \quad (27)$$

From the test results analysis and Figure 3, we can see that

- The relationship between the A , B , and C is $A > B > C$
- The factor 2 point is inflection point, and the line changes suddenly when through the factor 2 point.
- $A2, B3, C1$ is the closest value, respectively, in each factor for the prototype friction angle value

4.3. Analysis of Elastic Modulus as the Control Factor. According to the results of the orthogonal test for nine group data, calculate the relative error of nine group elastic modulus data. The smaller the value of relative error, the more accurate the results, as given in Table 11.

According to the orthogonal test and relative error of elastic modulus, the dispersion of factors for A , B , and C is

$$\begin{aligned} A: & (I_A - \delta)^2 + (II_A - \delta)^2 + (III_A - \delta)^2 = 50.27, \\ B: & (I_B - \delta)^2 + (II_B - \delta)^2 + (III_B - \delta)^2 = 9.14, \\ C: & (I_C - \delta)^2 + (II_C - \delta)^2 + (III_C - \delta)^2 = 207.40. \end{aligned} \quad (28)$$

From the test results analysis and Figure 4, we can see that

- The relationship between the A , B , and C is $C > A > B$
- The factor 2 point is inflection point, and the line changes suddenly when through the factor 2 point.
- $A3, B2, C1$ is the closest value, respectively, in each factor for the prototype elastic modulus value

As shown in Figures 5 and 6, according to the standard, the samples are damaged when the displacement of

TABLE 8: Orthogonal test conclusion.

Serial number	Proportion of iron and sand in mixture (%)	Quality ratio between iron and sand	Quality ratio between gypsum and lime	Elastic modulus (MPa)	Cohesion (kPa)	Friction angle (°)	Density (g/cm ³)	Poisson's ratio
1	80	2:3	2:1	9.76	16	29	2.24	0.30
2	80	1.5:3.5	1:1	17.95	2.8	31.28	2.16	0.35
3	80	1:4	1:2	23.78	16.05	28.80	2.11	0.37
4	85	2:3	1:1	19.94	29.69	26.60	2.28	0.34
5	85	1.5:3.5	1:2	21.56	22.87	27.19	2.17	0.36
6	85	1:4	2:1	8.43	27.29	25.11	2.05	0.31
7	90	2:3	1:2	16.37	20.06	27.91	2.25	0.35
8	90	1.5:3.5	2:1	2.48	24.48	27.58	2.15	0.30
9	90	1:4	1:1	13.68	10.43	28.48	2.09	0.33

TABLE 9: Cohesive force of relative error analysis.

Serial number	Proportion of iron and sand in mixture (%)	Quality ratio between iron and sand	Quality ratio between gypsum and lime	Relative error
1	80	2:3	2:1	15
2	80	1.5:3.5	1:1	1.8
3	80	1:4	1:2	15.05
4	85	2:3	1:1	28.69
5	85	1.5:3.5	1:2	21.87
6	85	1:4	2:1	26.29
7	90	2:3	1:2	19.06
8	90	1.5:3.5	2:1	23.48
9	90	1:4	1:1	9.43
I	10.62	20.92	21.59	$P = 160.68$
II	25.62	15.72	13.31	$\delta = P/9 = 17.85$
III	17.32	16.92	18.66	

P , the sum of the data for every factor; δ , the average of the data for every factor; I, the average of relative error for factor 1; II, the average of relative error for factor 2; III, the average of relative error for factor 3.

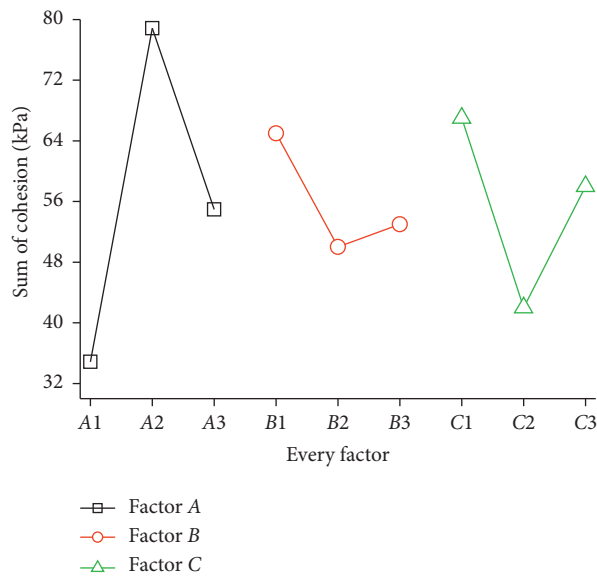


FIGURE 2: Cohesive force of trend diagram.

TABLE 10: Friction angle of relative error analysis.

Serial number	Proportion of iron and sand in mixture (%)	Quality ratio between iron and sand	Quality ratio between gypsum and lime	Relative error
1	80	2:3	2:1	1.64
2	80	1.5:3.5	1:1	1.84
3	80	1:4	1:2	1.62
4	85	2:3	1:1	1.42
5	85	1.5:3.5	1:2	1.47
6	85	1:4	2:1	1.28
7	90	2:3	1:2	1.54
8	90	1.5:3.5	2:1	1.51
9	90	1:4	1:1	1.59
I	1.7	1.53	1.48	$P = 13.92$
II	1.39	1.61	1.62	$\delta = P/9 = 1.55$
III	1.55	1.50	1.54	

P , the sum of the data for every factor; δ , the average of the data for every factor; I, the average of relative error for factor 1; II, the average of relative error for factor 2; III, the average of relative error for factor 3.

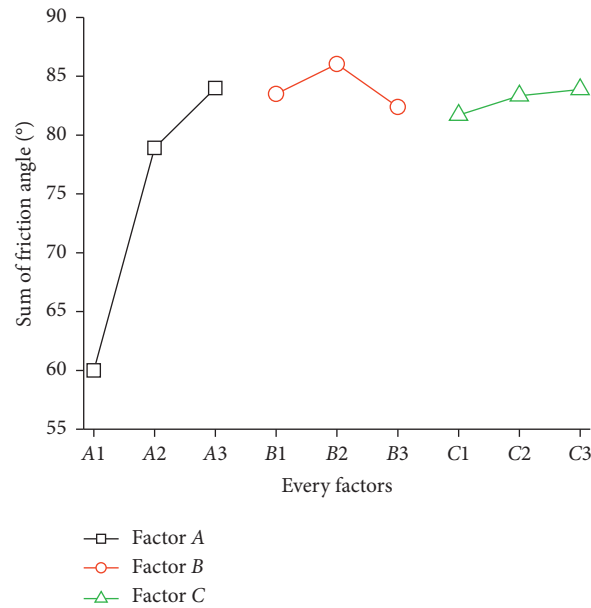


FIGURE 3: Friction angle of trend diagram.

TABLE 11: Elastic modulus of relative error analysis.

Serial number	Proportion of iron and sand in mixture (%)	Quality ratio between iron and sand	Quality ratio between gypsum and lime	Relative error
1	80	2:3	2:1	12.94
2	80	1.5:3.5	1:1	24.64
3	80	1:4	1:2	32.97
4	85	2:3	1:1	27.49
5	85	1.5:3.5	1:2	29.8
6	85	1:4	2:1	11.04
7	90	2:3	1:2	22.39
8	90	1.5:3.5	2:1	2.54
9	90	1:4	1:1	18.54
I	23.52	20.94	8.84	$P = 182.36$
II	22.78	18.99	23.56	$\delta = P/9 = 20.26$
III	14.49	20.85	28.39	

P , the sum of the data for every factor; δ , the average of the data for every factor; I, the average of relative error for factor 1; II, the average of relative error for factor 2; III, the average of relative error for factor 3.

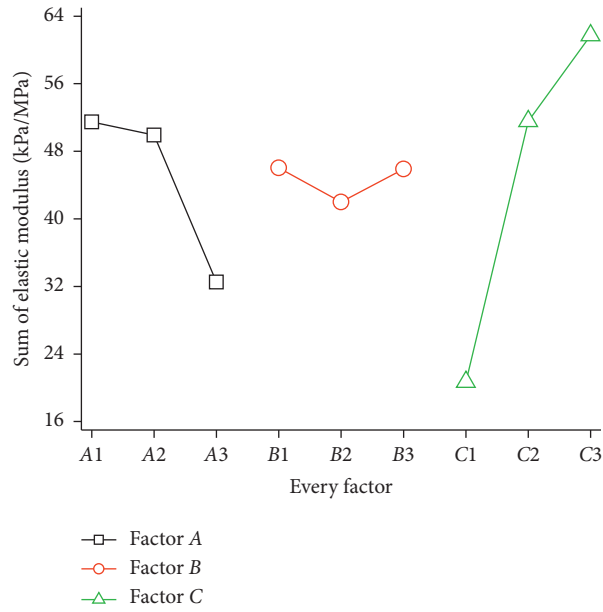


FIGURE 4: Elastic modulus of trend diagram.

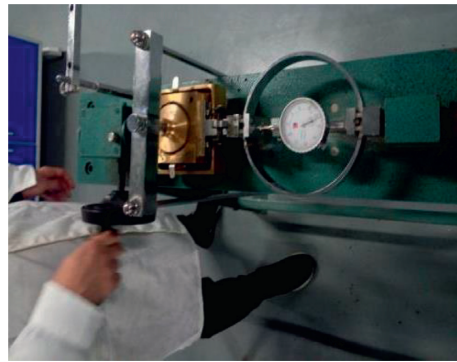


FIGURE 5: Action cycle of direct shear apparatus.

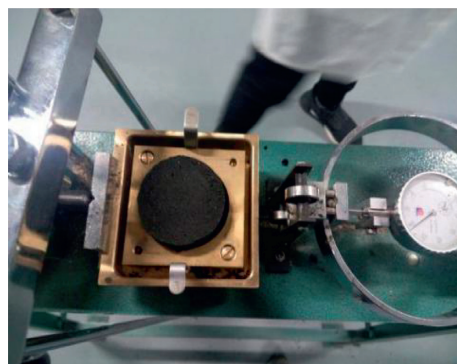


FIGURE 6: Failure model of test piece.

samples has no change obviously in the direct shear test. Finally, the proportion of mixed materials is shown in Figure 7. Based on the above three control factors, use the direct shear test to get the proportion of mixed materials, as given in Table 12.

Use the parameters of mixed materials to compare with the parameters of the prototype and model. It is proved that the proportion of mixed materials is reasonable and meets the requirements of symmetry ratio, as given in Tables 13 and 14.

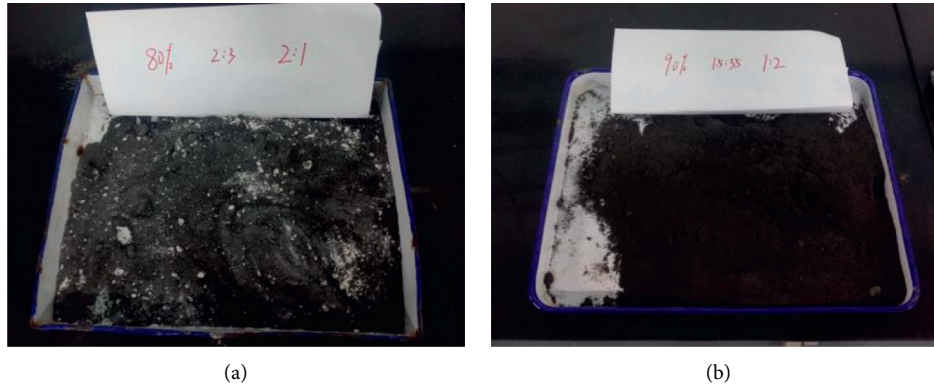


FIGURE 7: Proportion of mixed materials.

TABLE 12: Mixed material proportion table.

Mixed materials	Proportion of iron and sand in mixture (%)	Quality ratio between iron and sand	Quality ratio between gypsum and lime
Silt soil	80	2:3	2:1
Silty clay	90	1.5:3.5	1:2

TABLE 13: Comparison of physical mechanical parameters for silty clay.

Materials	Elastic modulus (MPa)	Density (kN/m ³)	Cohesion (kPa)	Friction angle (°)	Poisson's ratio
Prototype	30.8	19.8	29	15	0.36
Model	1.92	19.8	1.81	15	0.36
Test	2.08	21.03	1.98	20.36	0.33

TABLE 14: Comparison of physical mechanical parameters for silt soil.

Materials	Elastic modulus (MPa)	Density (kN/m ³)	Cohesion (kPa)	Friction angle (°)	Poisson's ratio
Prototype	10	17.5	13	11	0.31
Model	0.7	17.5	1	11	0.31
Test	0.95	18.7	2.11	12.21	0.34

5. Conclusion

- (1) According to the symmetry theory, establish the equilibrium equation, geometric equation, and physical equation for the prototype and model. The symmetry ration of mixed materials is 16:1.
- (2) Select the iron ore powder, natural sands, gypsum, and lime to be the mixed materials for model stratum. Use the orthogonal tests to get the proportion of compositions in mixed materials and analyze the results by the deviation.
- (3) The proportion of compositions in mixed materials of silt soil is that the proportion of iron and sand in mixture is 80%, the quality ratio between iron and sand is 2:3, and the quality ratio between gypsum and lime is 2:1.

The proportion of compositions in mixed materials of silty clay is that the proportion of iron and sand in mixture is 90%, the quality ratio between iron and sand is 1.5:3.5, and the quality ratio between gypsum and lime is 1:2.

It is proved that the proportion of compositions in mixed materials is reasonable and meets the requirements of symmetry ratio compared with the parameters of the prototype and model.

Data Availability

The data used to support the findings of this study are included within the article.

Conflicts of Interest

The authors declare that there are no conflicts of interest.

Acknowledgments

The research was supported by the Fundamental Scientific Research Business Expenses of Provincial Universities in Hebei Province (JQN2020027) and North China University of Science and Technology Doctoral Research Startup Fund (BS201813).

References

- [1] D. L. Luo, B. Gao, and Y. S. Sheng, "Study on similar materials of surrounding rock in tunnel anti-damping model test," *Journal of Shijiazhuang Railway Institute (Natural Science)*, vol. 21, no. 3, pp. 70–73, 2008.
- [2] A. M. Chen, J. C. Gu, and J. Shen, "Application study on the geomechanical model experiment techniques," *Chinese Journal of Rock Mechanics and Engineering*, vol. 23, no. 22, pp. 3785–3789, 2004.
- [3] H. M. Peng, Z. B. Peng, and J. T. Han, "Study on lithologic similar materials," *Guangdong Architecture Civil Engineering*, vol. 12, no. 12, pp. 12–17, 2002.
- [4] E. Fumagalli, *Static and Geomechanical Models*, China Water Conservancy and Hydropower Press, Beijing, China, 1979.
- [5] B. L. Han, X. L. Chen, and Y. L. Song, "Study on similar materials of rock mass," *Journal of Wuhan University of Hydraulic and Electrical Engineering*, vol. 30, no. 2, pp. 6–9, 1997.
- [6] S. P. Wang, *Model Test Study on the Tunnel with in Cracked Surrounding Rocks*, Zhejiang University, Zhejiang, China, 2004.
- [7] X. H. Chen, *Brittle Material Structure Model Test*, Water Resources and Electricity Press, Beijing, China, 2000.
- [8] D. Q. Zuo, *The Theory and Method of Model Test*, Water Resources and Electricity Press, Beijing, China, 2001.
- [9] W. F. Chen, *Constitutive Equations for Engineering Materials: Plasticity and Modeling*, Vol. 2, Elsevier, Amsterdam, The Netherlands, 1994.
- [10] F. Armero and S. Oller, "A general framework for continuum damage models. I. infinitesimal plastic damage models in stress space," *International Journal of Solids and Structures*, vol. 37, no. 48–50, pp. 7409–7436, 2000.
- [11] G. Meschke, R. Lackner, and H. A. Mang, "An anisotropic elastoplastic-damage model for plain concrete," *International Journal for Numerical Methods in Engineering*, vol. 42, no. 4, pp. 703–727, 1998.
- [12] J. Y. Wu, J. Li, and R. Faria, "An energy release rate-based plastic-damage model for concrete," *International Journal of Solids and Structures*, vol. 43, no. 3–4, pp. 583–612, 2006.
- [13] I. Carol, P. C. Prat, and C. M. López, "Normal/shear cracking model: application to discrete crack analysis," *Journal of Engineering Mechanics*, vol. 123, no. 8, pp. 765–773, 1997.
- [14] G. T. Camacho and M. Ortiz, "Computational modelling of impact damage in brittle materials," *International Journal of Solids and Structures*, vol. 33, no. 20–22, pp. 2899–2938, 1996.
- [15] F. Armero, "Large-scale modeling of localized dissipative mechanisms in a local continuum: applications to the numerical simulation of strain localization in rate-dependent inelastic solids," *Mechanics of Cohesive-frictional Materials*, vol. 4, no. 2, pp. 101–131, 1999.
- [16] J.-Y. Wu, "Unified analysis of enriched finite elements for modeling cohesive cracks," *Computer Methods in Applied Mechanics and Engineering*, vol. 200, no. 45–46, pp. 3031–3050, 2011.
- [17] J.-Y. Wu and S.-L. Xu, "An augmented multicrock elastoplastic damage model for tensile cracking," *International Journal of Solids and Structures*, vol. 48, no. 18, pp. 2511–2528, 2011.
- [18] C. Zhu, K. Zhang, H. Cai et al., "Combined application of optical fibers and CRLD bolts to monitor deformation of a pit-in-pit foundation," *Advances in Civil Engineering*, vol. 2019, Article ID 2572034, 16 pages, 2019.
- [19] M. Cervera and J.-Y. Wu, "On the conformity of strong, regularized, embedded and smeared discontinuity approaches for the modeling of localized failure in solids," *International Journal of Solids and Structures*, vol. 71, pp. 19–38, 2015.
- [20] E. Haghghat and S. Pietruszczak, "On modeling of discrete propagation of localized damage in cohesive-frictional materials," *International Journal for Numerical and Analytical Methods in Geomechanics*, vol. 39, no. 16, pp. 1774–1790, 2015.
- [21] C. Zhu, Z. Yan, Y. Lin, F. Xiong, and Z. Tao, "Design and application of a monitoring system for a deep railway foundation pit project," *IEEE Access*, vol. 7, pp. 107591–107601, 2019.
- [22] J. Su, Y. Wang, P. Yang, S. Han, N. Han, and W. Li, "Evaluating and modeling the idb of microencapsulated rejuvenator in aged bitumen by FTIR-ATR tests," *Materials*, vol. 9, no. 11, pp. 932–947, 2016.
- [23] Q.-X. Meng, W.-Y. Xu, H.-L. Wang, X.-Y. Zhuang, W.-C. Xie, and T. Rabczuk, "DigiSim-an open source software package for heterogeneous material modeling based on digital image processing," *Advances in Engineering Software*, vol. 148, Article ID 102836, 2020.
- [24] C. Zhu, M.-c. He, M. Karakus, X.-h. Zhang, and Z. Guo, "The collision experiment between rolling stones of different shapes and protective cushion in open-pit mines," *Journal of Mountain Science*, vol. 18, no. 5, pp. 1391–1403, 2021.
- [25] Q. Yin, J. Y. Wu, C. Zhu, M. C. He, and Q. X. Meng, "Shear mechanical responses of sandstone exposed to high temperature under constant normal stiffness boundary conditions," *Geomechanics and Geophysics for Geo-Energy and Geo-Resources*, vol. 7, p. 35, 2021.
- [26] Q. Wang, Z. Jiang, B. Jiang, H. Gao, Y. Huang, and P. Zhang, "Research on an automatic roadway formation method in deep mining areas by roof cutting with high-strength bolt-grouting," *International Journal of Rock Mechanics and Mining Sciences*, vol. 128, Article ID 104264, 2020.